

TEXTS AND READINGS IN THE PHYSICAL SCIENCES - 10

COMPUTATIONAL STATISTICAL PHYSICS

Edited by
Sitangshu Bikas Santra
and
Purusattam Ray

 HINDUSTAN
BOOK AGENCY

Computational Statistical Physics

Lecture Notes, Guwahati SERC School

Texts and Readings in Physical Sciences

Managing Editors

H. S. Mani, Chennai Mathematical Institute, Chennai.
hsmani@gmail.com

Ram Ramaswamy, Jawaharlal Nehru University, New Delhi.
r.ramaswamy@gmail.com

Editors

Kedar Damle (TIFR, Mumbai) kedar@tifr.res.in
Debashis Ghoshal (JNU, New Delhi) dghoshal@mail.jnu.ac.in
Rajaram Nityananda (NCRA, Pune) rajaram@ncra.tifr.res.in
Gautam Menon (IMSc, Chennai) menon@imsc.res.in
Tarun Souradeep (IUCAA, Pune) tarun@iucaa.ernet.in

Volumes published so far

1. Field Theories in Condensed Matter Physics, *Sumathi Rao* (Ed.)
2. Numerical Methods for Scientists and Engineers (2/E), *H. M. Antia*
3. Lectures on Quantum Mechanics, *Ashok Das*
4. Lectures on Electromagnetism, *Ashok Das*
5. Current Perspectives in High Energy Physics, *Debashis Ghoshal* (Ed.)
6. Linear Algebra and Group Theory for Physicists (2/E), *K. N. Srinivasa Rao*
7. Nonlinear Dynamics: Near and Far from Equilibrium, *J. K. Bhattacharjee and S. Bhattacharyya*
8. Spacetime, Geometry and Gravitation, *Pankaj Sharan*
9. Lectures on Advanced Mathematical Methods for Physicists, *Sunil Mukhi and N. Mukunda*

Computational Statistical Physics

Lecture Notes, Guwahati SERC School

Edited By
Sitangshu Bikas Santra
and
Purusattam Ray



Published in India by
Hindustan Book Agency (India)
P 19 Green Park Extension
New Delhi 110 016
India

email: info@hindbook.com
www.hindbook.com

Copyright © 2011, Hindustan Book Agency (India)

No part of the material protected by this copyright notice may be reproduced or utilized in any form or by any means, electronic or mechanical, including photocopying, recording or by any information storage and retrieval system, without written permission from the copyright owner, who has also the sole right to grant licences for translation into other languages and publication thereof.

All export rights for this edition vest exclusively with Hindustan Book Agency (India). Unauthorized export is a violation of Copyright Law and is subject to legal action.

ISBN 978-93-80250-15-1 ISBN 978-93-86279-50-7 (eBook)
DOI 10.1007/978-93-86279-50-7

Texts and Readings in the Physical Sciences

The Texts and Readings in the Physical Sciences (TRiPS) series of books aims to provide a forum for physical scientists to describe their fields of research interest. Each book is intended to cover a subject in a detailed manner and from a personal viewpoint, so to give students in the field a unique exposure to the subject that is at once accessible, pedagogic, and contemporary. The monographs and texts that have appeared so far, as well as the volumes that we plan to bring out in the coming years, cover a range of areas at the core as well as at the frontiers of physics.

In addition to texts on a specific topic, the TRiPS series includes lecture notes from a thematic School or Workshop and topical volumes of contributed articles focussing on a currently active area of research. Through these various forms of exposition, we hope that the series will be valuable both for the beginning graduate student as well as the experienced researcher.

H.S. Mani
Chennai

R. Ramaswamy
New Delhi

Contents

Preface	xiii
1 Statistical Mechanics and Critical Phenomena: A Brief Overview	1
<i>Sitangshu Bikas Santra and Purusattam Ray</i>	1
1.1 Introduction	1
1.2 Specification of Macro and Microstates	2
1.3 Statistical Ensembles	4
1.4 Condition of Statistical Equilibrium	5
1.5 Postulates of Statistical Mechanics	6
1.5.1 Equal a priori probability	6
1.5.2 Principle of ergodicity	6
1.6 Thermodynamics in Different Ensembles	7
1.6.1 Microcanonical ensemble (E, N, V)	7
1.6.2 Canonical ensemble (N, V, T)	9
1.6.3 Grand canonical ensemble (μ, V, T)	10
1.7 Statistical Definitions of Thermodynamic Quantities	12
1.7.1 Fluid system	12
1.7.2 Magnetic system:	13
1.8 Stability and Positive Response Functions	13
1.9 Positive Response Function and Free Energy	14
1.10 Fluctuation and Response Functions	15
1.11 Phase Transitions	17
1.11.1 Metastability and symmetry breaking	20
1.12 Critical Phenomena	22
1.12.1 Fluctuation and correlation	24
1.12.2 Critical exponents and universality	25
1.12.3 Models and universality	27
1.12.4 Homogeneity and scaling	30
1.13 Concluding Remarks	32

2 Graphical Enumeration Techniques: Series Expansions and Animal Problems	35
<i>Deepak Dhar</i>	35
2.1 Introduction	35
2.2 Ising Model in One Dimension	36
2.3 High-temperature Expansions for Ising Systems	37
2.4 Low-temperature Expansion of the Ising Model and Self-duality	41
2.5 Percolation and Animal Problems	42
2.6 Algorithm for Enumerating Clusters	44
2.7 The Animal Problem	46
2.7.1 The Bethe lattice	47
2.7.2 Directed Animals	48
2.8 Heaps	50
3 Graphical Enumeration Techniques: Application to Polymers	55
<i>Sanjay Kumar</i>	55
3.1 Introduction	55
3.2 Upper and Lower Bounds on the Connectivity Constant	57
3.3 Method: Exact Enumeration Technique and Series Analysis	57
3.4 The SAWs on Fractals	59
3.5 Application to Polymers	62
3.5.1 Coil-Globule transition	62
3.5.2 Adsorption of a polymer Chain	63
3.5.3 Simultaneous Adsorption and Collapse Transition	64
3.5.4 Stretching of Polymers	65
3.6 Conclusion	65
4 Classical Monte Carlo Simulation	67
<i>Sitangshu Bikas Santra and Purusattam Ray</i>	67
4.1 Introduction	67
4.2 Probability Theory: A Few Definitions	68
4.2.1 Conditional Probability: Dependent and Independent Events	68
4.2.2 Mutually Exclusive Events	69
4.2.3 Expectation and Variance of Random Events	70
4.3 Probability Distributions	71
4.3.1 Binomial Distribution	71
4.3.2 Normal Distribution	71
4.3.3 Poisson Distribution	72
4.4 Central Limit Theorem	72
4.5 Markov Process and Markov Chain	72
4.6 Random Number Generators	75
4.6.1 Congruential Method	76

4.6.2	Shift Register Algorithms	77
4.6.3	Lagged Fibonacci Generators	77
4.7	Test of Quality	77
4.7.1	Frequency Test	78
4.7.2	Correlation Test	78
4.7.3	Parking Lot Test	78
4.8	Monte Carlo Technique for Physical Systems	79
4.9	Simple Sampling Monte Carlo	81
4.10	Importance Sampling Monte Carlo	96
4.11	Error Analysis	105
4.11.1	Statistical Error	105
4.11.2	Systematic Error	106
4.12	Finite Size Scaling analysis	106
4.12.1	Finite Size Scaling in Second Order Phase Transitions	109
4.12.2	Finite Size Scaling in First Order Phase Transitions	111
4.13	Critical Slowing Down and Cluster Algorithm	114
4.13.1	Relaxation Effects	114
4.13.2	Critical Slowing Down	114
4.14	Fortuin-Kasteleyn Mapping	115
4.15	Swendsen-Wang Algorithm	116
4.16	Wolff Algorithm	118
5	Kinetics of Phase Transitions: Numerical Techniques and Simulations	123
	<i>Sanjay Puri</i>	123
5.1	Introduction	123
5.2	Kinetic Ising Models and their Coarse-Grained Counterparts	126
5.2.1	Introduction	126
5.2.2	The Spin-Flip Glauber Model	127
5.2.3	Phase Ordering Dynamics: Nonconserved Kinetics	131
5.2.4	The Spin-Exchange Kawasaki Model	136
5.2.5	Phase Ordering Dynamics: Conserved Kinetics	143
5.3	Monte Carlo Techniques	149
5.3.1	Equilibrium Systems	149
5.3.2	Nonequilibrium Systems	151
5.4	Simulation of Coarse-Grained Models	153
5.4.1	The Diffusion Equation	153
5.4.2	Domain Growth Models	155
5.5	Summary and Discussion	157

6	Introduction to Molecular Dynamics Simulation	161
	<i>Hemant Kumar and Prabal K Maiti</i>	161
6.1	Introduction	161
6.1.1	History Of Simulation	162
6.2	Building Model	163
6.2.1	Discussion on Force Fields	165
6.3	Various Schemes of Integration	168
6.3.1	Verlet Algorithm	168
6.3.2	Leap-Frog Algorithm-	169
6.3.3	Velocity-Verlet Algorithm	170
6.3.4	Higher Order Integrator	171
6.3.5	Hamilton Dynamics	172
6.3.6	Dealing with Molecules: SHAKE Alogrithm	175
6.3.7	Boundary Condition	176
6.4	Complexity of Force Calculation	178
6.4.1	Shifted Potential and Force	179
6.4.2	Switching Function	180
6.4.3	Verlet List	180
6.4.4	Cell Lists or Linked List	181
6.4.5	Long Range Interactions: Ewald Sum	182
6.5	Thermostat and Barostat	185
6.5.1	Velocity Rescaling Method	185
6.5.2	Berendsen Weak Coupling method	185
6.5.3	Weak Coupling Barostat for Constant P	188
6.6	Example of MD Simulation	188
6.6.1	Structure and Dynamics of water in Confined Systems	189
6.6.2	Elastic Properties of Boron-Nitride Nanotube	192
7	Applications of Molecular Dynamics Simulations	199
	<i>Subhankur Mitra and Samrath Lal Chaplot</i>	199
7.1	Introduction	199
7.2	Theoretical Background	200
7.2.1	Dynamic Structure Factor	200
7.2.2	Classical Framework	202
7.2.3	Elastic Incoherent Structure Factor	203
7.2.4	Velocity Correlation Functions	204
7.2.5	Mean-square Displacements	205
7.2.6	Structural Quantities	206
7.3	Case Study	207
7.3.1	Diffusion of Hydrocarbons in Zeolitic Pores	207
7.3.2	Phase Transitions in $MgSiO_3$	216
7.3.3	Shock-induced Amorphization of Alpha-quartz	218
7.3.4	Diffuse Scattering from Solid Fullerene	220

7.4	Appendix	222
7.4.1	Computation of Time Correlation Functions	222
7.4.2	Computation of Mean-square Displacements	225
7.4.3	Computation of Intermediate Scattering Functions	226
7.4.4	Computation of Radial Distribution Function, $g(r)$	227
7.4.5	Spatial Distribution Function (SDF)	227
8	The Conjugate Gradient Method for Unconstrained Minimization	231
	<i>Subir K. Sarkar</i>	231
8.1	Introduction	231
8.2	The Conjugate Gradient Method	233
8.3	The Geometry of the Conjugate Directions Method	241
8.4	The Steepest Descent Method	245
8.5	Quasi-Newton Methods	247
8.5.1	Davidon-Fletcher-Powell (DFP) algorithm	248
9	Optimization and Quantum Annealing	251
	<i>Anjan Kumar Chandra and Bikas K. Chakrabarti</i>	251
9.1	Introduction	251
9.2	Some Combinatorial Optimization Problems	253
9.2.1	The Traveling Salesman Problem (<i>TSP</i>)	253
9.2.2	Spin Glass and Optimization	258
9.3	Details of a Few Optimization Techniques	263
9.3.1	Local Search	263
9.3.2	Simulated Annealing	264
9.3.3	Quantum Annealing	266
9.4	Summary	274
List of Authors		279
Index		281

Preface

Computer simulations are now standard tools in the study of physical processes. Moreover, computational studies, viewed as controlled experiments, have always been extremely useful. Recent advances in computer technology have triggered the use of various techniques which involve intricate applications of the knowledge of the concerned physical phenomena in large scale computations. These techniques are particularly useful in statistical physics where a typical problem involves a large number of particles with long range correlations and complicated dynamics.

The Science and Engineering Research Council (SERC) of the Department of Science and Technology (DST), Government of India, provides platform for in-depth discussions and hands-on training to young researchers by sponsoring SERC schools. The aim of the SERC school on “Computational Statistical Physics” held at Indian Institute of Technology Guwahati, Guwahati, India during December 01-21, 2008 was to demonstrate different numerical techniques and their applications in statistical physics problems to young researchers by experts from all over India. The objective was to get them to develop familiarity with the general principles underlying computational techniques and the key attributes pertaining to the various important aspects of statistical physics.

The chapters contained in this book are based on the invited lectures delivered at the school. The topics cover a wide range of issues in statistical physics. We hope that the book will be a useful guide and a valuable reference for researchers working in various areas of statistical physics.

We gratefully acknowledge the full financial support received from the DST. We are grateful to IIT Guwahati as well as the Department of Physics, IIT Guwahati for providing infrastructural facilities to organize this school. We are deeply indebted to the patron, Professor Gautam Barua, Director of IIT Guwahati for his overall support and constant encouragement in organizing the school. We would like to thank the advisory board members, Professors Mustansir Barma (TIFR, Mumbai), Indrani Bose (Bose Institute, Kolkata), Bikas K. Chakrabarti (SINP, Kolkata), Chandan Dasgupta (IISc, Bangalore), Deepak Dhar (TIFR, Mumbai), Ram Ramaswamy (JNU, New Delhi) and Prabodh Shukla (NEHU, Shillong) for their invaluable suggestions and guidance throughout the organization of this school. We are also thankful to the organizing committee members, Dr. Saurabh Basu and Dr. Subhradip Ghosh, for

their kind help in organizing the school. Finally we are thankful to all the contributing authors for their efforts in making the publication of these lecture notes possible.

Sitangshu Bikas Santra and Purusattam Ray

March, 2010

Chapter 1

Statistical Mechanics and Critical Phenomena: A Brief Overview

Sitangshu Bikas Santra and Purusattam Ray

1.1 Introduction

The basic concepts of statistical mechanics and its application to many-body systems, phase transitions and critical phenomena will be discussed briefly in this chapter. We will be using these ideas frequently in the subsequent lectures. Statistical mechanics describes the thermodynamic behaviour of macroscopic systems from the laws which govern the behaviour of the constituent elements at the microscopic level. The microscopic elements can be atoms, molecules, dipole moments or magnetic moments, etc. A macroscopic system is generally composed of a large number of these elements (of the order of Avogadro number $N_A \approx 6.022 \times 10^{23}$ per mole). Each element may have a large number of internal degrees of freedom associated with different types of motion such as translation, rotation, vibration etc. The constituent elements may interact with the external field applied to the system. There can also be very complex interaction among the constituent elements. The macroscopic properties of a system in the thermodynamic limit is thus determined by the properties of the constituent molecules, their interaction with external field as well as interaction among themselves. For a system of N elements, volume V and density ρ , the thermodynamic limit is defined as $\lim N \rightarrow \infty$, $\lim V \rightarrow \infty$ keeping $\rho = N/V$ finite. In this limit, the extensive properties of the system become directly proportional to the size of the system (N or V), while the intensive properties become independent of the size of the system. In the formalism of statistical

mechanics, a macroscopic property is obtained by taking a “statistical average” (or “ensemble average”) of the property over all possible microstates of the system. Thermodynamic equilibrium of a system can be achieved in different ways depending upon the interaction of the system with the rest of the universe (heat bath, pressure bath, etc). Different external conditions leading to thermodynamic equilibrium of a system give rise to different ensembles. Once microstates and ensembles are specified, macroscopic quantities can be obtained by taking appropriate statistical averages corresponding to a given ensemble. Below, we will provide definitions for statistical averages in different ensembles. Beside macroscopic quantities, definitions for different microscopic quantities such as fluctuations (in energy, density, spin, etc) and correlation functions will be given and a relationship between the macroscopic and microscopic quantities will be discussed. Finally, we will extend the discussion to strongly interacting systems and demonstrate the features of phase transition and critical phenomena.

1.2 Specification of Macro and Microstates

The macroscopic state of a thermodynamic system at equilibrium is specified by the values of a set of measurable thermodynamic parameters. For example, the macrostate of a fluid system can be specified by pressure, temperature and volume, (P, V, T) . For an isolated system for which there is no exchange of energy or mass with the surroundings, the macrostate is specified by the internal energy E , number of particles N and volume V ; (E, N, V) . In case of a closed system which exchanges only energy with the surroundings (and no particle) and is in thermodynamic equilibrium thermodynamic equilibrium with a heat bath at temperature T , the macrostate is given by (N, V, T) . For an open system, exchange of both energy and particle with the surroundings can take place. For such systems, at equilibrium with a heat bath at temperature T and a pressure bath at pressure P (or a particle bath of chemical potential μ), the macrostate is specified by (N, P, T) (or (μ, V, T)). The equilibrium of an isolated system corresponds to maximum entropy $S(E, N, V)$, for a closed system it corresponds to minimum Helmholtz free energy $F(N, V, T)$, and for an open system the equilibrium corresponds to minimum of Gibb's free energy $G(N, P, T)$ (or minimum of the grand potential $\Phi(\mu, V, T)$).

A microstate of a system is obtained by specifying the states of all of its constituent elements. In a system of classical particles, for example, one needs to know the position q and the conjugate momentum p of each and every particles. The time evolution of q and p is governed by the Hamiltonian $\mathcal{H}(p, q)$ and Hamilton's equation of motion

$$\dot{q}_i = \frac{\partial \mathcal{H}(p, q)}{\partial p_i} \quad \text{and} \quad \dot{p}_i = -\frac{\partial \mathcal{H}(p, q)}{\partial q_i}; \quad i = 1, 2, \dots, 3N \quad (1.1)$$

for a system of N particles. The state of a single particle at any time is then given by the pair of conjugate variables (q_i, p_i) . Each single particle

then constitutes a 6-dimensional phase space (3-coordinate and 3-momentum). For N particles, the state of the system is then completely and uniquely defined by $3N$ canonical coordinates q_1, q_2, \dots, q_{3N} and $3N$ canonical momenta p_1, p_2, \dots, p_{3N} . These $6N$ variables constitute a $6N$ -dimensional Γ -space or phase space of the system and each point of the phase space represents a microstate of the system. The locus of all the points in Γ -space satisfying the condition $\mathcal{H}(p, q) = E$, total energy of the system, defines the energy surface.

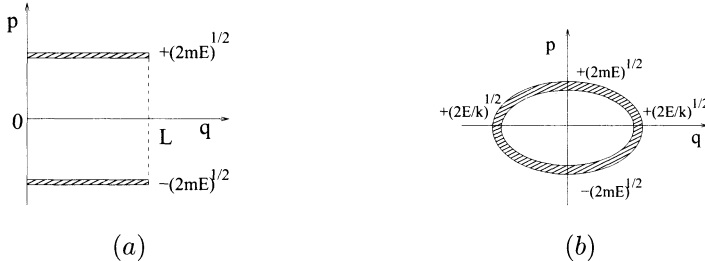


Figure 1.1: (a) Accessible region of phase space for a free particle of mass m and energy E in a one dimensional box of length L . (b) Region of phase space for a one dimensional harmonic oscillator with energy E , mass m and spring constant k .

Example: Consider a free particle of mass m inside a one dimensional box of length L , such that $0 \leq q \leq L$, with energy between E and $E + \delta E$. The macroscopic state of the system is defined by (E, N, L) with $N = 1$. The microstates are specified in certain region of phase space. Since the energy of the particle is $E = p^2/2m$, the momentum will be $p = \pm\sqrt{2mE}$ and the position q is within 0 and L . However, there is a small width in energy δE , so the particles are confined in small strips of width $\delta p = \sqrt{m/2\delta E}$ as shown in Fig.1.1(a). Note that if $\delta E = 0$, the accessible region of phase space representing the system would be one dimensional in a two dimensional phase space. In order to avoid this artifact a small width in E is considered which does not affect the final results in the thermodynamic limit . In Fig.1.1(b), the phase space region of a one dimensional harmonic oscillator with mass m , spring constant k and energy between E and $E + \delta E$ is shown. The Hamiltonian of the particle is: $\mathcal{H} = p^2/2m + kq^2/2$ and for a given energy E , the accessible region is an ellipse: $p^2/(2mE) + q^2/(2E/k) = 1$. With the energy between E and $E + \delta E$, the accessible region is an elliptical shell of area $2\pi\sqrt{m/k}\delta E$.

For a quantum particle, the state is characterized by the wave function $\Psi(q_1, q_2, q_3, \dots)$. Generally, the wave function is written in terms of a complete orthonormal basis of eigenfunctions of the Hamiltonian operator of the system. Thus, the wave function may be written as

$$\Psi = \sum_n c_n \phi_n, \quad \hat{\mathcal{H}}\phi_n = E_n \phi_n \quad (1.2)$$

where E_n is the eigenvalue corresponding to the state ϕ_n . The eigenstates ϕ_n , characterized by a set of quantum numbers n provides a way to count the microscopic states of the system.

Example: Consider a localized magnetic ion of spin 1/2 and magnetic moment μ in thermal equilibrium at temperature T . The particle has two eigenstates, (1, 0) and (0, 1) associated with spin up (\uparrow) and down spin (\downarrow) respectively. In the presence of an external magnetic field \vec{H} , the energy is given by

$$E = -\vec{\mu} \cdot \vec{H} = \begin{cases} +\mu H, & \text{for spin } \downarrow \\ -\mu H, & \text{for spin } \uparrow \end{cases} \quad (1.3)$$

Thus, the system with macrostate (N, H, T) with $N = 1$ has two microstates with energy $-\mu H$ and $+\mu H$ corresponding to up spin (parallel to \vec{H}) and down spin (antiparallel to \vec{H}). If there are two such magnetic ions in the system, it will have four microstates: $\uparrow\uparrow$ with energy $-2\mu H$, $\uparrow\downarrow$ & $\downarrow\uparrow$ with zero energy and $\downarrow\downarrow$ with energy $+2\mu H$. For a system of N spins of spin-1/2, there are total 2^N microstates and specification of the spin-states of all the N spins will give one possible microstate of the system.

1.3 Statistical Ensembles

An ensemble is a collection of a large number of replicas (or mental copies) of the microstates of the system under the same macroscopic condition or having the same macrostate. However, the microstates of the members of an ensemble can be arbitrarily different. Thus, for a given macroscopic condition, a system of an ensemble is represented by a point in the phase space. The ensemble of a macroscopic system of given macrostate then corresponds to a large number of points in the phase space. During time evolution of a macroscopic system in a fixed macrostate, the microstate is supposed to pass through all these phase points.

Depending on the interaction of a system with the surroundings (or universe), a thermodynamic system is classified as isolated, closed or open system. Similarly, statistical ensembles are also classified into three different types. The classification of ensembles again depends on the type of interaction of the system with the surroundings which can either be by exchange of energy only or exchange of both energy and matter (particles or mass). In an isolated system, neither energy nor matter is exchanged and the corresponding ensemble is known as *microcanonical* ensemble. A closed system exchanging only energy (not matter) with its surroundings is described by *canonical* ensemble. Both energy and matter are exchanged between the system and the surroundings in an open system and the corresponding ensemble is called a *grand canonical* ensemble.

1.4 Condition of Statistical Equilibrium

Consider an isolated system with the macrostate (E, N, V) . A point in the phase space corresponds to a microstate of such a system and its internal dynamics is described by the corresponding phase trajectory. The density of phase points $\rho(p, q)$ is the number of microstates per unit volume of the phase space and it is the probability to find a state around a phase point (p, q) . At any time t , the number of representative points in the volume element $d^{3N}qd^{3N}p$ around the point (p, q) of the phase space is then given by

$$\rho(p, q)d^{3N}qd^{3N}p. \quad (1.4)$$

By Liouville's theorem, in the absence of any source and sink in the phase space, the total time derivative in the time evolution of the phase point density $\rho(p, q)$ is given by

$$\frac{d\rho}{dt} = \frac{\partial\rho}{\partial t} + \{\rho, \mathcal{H}\} = 0 \quad (1.5)$$

where

$$\{\rho, \mathcal{H}\} = \sum_{i=1}^{3N} \left(\frac{\partial\rho}{\partial q_i} \frac{\partial\mathcal{H}}{\partial p_i} - \frac{\partial\rho}{\partial p_i} \frac{\partial\mathcal{H}}{\partial q_i} \right) \quad (1.6)$$

is the Poisson bracket of the density function ρ and the Hamiltonian \mathcal{H} of the system. Thus, the cloud of phase points moves in the phase space like an incompressible fluid.

The ensemble is considered to be in statistical equilibrium if $\rho(p, q)$ has no explicit dependence on time at all points in the phase space, *i.e.*,

$$\frac{\partial\rho}{\partial t} = 0. \quad (1.7)$$

Under the condition of equilibrium, therefore,

$$\{\rho, \mathcal{H}\} = \sum_{i=1}^{3N} \left(\frac{\partial\rho}{\partial q_i} \frac{\partial\mathcal{H}}{\partial p_i} - \frac{\partial\rho}{\partial p_i} \frac{\partial\mathcal{H}}{\partial q_i} \right) = 0 \quad (1.8)$$

and it will be satisfied if ρ is an explicit function of the Hamiltonian $\mathcal{H}(q, p)$ or ρ is a constant independent of p and q . That is

$$\rho(p, q) = \text{constant}. \quad (1.9)$$

The condition of statistical equilibrium then requires no explicit time dependence of the phase point density $\rho(p, q)$ as well as uniform distribution of $\rho(p, q)$ over the relevant region of phase space. The value of $\rho(p, q)$ will, of course, be zero outside the relevant region of phase space. Physically the choice corresponds to an ensemble of systems which at all times are uniformly distributed over all possible microstates and the resulting ensemble is referred to as the microcanonical ensemble. However, in canonical ensemble it can be shown that $\rho(q, p) \propto \exp[-\mathcal{H}(q, p)/k_B T]$.

1.5 Postulates of Statistical Mechanics

The principles of statistical mechanics and their applications are based on the following two postulates.

1.5.1 Equal a priori probability

For a given macrostate (E, N, V) , specified by the number of particles N in the system of volume V and at energy E , there is usually a large number of possible microstates of the system. In case of classical non-interacting system, the total energy E can be distributed among the N particles in a large number of different ways and each of these different ways corresponds to a microstate. In the fixed energy ensemble, the density $\rho(q, p)$ of the representative points in the phase space corresponding to these microstates is constant or the phase points are uniformly distributed. Thus, any member of the ensemble is equally likely to be in any of the various possible microstates. In case of a quantum system, the various different microstates are identified as the independent solutions $\Psi(\mathbf{r}_1, \mathbf{r}_2, \dots, \mathbf{r}_N)$ of the Schrödinger equation of the system, corresponding to an eigenvalue E . At any time t , the system is **equally likely** to be in any one of these microstates. This is generally referred as the postulate of *equal a priori probability* for all microstates of a given macrostate of the system.

1.5.2 Principle of ergodicity

The microstates of a macroscopic system are specified by a set of points in the $6N$ -dimensional phase space. At any time t , the system is equally likely to be in any one of the large number of microstates corresponding to a given macrostate, say (E, N, V) as for an isolated system. With time, the system passes from one microstate to another. After a sufficiently long time, the system passes through all its possible microstates. In the language of statistical mechanics, the system is considered to be in equilibrium if it samples all the microstates with equal a priori probability. The equilibrium value of the observable X can be obtained by the statistical or ensemble average

$$\langle X \rangle = \frac{\int \int X(p, q) \rho(p, q) d^{3N}q d^{3N}p}{\int \rho(p, q) d^{3N}q d^{3N}p}. \quad (1.10)$$

On the other hand, the mean value of an observable (or a property) is given by its time-averaged value:

$$\bar{X} = \lim_{T \rightarrow \infty} \frac{1}{T} \int_0^T X(t) dt. \quad (1.11)$$

The ergodicity principle suggests that statistical average $\langle X \rangle$ and the mean value \bar{X} are equivalent: $\bar{X} \equiv \langle X \rangle$.

1.6 Thermodynamics in Different Ensembles

1.6.1 Microcanonical ensemble (E, N, V)

In this ensemble, the macrostate is defined by the total energy E , the number of particles N and the volume V . However, for calculation purpose, a small range of energy E to $E + \delta E$ (with $\delta E \rightarrow 0$) is considered instead of a sharply defined energy value E . The systems of the ensemble may be in any one of a large number of microstates between E and $E + \delta E$. In the phase space, the representative points will lie within a hypershell defined by the condition

$$E \leq \mathcal{H}(p, q) \leq E + \delta E. \quad (1.12)$$

At statistical equilibrium, all representative points are uniformly distributed and $\rho(q, p) = \text{constant}$ between E and $E + \delta E$ otherwise zero. As per equal a priori probability, any accessible state is equally probable. Therefore, the probability P_x to find a system in a state x corresponding to energy E_x between E and $E + \delta E$ is given by

$$P_x = \begin{cases} \rho(q, p) / \int_E^{E+\delta E} \rho(q, p) d^{3N} q d^{3N} p & \text{if } E \leq E_x \leq E + \delta E \\ 0 & \text{otherwise.} \end{cases} \quad (1.13)$$

One may note that $\int_E^{E+\delta E} P_x d^{3N} q d^{3N} p = 1$.

The number of accessible microstates Ω is proportional to the phase space volume enclosed within the hypershell and it is given by

$$\Omega(E, N, V) = \frac{1}{h^{3N}} \int_E^{E+\delta E} d^{3N} q d^{3N} p \quad (1.14)$$

for a system of N particles and of total energy E . If the particles are indistinguishable, the number of microstates Ω should be divided by $N!$ as the Gibb's correction. The factor of $1/h^{3N}$ suggests that a tiny volume element of h^{3N} in the phase space represents the microstates of the system. This means that a small displacement within the volume element h^{3N} around the phase point does not correspond to any measurable change in the macrostate of the system. By Heisenberg's uncertainty principle ($\Delta q \Delta p \sim h$) for quantum particles, it can be shown that h is the Planck's constant. However, if the energy states are discrete, the particles are distributed among the different energy levels as, n_i particles in the energy level ϵ_i and satisfies the following conditions

$$N = \sum_i n_i \quad \text{and} \quad E = \sum_i n_i \epsilon_i, \quad (1.15)$$

The total number of possible distributions or microstates of N such particles is then given by

$$\Omega = \frac{N!}{n_1! n_2! \dots}. \quad (1.16)$$

The thermodynamic properties can be obtained by associating entropy S of the system to the number of accessible microstates Ω . The statistical definition of entropy by Boltzmann is given by

$$S(E, N, V) = k_B \ln \Omega \quad (1.17)$$

where k_B is the Boltzmann constant, $1.38 \times 10^{-23} \text{ JK}^{-1}$. In a natural process the equilibrium corresponds to maximum Ω or equivalently maximum entropy S as is stated in the second law of thermodynamics. It is to be noted that, as $T \rightarrow 0$, the system is going to be in its ground state and the value of Ω is going to be 1. Consequently, the entropy $S \rightarrow 0$ which is the third law of thermodynamics. If a thermodynamic potential like entropy S is known in terms of the number of microstates, the thermodynamic properties of the system can be obtained by taking suitable derivative of S with respect to the relevant parameters.

Problem: (a) Consider a monatomic ideal gas of N molecules confined in a volume V having total energy E in thermodynamic equilibrium. Calculate the number of microstates of the system considering

$$\begin{aligned}\Omega(E, N, V) &= \frac{1}{h^{3N}} \int_E^{E+\delta E} d^{3N}q d^{3N}p \quad \text{and} \\ \Omega(E, N, V) &= \frac{1}{h^{3N}N!} \int_E^{E+\delta E} d^{3N}q d^{3N}p.\end{aligned}$$

Calculate the entropy S of the system as a function of (E, N, V) considering both the formulae and taking $E = 3Nk_B T/2$.

(b) Consider a system with two compartments with an impenetrable partition. Both the compartments of equal volume V are filled with the same monatomic ideal gas of N molecules and total energy E each. The whole system is in thermodynamic equilibrium. Calculate the change in entropy ΔS after removing the partition once without dividing Ω by $N!$ and then dividing Ω by $N!$. Check that $\Delta S = 2Nk_B \ln 2$ in the first case and $\Delta S = 0$ in the second case. (Gibb's paradox is resolved only if the gas molecules are assumed to be indistinguishable).

Problem: Consider a system of N localized spin-1/2 magnetic ions of magnetic moment μ in an external magnetic field H having total energy E . Calculate the entropy of the system $S(E, N, H) = k_B \ln \Omega$ where $\Omega = N!/(N_1!N_2!)$ is total number of accessible states with N_1 up spins and N_2 down spins configurations. Check that

$$\frac{S}{Nk_B} = -\frac{N\mu H - E}{2N\mu H} \ln \left(\frac{N\mu H - E}{2N\mu H} \right) - \frac{N\mu H + E}{2N\mu H} \ln \left(\frac{N\mu H + E}{2N\mu H} \right).$$

Treating E to be continuous, plot S/Nk_B versus $E/N\mu H$. Show that this system can have negative absolute temperature for the positive energy region. Why negative absolute temperature is possible here but not for a gas in a box?

1.6.2 Canonical ensemble (N, V, T)

In the micro-canonical ensemble, a microstate was defined by a fixed number of particles N , a fixed volume V and a fixed energy E . However, the total energy E of a system is generally not measured. Furthermore, it is difficult to keep the total energy fixed. Instead of energy E , temperature T is a better alternate parameter of the system which is directly measurable and controllable. Let us consider an ensemble whose microstate is defined by N, V and T . Such an ensemble is known as *canonical* ensemble. In the canonical ensemble, the energy E can vary from zero to infinity. The set of microstates can be continuous as in most classical systems or it can be discrete like the eigenstates of a quantum mechanical Hamiltonian. Each microstate s is characterised by the energy E_s of that state. If the system is in thermal equilibrium with a heat-bath at temperature T , then the probability p_s that the system to be in the microstate s is $\propto e^{-E_s/k_B T}$, the Boltzmann factor. Since the system has to be in a certain state, the sum of all p_s has to be unity, *i.e.*, $\sum_s p_s = 1$. The normalized probability

$$p_s = \frac{\exp(-E_s/k_B T)}{\sum_s \exp(-E_s/k_B T)} = \frac{1}{Z} e^{-E_s/k_B T} \quad (1.18)$$

is the Gibbs probability and the normalization factor

$$Z(N, V, T) = \sum_s e^{-E_s/k_B T} = \sum_s e^{-\beta E_s} \quad (1.19)$$

is called the **canonical partition function**. Here, $\beta = 1/k_B T$.

The expectation (or average) value of a macroscopic quantity X is given by

$$\langle X \rangle = \frac{\sum_s X_s \exp(-\beta E_s)}{\sum_s \exp(-E_s/k_B T)} = \frac{1}{Z} \sum_s X_s e^{-E_s/k_B T} \quad (1.20)$$

where X_s is the property X measured in the microstate s .

In the thermodynamic limit, the consecutive energy levels are very close and can be considered as continuous. In this limit, the canonical partition function can be written as

$$Z(N, V, T) = \frac{1}{h^{3N} N!} \int \int \exp \{-\beta \mathcal{H}(p, q)\} d^{3N} q d^{3N} p \quad (1.21)$$

($N!$ is for indistinguishable particles only) and the expectation value of X is given by

$$\langle X \rangle = \frac{1}{Z} \int \int X(q, p) \exp \{-\beta \mathcal{H}(p, q)\} d^{3N} q d^{3N} p \quad (1.22)$$

Helmholtz free energy $F(N, V, T) = E - TS$ is the appropriate potential or free energy to describe the thermodynamic system when the system is in thermal equilibrium with a heat-bath at temperature T . It can be shown that

the Helmholtz free energy $F(N, V, T)$ of the system is related to the logarithm of the partition function $Z(N, V, T)$ and it is given by

$$F(N, V, T) = -k_B T \ln Z(N, V, T). \quad (1.23)$$

Thermal equilibrium corresponds to the minimum free energy or maximum entropy at finite temperature. All equilibrium thermodynamic properties can be calculated by taking appropriate derivatives of the free energy $F(N, V, T)$ with respect to its parameters.

Note: For non-interacting system of N particles, the partition function Z can be written as $Z = Z_1^N$ where Z_1 is the partition function for a single particle. Consequently one obtains ideal gas behaviour for $N \rightarrow \infty$.

Problem: (a) Consider N localized one dimensional classical Harmonic oscillators of frequency ω in thermal equilibrium at temperature T . Obtain the canonical partition function $Z = (\hbar\omega/k_B T)^{-N}$. Calculate the internal energy E of the system. Check that the energy obtained is satisfying the equipartition theorem, $k_B T/2$ thermal energy per square term in the Hamiltonian.

(b) Consider N localized one dimensional quantum Harmonic oscillators of frequency ω in thermal equilibrium at temperature T . Obtain the canonical partition function $Z = [2 \sinh(\hbar\omega/2k_B T)]^{-N}$. Show that the internal energy E of the system is given by

$$E = N \left[\frac{\hbar\omega}{2} + \frac{\hbar\omega}{e^{\hbar\omega/k_B T} - 1} \right]. \quad (1.24)$$

(Note that E is not satisfying equipartition theorem.) Check that $E \approx Nk_B T$ as $T \rightarrow \infty$ and $E \approx N\hbar\omega/2$ as $T \rightarrow 0$ as expected.

1.6.3 Grand canonical ensemble (μ, V, T)

Consider a system in contact with an energy reservoir as well as a particle reservoir and the system could exchange energy as well as particles (mass) with the reservoirs. Canonical ensemble theory has limitations in dealing these systems and needs generalization. It comes from the realization that not only the energy E but also the number of particles N of a physical system is difficult to measure directly. However, their average values $\langle E \rangle$ and $\langle N \rangle$ are measurable quantities. The system interacting with both energy and particle reservoirs comes to an equilibrium when a common temperature T and a common chemical potential μ with the reservoir is established. In this ensemble, each microstate (r, s) corresponds to energy E_s and number of particles N_r in that state. If the system is in thermodynamic equilibrium at temperature T and chemical potential μ , the probability $p_{r,s}$ is given by

$$p_{r,s} = C \exp(-\alpha N_r - \beta E_s), \quad (1.25)$$

where $\alpha = -\mu/k_B T$ and $\beta = 1/k_B T$. After normalizing,

$$p_{r,s} = \frac{\exp(-\alpha N_r - \beta E_s)}{\sum_{r,s} \exp(-\alpha N_r - \beta E_s)}, \quad \text{since} \quad \sum_{r,s} p_{r,s} = 1 \quad (1.26)$$

where the sum is over all possible states of the system. The numerator $\exp(-\alpha N_r - \beta E_s)$ is the Boltzmann factor here and the denominator $Q = \sum_{r,s} \exp(-\alpha N_r - \beta E_s)$ is called the grand canonical partition function. The **grand canonical partition function** then can be written as

$$Q = \sum_{r,s} \exp\left(\frac{\mu N_r}{k_B T} - \frac{E_s}{k_B T}\right) = \sum_{r,s} \mathfrak{z}^{N_r} e^{-E_s/k_B T} \quad (1.27)$$

where $\mathfrak{z} = e^{\mu/k_B T}$ is the fugacity of the system. In case of a system of continuous energy levels, the grand partition function can be written as

$$Q = \sum_{N=1}^{\infty} \frac{1}{h^{3N} N!} \int \int \exp\left\{-\beta \mathcal{H}(p, q) + \frac{\mu N}{k_B T}\right\} d^{3N} q d^{3N} p. \quad (1.28)$$

Note that division by $N!$ is only for indistinguishable particles.

The mean energy $\langle E \rangle$ and the mean number of particle $\langle N \rangle$ of the system are then given by

$$\begin{aligned} \langle E \rangle &= \frac{\sum_{r,s} E_s \exp(-\alpha N_r - \beta E_s)}{\sum_{r,s} \exp(-\alpha N_r - \beta E_s)} \\ &= -\frac{\partial}{\partial \beta} \ln \left\{ \sum_{r,s} e^{-\alpha N_r - \beta E_s} \right\} \\ &= -\frac{\partial \ln Q}{\partial \beta} = -\frac{1}{Q} \frac{\partial Q}{\partial \beta} \end{aligned} \quad (1.29)$$

and

$$\begin{aligned} \langle N \rangle &= \frac{\sum_{r,s} N_r \exp(-\alpha N_r - \beta E_s)}{\sum_{r,s} \exp(-\alpha N_r - \beta E_s)} \\ &= -\frac{\partial}{\partial \alpha} \ln \left\{ \sum_{r,s} e^{-\alpha N_r - \beta E_s} \right\} \\ &= -\frac{\partial \ln Q}{\partial \alpha} = -\frac{1}{Q} \frac{\partial Q}{\partial \alpha}. \end{aligned} \quad (1.30)$$

The grand potential $\Phi(T, V, \mu) = E - TS - \mu N$ is the appropriate potential or free energy to describe the thermodynamic system in equilibrium with temperature T and chemical potential μ . It can be shown that

$$\Phi(\mu, V, T) = -k_B T \ln Q. \quad (1.31)$$

All equilibrium thermodynamic properties can now be calculated by taking appropriate derivatives of the grand potential $\Phi(T, V, \mu)$ with respect to its parameters.

Problem: Consider a single component system of volume V , having two phases - solid and vapour, in equilibrium at temperature T . Treating the vapour as a monatomic ideal gas and the solid as quantum harmonic oscillator, show that a solid phase exists below a characteristic temperature T_c given by $f(T_c)/\phi(T_c) = N/V$ where N is the total number of particles in the system, $f(T) = [2\pi m k_B T / h^2]^{3/2}$ and $\phi(T) = [2 \sinh(\hbar\omega/k_B T)]^{-1}$.

1.7 Statistical Definitions of Thermodynamic Quantities

In this section we will be proving the relations of thermodynamic quantities with the thermodynamic potentials as well as the partition functions. In the table below, statistical quantities and the corresponding thermodynamic functions in cases of different ensembles are given.

Ensemble	Statistical quantity	Thermodynamic functions
Microcanonical	Number of microstates: Ω	Entropy: $S = k_B \ln \Omega$
Canonical	Canonical partition function: Z	Helmholtz free energy: $F = -k_B T \ln Z$
Grand Canonical	Grand partition function: Q	Grand potential: $\Phi = -k_B T \ln Q$

Thermodynamic quantities and response functions are different derivatives of the free energy function. Obtaining Helmholtz free energy from the canonical partition function one may derive the thermodynamic quantities. The thermodynamic quantities for fluid and magnetic systems in canonical ensemble are provided below.

1.7.1 Fluid system

The macrostate of the system at equilibrium is represented by (N, V, T) , the energy of the system is given by the classical Hamiltonian $\mathcal{H}(p, q)$ and N molecules are assumed to be identical.

$\text{Canonical Partition function}$ $Z(N, V, T) = \frac{1}{h^{3N} N!} \int e^{-\beta \mathcal{H}} d^3N q d^3N p$	\downarrow $\text{Free energy: } F = -k_B T \ln Z$	\downarrow
\downarrow Internal Energy $E = -\frac{\partial \ln Z}{\partial \beta}$	\downarrow Entropy $S = -\left(\frac{\partial F}{\partial T}\right)_V$	\downarrow Pressure $P = -\left(\frac{\partial F}{\partial V}\right)_T$
\downarrow Specific heat $(constant V)$ $C_V = \left(\frac{\partial E}{\partial T}\right)_V$	\downarrow Specific heat $(constant X = P, V)$ $C_X = T \left(\frac{\partial S}{\partial T}\right)_X$	\downarrow Isothermal compressibility $\kappa_T = -\frac{1}{V} \left(\frac{\partial V}{\partial P}\right)_T$

The specific heat and compressibility are the response functions of the fluid system.

1.7.2 Magnetic system:

The macrostate of the system is represented by, say, (N, H, T) and the energy levels of the system are discrete corresponding to different orientation of magnetic moment in the external field H .

$\text{Canonical Partition function}$ $Z(N, H, T) = \sum_s e^{-\beta E_s}$	\downarrow $\text{Free energy: } F = -k_B T \ln Z$	\downarrow
\downarrow Internal Energy $E = -\frac{\partial \ln Z}{\partial \beta}$	\downarrow Entropy $S = -\left(\frac{\partial F}{\partial T}\right)_H$	\downarrow Magnetization $M = -\left(\frac{\partial F}{\partial H}\right)_T$
\downarrow Specific heat $(constant H)$ $C_H = \left(\frac{\partial E}{\partial T}\right)_H$	\downarrow Specific heat $(constant X = H, M)$ $C_X = T \left(\frac{\partial S}{\partial T}\right)_X$	\downarrow Isothermal susceptibility $\chi_T = \left(\frac{\partial M}{\partial H}\right)_T$

The specific heat and susceptibility are the response functions of the magnetic system.

1.8 Stability and Positive Response Functions

If a system is in thermal equilibrium any small spontaneous fluctuation in the system tends to restore the system back to equilibrium. This is the idea behind

Le Chatelier's principle for stable equilibrium. Suppose there has occurred a spontaneous temperature fluctuation in which the temperature of the system increases from T to T' . In order to maintain the stability, the system should release certain amount of heat ΔQ and as a consequence the specific heat $C = \Delta Q/\Delta T$ must be positive since both ΔQ and ΔT are positive. If there occurs a spontaneous pressure fluctuation, $P \rightarrow P'$ and $P' > P$, then the system will reduce its volume by certain amount ΔV to maintain the stability. As a consequence the compressibility $\kappa = -\Delta V/\Delta P$ is also be positive since ΔP is positive but ΔV is negative. Thus, for thermally and mechanically stable fluid system, the specific heat and compressibility should be positive for all T . However, for a magnetic system such arguments that the susceptibility χ and specific heat C both are positive can not be made. It is known that for diamagnetic materials, $\chi < 0$. The ferromagnetic materials on the other hand have positive χ . It can be shown that such systems are described by the Hamiltonian $\mathcal{H} = \mathcal{H}_0 - \vec{H} \cdot \vec{M}$.

The response functions are not all independent. One could show for a fluid system,

$$C_P - C_V = TV\alpha_P^2/\kappa_T \quad \text{and} \quad \kappa_T - \kappa_S = TV\alpha_P^2/C_P \quad (1.32)$$

where $\alpha_P = (\partial V/\partial T)_P/V$, the thermal expansion coefficient and similarly for a magnetic system,

$$C_H - C_M = T\alpha_H^2/\chi_T \quad \text{and} \quad \chi_T - \chi_S = T\alpha_H^2/C_H \quad (1.33)$$

where $\alpha_H = (\partial M/\partial T)_H$. Since, the specific heat and compressibility are positive, it could be shown from the above relations that $C_P \geq C_V$ and $\kappa_T \geq \kappa_S$. The equality holds either at $T = 0$ or at $\alpha = 0$, for example, $\alpha = 0$ for water at 4°C .

Problem: Show that (a) for a fluid system, $C_P - C_V = TV\alpha_P^2/\kappa_T$ and $\kappa_T - \kappa_S = TV\alpha_P^2/C_P$ where $\alpha_P = (\partial V/\partial T)_P/V$, the thermal expansion coefficient and (b) for a magnetic system, $C_H - C_M = T\alpha_H^2/\chi_T$ and $\chi_T - \chi_S = T\alpha_H^2/C_H$ where $\alpha_H = (\partial M/\partial T)_H$.

1.9 Positive Response Function and Free Energy

The positive values of the specific heat and compressibility implies certain convexity properties of the free energy functions $F = E - TS$ or $G = F + PV$. A function $f(x)$ is called a convex function of x if

$$f\left(\frac{x_1 + x_2}{2}\right) \leq \frac{f(x_1) + f(x_2)}{2} \quad \text{for all } x_1 \text{ and } x_2. \quad (1.34)$$

That is to say, the chord joining the points $f(x_1)$ and $f(x_2)$ lies above or on the curve $f(x)$ for all x in the interval $x_1 < x < x_2$ for a convex function. Similarly,

a function $f(x)$ is called a concave function of x if

$$f\left(\frac{x_1 + x_2}{2}\right) \geq \frac{f(x_1) + f(x_2)}{2} \quad \text{for all } x_1 \text{ and } x_2. \quad (1.35)$$

Thus, for a concave function, the chord joining the points $f(x_1)$ and $f(x_2)$ lies below or on the curve $f(x)$ for all x in the interval $x_1 < x < x_2$. If the function is differentiable and the derivative $f'(x)$ exists, then a tangent to a convex function always lies below the function except at the point of tangent whereas for a concave function it always lies above the function except at the point of tangency. If the second derivative exists, then for a convex function $f''(x) \geq 0$ and for a concave function $f''(x) \leq 0$ for all x

From thermodynamic relations, it is already known that

$$\left(\frac{\partial^2 G}{\partial T^2}\right)_P = -\frac{C_P}{T} \quad \text{and} \quad \left(\frac{\partial^2 F}{\partial T^2}\right)_V = -\frac{C_V}{T}. \quad (1.36)$$

Since the specific heats are positive, these second derivatives are negative and as a consequence G and F both are concave function of temperature T . It is also known that

$$\left(\frac{\partial^2 G}{\partial P^2}\right)_T = -V\kappa_T \quad \text{and} \quad \left(\frac{\partial^2 F}{\partial V^2}\right)_T = \frac{1}{V\kappa_T}. \quad (1.37)$$

Since the compressibility is a positive quantity, G is a concave function of P whereas F is a convex function of V .

For magnetic systems, described by Hamiltonian $\mathcal{H} = \mathcal{H}_0 - \vec{H} \cdot \vec{M}$, it can be shown that the $G(T, H)$ is a concave function of both T and H whereas $F(T, M)$ is a concave function of T but a convex function of M .

1.10 Fluctuation and Response Functions

Apart from macroscopic thermodynamics quantities, statistical mechanics can also provide information about microscopic quantities such as fluctuations and correlation. Even if the system is in thermal equilibrium (constant T) or mechanical equilibrium (constant P) or chemical equilibrium (constant μ), the energy E , magnetization M , number of particles N may vary indefinitely and only the average values remain constant. It would be interesting to check that the thermodynamics response functions such as specific heat C_V , isothermal compressibility κ_T or isothermal susceptibility χ_T are directly proportional to the fluctuation in energy, density or magnetization respectively.

The fluctuation in energy is defined as

$$\langle(\Delta E)^2\rangle = \langle(E - \langle E \rangle)^2\rangle = \langle E^2 \rangle - \langle E \rangle^2. \quad (1.38)$$

By calculating $\langle E^2 \rangle$, it can be shown that

$$\langle (\Delta E)^2 \rangle = -\frac{\partial \langle E \rangle}{\partial \beta} = k_B T^2 C_V \quad \text{or} \quad C_V = \frac{1}{k_B T^2} (\langle E^2 \rangle - \langle E \rangle^2). \quad (1.39)$$

Thus the specific heat is nothing but fluctuation in energy.

The fluctuation in number of particles N is defined as

$$\langle (\Delta N)^2 \rangle = \langle (N - \langle N \rangle)^2 \rangle = \langle N^2 \rangle - \langle N \rangle^2 = k_B T \frac{\partial \langle N \rangle}{\partial \mu} = -\frac{N k_B T}{V} \kappa_T \quad (1.40)$$

where κ_T is the isothermal compressibility. The isothermal compressibility is then proportional to density fluctuation.

Similarly, the isothermal susceptibility is proportional to the fluctuation in magnetization

$$\chi_T = \frac{k_B T}{N} (\langle M^2 \rangle - \langle M \rangle^2). \quad (1.41)$$

These are system-independent general results. Generally these fluctuations are negligibly small at normal conditions. At room temperature, the rms energy fluctuation for 1 kg of water is $\sim 4.2 \times 10^{-8}$ J [$T(k_B C_V)^{1/2}$], whereas to change the water temperature by 1 degree the energy needed is $10^{11} \times C_V$. Since the heat capacity grows linearly with the system size, the relative energy fluctuation goes to zero at the thermodynamic limit.

Differentiation of the partition function to find the thermal averages and fluctuations of a quantity is a very useful technique. Suppose that the Hamiltonian has a term like $H_1 = -XY$, then the rules to find $\langle X \rangle$ is (a) calculate the partition function Z out in terms of Y (acts like a constraint), (b) differentiate $\log Z$ with respect to Y and finally (c) take the limit $Y \rightarrow 0$:

$$\begin{aligned} \left. \frac{1}{\beta} \frac{\partial \log Z}{\partial Y} \right|_{Y=0} &= \left. \frac{1}{\beta Z} \frac{\partial}{\partial Y} \right|_{Y=0} \sum_{\alpha} e^{-\beta(E_{\alpha} - X_{\alpha} Y)} \\ &= \frac{1}{Z} \sum_{\alpha} X_{\alpha} e^{-\beta E_{\alpha} - X_{\alpha} Y} \Big|_{Y=0} \\ &= \frac{1}{Z} \sum_{\alpha} X_{\alpha} e^{-\beta E_{\alpha}} \\ &= \langle X \rangle \end{aligned} \quad (1.42)$$

Differentiating again with respect to Y gives the fluctuation in X as:

$$\langle X^2 \rangle - \langle X \rangle^2 = \left. \frac{1}{\beta} \frac{\partial \langle X \rangle}{\partial Y} \right|_{Y=0} \equiv \frac{\chi}{\beta}, \quad (1.43)$$

where χ is the generalized susceptibility which gives the response of the variable X due to small change in its conjugate field Y . The above relation shows that χ is proportional to the fluctuation in X - this is known as **linear response theorem**.

So far, we have discussed how to calculate the thermal-average value of macroscopic variables from the knowledge of the probability distribution for the microstates of the system. We will see now how we can obtain local information like a spin at a point or how the spins at different points are correlated. Suppose our system consists of N variables (spins) s_1, \dots, s_N . If we want to find the magnetization M , which is equivalent to the thermal average of the total spin $S = \sum_i s_i$, we should add a term like $H_1 = (-1/\beta)hS$ to the Hamiltonian and follow the steps as mentioned above. Then,

$$M = \left. \frac{\partial \log Z}{\partial h} \right|_{h=0} \quad (1.44)$$

If the field h is different at different points, then we should add $F_1 = (-1/\beta) \sum_i h_i s_i$ to the Hamiltonian. Then,

$$\langle s_i \rangle = \frac{1}{Z} \frac{\partial Z}{\partial h_i}, \quad \langle s_i s_j \rangle = \frac{1}{Z} \frac{\partial^2 Z}{\partial h_i \partial h_j}, \quad \langle s_i s_j s_k \rangle = \frac{1}{Z} \frac{\partial^3 Z}{\partial h_i \partial h_j \partial h_k} \quad (1.45)$$

and so on. These quantities $G(s_i, s_j) = \langle s_1 \dots s_m \rangle$ are called **correlation functions** or more precisely m -point correlation function of the variables s .

If the spins are non-interacting, the correlation gives us no more information than that we get from each of the spins individually. In that case:

$$\langle s_i s_j \rangle = \langle s_i \rangle \langle s_j \rangle. \quad (1.46)$$

For a magnet at high temperature paramagnetic phase, $\langle s_i \rangle = 0$ and hence $\langle s_i s_j \rangle = 0$. If the spins interact with each other, the correlation function tells us how correlated different parts of the system are. In presence of a magnetic field, the spins tend to align in the direction of the field and $\langle s_i \rangle \neq 0$. In that case, even in the absence of any interaction and hence correlation between two spins s_i and s_j , $\langle s_i s_j \rangle \neq 0$. So, in general, it is customary to work with **connected correlation function** defined as:

$$G_c(s_i, s_j) = \langle s_i s_j \rangle - \langle s_i \rangle \langle s_j \rangle = \langle (s_i - \langle s_i \rangle)(s_j - \langle s_j \rangle) \rangle. \quad (1.47)$$

The connected correlation function is always zero if the spins are non-interacting, even if the spins are in a magnetic field. It is clear that $G_c(s_i, s_j)$ measures the correlation in the fluctuations at the two sites i and j which vanishes if there is no interaction between the spins. It is to be noted that:

$$G_c(s_i, s_j) = \frac{\partial^2 \log Z}{\partial h_i \partial h_j}. \quad (1.48)$$

1.11 Phase Transitions

A phase is a state of matter in thermodynamic equilibrium. The same matter (or system) could be in several different states or phases depending upon the

macroscopic condition of the system. Different phases of water is our everyday experience. Ice, water and steam are the different states or phases of a collection of large number of H_2O molecules. Given a macroscopic condition, the system spontaneously goes to a particular phase corresponding to minimum free energy of the system. We have already discussed that a closed system which exchange only energy with the surroundings has lowest Helmholtz free energy (F) at equilibrium and for an open system the equilibrium corresponds to lowest Gibb's free energy (G). The free energy is the sum of various energies associated with a collection of large number of atoms or molecules. Beside the kinetic energies of the particles, the potential energies due to inter atomic (or molecular) interactions contribute mostly to the free energy. Essentially, the different phases of matter is a consequence of interaction among a large number of atoms or molecules at a given thermodynamic condition.

There is a wide variety of phase transitions starting from solid-liquid-gas to magnetic transition, normal to super conductor, liquid to liquid crystal and many other transitions. Most phase transitions belong to one of the two types - first order and second order phase transition. In a first order phase transition there is generally a radical change in the structure of the material. The transition mostly, but not always, is associated with an emission (or absorption) of heat called the latent heat. This heat is released when the material cools through an infinitesimally small temperature change around the transition temperature. Most crystallization and solidification are first order transitions. For example, the latent heat $L \simeq 334 \text{ Jg}^{-1}$ comes out when water becomes ice. This happens sharply at 0°C temperature under the atmospheric pressure, when the H_2O molecules which wander around in the water phase gets packed in FCC ice structure releasing the excess energy as the latent heat. The term 'first' in the first order transition comes from Ehrenfest's classification of phase transitions: n th order phase transition corresponds to the discontinuity of the n th derivative of the free energy functions. In the modern classification scheme, the first order transitions are abrupt transitions and are associated with the emission (or absorption) of latent heat. In Fig.1.2, variation of the Helmholtz free energy (F) with temperature T and the Gibb's free energy (G) with pressure P are shown around a first order transition point (T^*, P^*) for a fluid system. The free energy curves of the two phases meet with difference in slopes and both stable and metastable states exist for some region of temperature and pressure. At the transition temperature T^* , the tangent to the curve $F(T)$ versus T changes discontinuously and similarly for $G(P)$ versus P the tangent changes discontinuously at the transition pressure P^* . The change in the slope of F with respect to T corresponds to entropy $S = -(\partial F / \partial T)_P$ discontinuity, equivalent to latent heat $L = T\Delta S$. The change in the slope of G with respect to P corresponds to discontinuity in the volume $V = (\partial G / \partial P)_T$.

First order transition often (not always) ends up at a critical point where second order transition takes place. In Fig.1.3 the characteristic behaviour of second order phase transitions is shown for a fluid system. At a first order phase transition the free energy curves of the two phases meet with a fine difference

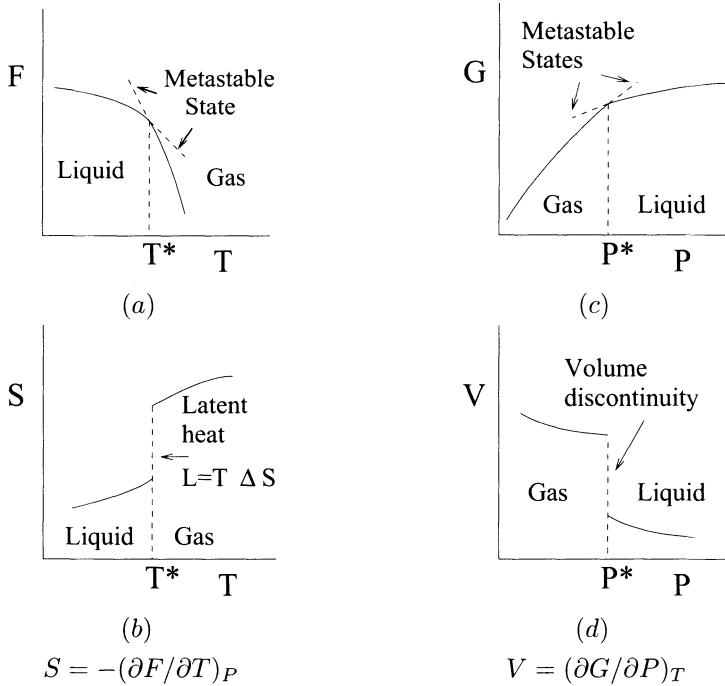


Figure 1.2: Variation of free energies and their first derivatives with respect to the respective parameters around a first order transition. (a) Plot of Helmholtz free energy F against temperature T at a constant pressure. (b) Plot of the entropy S , first derivative of F with respect to T , against T . (c) Plot of Gibb's free energy G against pressure P at a constant temperature. (d) Plot of the volume V , first derivative of G with respect to P , against P . Discontinuities in entropy S (latent heat) as well as in volume V are marks of a first order transition.

in slopes whereas at a second order transition the two free energy curves meet tangentially at the critical point (T_c, P_c) . The slopes of the curves changes continuously across the critical point. Therefore, there is no discontinuity either in entropy or in volume. Since there is no entropy discontinuity in second order transition, there is no emission (or absorption) of latent heat in this transition. It is a continuous phase transition where the system goes continuously from one phase to another without any supply of latent heat.

Not only the first derivatives but also the second derivatives of the free energy show a drastic difference in their behaviour around the transition point in the first and second order transitions. For example, the specific heat $C_P = -T(\partial^2 G / \partial T^2)_P$ diverges in the first order transition whereas in the second order transition specific heat has a finite discontinuity or logarithmic divergence at the critical point. Infinite specific heat in first order transition can be easily

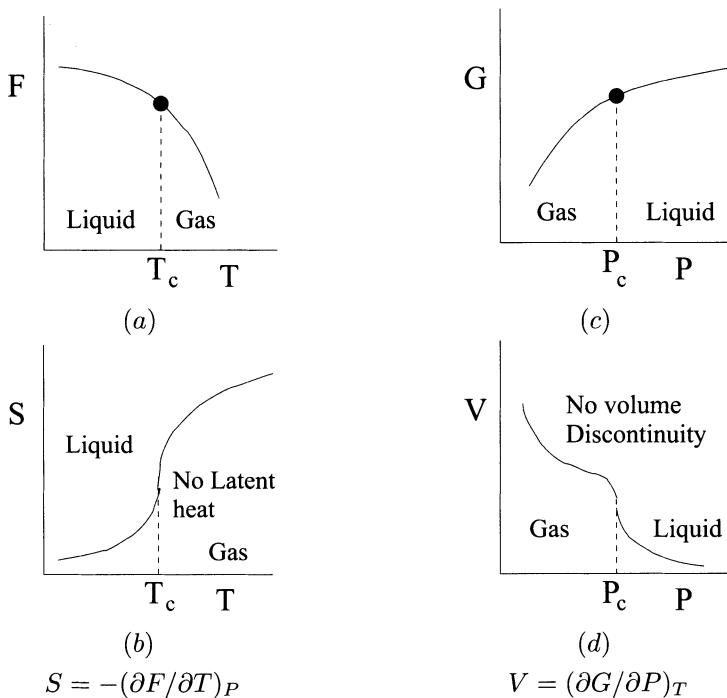


Figure 1.3: Variation of free energies and their first derivatives with respect to the respective parameters around a second order transition. (a) Plot of Helmholtz free energy F against temperature T at a constant pressure. (b) Plot of the entropy S , the first derivative of F with respect to T , against T . (c) Plot of Gibb's free energy G against pressure P at a constant temperature. (d) Plot of the volume V , the first derivative of G with respect to P , against P . No discontinuity is present in either entropy S or volume V .

visualized by considering boiling of water. Any heat absorbed by the system will drive the transition (100°C water to 100°C steam) rather than increasing the temperature of the system. There is then an infinite capacity of absorption of heat by the system.

Problem: One mole of nitrous oxide becomes $\text{N}_2 + \text{O}_2$ at 25°C and one atmospheric pressure. In this process the entropy increases by 76 Joule/K and enthalpy decreases by 8.2×10^4 Joule. Calculate the change in Gibb's free energy and determine the stable phase under these conditions.

1.11.1 Metastability and symmetry breaking

We have seen how to calculate the thermal averages and fluctuations of a macroscopic variable or correlations in a system in thermal equilibrium from the

knowledge of its phase space distribution. But thermal equilibrium alone cannot fix all the properties of the system. If a system is in a metastable state, it may take long time for the system to get over the potential barrier. In such a situation, the system restricts itself to the local minima of the free energy configurations and cannot sample the full phase space in a reasonable time. In such cases we have to be careful of the time period over which we must average our observations so that the corresponding phase space distribution follows Gibbs distribution.

Problem: Consider a two-dimensional Ising model at a temperature ($T \approx 0^{\circ}K$) well below the critical temperature. Start with all the spin down configuration and apply a small positive field $h \ll J$ where J is the interaction strength of the spins. Study the behavior of the total magnetization with time.

In the above problem, spins should mostly align along the direction of the field. But it has to overcome a huge activation barrier as it has to flip too many spins. Depending on the temperature or the thermal energy, the system may get stuck at the metastable state and take long time to reach the true equilibrium state (after sampling the full phase space).

Consider a spin system where the Hamiltonian is spherically symmetric. Such a spin system may show magnetic transition at Curie point. Above the curie point the system as a whole does not have any magnetization. Below the Curie point, the system is spontaneously magnetized: all the spins being aligned in the same direction. The direction of the spin alignment is randomly chosen by the system as it is cooled below the transition temperature. The state of the system, when magnetized, does not reflect the symmetry of the Hamiltonian. The symmetry is reduced and it is often referred to as the symmetry being spontaneously broken.

If one calculates the magnetization as one calculates by averaging over all the microstates of the system, the magnetization will vanish even below the Curie point or transition temperature. This is because the spins can point in any directions with equal probability. The discrepancy between the prediction of statistical mechanics and what we see in nature is explained using ideas similar to that for metastable systems: the time needed for all the spins to go to any other state is very long. If the spins are correlated and aligned to a particular direction, it is of no use for few spins to turn to some other direction. The interactions and correlation will bring back these spins to their original direction in no time. If all the spins have to change direction then it is required for a large fraction of spins to rotate simultaneously, the probability of which decreases sharply as the system size gets larger.

On the other hand, a small system shows magnetization at a temperature higher than the transition temperature. As the system size gets larger the magnetization decreases and eventually go to zero. This is because even at a temperature higher than Curie point, the system will have a finite correlation length and the spins within the correlated region will tend to align in the same

direction. If the system size is smaller than the correlation length, the system will show signs of phase transition. In a system of finite size, the spins can rotate more easily; a symmetry breaking transition and the associated singularities are smeared out and are observed only at the thermodynamic limit. In numerical simulation of phase transitions, special care must be taken for the system size and relaxation or equilibration time. We will discuss these two issues later in details.

1.12 Critical Phenomena

Critical phenomena is the phenomena that accompany the second order phase transition at a critical point. The critical point is reached by tuning thermodynamic parameters (for example temperature T or pressure P or both). Critical phenomena is seen as $T(P)$ approaches the critical point $T_c(P_c)$. In principle, all macroscopic properties can be obtained from the free energy or the partition function. However, since continuous phase transitions (or critical phenomena) involve discontinuities in the response functions at the critical point their must be singularities in the free energy at the critical point. On the other hand, the canonical partition function of a finite number of particles is always analytic. The critical phenomena then can only be associated with infinitely many particles, *i.e.* in the “thermodynamic limit”, and to their cooperative behaviour. The study of critical phenomena is thus essentially related to finding the origin of various singularities in the free energy and characterizing them. Features of critical phenomena are described below.

Let us consider more carefully the two classic examples of second order phase transition involving condensation of gas into liquid and transformation of paramagnet to ferromagnet. In fluid system the thermodynamic parameters are (P, V, T) and in magnetic system the corresponding thermodynamic parameters are (H, M, T) . One may note the correspondence between the thermodynamic parameters of fluid and magnetic systems as: $V \rightarrow -M$ and $P \rightarrow H$. In the case of fluid, instead of volume V we will be considering the density ρ as a parameter. The equation of states in these systems are then given by $f(P, \rho, T) = 0$ and $f(H, M, T) = 0$ respectively. A second order phase transition is a qualitative change in the system behaviour at a sharply defined parameter value, the critical point, when the parameter changes continuously. The critical points are usually denoted by (P_c, ρ_c, T_c) and (H_c, M_c, T_c) . Commonly, phase transitions are studied varying the temperature T of the system and a phase transition occurs at $T = T_c$. We will be describing the features at the critical point by considering different phase diagrams.

First we consider the $P - T$ and $H - T$ diagrams shown in Fig.1.4. It can be seen that the the first order transition line (the vapour pressure curve and $H - T$ line) terminates in a critical point at $T = T_c$. This means that the liquid can be converted to gas continuously without crossing the first order transition line following a path shown by a curved dotted line. Similarly, in the case of

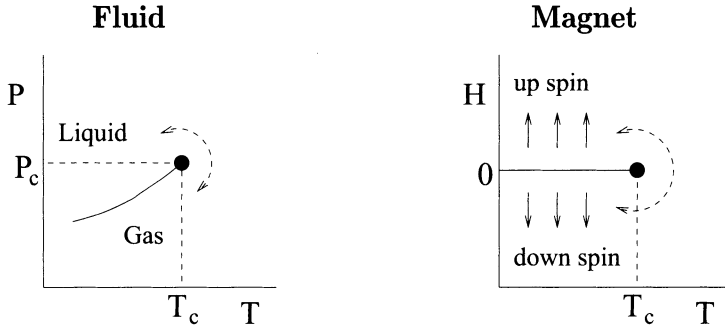


Figure 1.4: Schematic plot of pressure P versus temperature T for a fluid in a gas-liquid transition and of magnetic field (H) versus temperature T for an Ising ferromagnet. The solid line is the first order transition line which ends at a critical point at T_c .

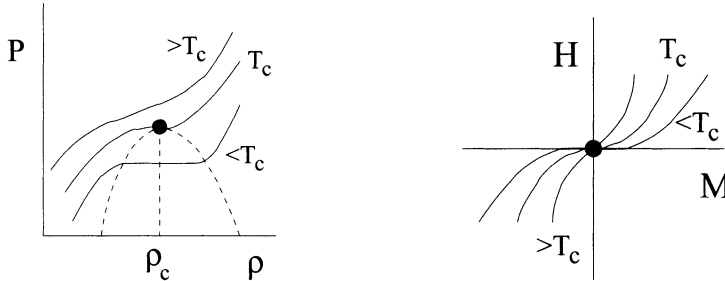


Figure 1.5: Schematic plot of pressure P versus density ρ isotherms for a fluid system and of H versus M for a magnetic system.

magnetic system a continuous change from up spin region to down spin region is also possible.

Next we consider the $P - \rho$ and $H - M$ phase diagrams shown in Fig.1.5. The most striking feature in this phase diagram is the change in shape of the isotherms as the critical point is approached. At high temperature ($T \gg T_c$), the isotherms are expected to be the straight lines given either by the ideal gas equation of state $P = \rho k_B T / m$ or by the Curie law $M = cH/T$, where m is the mass of a molecule and c is a constant. As the temperature decreases toward the critical temperature T_c , the isotherms develop curvature. At $T = T_c$ the isotherms are just flat and one have $\partial P / \partial \rho = 0$ and $\partial H / \partial M = 0$. As a consequence, the response functions: isothermal compressibility $\kappa_T = \frac{1}{\rho} \partial \rho / \partial P$ and the isothermal susceptibility $\chi_T = \partial M / \partial H$ diverges as $T \rightarrow T_c$. These response functions are second derivative of the respective free energy function: $\kappa_T = -\frac{1}{V} (\partial^2 G / \partial P^2)_T$ and $\chi_T = -(\partial^2 F / \partial H^2)_T$. We see that the second derivatives of the free energy are singular (the first derivatives are continuous) as we expect in second order phase transitions.

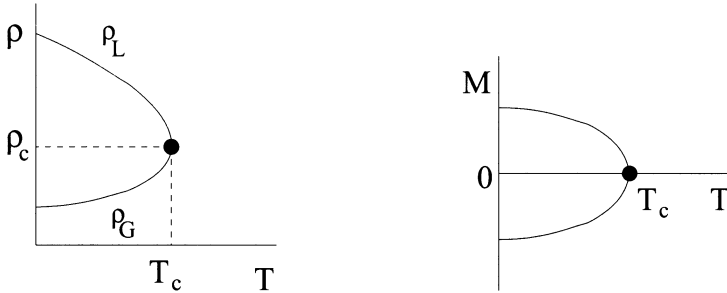


Figure 1.6: Schematic plot of density ρ against temperature T for fluid system and of spontaneous magnetization M against temperature T for magnetic system.

$\rho - T$ and $M - T$ diagrams are shown in Fig. 1.6. From these diagrams as well as from Fig. 1.4, it can be seen that there is a large difference in densities in the liquid and gas phases of a fluid at low temperature. In the magnetic system, there is a large difference in spontaneous magnetization below T_c . As T_c is approached from below, the density difference $\Delta\rho = \rho_L - \rho_G$ of a fluid system and the spontaneous magnetization M of a magnetic system tend to zero. A quantity which is non-zero below T_c and zero above T_c is called the *order parameter* of the transition. Thus, $\Delta\rho$ and M serve as order parameter of the fluid and magnetic system respectively. Note that below T_c the order parameter is multivalued where as it is single valued (zero) above T_c . Thus, the order parameter has a branch point singularity at $T = T_c$.

1.12.1 Fluctuation and correlation

As one have noticed in Fig.1.5, the isotherms develop curvature as the system approaches the critical temperature T_c from above. The curvature in the isotherms is the manifestation of the long range correlation of the molecules in the fluid or spins in magnets. At high temperature, the gas molecules move randomly or the magnetic moments flip their orientation randomly. Due to the presence of interactions small droplets or domains of correlated spins appear as the temperature decreases. These droplets grow in size as T decreases closer to T_c . At $T = T_c$, droplets or domains of correlated spins of all possible sizes appear in the system. Lateral dimension of these droplets become of the order of the wavelength of ordinary light. Upon shining light on the fluid at $T = T_c$, a strong scattering is observed and the fluid appears as milky white. The phenomenon is known as *critical opalescence*. Similarly in magnetic systems, domains of correlated spins of all possible sizes appear in the system and a huge neutron scattering cross section is observed at $T = T_c$. As $T \rightarrow T_c$, there appears droplet or domain of correlated spins of the order of system size. One may define a length scale called correlation length which is the lateral dimension of the droplets or domains of correlated spins. Therefore, the correlation

length diverges as $T \rightarrow T_c$. One should note that the system does not correspond to a ordered state at T_c and a completely ordered state is achieved only at $T = 0$.

As the system approaches T_c , there are long wave-length fluctuations in density in fluid or in the orientation of magnetic moments in the magnetic system. These fluctuations occur at every scale. If ξ is the largest scale of fluctuation and a is the lattice spacing, then the system appears to be self-similar on all length scales x for $a < x < \xi$. At $T = T_c$, ξ is infinite and the system becomes truly scale invariant. The correlation between the spins (or molecules) are measured in terms of fluctuations of spins (or density) away from their mean values (see section 10):

$$G(s_i, s_j) = \langle (s_i - \langle s_i \rangle)(s_j - \langle s_j \rangle) \rangle \sim r^{-(d-2+\eta)} \exp(-r/\xi) \quad (1.49)$$

where r is the distance between s_i and s_j , ξ is the correlation length and η is some exponent. At the criticality, ξ diverges to infinity and $G(\vec{r})$ decays as a power law.

Close to a critical point, the large spatial correlations which develop in the system are associated with long temporal correlations as well. At the critical point, the relaxation time and characteristic time scales diverge as determined by the conservation laws. This is known as the *critical slowing down*. A relaxation function $\phi(t)$ may decay exponentially at long times as $\phi(t) \sim e^{-t/\tau}$, where τ is the relaxation time. τ diverges at the critical point and the dynamic critical behavior can be expressed in terms of the power law as $\tau \propto \xi^z$, where z is called the dynamic critical exponent.

1.12.2 Critical exponents and universality

Thermodynamic variables show singular or non-analytic behavior as one approaches the critical point. The singular behaviour in the vicinity of the critical point ($T \rightarrow T_c$) is characterized by a set of *critical exponents* such as $\alpha, \beta, \gamma, \delta$ and ν , etc. For example, the singularity in the order parameter is defined by the exponent β , γ defines the singularity in susceptibility or compressibility, α defines the singularity in specific heat, etc. The critical exponents which are most commonly encountered are defined below. Note that the singularity in specific heat is either of finite discontinuity ($\alpha = 0$) or of logarithmic divergence. It is assumed that the critical exponent associated with a given thermodynamic quantity is the same as $T \rightarrow T_c$ from above or below. Though it seems such an assumption is unjustified but with the help of renormalization group it can be proved that they are same.

	Fluid system	Magnetic system
Order parameter:	Density difference: $\Delta\rho \sim (T_c - T)^\beta$	Spontaneous magnetization: $M \sim (T_c - T)^\beta$
Critical isotherm at $T = T_c$:	$\Delta\rho \sim (P - P_c)^{1/\delta}$	$M \sim H^{1/\delta}$
Response functions:	Compressibility: $\kappa_T \sim T - T_c ^{-\gamma}$	Susceptibility: $\chi_T \sim T - T_c ^{-\gamma}$
	Specific heat: $C_V \sim T - T_c ^{-\alpha}$	Specific heat: $C_H \sim T - T_c ^{-\alpha}$
Correlation length:	$\xi \sim T - T_c ^{-\nu}$	$\xi \sim T - T_c ^{-\nu}$
Correlation function at $T = T_c$:	$G(\vec{r}) \sim r^{-(d-2+\eta)}$	$G(\vec{r}) \sim r^{-(d-2+\eta)}$

The critical temperature T_c at which the transition occurs is found to be dependent on the details of interatomic interactions or underlying lattice structure and varies from material to material. Critical temperatures of different materials are listed in table 1.1.

Table 1.1: List of critical parameters for different fluid and magnetic systems. For magnetic systems, other critical parameters are spontaneous magnetization (M) and external magnetic field (H). Both M and H are zero at the critical point. Data have been collected from reference [9].

Fluids	T_c (K)	P_c (atm)	ρ_c (g/cm ³)	Magnets	T_c (K)
Water	647.5	218.50	0.325	Fe	1043.00
Alcohol	516.6	63.10	0.280	Ni	627.20
CO_2	304.2	72.80	0.460	CrBr_3	32.56
Argon	150.8	48.34	0.530	EuS	16.50

On the other hand, the critical exponents are somewhat universal and depends only on a few fundamental parameters. Relevant factors which govern the universal values of the exponents for models with short range interactions are spatial dimensionality, spin dimensionality, symmetry of the ordered state, presence of symmetry breaking fields whereas it is independent of lattice structure and the type of interaction. It is remarkable to note that the transitions as different as “liquid to gas” and “ferromagnet to paramagnet” are described by the same set of critical exponents. In table 1.2, the values of the critical exponents for some fluid and magnetic systems are listed.

Table 1.2: List of critical exponents for different fluid and magnetic systems. Data have been collected from [9].

Fluids	α	β	γ	δ	Magnets	α	β	γ	δ
CO ₂	0.1	0.34	1.35	4.2	Ni	0	0.42	1.35	4.22
Xe	0.2	0.35	1.30	4.4	CrBr ₃	—	0.308	1.215	4.3

1.12.3 Models and universality

Critical phenomena has been studied constructing several lattice models. Some of the most fundamental models with their corresponding Hamiltonian are listed below. The system with magnetic moment μ of each atom is placed in an external magnetic field \vec{H} , say along the z -axis.

$$\text{Spin-1/2 Ising model: } \mathcal{H} = -J \sum_{\langle ij \rangle} s_i s_j - h \sum_i s_i, \quad s_i = \pm 1; \quad h = \mu H$$

$$\text{q-state Potts model: } \mathcal{H} = -J \sum_{\langle ij \rangle} \delta_{\sigma_i \sigma_j}, \quad \sigma_i = 1, 2, 3, \dots, q; \quad H = 0$$

$$\text{X-Y model: } \mathcal{H} = -J_{\perp} \sum_{\langle ij \rangle} (s_i^x s_j^x + s_i^y s_j^y) - h \sum_i s_i^z, \quad h = \mu H$$

x,y,z are labels of Cartesian axes in spin space.

$$\text{Heisenberg model: } \mathcal{H} = -J \sum_{\langle ij \rangle} \vec{s}_i \cdot \vec{s}_j - \sum_i \vec{h} \cdot \vec{s}_i, \quad h \hat{k} = \mu H \hat{k}$$

\vec{s}_i : 3 dimensional vector in the classical model.
(In quantum model, s_j are the quantum spin operators, the Pauli spin matrices.)

In order to estimate the values of the critical exponents, these models have to be studied at their respective critical points. Mean field theories are often applied to estimate the critical exponents. In a mean field theory, the molecular interaction (or spin-spin interaction) term in the Hamiltonian is replaced by an average (or mean) field. The “interacting system” is then approximated as a “non-interacting system” in a self-consistent external field. The approximation enables one to obtain the partition function and hence the free energy exactly. The mean field exponents however do not agree with those of the real magnets or fluids (see table 1.2). This is because of the fact that fluctuations are ignored in mean field approximation. The theory is expected to be consistent and the exponents would be correct at space dimensionality $d \geq d_c$. d_c is called the upper critical dimension and it depends on the model. $d_c = 4$ for Ising model and ϕ^4 Landau-Ginzberg model. Moreover, mean field wrongly predicts phase transition in $d = 1$ at finite temperature.

Since evaluation of partition function for an interacting system is difficult, the exact solution of these models near the critical point is rarely available. Moreover, the partition function as well as the free energy function become singular at $T = T_c$. Spin-1/2 Ising model is exactly solved in $d = 1$ and with zero field in $d = 2$. In $d = 3$, exact solution of Ising model is not obtained. On the other hand, exact solution of quantum models exists only in $d = 1$. Transfer matrix technique is often useful to obtain exact solutions. In this technique, the partition function is obtained as a matrix and the free energy is obtained as a function of the largest eigenvalue.

Renormalization group (RG) technique provides a direct method of calculating the properties of a system arbitrarily close to the critical point. RG is able to explain the universality, explains why the free energy function is a generalized homogeneous function and estimates the values of the critical exponents. The essence of RG is to break a large system down to a sequence of smaller systems. Instead of keeping track of all the spins (or particles) in a region of size ξ , the correlation length, the long range properties are obtained from short range fluctuations in a recursive manner. Each time after eliminating the short range fluctuations, the system is restored to its original scale. Most often the recursion relations of the system parameters are found to be complicated and estimation of critical exponents become difficult.

Table 1.3: List of critical exponents obtained from different analytical models. Data have been taken from reference [7].

Models	Symmetry of order parameter	α	β	γ	δ	ν	η
2d Ising	2-component scalar	0 (log)	1/8	7/4	15	1	1/4
3d Ising	2-component scalar	0.10	0.33	1.24	4.8	0.63	0.04
2d Potts, $q = 3$	q -component scalar	1/3	1/9	13/9	14	5/6	4/15
3d X-Y	$2 - d$ vector	0.01	0.34	1.30	4.8	0.66	0.04
3d Heisenberg	$3 - d$ vector	-0.12	0.36	1.39	4.8	0.71	0.04
Mean field		0 (dis)	1/2	1	3	1/2	0

The critical exponents obtained in the above models using different methods are listed in table 1.3. It can be seen that the values of the critical expo-

nents depend on the space dimension as well as on the symmetry of the order parameter. A class of systems found to have the same values of the critical exponents if the number of components of order parameter and dimension d of the embedding space are the same. Hence, these critical exponents define a universality class. In other words, those systems which have the same set of critical exponents are said to belong to the same universality class. For example, nearest neighbor Ising ferromagnets on square and triangular lattices have identical critical exponents and belong to the same universality class. Critical exponents of $d = 3$ Ising model is similar to those of fluid systems because of the same symmetry of the order parameter.

Problem: The spin-1/2 Ising Hamiltonian is given by

$$\mathcal{H} = -J \sum_{\langle ij \rangle} s_i s_j - h \sum_i s_i$$

where the external field is in units of energy. Show that the mean field Hamiltonian for this system with nearest neighbour interaction of strength $J > 0$ on a lattice with coordination number z under a uniform external magnetic field h is given by

$$\mathcal{H}_i = -(Jzm + h)s_i$$

where m is the per spin magnetization. Calculate the free energy density $f = -k_B T \ln Z_1$, Z_1 is the single particle partition function. Show that per spin magnetization m is given by

$$m = \tanh \frac{Jzm + h}{k_B T}.$$

Solve the self-consistent equation of magnetization and obtain the critical temperature $T_c = Jz/k_B$. Calculate the critical exponents α, β, γ and δ and verify the scaling relations $\alpha + 2\beta + \gamma = 2$ and $\gamma = \beta(\delta - 1)$. From the correlation function one may obtain $\nu = 1/2$. Check that upper critical dimension $d_c = 4$ in order to satisfy the scaling relation $2 - \alpha = d\nu$.

Problem: The classical Heisenberg model used for ferromagnetism is described by

$$\mathcal{H} = -J \sum_{\langle ij \rangle} \vec{s}_i \cdot \vec{s}_j - \sum_i \vec{h} \cdot \vec{s}_i$$

where \vec{s}_i is a 3-dimensional unit vector in a d -dimensional lattice. Consider $J > 0$ and let the external field $\vec{h} = \mu \vec{H}$ be uniform and along z -direction. Using mean field approximation $\langle \vec{s}_j \rangle = m \hat{k}$, show that the Hamiltonian can be obtained as

$$\mathcal{H} = -(cJm + h) \sum_i s_i^z$$

where c is the coordination number of a d -dimensional lattice. Assuming s^z can take on an entire continuum of orientations and the magnitude of the spin as 1, obtain the per spin magnetization m as

$$m = \coth\left(\frac{cJm + h}{k_B T}\right) - \frac{1}{(cJm + h)/k_B T}.$$

Find the critical temperature $T_c = cJ/(3k_B)$ and the values of the critical exponents β, γ and δ . Check that the values of β, γ and δ are the same as those obtained in Ising mean field.

Problem: The Hamiltonian of a one dimensional spin-1/2 Ising model of N spins with nearest neighbour interaction is given by

$$\mathcal{H} = -J \sum_{j=1}^N s_j s_{j+1} - h \sum_i s_i$$

where h is external field in units of energy. Applying periodic boundary condition, obtain the transfer matrix of the system

$$\mathbf{T} = \begin{pmatrix} e^{\beta(J+h)} & e^{-\beta J} \\ e^{-\beta J} & e^{\beta(J-h)} \end{pmatrix}$$

where $\beta = 1/k_B T$. Obtain the free energy density $f = -k_B T \ln \lambda_{max}$ where λ_{max} is largest eigenvalue of the transfer matrix \mathbf{T} . Calculate magnetization

$$m = \frac{e^{\beta J} \sinh \beta J}{\sqrt{e^{2\beta J} \sinh^2 \beta J + e^{-2\beta J}}}$$

Check that no phase transition is possible at any finite temperature T except at $T = 0$.

1.12.4 Homogeneity and scaling

From thermodynamic consideration it can be shown that the critical exponents satisfy certain relations among them as inequalities. For example, the positive values of the specific heats leads to

$$\alpha + 2\beta + \gamma \geq 2, \tag{1.50}$$

known as Rushbrooke inequality. From the convexity property of the free energy, another exponent inequality can be obtained as

$$\alpha + \beta(1 + \delta) \geq 2. \tag{1.51}$$

Other well known inequalities are:

$$\gamma \leq (2 - \eta)\nu; \quad d\nu \geq 2 - \alpha; \quad \gamma \geq \beta(\delta - 1). \tag{1.52}$$

However, studying the values of critical exponents given in tables 1.2 and 1.3, it can be verified that the inequalities are satisfied as exact equality. Assuming the free energy functions as generalised homogeneous function in the critical regime, one can show that the scaling relations among the critical exponents are satisfied as exact equalities.

A function $f(x, y)$ is said to be a generalised homogeneous function if

$$f(\lambda^a x, \lambda^b y) = \lambda f(x, y) \quad (1.53)$$

for all values of the parameter λ , where a and b are two arbitrary numbers. Since the parameter λ is arbitrary, one can make a choice of λ as $\lambda = 1/x^{1/a}$ so that the above equation reduces to the form

$$\begin{aligned} f(1, y/x^{b/a}) &= F(y/x^{b/a}) = \frac{1}{x^{1/a}} f(x, y) \\ f(x, y) &= x^{1/a} F(y/x^{b/a}). \end{aligned} \quad (1.54)$$

In the case of magnetic phase transition, x may represent the reduced temperature, $t = (T - T_c)/T_c$ and y the reduced magnetic field $h (= \mu H/k_B T)$. Thus, at the critical regime, when both the field h and the temperature t are close to zero, the free energy function $f(t, h)$ can be written as

$$f(\lambda^{a_t} t, \lambda^{a_h} h) = \lambda f(t, h). \quad (1.55)$$

The homogeneous free energy function can be rewritten as a scaled function $F(z) = f(x, y)/x^{1/a}$ of a scaled variable $z = y/x^{b/a}$. Hence, the plots of $F(z)$ versus z for different values of x and y all collapse into a single curve, the function $F(z)$. This is known as data collapse. In the case of magnetic transition, the scaling function of magnetization M is given by

$$M(t, h) \sim |t|^\beta \mathcal{M}(\pm 1, h|t|^{-\beta\delta}) \quad (1.56)$$

where t is the reduced temperature, h is the reduced magnetic field and β, δ are critical exponents. The scaled magnetization and magnetic field can be defined as

$$\bar{m} = M(t, h)/|t|^\beta; \quad \bar{h} = h|t|^{-\beta\delta}, \quad (1.57)$$

and the scaled magnetization becomes

$$\bar{m} = \mathcal{M}(\pm 1, \bar{h}). \quad (1.58)$$

Hence a plot of \bar{m} against \bar{h} should lie on the same curve for all values of temperature greater than or less than T_c respectively, provided that they lie in the critical regime.

The scaling implies a scale invariance in the problem. Any observable, be it magnetization, susceptibility or specific heat, if it is known at a certain temperature T_1 , its value can be scaled appropriately for any other temperature T_2 , provide the temperatures T_1 and T_2 are in the scaling regime. The feature of scale invariance greatly helps in understanding complexities of the

strongly correlated processes of critical phenomena by means of scaling and renormalization group methods.

Since the thermodynamic quantities are different derivatives of the free energy function, the critical exponents are not all independent and can be obtained in terms of a_t and a_h . Taking appropriate derivatives of the free energy function in the limit $h = 0$ and $t \rightarrow 0$, one finds

$$\alpha = 2 - \frac{1}{a_t}; \quad \beta = \frac{1 - a_h}{a_t}; \quad \gamma = \frac{2a_h - 1}{a_t}; \quad \delta = \frac{a_h}{1 - a_h}. \quad (1.59)$$

The scaling relations among the critical exponents α , β , γ and δ are then obtained as

$$\alpha + 2\beta + \gamma = 2 \quad \text{and} \quad \gamma = \beta(\delta - 1). \quad (1.60)$$

Assuming the homogeneity of the correlation length ξ and the correlation function $G(\vec{r})$, one can establish the hyperscaling relations

$$2 - \alpha = d\nu \quad \text{and} \quad \gamma = (2 - \eta)\nu. \quad (1.61)$$

Problem: From thermodynamic consideration prove Rushbrooke inequality.

Problem: Consider a model equation of state

$$H \approx aM(t + bM^2)^\theta; \quad 1 < \theta < 2; \quad a, b > 0$$

near the critical point, the reduced temperature $t = 0$. Find the exponents β , γ and δ and check that the inequality $\gamma \geq \beta(\delta - 1)$ is satisfied as an equality.

Problem: Starting from the scaling form of the free energy

$$f(t, h) = b^{-d} f(b^{\theta_1} t, b^{\theta_2} h)$$

where t, h are the reduced temperature and $h = H/k_B T$, obtain the critical exponents α, β, γ and δ and confirm that $\alpha + 2\beta + \gamma = 2$, $\gamma = \beta(\delta - 1)$.

1.13 Concluding Remarks

A brief account of statistical mechanics and critical phenomena is presented. For details one needs to consult the texts mentioned in the reference. However, these basic concepts will be useful in the later chapters where we will be talking about different numerical techniques for studying interacting systems. In this briefing we have only mentioned about equilibrium statistical mechanics. In certain chapters dynamical systems at out of equilibrium situations will also be discussed and the necessary background will be developed there itself.

References

- [1] S. R. A. Salinas, *Introduction to Statistical Physics*, (Springer, New York, 2004).
- [2] J. K. Bhattacharjee, *Statistical Physics: Equilibrium, and Non-equilibrium Aspects*, (Allied Publishers Ltd., New Delhi, 1997).
- [3] R. K. Pathria, *Statistical Mechanics*, (Butterworth-Heinemann, Oxford, 1996).
- [4] K. Huang, *Statistical Mechanics*, (John Wiley & sons, New York, 2000).
- [5] M. Plischke and B. Bergersen, *Equilibrium Statistical Physics*, (World Scientific, Singapore, 1994).
- [6] R. Kubo, *Statistical mechanics: an advanced course with problems and solutions* (North Holland, Amsterdam, 1965).
- [7] J. M. Yeomans, *Statistical Mechanics of Phase Transitions*, (Oxford University Press, New York, 1994).
- [8] J. J. Binney, N. J. Dowrick, A. J. Fisher and M. E. J. Newman, *The Theory of Critical Phenomena*, (Oxford University Press, Oxford, 1992).
- [9] H. E. Stanley, *Introduction to Phase Transitions and Critical Phenomena*, (Oxford University Press, New York, 1987).
- [10] D. A. R. Dalvit, J. Frastai and I. D. Lawrie, *Problems on Statistical Mechanics*, (IOP Publishing, Bristol and Philadelphia, 1999).
- [11] L. P. Kadanoff, *Statistical Physics: Statics, Dynamics and Renormalization*, (World scientific, Singapore, 2000).
- [12] J. L. Cardy, *Scaling and Renormalization in Statistical Physics*, (Cambridge University Press, Cambridge, 1996).
- [13] S. K. Ma, *Modern Theory of Critical Phenomena*, (Levant books, Kolkata, 2007).
- [14] M. E. Fisher, Rev. Mod. Phys. **46**, 597 (1974); **70**, 653 (1998).

Chapter 2

Graphical Enumeration Techniques: Series Expansions and Animal Problems

Deepak Dhar

2.1 Introduction

In this pedagogical introduction to some graphical enumeration problems in statistical physics, I start with the high-temperature and low-temperature expansions of the Ising model. I then discuss enumeration of clusters in the percolation problem, and Martin's algorithm for their enumeration. The exact enumeration of two-dimensional directed animals is then described, and the extension of this result to the generating function of more general heaps is explained.

The aim of these lecture notes is to introduce the readers to the techniques of graphical enumeration, for solving problems in statistical physics. I assume that you have already had the first course in statistical physics, and basic principles of equilibrium statistical physics are known. In particular, I assume that you have already seen the statistical mechanical treatment of ideal gases (classical monoatomic ideal gases, and the ideal Bose and Fermi gases). The problem of a system of coupled harmonic oscillators reduces to that of non-interacting normal modes, and can be solved similarly. Thus one can calculate the partition function of a system of non-interacting *phonons*, or of photons, and see how the average energy of the system varies as a function of temperature.

2.2 Ising Model in One Dimension

Let us consider a line of N sites, labeled by integers 1 to N . At each site i , we have a spin σ_i , which takes values ± 1 . The Hamiltonian of the system is

$$H = -J \sum_{i=1}^{N-1} \sigma_i \sigma_{i+1} \quad (2.1)$$

There are 2^N distinct configurations. The system is in contact with a heat bath at temperature T , and each configuration \mathcal{C} occurs in the canonical ensemble, with a probability $Prob(\mathcal{C}) = \exp[-\beta H(\mathcal{C})]/\mathcal{Z}$, where

$$\mathcal{Z} = \sum_{\mathcal{C}} e^{-\beta H(\mathcal{C})} \quad (2.2)$$

Our first problem is to calculate $\mathcal{Z}(\beta)$.

Method 1: We consider a change of variables. Define Ising variables $\{\tau_i\}$, with $\tau_1 = \sigma_1$, and $\tau_i = \sigma_{i-1}\sigma_i$, for $i > 1$.

Then, we get $H = -J \sum_{i=2}^N \tau_i$. The summation over 2^N values of $\{\sigma_i\}$ is same as summation over 2^N values of $\{\tau_i\}$. And we get

$$\mathcal{Z} = 2^N [\cosh \beta J]^{N-1} \quad (2.3)$$

We can define free energy per site in the thermodynamical limit of large N as $f(\beta) = \lim_{N \rightarrow \infty} -k_B T (\log \mathcal{Z})/N$. Then we get

$$f(\beta) = -k_B T \log(2 \cosh \beta J) \quad (2.4)$$

Method 2: The Transfer Matrix Method:

Define $Z_n(+)$ = partition function of a chain of n sites with left-most site held fixed +1, and sum over the rest. Define $Z_n(-)$ similarly. Then we can write the recursion equation

$$\begin{bmatrix} Z_{n+1}(+) \\ Z_{n+1}(-) \end{bmatrix} = \begin{bmatrix} e^{\beta J} & e^{-\beta J} \\ e^{-\beta J} & e^{\beta J} \end{bmatrix} \begin{bmatrix} Z_n(+) \\ Z_n(-) \end{bmatrix} \quad (2.5)$$

Calling the matrix on the right hand side of this equation as the transfer matrix \mathbf{T} , we write

$$\begin{bmatrix} Z_{n+1}(+) \\ Z_{n+1}(-) \end{bmatrix} = \mathbf{T} \begin{bmatrix} Z_n(+) \\ Z_n(-) \end{bmatrix}. \quad (2.6)$$

These recursion equations can be easily solved to give $Z_n(+)$ and $Z_n(-)$ explicitly as functions of n

$$\begin{bmatrix} Z_n(+) \\ Z_n(-) \end{bmatrix} = \mathbf{T}^{n-1} \begin{bmatrix} 1 \\ 1 \end{bmatrix} \quad (2.7)$$

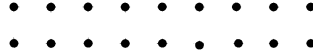


Figure 2.1: A ladder graph.

with

$$Z_n = Z_n(+) + Z_n(-) \quad (2.8)$$

Let the eigenvalues of T be λ_+ and λ_- , with $\lambda_+ > \lambda_-$. Then, for large N , we get $Z_N \sim \lambda_+^N$, and $f(\beta)$ is as calculated before.

Exercise. 1: Show that the partition function of Ising model on a one-dimensional ring of N sites is $Z_N = \text{Tr}[T^N]$.

Exercise. 2: Calculate the partition function of the Ising model on a $2 \times N$ ladder graph (Fig.2.1). In this case, the transfer matrix T is a 4×4 matrix.

Exercise. 3: Suppose we add an external magnetic field, so that the Hamiltonian is $H' = H - h \sum_i \sigma_i$. Extend the treatment above, using the transfer matrix, to calculate the free energy per spin $f(\beta, h)$.

2.3 High-temperature Expansions for Ising Systems

We now want to calculate Z for a more non-trivial case. Consider the two-dimensional Ising model. Here we have Ising spins on the vertices of an $L \times M$ square lattice. Each spin has a ferromagnetic coupling to its nearest neighbor of strength J . Let $\sigma_{i,j}$ be the spin at site (i, j) . The Hamiltonian is now written as

$$H = -J \sum_{i,j} [\sigma_{ij}\sigma_{i+1,j} + \sigma_{i,j}\sigma_{i,j+1}] \quad (2.9)$$

We want to calculate the partition function

$$Z = \sum_{\{\sigma\}} \exp[-\beta H(\{\sigma\})] \quad (2.10)$$

where $\{\sigma\}$ denotes a configuration of spins on the lattice, and the sum over $\{\sigma\}$ is sum over all spin configurations.

For Ising variables σ and σ' , which take only values ± 1 , we have the identity

$$\exp(\beta J \sigma \sigma') = \cosh(\beta J)[1 + x \sigma \sigma'] \quad (2.11)$$

where $x = \tanh(\beta J)$.

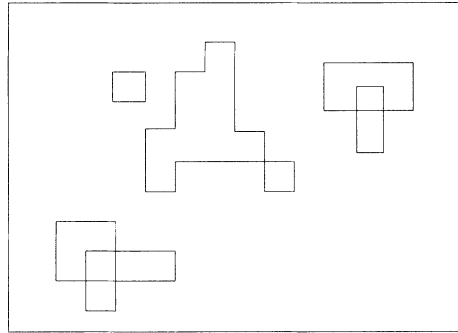


Figure 2.2: A configuration that contributes to the high temperature expansion for the Ising model

Then we get

$$Z = [\cosh \beta J]^{N_B} \sum_{\{\sigma\}} \prod_B (1 + x\sigma_B \sigma'_B) \quad (2.12)$$

where the product over B is over all bonds of the lattice, and σ_B and σ'_B denote two spins at the end of the bond B . N_B is the number of bonds in the graph. Now Z is a polynomial in x (apart from the simple multiplying prefactor). We expand the product, and then first do the summation over $\{\sigma\}$ for each term, and then sum the terms.

Since the number of terms is very large, we need a good way of specifying the different terms. The most convenient scheme that has been found to work is this: we think of the square lattice as specified by its graph, i.e. a set of vertices, with a bond between vertices that are nearest neighbor on the square lattice. After this, we do not worry about the actual distances between vertices, or angles between bonds. Each term in the expansion is associated with a diagram; we draw a bond between two sites for the term $x\sigma_B \sigma'_B$, and no bond corresponding to the 1 in $(1 + x\sigma_B \sigma'_B)$. Each such diagram has only a subset of bonds of the original graph. There is a one-to-one correspondence between different terms in the expansion, and different diagrams. Then the summation over the 2^{N_B} terms in the expansion Eq.(2.12) is equivalent to summing over all possible 2^{N_B} diagrams.

Now consider one particular diagram corresponding to specific term. It is easy to sum over $\{\sigma_i\}$, and we get zero, if there is any vertex in the diagram that has an odd number of bonds. If the number is even at all vertices (an example of such a diagram is shown in Fig.2.2), then the weight is 2^{N_s} , where N_s is the number of sites in the graph (using $\sigma_{i,j}^2 = 1$).

Then, the partition function Z can be written as $Z = 2^{N_s} [\cosh(\beta J)]^{N_B} \tilde{Z}$, with

$$\tilde{Z} = \sum_{\ell} C(\ell, L, M) x^{\ell} \quad (2.13)$$

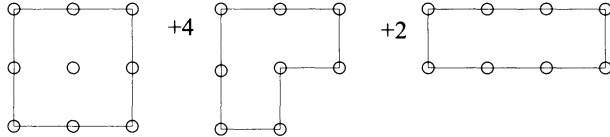


Figure 2.3: All possible lattice polygons of perimeter 8 on the square lattice.

where $C(\ell, L, M)$ is the number of ways one can draw a diagram with ℓ links on the $L \times M$ square lattice, where each vertex has even number of bonds. The problem of determining the partition function of the Ising model has been reduced to the enumeration problem of some kinds of diagrams. For high temperatures (small x), we may keep only terms upto some maximum power of x . Then the result is exact upto that order in x . Hence the name “high temperature expansion”.

We note that $C(0, L, M) = 1$. Let us assume periodic boundary conditions for the lattice. For $\ell = 1, 2, 3$, we have $C(\ell, L, M) = 0$. The coefficient $C(4, L, M)$ is the number of ways one can put a small square in different positions on the lattice. Hence this number is $LM = N_s$. For $\ell = 6$, only diagram possible is a hexagon enclosing two adjacent small squares. Thus, the RHS of Eq.(2.13) can be written as

$$1 + N_s x^4 + 2N_s x^6 + \mathcal{O}(x^8) \quad (2.14)$$

The enumeration of terms of order x^8 is more complicated. One can have two small squares, separated from each other, or one can have one simple polygon of perimeter 8. There are $N_s(N_s - 5)/2$ terms of the first type. An exhaustive enumeration of possible lattice octagons (see Fig.2.3) shows that the term is $N_s(N_s + 9)x^8/2$.

We define

$$F(x) = \lim_{N_s \rightarrow \infty} \frac{1}{N_s} \log \tilde{Z} \quad (2.15)$$

We assume that $F(x)$ has a Taylor expansion in powers of x :

$$F(x) = F_4 x^4 + F_6 x^6 + F_8 x^8 + \dots \quad (2.16)$$

Then clearly $\exp[N_s F(x)]$ has a Taylor expansion in powers of x given by

$$\exp[N_s F(x)] = 1 + N_s F_4 x^4 + N_s F_6 x^6 + [(1/2)F_4^2 N_s^2 + F_8 N_s] x^8 + \mathcal{O}(x^{10}) \quad (2.17)$$

Comparing with the exact calculated numbers $C(\ell, L, M)$, we see that $F_4 = 1$, $F_6 = 2$, and $F_8 = 9/2$. So that we have

$$F(x) = x^4 + 2x^6 + \frac{9}{2}x^8 + \dots \quad (2.18)$$

We can also write series expansion for $e^{F(x)}$, which is called the partition function per site

$$e^{F(x)} = 1 + x^4 + 2x^6 + 5x^8 + \dots \quad (2.19)$$

At higher orders, $C(\ell, L, M)$ would have terms that vary as larger powers of N_s . However, these higher powers cancel out exactly automatically, *if we have matched the terms of order N exactly to all lower orders in x* . Then, the coefficients F_ℓ are independent of N_s . The fact that terms in the partition function that vary as higher power of N_s than 1 cancel on taking the logarithm, is a consequence of the extensivity of free energy. This important technique is variously called the linked cluster expansion, or the cumulant expansion. For a more general discussion, see [1]. A very readable elementary account of series expansion methods in statistical physics may be found in [2].

So, now, with the linked cluster expansion theorem, the graphical enumeration problem, for any fixed order ℓ , reduces to a *finite* enumeration problem, where the formal limit $L, M \rightarrow \infty$ has been taken already.

Clearly, evaluation of still higher orders requires some practice in graphical enumerations. One can use the enormous power provided by digital computers, to calculate these series to very high orders. For example, for the three dimensional Ising model, the high-temperature series has been extended up to 46th order in x [3]. For many other lattice models, similarly long series expansions have been calculated. For special cases, one can get much longer series. For example, for the directed percolation on the square lattice, the series expansion is known exactly to 171 orders! And this is the best one can do, the exact solution is not known [4]. The series expansion method provides a *systematic* method of making better and better approximations to the exact answer for a problem with no analytical exact solution. Note that, in contrast, most other approximations used in different branches of physics often involve an error that cannot be made “as small as you wish” if you are willing to work harder (e.g. “the effective medium approximation”, or the “random phase approximation”).

Since one can generate such series to very high orders, the analysis of such series has also become quite sophisticated. For example, in [5], a high order series is used to guess the exact functional form of the answer for counting a type of almost-convex polygons (polygons whose perimeter differs from that of bounding rectangle by at most 4 units), by exact enumeration of the series for perimeter up to $\ell = 110!$. [An exclamation mark, not a factorial sign.]

Exercise. 4: Use the high temperature expansion, to show that for the problem in Exercise 1, $Z_N = [2 \cosh \beta J]^N (1 + x^N)$.

Exercise. 5: Consider the Ising model on the square lattice with 4-spin couplings

$$H_4 = -J \sum_{\text{squares}} \sigma_{i,j} \sigma_{i,j+1} \sigma_{i+1,j} \sigma_{i+1,j+1} \quad (2.20)$$

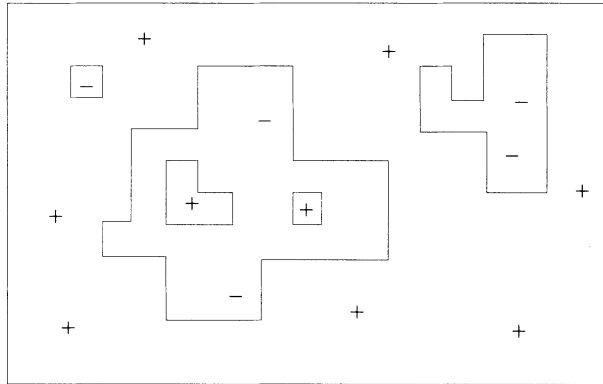


Figure 2.4: A configuration of the Ising model at low temperatures. The + and - signs denote regions where the spins are + and - respectively.

Show that in the high temperature expansion of this model, all terms except the lowest order are zero.

Exercise. 6: Extend the calculation of high temperature series expansion given in Eq.(2.19) to order x^{10} .

2.4 Low-temperature Expansion of the Ising Model and Self-duality

One can also develop a low-temperature expansion for the free energy of the Ising model. We note that at low temperatures, a typical configuration would have most spins aligned parallel (say +), and a few - spins interspersed [Fig.2.4]. Then, a configuration in which there are ℓ ‘bad’ bonds has a relative weight $\exp(-2\ell\beta J)$, compared to the ground state. writing this weight as y^ℓ , we see that the partition function looks like

$$Z = e^{2N_s\beta J}[1 + N_s y^4 + 2N_s y^6 + \dots] \quad (2.21)$$

These graphs are the same as in the high temperature expansion! We thus get a non-trivial relation between the partition function $Z(\beta)$ and partition function $Z(\beta')$ at a different value β' given by

$$\tanh \beta' J = e^{-2\beta J}, \quad \sinh \beta J \sinh \beta' J = 1 \quad (2.22)$$

and

$$Z(\beta) \exp(-2N_s\beta J) = Z(\beta')[2 \cosh^2 \beta' J]^{-N_s} \quad (2.23)$$

If β is small, β' is large, and vice versa. At one particular value β^* we have $\beta = \beta'$. Then this point must be the common boundary between the high

- and low-temperature phases. Thus, we get that the critical temperature for the square lattice Ising model is given by the condition

$$\sinh(J/k_B T_c) = 1 \quad (2.24)$$

More generally, the high-temperature graphical expansion of the partition function of a lattice model can often be reinterpreted as the low-temperature graphical expansion of some other model. Such models are said to be low-temperature-high temperature duals of each other. The Ising model on the square lattice is said to be *self-dual*.

2.5 Percolation and Animal Problems

We will now discuss the use of graphical enumeration technique in percolation and animal problems. The percolation problem is easy to state, and quite non-trivial to study. In particular, it provides a very simple setting for studying phase transitions.

Consider a box full of many small wooden and metal balls, equal in size, and thrown in at random. These will form what is known in literature as a random closed pack structure. We would like to determine the bulk electrical conductivity of this mixture, as a function of the relative fraction of metal balls. Call this fraction p . If p is very small, there are few isolated metal balls in a sea of insulating spheres, and the bulk material is an insulator. If p is near 1, the material will be conducting. Also, we note that if we change any ball from insulating to conducting, the conductivity can only increase. Thus, the conductance of this disordered medium is a non-decreasing function of p . And there is some value p_c , such that for $p < p_c$, the conductance is zero, but for $p > p_c$, there are conducting paths between opposite faces of the sample, and the mean bulk conductance is non-zero (Fig.2.5).

Thus, we have a phase transition from an insulating to a conducting phase, as p is increased above p_c . Perhaps this is *the* simplest example of a phase transition. It is a geometrical phase transition, and the phase transition occurs as a function of the concentration p . Temperature does not play any role.

One can define a lattice model of percolation, instead of the continuum model defined above, which is simpler to study. In our mixed bead example, we imagine that the beads are packed in a regular closed packed lattice structure. In the site percolation model, we have a lattice, say a hypercubical lattice in d dimensions, and each site is occupied or empty, independent of other sites, with probability p or $(1 - p)$ respectively. In the bond-percolation model, all sites are present, but links between nearest neighbor sites may be present or absent, again independent of other links, with probability p and $(1 - p)$ respectively. In Fig.2.6, we have shown a realizations of site percolation on a square lattice for different p .

In fact, the percolation transition is one of the simplest examples of a *continuous* phase transition. As p tends to p_c from below, The mean size of a

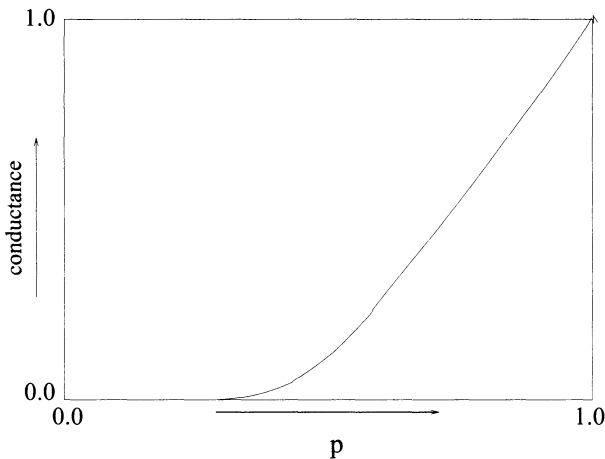


Figure 2.5: Schematic dependence of the normalized conductance of a medium containing insulating and conducting beads, on the concentration p of conducting beads

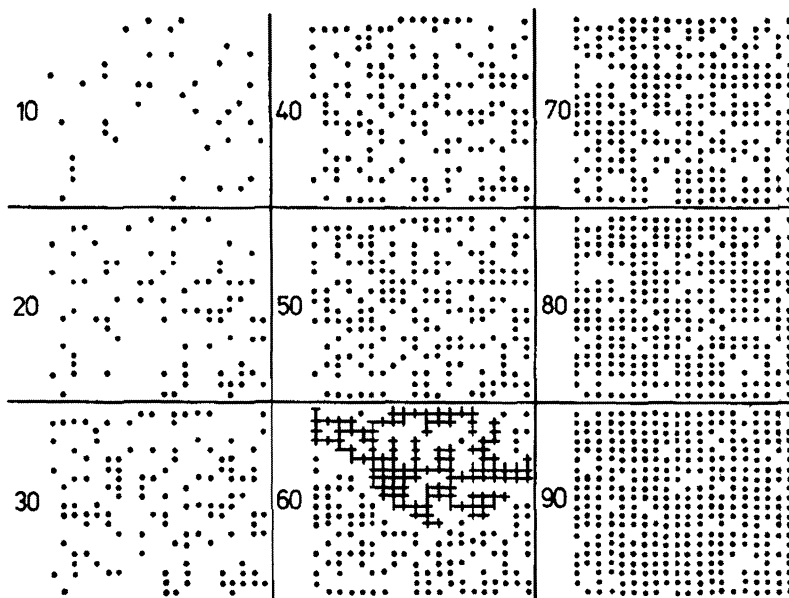


Figure 2.6: Site percolation on a square lattice. some typical configurations as a function of density of occupied sites. The number in each panel gives the density in percent. A spanning cluster is indicated for $p = 0.60$. Figure taken from [7].

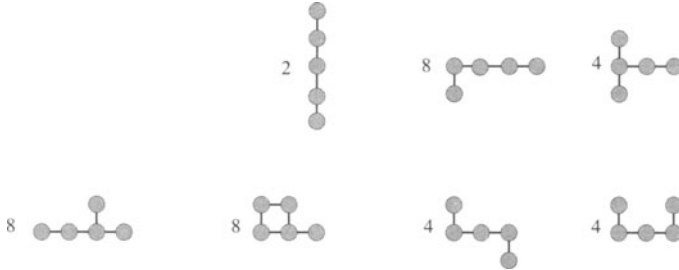


Figure 2.7: Different unrooted clusters with 5 sites on the square lattice.

connected cluster diverges as $|p_c - p|^{-\nu}$. The mean number of sites in the cluster to which a randomly chosen site belongs, diverges as $|p_c - p|^{-\gamma}$. For $p > p_c$, the mean fraction of sites in the infinite cluster increases as $(p - p_c)^\beta$.

These exponents ν , γ , and β are similar to the exponents defined in other critical phase transitions. In fact, the relationship of percolation model to Ising model is quite deep. One can define a more general model, called the q -state Potts model, for which $q = 1$ is the percolation problem, and $q = 2$ corresponds to the Ising model [6]. Constraints of time and space do not permit us to pursue this direction here.

Consider site-percolation on the square lattice. Define $P_p(s)$ as the probability that the origin belongs to a connected cluster of exactly s occupied sites. This is independent of the size of the lattice, so long as the boundaries are far enough, and the largest s -site cluster cannot reach the boundary.

It is easy to see that $P_p(s = 0) = q$, $P_p(s = 1) = pq^4$, and $P_p(s = 2) = 4p^2q^6$. Here $q = 1 - p$. For larger s , one has to consider all possible different clusters that can occur having s sites. For a cluster having s sites, and t perimeter sites (nearest neighbor of sites in cluster, but not part of cluster), the probability weight is $p^s q^t$. In general, we have

$$P_p(s) = \sum_t N(s, t) p^s q^t \quad (2.25)$$

We would like to determine $N(s, t)$ for different s and t , and for different lattices. In Fig.2.7, we have shown all the different types of clusters with 5 sites. The number in front of the cluster is the total number of distinct clusters obtainable from it by reflections or rotations. Also, the clusters shown are unrooted. The number of rooted clusters is larger than this by a factor 5, as in any cluster, there are 5 ways of marking which site is the origin.

2.6 Algorithm for Enumerating Clusters

While, in principle, for any finite s , there is a finite number of possible clusters, which can be put into a finite list, producing such a list becomes quite nontrivial,

even for $s = 6$. One has to ensure that no cluster is omitted, and there is no double counting. One needs an algorithm to organize such a list. Then the actual tedious enumeration can be done by a computer. One such algorithm is called the Martin's algorithm. It allows us to encode a complicated branched structure of the cluster by a finite binary sequence $10011001\dots1$.

Given a cluster of s sites on the square lattice, Martin's algorithm assigns a label $1, 2, 3\dots$ to the sites of the cluster, and its perimeter sites. Let us denote the i th entry of the list as $S(i)$, which is the site with label i . We define the occupation number $N(i) = 1$, if $S(i)$ is occupied, and 0 otherwise. Since in this process we assign labels to all occupied sites, and their neighbors, the number of labels used when the above process stops is greater than s . Let the number be r . Then the cluster is coded by an r -bit binary sequence $10011100101\dots$, where the i -th bit in the sequence gives the value of $N(i)$.

The algorithm proceeds to generate the labeling of sites as follows:

1. We first choose a priority ordering of neighbors for each site of the lattice. This rule can be different at different sites, but will remain the same for all clusters. For example, on the square lattice, we may choose the ordering $N > E > W > S$ for all sites.
2. The root is labeled as site 1. Clearly, $N(1) = 1$.
3. At this point, there is only 1 entry in the list S , i.e. the root.
4. Go to the first unvisited occupied site in the list.
5. Assign labels to all unassigned neighbors of this site consecutively, using the chosen priority rule, and add them to the list.
6. If there are no occupied sites without assigned labels, stop. Else, go to step 4.

Clearly, the algorithm will produce a unique binary sequence $N(i)$ for any given cluster. But, a little bit of thought shows that given the sequence $N(i)$, and the known priority rule for neighbors at each site, one can reconstruct the cluster completely.

As an example, for the left-most cluster in Fig. 2.7 in the lower row, if the root site is the left-most occupied site, the corresponding binary sequence is 101000101100000 . Also, there is no valid cluster corresponding to the binary sequence 100001 .

A cluster with s sites will have a binary sequence with s ones. The number of zeroes in the sequence will be different for different clusters, but it is $\leq 2s + 2$ for the square lattice. Then, one can produce all binary sequences with s ones, and at most $2s + 2$ zeroes, list the sequences that correspond to valid connected clusters in (say) the dictionary order. This can be done efficiently on the computer using the backtracking strategy. A very elegant and short computer program in FORTRAN that implements this for a general translationally invariant lattice, using less than 40 lines of program, is given in [8].

2.7 The Animal Problem

The solution of the percolation problem, then, involves determination of the cluster numbers $N(s, t)$, for different s, t , and for different lattices. In particular, we are interested in studying how these numbers vary when s and t are much greater than 1. This is usually a difficult problem, and has been solved exactly only in a few lucky cases.

One can define the two-variable generating function for $N(s, t)$ as

$$\tilde{N}(x, y) = \sum_{s=1}^{\infty} \sum_{t=1}^{\infty} N(s, t) x^s y^t \quad (2.26)$$

For the original percolation problem, $y = 1 - x$. A simpler case of the problem corresponds to setting $y = 1$. This was given the catchy name “the Animal problem” by Harary, where one imagines all possible shapes an animal with s cells, living on a lattice, can have, with the only constraint being the connectivity constraint that all cells must be connected. We define $A(s)$ as the number of animals of s sites. Then

$$A(s) = \sum_{t=1}^{\infty} N(s, t) \quad (2.27)$$

and the corresponding generating function

$$\tilde{A}(x) = \sum_{s=1}^{\infty} A(s) x^s = \tilde{N}(x, y = 1) \quad (2.28)$$

Let us first prove that $A(s)$ increases at most exponentially with s . We note that on a lattice with coordination number z , a cluster of s sites, will have at most zs perimeter sites. Then the corresponding binary sequence will be at most of length $(z + 1)s$. This number is $\leq 2^{(z+1)s}$. Not all of binary sequences correspond to connected clusters. Hence

$$A(s) \leq 2^{(z+1)s}. \quad (2.29)$$

Exercise. 7: Improve the bound in Eq.(2.29).

Also, it is easy to see that $A(s) > 2^s$. Thus, it grows exponentially with s , for large s . In fact, one finds that

$$A(s) \sim C \lambda^s s^{-\theta} \quad (2.30)$$

where C and λ are constants, and θ is some exponent, that is found to be independent of the details of the lattice, and only depends on dimension.

In the original percolation problem, for $p < p_c$, the probability that a randomly chosen site belongs to a cluster of size s varies as $D_p e^{-C_p s} s^{-\theta}$, where

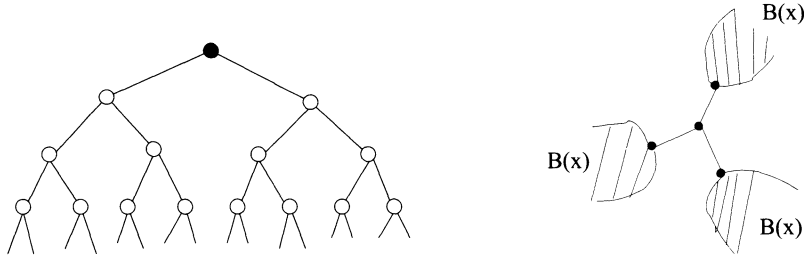


Figure 2.8: (a) A binary tree. The root site is denoted by a filled circle. (b) Generating function for enumerating animals on the 3-coordinated Bethe lattice. Here $B(x)$ denotes sum over all animals on the binary tree with that root.

C_p and D_p are p -dependent functions, for $C_p s \gg 1$. The exponent θ is independent of p . It can thus be considered as an off-critical exponent of the percolation problem. Thus, while the “critical exponents” of percolation can only be seen only very near the critical point, the “off-critical exponent” θ is seen in the entire low-density phase of percolation theory. For a discussion of other off-critical exponents of the percolation theory, see [9].

2.7.1 The Bethe lattice

One simple case where the function $\tilde{A}(x)$ can be determined exactly is for a Bethe lattice with coordination number z . We will consider here the case $z = 3$. We define $\tilde{A}(x)$ as the sum over all animals containing the origin, with the weight of an animal of size s being x^s . Let $B(x)$ be the generating function of all animals rooted to the vertex of an infinite binary tree (see Fig.2.8). Then, clearly, we have

$$B(x) = x[1 + B(x)]^2 \quad (2.31)$$

This quadratic equation can be solved for $B(x)$, giving

$$B(x) = \frac{1}{2x}[1 - 2x - \sqrt{1 - 4x}] \quad (2.32)$$

Which can be Taylor expanded to give

$$B(x) = x + 2x^2 + 5x^3 + \dots \quad (2.33)$$

Finally, the generating function $\tilde{A}(x)$ is given by

$$\tilde{A}(x) = x[1 + B(x)]^3 \quad (2.34)$$

Which then gives

$$\tilde{A}(x) = x + 3x^2 + 9x^3 + 28x^4 + \dots \quad (2.35)$$

The singularity closest to origin of $\tilde{A}(x)$ in the complex x -plane occurs at $x = 1/4$, and from Eq.(2.31) and 2.33, it is easy to see that $\tilde{A}(x = 1/4 - \epsilon) \sim 2 - 12\sqrt{\epsilon}$ to leading order in ϵ , for small ϵ . This implies that $A_n \sim 4^n n^{-3/2}$, for large n .

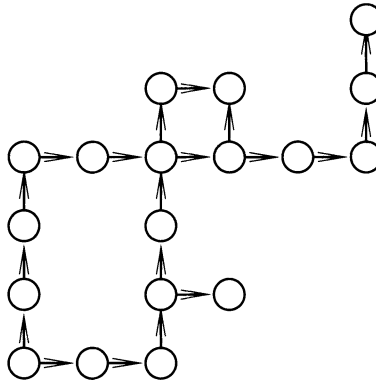


Figure 2.9: A directed animal on a square lattice.

2.7.2 Directed Animals

One can also obtain the exact animal generating function for a variant of the animal problem for a regular two dimensional graph. We consider a directed square lattice, where all bonds are directed right or up. A directed animal is a connected cluster of sites where each site belonging to the cluster is either the origin, or has a downward or leftward neighbor that also belongs to the cluster. An example is shown in Fig.2.9.

The directed animal problem turns out to be much simpler than the corresponding undirected problem, as the allowed configurations of animals for $x + y > T$ depend on the sites occupied on the line $x + y = T$ and not on the configuration of the animal below this line. In fact, one can think of T as a “time” coordinate, and then the directed animal becomes the space-time plot of a process where a particle can move one step left or right, divide into two, or die.

Let A_n be the number of animals with n sites on the square lattice. We define $A(x) = \sum_n A_n x^n$. Then it is easily seen that

$$A(x) = x[1 + 2A(x) + A_{11}(x)] \quad (2.36)$$

where $A_{11}(x)$ is the generating function for all directed animals that have a source at two adjacent point along the line $x + y = 1$, say $(1, 0)$ and $(0, 1)$. Similarly, we can write $A_{11}(x)$ in terms of more complicated functions

$$A_{11}(x) = x^2[1 + 3A(x) + 2A_{11}(x) + A_{101}(x) + A_{111}(x)] \quad (2.37)$$

Here $A_{101}(x)$ and $A_{111}(x)$ are generating function for animal with source 101 and 111 along a constant $-T$ line (in a fairly self-explanatory notation).

One can similarly write recursion equations for $A_{101}(x)$ etc. More generally, let C be a configuration of occupied sites on a line of constant time $x + y = T$. Then $A_C(x)$ is the generating function for all directed animals with

starting from a point in C . Then it is easy to see that $A_C(x)$ satisfies the recursion equation

$$A_C(x) = x^{|C|} \left[1 + \sum_{C'} A_{C'}(x) \right] \quad (2.38)$$

where C' is a possible nonempty configuration of occupied sites on the line $x + y = T + 1$, and the sum over C' is over all such sources. $|C|$ is the number of sites in C .

One can use such recursion relations to generate the series expansions for $A_C(x)$ to very high orders [10].

We can use these recursion relations to establish the equivalence of the $1 + 1$ -dimensional directed animal problem to that of time evolution of a one dimensional lattice gas with nearest neighbor exclusion, and no particle conservation. This then gives us a very simple example of the important phenomena of *dimensional reduction*, where the calculation of properties of some d -dimensional system reduces to that of a different lower -dimensional problem (here lower by 1). This is very useful, as the lower dimensional problems are usually easier to solve [11].

Let us consider time evolution of a lattice gas on a line. Assume that evolution is discrete time, Markovian, with odd-even parallel update with the following evolution rule: A site x at time t is occupied with probability p , if at time $t - 1$ both sites $x - 1$ and $x + 1$ were empty, and is unoccupied otherwise, irrespective of its earlier value. It is easy to see that these rules satisfy detailed balance condition corresponding to the Hamiltonian

$$H = +\infty \sum_i n_i n_{i+1} - \mu \sum_i n_i \quad (2.39)$$

The somewhat non-standard notation is a short hand for interaction strength J , in the limit J tends to infinity. In the long time steady state of the Markov chain, the probabilities of different configurations are the same as in the Boltzmann-Gibbs measure corresponding to H . In the latter, one can easily determine the average density $\rho(z)$ of the gas corresponding to the activity $z = \exp(\beta\mu)$. We have

$$\rho(z) = \frac{1}{2} \left[1 - \frac{1}{\sqrt{1 + 4z}} \right] \quad (2.40)$$

We can now ask what is the probability that in the steady state of this Markov process, if we observe at a particular time T , the set of sites C will be all occupied. Denote this by $Prob(C)$. Clearly, $Prob(C)$ is equal to the probability that each of the sites was available of occupation, and it was occupied. The latter probability is $p^{|C|}$. the former is the probability that each of the neighbors of sites in C was *not occupied*. This is easily determined using the inclusion - exclusion principle. Thus, $Prob(C)$ satisfies the recursion equation

$$Prob(C) = p^{|C|} \left[1 + \sum_{C'} (-1)^{|C'|} Prob(C') \right] \quad (2.41)$$

Here the sum over C' is over all proper subsets of set of neighbors of C . Comparing with the Eq.(2.34), we can make the identification

$$A_C(x = -p) = (-1)^{|C|} \text{Prob}(C) \quad (2.42)$$

In particular, the mean density of this Markovian evolving gas gives us the generating function of the 2-d site animals. We note that the activity of the gas in terms of p is $z = p/(1-p) = -x/(1+x)$. This gives

$$A(x) = -\rho(z = \frac{-x}{1+x}) \quad (2.43)$$

Eq.(2.40) then gives

$$A(x) = \frac{1}{2} \left[\sqrt{\frac{1+x}{1-3x}} - 1 \right] \quad (2.44)$$

From this it is easily seen that for large n , A_n increases as $3^n n^{-1/2}$.

Note that the singularity of $A(x)$ closest to the origin occurs for $x = 1/3$. This corresponds to the Markovian evolution of the 1-dimensional lattice gas, but with $p = -1/3$ [12]. Negative values of p , of course, are unphysical. One has to think of the Markov matrix (whose matrix elements are simple polynomial functions of p), and analytically continue this matrix to negative values of p . Equivalently, one can think of the stochastically evolving lattice -gas as a particular kinetic Ising model, where the spins are evolving in the presence of a field, and then take the analytical continuation to magnetic fields that are imaginary. Then this problem becomes equivalent to the *critical dynamics of Ising model near the Lee-Yang Edge singularity*. The study of Lee-Yang edge singularity is an important problem in statistical physics, as it relates to the analytical structure of singularities of equation of state of hard core gases (see [13] for a longer discussion of this point). But it is difficult to study, as the corresponding Boltzmann weights are non-positive, and usual thermodynamic convexity relations do not hold. The directed animals problem gives us a realization of the Lee-Yang problem with positive weights.

This relationship between equilibrium statistics of a d -dimensional nearest neighbor exclusion gas to the $d+1$ -dimensional directed animal is valid for arbitrary d . In particular, one can use the known exact solution of the hard hexagon lattice gas by Baxter [14] to determine the exact number of 3-dimensional directed animals [15]. One can also relate correlation functions of the lattice gas to those of the animals problem [16].

2.8 Heaps

The problem of directed animals has a very elegant, and nontrivial generalization to heaps [17]. Informally, heaps are like directed animals, but are made up of different types of “pieces”. In Fig.2.10, we have shown a 3-dimensional heap made of two types of rectangles. The heap is made up of different layers of tiles.

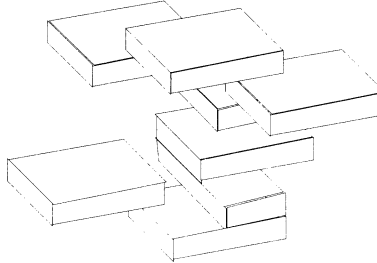


Figure 2.10: A heap in three dimensions, made of two different types of horizontal rectangular pieces.

In each layer, the tiles are non-overlapping, and each tile is “supported” from below, i.e. it can not fall down to the lower layer under gravity, as at least one site below is already occupied by another tile in the lower layer.

We consider heaps defined on a discrete space. The “base” is the lowermost layer, and consists of a finite number of sites. Each higher layer is an exact copy of the base placed “vertically above” it. Each tile covers a finite number of sites in one layer. We assume we have a finite number of different types of tiles. We associate activity $z_1, z_2, z_3 \dots$, with tiles of type 1, 2, 3 The weight of a heap \mathcal{H} containing n_i tiles of type i is $z^{\mathcal{H}} = \prod_i z_i^{n_i}$. We define the heap generating function

$$H(\{z_i\}) = \sum_{\mathcal{H}} z^{\mathcal{H}} \quad (2.45)$$

Let $D(\{z_i\})$ be the grand partition function of the gas of non-overlapping tiles placed on the base space. This is just all possible heaps with tiles only in the first layer. i.e.

$$D(\{z_i\}) = \sum_{\mathcal{H}_1} z^{\mathcal{H}_1} \quad (2.46)$$

Example: Consider a base space consisting of only four sites forming a 2×2 square. There are two types of tiles : dimers that occupy two adjacent sites, and have activity z_1 , and triangular pieces that occupy three sites, and have activity z_2 . Then clearly, $D(z_1, z_2)$ is a finite polynomial in z_1, z_2 , given by

$$D(z_1, z_2) = 1 + 4z_1 + 2z_1^2 + 4z_2 \quad (2.47)$$

Here $H(z_1, z_2)$ is the formal infinite series, which starts as

$$H(z_1, z_2) = 1 + 4z_1 + 4z_2 + 14z_1^2 + 8z_1z_2 + 16z_2^2 + \dots \quad (2.48)$$

Then, with H and D defined by Eqs.2.45 and 2.46, we have the remarkable general result

$$H(\{z_i\}) = 1/D(\{-z_i\}) \quad (2.49)$$

where $D(\{-z_i\})$ is the polynomial obtained by replacing z_i by $-z_i$, for all i in $D(\{z_i\})$. Note that the result is valid independent of the number and shape of tiles. In fact, the structure of the base space also does not come into picture. It shows the dimensional reduction, by expressing that the partition function of “3-dimensional” heaps in terms of the “two-dimensional” partition function D .

Proof: We define a tile in a heap to be maximal, if there is no tile above it, i.e. it can be removed from top without encountering other obstructing tiles. We can write Eq.(2.49) as

$$H(\{z_i\})D(\{-z_i\}) = \sum_{\mathcal{H}, \mathcal{H}_1} (-1)^{|\mathcal{H}_1|} z^{\mathcal{H}} z^{\mathcal{H}_1} = 1 \quad (2.50)$$

The proof of relation follows by showing different terms in the expansion corresponding to configurations having at least one tile can be paired in way that each pair adds up to zero. Then the total sum is equal to the only unpaired term in the summation, which corresponds to the trivial configuration with no tiles.

Given the heaps \mathcal{H} and \mathcal{H}_1 , we define a set of tiles \mathcal{T} , which contains tiles in \mathcal{H}_1 , and those maximal tiles in \mathcal{H} that do not overlap with any tile in \mathcal{H}_1 . Now, the sum over $\mathcal{H}, \mathcal{H}_1$ in Eq.(2.50) can be written as sum over different possible \mathcal{T} , and \mathcal{H}' , the remainder of \mathcal{H} on removing the maximal pieces. Now, consider the summation over \mathcal{T} , for a fixed \mathcal{H}' . In this summation, each allowed \mathcal{T} contains non-overlapping tiles. Any one tile may come from \mathcal{H} , or from \mathcal{H}_1 . If the tile i is allowed in this sum, and comes from \mathcal{H} , it contributes a factor z_i , but if it comes from \mathcal{H}_1 , it contributes a factor $(-z_i)$. These factors cancel exactly, and the only nonvanishing term in the sum in Eq.(2.50) comes from the term where \mathcal{H} and \mathcal{H}_1 are both empty sets. This contribution is exactly 1, proving the claim.

Note that the theorem remains valid, if we make the weights of pieces space-dependent and associate activities $z_i(\{\vec{x}\})$ for the tile i at positions \vec{x} along the base. Then differentiating the logarithm of the grand partition function $D(\{z_i\})$ with respect to $z_i(\vec{x})$ gives the probability that tile i will be present at position \vec{x} in the ensemble. Interestingly, this has a direct combinatorial interpretation, which is a generalization of the Eq.(2.43). The analogue a single directed animal in the heaps is called a ‘pyramid’, that is a heap with a single maximal piece (one should think of the inverted pyramid as a heap supported at base by only one tile). The generating function of a pyramid with maximal piece M is given by $P_M(\{z_i\}) = N(\{z_i\})/D(\{z_i\})$ where

$$N(\{z_i\}) = \sum_{\mathcal{H}'_1} (-1)^{|\mathcal{H}'_1|} z^{\mathcal{H}'_1} \quad (2.51)$$

where the prime over summation indicates that the summation in which the tile M is not used. The proof of this proposition is very similar to the earlier proof, and is omitted here [17].

The heaps were first discussed in the context of applications in computer science. One thinks of distributed computing, where there are N different processors, and several jobs to be executed. Let us consider for simplicity the case where each job takes one unit of time. Each job corresponds to a tile and may occupy more than one processor. There is a time ordering of jobs on any one processor, but no necessary relative time order between jobs that do not involve common processors. Then, in the optimal scheduling, the space-time-history of computation is a heap, where occupied/unoccupied sites denote which processors are busy /idle at what times [18].

More recently, heaps have been used in modeling random space -time structures involved in theories of quantum gravity. Unfortunately, details of this very interesting subject are outside the scope of these lectures. The interested reader may consult [19].

References

- [1] Uhlenbeck, G. E. and Ford, G. W. (1962), In Studies in Statistical Mechanics, Vol. I (J. de Boer and G. E. Uhlenbeck, eds), North-Holland, Amsterdam, pp. 119–211.
- [2] C. Domb, Advances in Physics, **9**, 140(1960).
- [3] H. Arisue and T. Fujiwara, Phys. Rev. E, **67**, 066109(2003).
- [4] I. Jensen, J. Phys.A: Math. Gen. **32** (1999) 5233.
- [5] W. R. G. James, I. Jensen and A. J. Guttmann, J. Phys. A: Math. Theo. **41** (2008) 055001.
- [6] F. Y. Wu, Rev. Mod. Phys. **54**, 235(1982).
- [7] D. Stauffer and A. Aharony, *Introduction to Percolation theory*, (Taylor and Francis, UK, 1994); G. Grimmett, *Percolation*, (Springer-Verlag, Berlin, 1989); M. Sahimi, *Applications of Percolation Theory*, (Taylor and Francis, London, 1994).
- [8] S. Redner, J. Stat. Phys., **29**, 309 (1982).
- [9] D. Dhar, Pramana, **58** (2002) 419. [cond-mat 0108280]
- [10] D. Dhar, M. K. Phani and M. Barma, J. Phys. A: Math. Gen. **15** (1982) L279; A. R. Conway, R. Brak and A. J. Guttmann, J. Phys. A: Math. Gen, **26** (1993) 3085.
- [11] In fact, one can show that the critical exponents of the $(d+2)$ -dimensional *undirected* animals problem are related to those of the hard core d -dimensional lattice gas. The arguments use field theory techniques, and supersymmetry, and are outside the scope of these lectures. See J. Z. Imbrie, J. Phys. A: Math. Gen., **37** (2004) L137.
- [12] D. Dhar, Phys. Rev. Lett. **49** (1982) 959.

- [13] S. N. Lai and M. E. Fisher, J. Chem. Phys. **103** (1995) 8144.
- [14] R. J. Baxter, J. Phys. A: Math. Gen. **13** L61(1980).
- [15] D. Dhar, Phys. Rev. Lett. **57**, 853(1983).
- [16] Sumedha and D. Dhar, J. Phys. A: Math. Gen. **36** 3701(2003).
- [17] G. X. Viennot, in *Proc. of the Colloque de Combinatoire Enumerative*, Lecture Notes in Mathematics Vol. 1234, pp 321–350 (Springer-Verlag, Berlin, 1986).
- [18] C. Krattenthaler, ‘*The Theory of Heaps and Cartier-Foata Monoids*’, <http://www.emis.de/journals/SLC/books/heaps.ps>.
- [19] P. di Francesco and E. Guitter, J. Phys. A, **35**, 897,(2002); see also P. di Francesco and R. Kedem, arXiv:0811.3027v1 [math.CO].

Chapter 3

Graphical Enumeration Techniques: Application to Polymers

Sanjay Kumar

Abstract

We briefly discuss lattice models of polymers. Using exact enumeration technique and renormalization group theory, we show how to calculate their equilibrium properties. We apply the method developed here to study the collapse transition, adsorption transition and collapse & adsorption transitions near an attractive wall. We also discuss the exact enumeration technique, which may be used to interpret the results of single molecule force spectroscopy.

3.1 Introduction

Polymers are long chain molecules consisting of a large number of units called monomers, which are held together by covalent bonds [1, 2]. A linear polymer chain in a solvent can be modeled by a walk on a lattice in which a step or vertex of the walk represents a monomer. In a random walk model of a polymer, walker is allowed to cross the visited sites, but a polymer can not. We model equilibrium polymer as equal weight of all random walks configurations that do not cross itself. This takes care of an excluded volume effect which restricts two monomers to occupy the same space. This kind of walk [1] is known as self-avoiding walks (SAWs), which simulates a linear polymer chain in a good solvent as shown in Fig. 3.1(a). There is another class of walk known as the directed walk (DW) which also simulates a polymer chain in a good solvent. In

such walks, walkers are allowed to take steps only in the preferred direction as shown in Fig. 3.1(b). The directed walk model can be solved analytically [2].

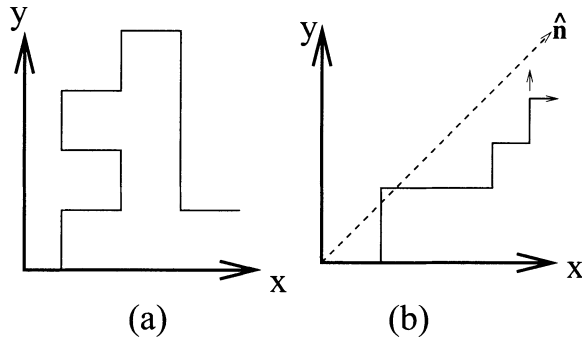


Figure 3.1: Schematic diagrams of SAW and Directed Walk model.

It is known that the certain quantities associated with SAWs *e.g.* number of distinct conformation (C_N), number of closed polygons (P_N) and end-to-end distance of chain (R_e) of step N scale as [1]

$$\begin{aligned} C_N &\sim \mu^N N^{\gamma-1}, \\ P_N &\sim \mu^N N^{\alpha-3}, \\ R_e &\sim N^\nu, \end{aligned} \quad (3.1)$$

where μ is the connectivity constant giving the number of choices per step for an infinitely long walk. From the phase transition and critical phenomena, we also know that certain physical quantities like susceptibility (χ), specific heat (C) and correlation length (ξ) near the transition point T_C , scale as

$$\begin{aligned} \chi &\sim \chi_0 \left| \frac{T - T_c}{T_c} \right|^{-\gamma}, \\ C &\sim C_0 \left| \frac{T - T_c}{T_c} \right|^{-\alpha}, \\ \xi &\sim \xi_0 \left| \frac{T - T_c}{T_c} \right|^{-\nu}. \end{aligned} \quad (3.2)$$

A relation between polymer statistics and phase transition was established by de Gennes [1] and des Cloiseaux [3] showing the correspondence between the polymer chain modeled by SAWs and the n -vector spin model of magnetization in the limit $n \rightarrow 0$. Similarities between correlation length (ξ) and the end-to-end distance (R_e) can be noticed by comparing Eq.3.1 and Eq.3.2. Correspondence between $1/N$ and $\frac{T - T_c}{T_c}$ is viewed as $\frac{T - T_c}{T_c} \rightarrow 0$ and $N \rightarrow \infty$. This equivalence allowed polymer science to benefit from the vast knowledge accumulated in the study of critical phenomena. For example, the following

relations, which are quite non-trivial to derive directly, are also valid here [1].

$$\begin{aligned}\alpha + 2\beta + \gamma &= 2 \\ 2 - \alpha &= d\nu, \\ \gamma &= \nu(2 - \eta).\end{aligned}\tag{3.3}$$

Here α , β , γ and η are the critical exponents and d represents the dimensionality of the system. The above equivalence may serve an important role in describing the long range behavior of the polymers.

3.2 Upper and Lower Bounds on the Connectivity Constant

In this section, we discuss how to determine the number C_N of N step walks. There are two kinds of result on this quantity: (i) exact numerical results for small N and (ii) rigorous asymptotic results [4]. Let us first discuss on the number C_N . Because of excluded volume effect, there must be fewer SAWs than random walks. Second there must be more number of walks than the DWs shown in Fig. 3.1b. For 2d, we can have following inequality

$$2^N \leq C_N \leq 4^N\tag{3.4}$$

The above argument can be extended to higher dimensions. Eq.3.4 suggests that to the leading order in N , C_N will grow exponentially. In order to prove this, let us consider SAWs of $(N + M)$ steps. These walks can be cut in two parts creating an N step SAWs and M step SAWs. For this, following inequality holds

$$C_{N+M} \leq C_N C_M\tag{3.5}$$

or

$$\log C_{N+M} \leq \log C_N + \log C_M\tag{3.6}$$

From Eq.3.6 and the fact that C_N is bounded from above Eq.3.4, it can be proved that [4]

$$\lim_{N \rightarrow \infty} \frac{1}{N} \log C_N = \log \mu\tag{3.7}$$

A lot of hard mathematical work has been done to get better estimate of the bound of μ .

3.3 Method: Exact Enumeration Technique and Series Analysis

The conformational properties of a polymer chain and phase transition phenomena can be understood if one has the complete information about the partition

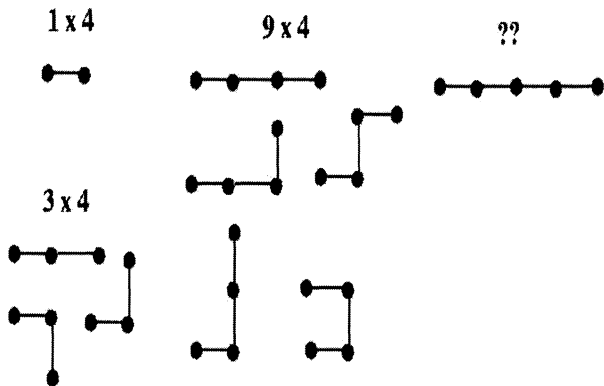


Figure 3.2: Schematic diagrams of different possible conformations of one, two and three steps walks. The effect of excluded volume will appear in $N \geq 4$ step walk.

function of the chain. In the lattice model, the canonical partition function of a polymer chain is calculated [5] by enumerating all possible walks of a given length (Fig. 3.2). For example, we show total number of conformations (C_N) for N step walk in Table 3.1. The grand canonical partition function is defined as

$$\mathcal{Z}(z) = \sum_N C_N z^N \quad (3.8)$$

Table 3.1: Values of C_N for different N for the square lattice. The value of C_N can be obtained numerically or one may see the following webpage: <http://www.ms.unimelb.edu.au/~iwan/saw/series/sqsaw.ser>

N	C_N	N	C_N
1	4	16	17245332
2	12	17	46466676
3	36	18	124658732
4	100	19	335116620
5	284	20	897697164
6	780
7	2172
8	5916
9	16268
10	44100
11	120292
12	324932
13	881500	53	99121668912462180162908
14	2374444	54	263090298246050489804708
15	6416596	55	698501700277581954674604

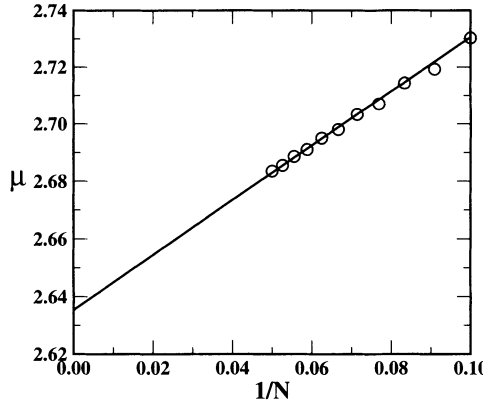


Figure 3.3: Variation of connectivity constant (μ) with $1/N$ for SAW on square lattice. The linear extrapolation gives $\mu = 2.636$ which is quite close to the best estimated value [5].

where z is the fugacity associated with each step of the walk. As the singularity of the partition function is associated with critical phenomena, the partition function defined in Eq.3.8 will follow $\mathcal{Z}(z) \sim (1 - \mu z)^{-\gamma}$ in the thermodynamic limit. In most of the cases, where model is not analytically solvable, one uses numerical techniques [5] to calculate the partition function. Once the partition function is known, other thermodynamic variables can be calculated.

Since in a system of finite size the true phase transition cannot take place, therefore, one has to use suitable extrapolation scheme to calculate C_N in the limit $N \rightarrow \infty$. For this purpose suitable techniques, *e.g.* ratio method, Pade approximants, Differential approximation etc. [5] can be used. In ratio method [5] the approximate value of μ for $N \rightarrow \infty$ can be calculated by taking the ratios of consecutive terms of the series. These quantities should, for large N , be a linear function of $1/N$

$$\log \frac{C_{N+1}}{C_N} \simeq \log \mu + (\gamma - 1)(1/N) \quad (3.9)$$

A simple fit then gives estimates for μ and γ [5]. However, there is an odd-even effect in $\frac{C_{N+1}}{C_N}$. To avoid this, one can use the square root of the successive ratios of C_N as $\mu = \sqrt{\frac{C_{N+2}}{C_N}}$ and extrapolate it to $N \rightarrow \infty$. Linear extrapolation of μ with $\frac{1}{N}$ is shown in Fig.3.3.

3.4 The SAWs on Fractals

The exact values of critical exponents for SAWs are known in 2d. However, the exact value of μ is known only for hexagonal lattices. In this section, we

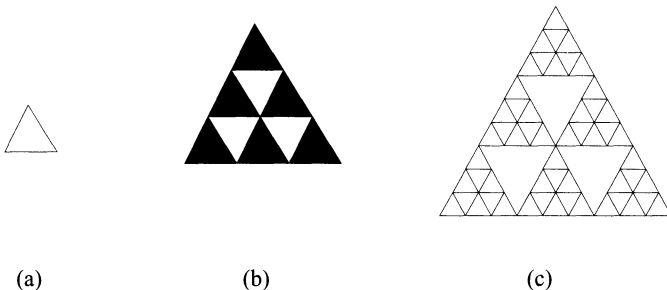


Figure 3.4: The recursive construction of 2d Sierpinski Gasket for $b = 3$: (a) The graph of first order triangle; (b) The graph of $(r + 1)$ -th order triangle, formed by joining $b(b + 1)/2$ r -th order triangle (shown as shaded triangles here); (c) The graph of the second order triangle.

shall show how to get exact solution on the artificially constructed graphs *e.g.* fractals. There are many reasons why to study SAWs on fractals which have been discussed in a recent review by Dhar and Singh [6].

Fractals are scale invariant objects (Fig. 3.4) whose fractal dimension may be non-integer. The study of the SAWs on fractal was initiated by Dhar [6]. The basic idea is a recursive construction of all possible SAWs between two points on the fractal (Sierpinski Gasket or 3-Simplex lattice) as shown in Fig. 3.5. In Fig. 3.5, we show the restricted partition function for a SAW on such fractal.

For example in Fig. 3.5, the situation in ‘A’ shows the case where the SAW starts in a particular triangle and goes out through one of the corner. In the situation ‘C’, the SAW starts through one of the corner, goes out through the other, but comes in a latter stage through the third corner. At ‘0’ level construction, the situation depicted in ‘C’ and ‘D’ can not occur.

In Fig. 3.6, we show the next label construction. We obtain the following relation for ‘B’

$$B_1 = B_0^2 + B_0^3 \quad (3.10)$$

Exercise. Obtain the recursion relation for A_1, C_1 and D_1 .

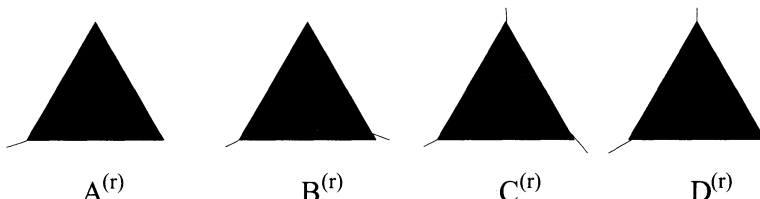


Figure 3.5: Restricted partition functions for the SAW on the Sierpinski Gasket (3-Simplex).

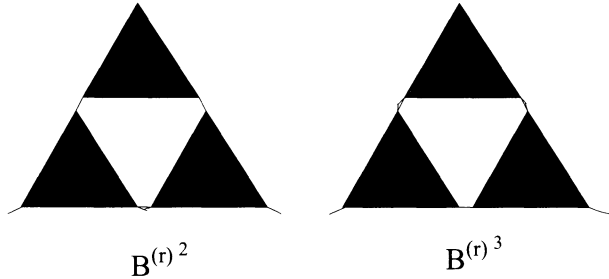


Figure 3.6: Graphs contributing to the renormalization of B.

Exercise. Obtain the recursion relation for B_{r+1} for the Fig. 3.4.

The fractal dimension of this lattice is $\frac{\log \frac{b(b+1)}{2}}{\log b}$ where b is the scaling factor.

Note that iteration of ‘B’ does not involve any other variables. Using Renormalization Group (RG) technique [1], one can interpret the recursion for ‘B’ as an RG equation for the fugacity associated with each step *i. e.* $B_0 = z$. Thus at any level r , B^r gives the weight of all walks going through two corners of r th level fractal. This quantity is interpreted as fugacity of that level. Therefore, RG equation for z is

$$z' = z^2 + z^3 \quad (3.11)$$

The flow of RG equation is simple in this case. It has two attractive fixed points (at $z = 0$ and $z = \infty$) and one repulsive fixed point

$$z_c = \frac{\sqrt{5} - 1}{2} \quad (3.12)$$

which gives connectivity constant $\mu = 1/z_c = 1.61803\dots$

In order to get critical exponent ν , we take derivative of z' at z_c . From which the value of ν , we get ≈ 0.7986 .

Exercise. Using the recursion relation for ‘A’ and ‘C’, calculate the value of γ .

Exercise. In Fig. 3.7, restricted partition functions for 4-simplex lattice have been shown. Write down the recursion relation for A^{r+1} and B^{r+1} in terms of A^r and B^r .

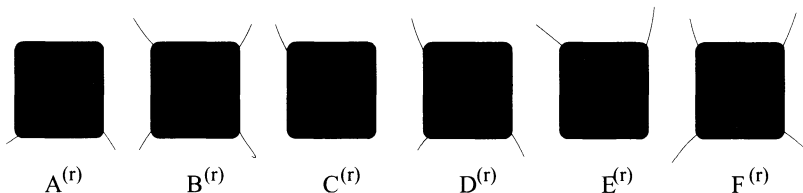


Figure 3.7: Restricted partition functions for the 4-Simplex lattice.

3.5 Application to Polymers

In the previous section, we studied some of the properties associated with a polymer in a good solvent. In the following, we shall discuss some of the problems, where application of the series analysis can give quite reliable estimates.

3.5.1 Coil-Globule transition

When the temperature is decreased the quality of solvent changes gradually, and at low enough temperatures, the solvent becomes a poor solvent [1]. Broadly speaking, there exists three different kinds of interaction in solution: the monomer-monomer (MM) interaction (χ_{MM}), the monomer-solvent (MS) interaction (χ_{MS}) and the solvent-solvent (SS) interaction (χ_{SS}). The Flory parameter χ is defined as

$$\chi = \chi_{MS} - \frac{1}{2}(\chi_{MM} + \chi_{SS}) \quad (3.13)$$

The good solvent has low χ while a poor solvent has high χ . In general the value of χ is found to be positive. This is because these interactions (MM,MS and SS) are mainly van der Waal attractions, which are essentially proportional to the product of the electronic polarizabilities [1] The self attraction among monomers leads polymer from an extended structure called as ‘coil’ to more denser ball like structure called as ‘globule’. This transition is called the collapse transition. This is also known as a coil- globule transition. The point at which this transition occurs usually referred as the θ -point. In order to study this transition using lattice models, one uses the self attracting self-avoiding walks (SASAWs) shown in Fig. 3.8. We assign an attractive energy $-\epsilon_p$ (arbitrary unit) with each non-bonded nearest neighbors. In an equilibrium situation, each SAW is weighted by a Boltzmann factor $\exp(\beta\epsilon_p N_p)$, where N_p is the

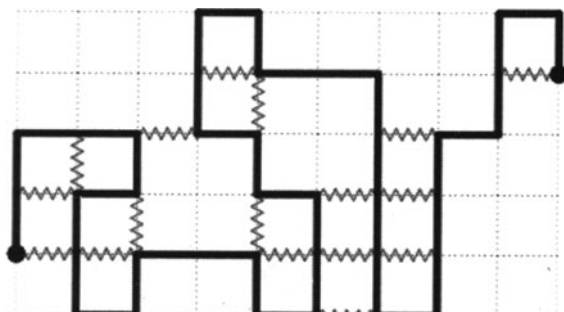


Figure 3.8: The schematic representation of SASAW. Here wiggle lines correspond to non-bonded nearest neighbor interaction.

number of nearest neighbor. The partition function for N -step walk [2] is

$$Z_N = \sum_{N_p} C_N(N_p) \exp(\beta \epsilon_p N_p) \quad (3.14)$$

where $C_N(N_p)$ is the number of N -step walks which have N_p non-bonded nearest neighbors. The free energy $f(\beta)$ can be written as

$$f(\beta) = \lim_{N \rightarrow \infty} \frac{1}{N} \log Z_N(\beta) \quad (3.15)$$

We assume free energy exists for all β and that it defines a connectivity constant $\mu_c(\beta)$ and γ_c

$$Z_N(\beta) = \mu_c(\beta)^N N^{\gamma_c - 1}. \quad (3.16)$$

It may be noted that μ of Eq.3.1 corresponds to $\beta = 0$. Once the partition function is known, the thermodynamic variables can be calculated by using the method developed in previous section.

Exercise. For the 4-Simplex lattice [6] the renormalization equations have two variables namely A and B . Obtain the flow diagram of the renormalization group flows in AB plane by setting $\epsilon_p = 1$.

3.5.2 Adsorption of a polymer Chain

Critical phenomena at surfaces have been extensively studied in recent years in the framework of equilibrium phase transition. These studies include several important physical problems such as wetting and polymer adsorption. Considerable attentions have been paid recently because of its technological importance in the stabilization of colloidal dispersions used in paints, pharmaceuticals and food stuffs, in lubrication, adhesion and membrane phenomena and in the development of artificial organs. While in practical applications one does not usually operate in the vicinity of the critical point, it is very desirable to understand how changes in the attractive interaction strength at the surface affect the adsorption behaviour of the polymer for all values of the interaction strength.

When a long flexible polymer chain interacts with an impenetrable surface, its conformational properties are strongly modified in comparison with its bulk properties [1, 2]. This is due to a subtle competition between the lowering of internal energy near an attractive surface and the loss of entropy due to constraints imposed by the impenetrable surface. For a strongly attractive surface, the polymer chain sticks to the surface, and for weak attraction it prefers to stay away from the surface. Thus, there is a transition from the state when chain is mostly attached to the surface (adsorbed) to the state of detachment (desorbed) when the temperature is increased. The transition between these two states is marked by a transition temperature T_a with the adsorbed phase for $T < T_a$ and the desorbed phase for $T > T_a$. In the following, we shall discuss the adsorption of a polymer chain on the surface. It was shown [2] that

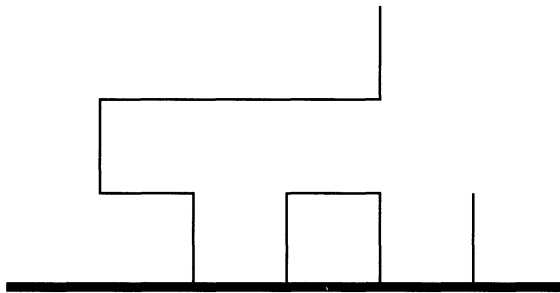


Figure 3.9: The schematic representation of a polymer chain interacting with surface.

the connectivity constant of the lattice does not change in presence of surface, however, entropic exponent γ may change.

Let us consider a polymer chain attached to the surface and there is an attractive interaction (ϵ_s) between surface and monomers (Fig.3.9). The partition function of this system [2] can be written as

$$Z_N = \sum_{N_s} \tilde{C}_N(N_s) \exp(\beta\epsilon_s N_s) \quad (3.17)$$

Here $\tilde{C}_N(N_s)$ is the number of SAW of N steps restricted to the upper half space starting at the origin with N_s number of monomers on the surface. $\tilde{C}_N(N_s)$ varies as $\tilde{\mu}^N N^{\tilde{\gamma}-1}$. It may be noted that $\tilde{\mu} = \mu$, however, $\tilde{\gamma} \neq \gamma$ and $\tilde{C}_N(N_s = 0) \neq C_N$. Once the partition function is known, other properties can be studied.

3.5.3 Simultaneous Adsorption and Collapse Transition

A long polymer chain immersed in a poor solvent and interacting with an impenetrable surface exhibits a rich variety of phases. Due to the self-attraction in the polymers, the possibility of a collapse transition both in the desorbed and adsorbed states occur. The phase diagram is generally plotted in variables $\omega = \exp(\beta\epsilon_s N_s)$ and $u = \exp(\beta\epsilon_p N_p)$, where ω and u are the Boltzmann weight for surface interaction and nearest neighbor interaction respectively.

Simultaneous adsorption and collapse transition can be studied by the method developed in the previous section. The partition function in this case can be written as

$$Z_N = \sum_{N_p, N_s} C_N(N_p, N_s) \exp(\beta\epsilon_p N_p) \exp(\beta\epsilon_s N_s) \quad (3.18)$$

Intuitively one expects four possible phases in three dimensions. For small u and large ω the polymer will be expected to be sticking to surface, and act as

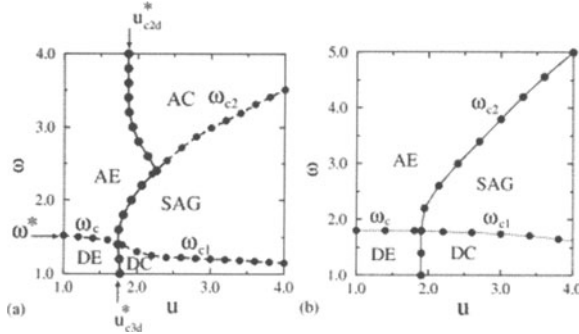


Figure 3.10: The phase diagrams for simultaneous adsorption and collapse for a polymer chain : (a) for cubic lattice, (b) for square lattice.

a $(d - 1)$ dimensional SAW. We call this phase adsorbed extended (AE) phase. If u is large and ω is large, we expect polymer to be in adsorbed collapsed (AC) phase (this phase will be absent in two dimensions as surface is a line). On the other hand for small u and small ω , polymer will be in desorbed extended (DE) phase and if we increase u further, polymer will go to desorbed collapsed (DC) phase. However, the phase diagram obtained by using series analysis shown in Fig.3.10 shows the existence of new phase, called surface attached globule (SAG). The detail of this may be found in ref. [7].

3.5.4 Stretching of Polymers

The methods developed in previous sections may be applied to study the force induced transitions in biopolymers. Recent Single Molecule Force Spectroscopy (SMFS) experiments have provided a wealth of information about structural, elastic and functional properties of biopolymers. It is important to note that unlike the above transitions which happens in the thermodynamic limit, the SMFS experiments involve chain of finite size. Hence it is possible to address some of the issues related to these experiments in the framework of series analysis [8, 9].

3.6 Conclusion

We have briefly discussed the lattice models for polymers and biopolymers. As we have exact information about the density of states, the exact enumeration technique may provide better understanding of the phase transition in polymers and biopolymers where exact solution are not available.

References

- [1] P. G. deGennes, *Scaling concepts in Polymer Physics* (Cornell Univ. Press, Ithaca, 1979).
- [2] C. Vanderzande, *Lattice Models of Polymers* (Cambridge Univ. Press: Cambridge, 1998)
- [3] J. D. Cloizeaux, Phys. Rev. A. **10** 1665 (1974).
- [4] N. Madras and G. Slade, *The Self Avoiding Walks* Birkhauser, (1993)
- [5] A. J. Guttmann, *Phase Transitions and Critical Phenomena*, Vol. 3 and 13, Edited by C. Domb and J. L. Lebowitz (Academic Press: New York
- [6] D. Dhar and Y. Singh in *Statistics of Linear polymer in Disordered Media*, Edited by B. K. Chakrabarti, Elsevier, Amsterdam (2005).
- [7] R. Rajesh, D. Dhar, D. Giri, S. Kumar and Y. Singh, Phys. Rev. E. **65** 056124 (2002); P. K. Mishra, D. Giri, S. Kumar and Y. Singh, Physica A **318**, 171 (2003).
- [8] A. R. Singh, D. Giri and S. Kumar, *Pramana* **71** 283 (2008).
- [9] S. Kumar and M. S. Li, Phys. Rep. **486**, 1–74 (2010).

Chapter 4

Classical Monte Carlo Simulation

Sitangshu Bikas Santra and Purusattam Ray

4.1 Introduction

In Monte Carlo simulation, our primary goal is to calculate an observable physical quantity X of a thermodynamic system in thermal equilibrium with a heat bath at temperature T . A macroscopic thermodynamic system consists of a large number of atoms or molecules, of the order of Avogadro number $N_A \approx 6.022 \times 10^{23}$ per mole. Moreover, in most general cases, the particles have complex interaction among themselves. The average property of a physical quantity of such a system is then determined not only by the large number of particles but also by the complex interaction among the particles. As per statistical mechanics, if the system is in thermal equilibrium with a heat bath at temperature T , the average of an observable quantity $\langle X \rangle$ can be calculated by evaluating the canonical partition function Z of the system and is given by $\langle X \rangle = \frac{1}{Z} \sum_s X_s \exp(-E_s/k_B T)$ where k_B is the Boltzmann constant. However, the difficulty in evaluating the exact partition function Z is two fold. First, there are large number of particles present in the system with many degrees of freedom. The calculation of the partition function Z usually leads to evaluation of an infinite series or an integral in higher dimension, a $(6N)$ dimensional space. Second, there exists a complex interaction among the particles which gives rise to unexpected features in the macroscopic behaviour of the system. Monte Carlo (MC) simulation method can be employed in evaluating such averages. In a MC simulation, a reasonable number of states are generated randomly (instead of infinitely large number of all possible states) with their right Boltzmann weight and an average of a physical property is taken over those states only. Judicious selection of some most important states which contribute most to the partition

sum, provides extremely reliable results in many situations. Simplicity of the underlying principle of the technique enables its application to a wide range of problems: random walks, transport phenomena, optimization, traffic flow, binary mixtures, percolation, disordered systems, magnetic materials, dielectric materials, etc. We will be addressing mostly the problems related to phase transitions and critical phenomena.

Before proceeding further, we will briefly summarize the basic concepts and definitions of probability theory and statistics required to generate random sequence of states and characterize their essential statistical parameters like mean, variance, standard deviation, etc.

4.2 Probability Theory: A Few Definitions

In an experiment, suppose the outcomes are $\{A_1, A_2, \dots, A_k\}$ and the experiment is performed repeatedly, say N times, $N \gg 1$. The probability for the outcome of A_k is given by

$$p_k = \lim_{N \rightarrow \infty} \frac{n_k}{N} \quad (4.1)$$

where the outcome A_k appeared n_k times out of N experiments. The probability of occurrence should remain between 0 and 1: $0 < p_k < 1$. $p_k = 0$ means A_k never occurred and $p_k = 1$ means A_k always occurred. The sum of the probabilities of occurrence of all the state must be 1: $\sum_k p_k = 1$. The basic definitions of probability can be found in Ref.[1, 2].

There are two ways of interpreting the above equation. First, we perform the same experiment over and over again, altogether N times. The experiments are carried out at different times, one after another. The number n_k is the *number of times* the outcome A_k occurred in this sequence of experiments. Second, we envisage N identical (indistinguishable) systems (an ensemble) and perform the same experiment at a time on all N such systems. The number n_k is the *number of systems* that yield the outcome A_k . For sufficiently large N , the final result would be the same in both the methods (ergodicity principle). If there is no apparent reason for one outcome to occur more frequently than another, then their respective probabilities are assumed to be equal (equal a priori probability) [1].

4.2.1 Conditional Probability: Dependent and Independent Events

Conditional probability measures the effect (if any) on the occurrence of an event E_2 when it is known that an event E_1 has occurred in the experiment. The conditional probability $p(E_2|E_1)$ is defined as

$$p(E_2|E_1) = \frac{p(E_1 E_2)}{p(E_1)} \quad (4.2)$$

where $p(E_1E_2)$ is the probability for both E_1 and E_2 to occur and $p(E_1) \neq 0$. In general $p(E_1|E_2) \neq p(E_2|E_1)$.

If the occurrence or nonoccurrence of E_1 does not affect the probability of occurrence of E_2 , then $p(E_2|E_1) = p(E_2)$ and we say that E_1 and E_2 are independent events, otherwise, they are dependent events. The probability that both the events E_1 and E_2 occur is given by $p(E_1E_2) = p(E_1)p(E_2|E_1)$ and $p(E_1E_2) = p(E_1)p(E_2)$ for dependent and independent events respectively.

For three dependent events E_1 , E_2 and E_3 , we have

$$p(E_1E_2E_3) = p(E_1)p(E_2|E_1)p(E_3|E_1E_2) \quad (4.3)$$

where $p(E_1)$ is the probability for E_1 to occur, $p(E_2|E_1)$ is the probability for E_2 to occur given that E_1 has occurred, and $p(E_3|E_1E_2)$ is the probability of E_3 to occur given that both E_1 and E_2 have occurred. For three independent events,

$$p(E_1E_2E_3) = p(E_1)p(E_2)p(E_3). \quad (4.4)$$

For N such independent events,

$$p(E_1 \cdots E_N) = \prod_{i=1}^N p(E_i). \quad (4.5)$$

Example 1. Consider tossing of a fair die for a large number of times. What is the probability to get 6 in all three tosses at 10^3 , 10^4 and 10^5 th tosses?

Three events are independent. Thus, the probability to have all three 6 is

$$p(6, 6, 6) = p(6)p(6)p(6) = \frac{1}{6} \times \frac{1}{6} \times \frac{1}{6} = \frac{1}{36} \quad (4.6)$$

Example 2. Suppose that a box contains 3 white balls and 2 black balls. Two balls are drawn successively from the box without replacing. What is the probability to have both the balls are black?

The events are dependent events. Thus, the probability to have both the black balls is

$$p(\text{black, black}) = p(\text{black})p(\text{black}|\text{black}) = \frac{2}{5} \times \frac{1}{4} = \frac{1}{10} \quad (4.7)$$

4.2.2 Mutually Exclusive Events

Two or more events are called mutually exclusive if the occurrence of any one of them excludes the occurrence of the others. Thus, if E_1 or E_2 are mutually exclusive events, then $p(E_1E_2) = 0$.

If $(E_1 + E_2)$ denotes the event that either E_1 or E_2 or both occur, then

$$p(E_1 + E_2) = p(E_1) + p(E_2) - p(E_1E_2). \quad (4.8)$$

In particular,

$$p(E_1 + E_2) = p(E_1) + p(E_2) \quad \text{for mutually exclusive events.} \quad (4.9)$$

As an extension of this, if $E_1, E_2 \dots E_N$ are N mutually exclusive events then the probability of occurrence of either E_1 or E_2 or \dots E_N is

$$p(E_1 + \dots + E_N) = \sum_{i=1}^N p(E_i). \quad (4.10)$$

Example 3. Consider a deck of 52 cards. (a) What is the probability of drawing a King or a Queen in a single draw? (b) What is the probability of drawing either a King or a Spade or both in a single draw?

(a) The events are mutually exclusive. Thus, the probability to have a King or a Queen in a single draw is

$$p(\text{King} + \text{Queen}) = p(\text{King}) + p(\text{Queen}) = \frac{1}{13} + \frac{1}{13} = \frac{2}{13} \quad (4.11)$$

(b) The events are not mutually exclusive. Thus, the probability of drawing either a King or a Spade or both in a single draw is

$$p(\text{King} + \text{Spade}) = p(\text{King}) + p(\text{Spade}) - p(\text{King, Spade}) = \frac{4}{52} + \frac{13}{52} - \frac{1}{52} = \frac{4}{13} \quad (4.12)$$

Problem: Three balls are drawn successively from a box containing 6 red balls, 4 white balls and 5 blue balls. Find the probability that they are drawn in the order red, white and blue if each ball is (a) replaced and (b) not replaced.

$$[\text{Ans: (a)} \frac{8}{225}, \text{(b)} \frac{4}{91}]$$

4.2.3 Expectation and Variance of Random Events

The outcome of certain random experiments may be represented by some real variable x_i . The expectation value of this random variable is given by

$$\langle x \rangle = \sum_{i=1}^N p_i x_i. \quad (4.13)$$

where p_i is the probability for a real variable x_i to occur. This is also called the mean or average value of the variable x .

The variance of the measurement is

$$\text{var}(x) = \sigma^2 = \langle (x - \langle x \rangle)^2 \rangle = \langle x^2 \rangle - \langle x \rangle^2, \quad \langle x^2 \rangle = \sum_{i=1}^N p_i x_i^2 \quad (4.14)$$

where σ is called the standard deviation.

4.3 Probability Distributions

4.3.1 Binomial Distribution

If p is the probability that an event will happen in any single trial and $q = 1 - p$ is the probability that the event will not happen, then the probability that the event will happen exactly n times in N independent identical trials is given by

$$P(n) = \binom{N}{n} p^n (1-p)^{N-n} \quad (4.15)$$

where $\binom{N}{n}$ being the binomial coefficients.

Problem: Calculate the mean $\langle x \rangle$ and variance σ^2 of N samples of a variable x which is binomially distributed. [Ans. $\langle x \rangle = Np$, $\sigma^2 = Np(1 - p)$]

4.3.2 Normal Distribution

The normal or Gaussian distribution is given by

$$p(x) = \frac{1}{\sqrt{2\pi\sigma^2}} \exp\left[-\frac{(x-\mu)^2}{2\sigma^2}\right] \quad (4.16)$$

which μ is the mean and σ is the standard deviation. The total area under the distribution function and the x -axis is 1.

$$\int_{-\infty}^{+\infty} p(x)dx = 1 \quad (4.17)$$

The mean and the variance of the distribution are defined as

$$\langle x \rangle = \int_{-\infty}^{+\infty} xp(x)dx \quad \text{and} \quad \sigma^2 = \int_{-\infty}^{+\infty} (x - \langle x \rangle)^2 p(x)dx. \quad (4.18)$$

If N is large and if neither p nor q is too close to zero, the binomial distribution can be approximated by a normal distribution with mean Np and standard deviation \sqrt{Npq} .

Problem: Calculate the mean $\langle x \rangle$ and variance $var(x)$ of a variable x which is normally distributed. [Ans. $\langle x \rangle = \mu$, $var(x) = \sigma^2$]

4.3.3 Poisson Distribution

The Poisson distribution is given by

$$p(x = n) = \frac{\lambda^n}{n!} \exp(-\lambda) \quad n = 0, 1, 2, , \dots \quad (4.19)$$

where λ is a given constant.

In the binomial distribution, if N is large while the probability p is of the occurrence of an event is close to zero, so that $q = 1 - p$ is close to 1, the event is called a rare event. In such case the binomial distribution is very closely approximated by the Poisson distribution with $\lambda = Np$.

Since there is a relation between the binomial and normal distribution, it follows that there also is a relation between the Poisson and normal distribution. It can be shown that the Poisson distribution approaches a normal distribution with mean $\langle x \rangle = \lambda$ and $\sigma^2 = \lambda$ as λ increases indefinitely.

Problem: Calculate the mean $\langle x \rangle$ and variance σ^2 of a variable x which follows Poisson distribution. [Ans. $\langle x \rangle = \lambda$, $\sigma^2 = \lambda$]

4.4 Central Limit Theorem

If a set of random variables x_1, x_2, \dots, x_N , all independent of each other and with finite variance, are drawn from the same distribution, the mean $\langle x \rangle = \sum_i x_i/N$ in the limit $N \rightarrow \infty$ will always be distributed according to Gaussian distribution with mean μ and standard deviation σ/\sqrt{N} , irrespective of distribution from which the x_i were drawn. This behavior is known as the “central limit theorem” and plays a very important role in the sampling of states of a system.

Problem: A population consists of five numbers 2, 3, 6, 8, and 11. Consider all possible samples of size 2 that can be drawn with replacement from this population. Find (a) the mean of the population, (b) standard deviation of the population, (c) the mean of the sampling distribution of the means, (d) the standard deviation of the sampling distribution of the means.

[Ans. (a) $\mu = 6.0$, (b) $\sigma^2 = 10.8$, (c) $\mu_{\langle x \rangle} = 6.0$, (b) $\sigma_{\langle x \rangle}^2 = 5.40$]

4.5 Markov Process and Markov Chain

Markov processes are stochastic processes. Consider a stochastic or random process at discrete times t_1, t_2, \dots for a system with a finite set of possible states S_1, S_2, \dots . The probability that the system is in the state S_n at time t_n given that at the preceding time the system states were in S_{n-i} at t_{n-i} , for $i < n$ is given by the conditional probability $P(S_n|S_{n-1}, S_{n-2}, \dots, S_1)$. If this probability depends only on the immediate previous state S_{n-1} and

independent of all other previous states, then the process is called a Markov process and the series of states $\{S_1, S_2, \dots\}$ is called a Markov chain. The conditional probability that the system is in the state S_n at time t_n then should reduce to

$$P(S_n|S_{n-1}, S_{n-2}, \dots, S_1) \rightarrow P(S_n|S_{n-1}) \quad (4.20)$$

for a Markov chain. The conditional probability can be interpreted as the transition probability W_{ij} to move from state i to state j ,

$$W_{ij} = W(S_i \rightarrow S_j) = P(S_j|S_i) \quad (4.21)$$

with further requirement

$$W_{ij} \geq 0 \quad \sum_j W_{ij} = 1, \quad (4.22)$$

as usual for the transition probability. Note that we kept the transition probability $W_{ij} = p(S_j|S_i)$ time independent. Such Markov chains are called “time homogeneous”. If there are N states in a Markov chain, the one-step transition probabilities W_{ij} s can be arranged in an $N \times N$ array called the (one-step) transition matrix \mathbf{W} of S and can be written as

$$\mathbf{W} = \begin{pmatrix} W_{11} & W_{12} & \cdots & W_{1N} \\ W_{21} & W_{22} & \cdots & W_{2N} \\ \vdots & \vdots & \ddots & \vdots \\ W_{N1} & W_{N2} & \cdots & W_{NN} \end{pmatrix}. \quad (4.23)$$

One can now find the total probability $p(S_j, t)$ to find the system in the state S_j at time t as

$$p(S_j, t) = \sum_i p(S_i, t-1) W_{ij}. \quad (4.24)$$

or in matrix notation, for N such states, it is given by

$$\mathbf{p}(t) = \mathbf{p}(t-1) \cdot \mathbf{W}. \quad (4.25)$$

Markov process and Markov chain is well described in Ref.[2].

For example, consider a three state Markov chain with states (1, 2, 3). Say, the transition matrix for such a chain is given by

$$\mathbf{W} = \begin{pmatrix} 0.2 & 0.7 & 0.1 \\ 0.4 & 0.3 & 0.3 \\ 0.6 & 0.2 & 0.2 \end{pmatrix}. \quad (4.26)$$

(Note that each row adds up to 1.) If the initial probability of the states is given by $p_0 = (0.1, 0.8, 0.1)$, (a) what is the probability to find the system in state $S = 1$ after one jump ($t = 1$)? (b) what is the probability to find the system in state $S = 2$ after two jumps ($t = 2$)? (c) what is the probability to find the

system in state $S = 3$ after three jumps ($t = 3$) if the system initially was at $S = 1$?

(a) $p_1(t = 1) = (\mathbf{p}_0 \cdot \mathbf{W})_1$, the first element of the row vector. Thus,

$$p_{1,t=1} = \left[(0.1, 0.8, 0.1) \begin{pmatrix} 0.2 & 0.7 & 0.1 \\ 0.4 & 0.3 & 0.3 \\ 0.6 & 0.2 & 0.2 \end{pmatrix} \right]_1 = (0.40, 0.33, 0.27)_1 = 0.40. \quad (4.27)$$

(b) $p_2(t = 2) = (\mathbf{p}_0 \cdot \mathbf{W}^2)_2$, the second element of the row vector. Thus,

$$p_{2,t=2} = (0.374, 0.433, 0.193)_2 = 0.433. \quad (4.28)$$

(c) This is the conditional probability $p(3, t = 3|1, t = 0) = (\mathbf{W}^3)_{13} = 0.199$, the $(1, 3)$ element of the \mathbf{W}^3 matrix.

The “steady-state” behavior of Markov chains as $t \rightarrow \infty$ is of considerable interest. In the limit $t \rightarrow \infty$, the steady state will be achieved if the probability flux out of a state i is equal to the probability flux into the state i . The steady state condition then can be written as

$$\sum_j p_i(t) W_{ij} = \sum_j p_j(t) W_{ji}. \quad (4.29)$$

This is called “global balance”. Since, $\sum_j W_{ij} = 1$, the above equation reduces to

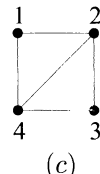
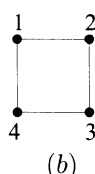
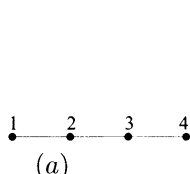
$$p_i(t) = \sum_j p_j(t) W_{ji} \quad (4.30)$$

or in matrix notation

$$\mathbf{p}(t) = \mathbf{p}(t) \cdot \mathbf{W}. \quad (4.31)$$

Thus, the probability distribution of the states $\{p_i\}$ under the transition matrix \mathbf{W} remains constant. Note that this condition may not be satisfied if the Markov chain is transient or recurrent [2].

Problem: Show that the (one-step) transition matrix W for following three Markov chains are as given below. The line between the sites indicate the connectivity between them and transition is possible. All transitions from a site are equally probable. Find the corresponding steady state distribution $\{p_j\}$.



$$(a) \quad W = \begin{pmatrix} 0 & 1 & 0 & 0 \\ 1/2 & 0 & 1/2 & 0 \\ 0 & 1/2 & 0 & 1/2 \\ 0 & 0 & 1 & 0 \end{pmatrix}$$

$$(b) \quad W = \begin{pmatrix} 0 & 1/2 & 0 & 1/2 \\ 1/2 & 0 & 1/2 & 0 \\ 0 & 1/2 & 0 & 1/2 \\ 1/2 & 0 & 1/2 & 0 \end{pmatrix} \quad (c) \quad W = \begin{pmatrix} 0 & 1/2 & 0 & 1/2 \\ 1/3 & 0 & 1/3 & 1/3 \\ 0 & 1/2 & 0 & 1/2 \\ 1/3 & 1/3 & 1/3 & 0 \end{pmatrix}$$

Solving the set of equations $p_i(t) = \sum_j p_j(t)W_{ji}$, one may find

$$(a) p = (1/6, 1/3, 1/3, 1/6), \quad (b) p = (1/4, 1/4, 1/4, 1/4), \\ (c) p = (1/5, 3/10, 1/5, 3/10).$$

In the continuous time representation, the change of the probability of occurrence of a state with time t is given by the master equation:

$$\frac{dp(S_j, t)}{dt} = - \sum_i W_{ji}p(S_j, t) + \sum_i W_{ij}p(S_i, t). \quad (4.32)$$

The above equation can be considered as a continuity equation expressing the fact that the total probability is conserved ($\sum_j p(S_j, t) = 1$ at all times) and the probability of a state i that is ‘lost’ by transitions to state j is gained in the probability of that state, and vice versa.

At equilibrium, $W_{ji}p_{eq}(S_j) = W_{ij}p_{eq}(S_i)$, the net flux of states must be zero and the steady state should be achieved. At this point, the master equation yields

$$\frac{dp_{eq}(S_j, t)}{dt} = 0, \quad (4.33)$$

since the gain and loss term cancel exactly.

Finally, it should be noted that the restriction to a discrete set of states $\{S_i\}$ is not at all important: one can generalize the discussion to a continuum of states, working with suitable probability densities in the appropriate space [3].

Problem: A system has two energy states labeled as 0 and 1, with energy E_0 and E_1 . Transition between the two states takes place at rates $W_{01} = R_0 \exp[-\beta(E_1 - E_0)]$ and $W_{10} = R_0$. Solve the master equation for the probabilities $p(0, t)$ and $p(1, t)$ of occupation of the two states as a function of time t with the initial conditions $p(0, 0) = 0$ and $p(1, 0) = 1$. Show that as $t \rightarrow \infty$ these solutions tend to the Boltzmann probabilities (See Ref.[4]).

4.6 Random Number Generators

Monte Carlo methods are heavily dependent on the fast and efficient production of streams of random numbers. Random number sequences can be produced

directly on the computer using software. Since such algorithms are actually deterministic, the random number sequences which are thus produced are only ‘pseudo-random’ and do indeed have limitations. These deterministic features are not always negative. For example, for testing a program it is often useful to compare the results with a previous run made using exactly the same random numbers. On the other hand, because of its deterministic nature, it has finite cycle of repetition. The cycle must be larger than the number of calls one makes during a simulation of a particular problem. For detailed discussion one may consult Ref.[5].

There are different algorithms to generate random numbers such as Congruential method, Shift register algorithms, Lagged Fibonacci generators etc. Below, we will be discussing these algorithms briefly. These algorithms generate a sequence of random integers. Usually floating point numbers uniformly distributed between 0 and 1 are needed for MC simulation. Random numbers uniformly distributed between 0 and 1 are then obtained by carrying out a floating point division by the largest integer which can fit into the word length of a computer.

4.6.1 Congruential Method

A simple and very popular method for generating random number sequences is the multiplicative or congruential method. Here, a fixed multiplier c is chosen along with a given seed and subsequent numbers are generated by simple multiplication:

$$X_n = (cX_{n-1} + a_0) \text{MOD}(N_{max}), \quad (4.34)$$

where X_n is an integer between 1 and N_{max} . X_0 is the initial seed to be supplied to generate the sequence. It is important that the value of the multiplier be chosen to have ‘good’ properties and various choices have been used in the past. In addition, the best performance is obtained when the initial random number X_0 is odd. Experience has shown that a ‘good’ congruential generator is the 32-bit linear congruential algorithm

$$X_n = (cX_{n-1}) \text{MOD}(N_{max}) \quad (4.35)$$

where $c = 7^5 = 16807$ and $N_{max} = 2^{31} - 1 = 2147483641$. A congruential generator which was quite popular earlier turned out to have quite noticeable correlation between consecutive triplets of random numbers.

The correlation in a random number sequence can be reduced by shuffling. Call a random number z , use z to find a random location in the sequence. For a sequence of length N , the location is $I = z \times N$. Replace the random number y at I th location by z , set $z = y$ and then repeat the procedure.

The period of the random number sequence obtained in the above congruential generator is $\approx 10^9$. In order to improve the period of the sequence, two different sequences with different periods are combined to produce a new sequence whose period is the lowest common multiple of the two periods. By

choosing, $N_{max,1} = 2147483562$ and $N_{max,1} = 2147483398$ (slightly less than 2^{31}), one can produce a sequence of period $\approx 10^{18}$. A few random number generators are provided in Numerical Recipes by W. H. Press *et al* [5] incorporating the measures and added safeguards.

Congruential generators which use a longer word length also have improved properties. Assembly language implementation using 64-bit product register is straightforward but not portable from machine to machine.

4.6.2 Shift Register Algorithms

The shift register algorithm was introduced to eliminate some of the problems with correlations in a congruential method. A table of random numbers is first produced and a new random number is produced by combining two different existing numbers from the table:

$$X_n = X_{n-p} \cdot \text{XOR} \cdot X_{n-q} \quad (4.36)$$

where p and q must be properly chosen to have good sequence. The ·XOR· operator is the bit wise exclusive-OR operator. The best choices of the pairs (p, q) are determined by the primitive trinomials given by

$$X^p + X^q + 1 = \text{primitive.} \quad (4.37)$$

4.6.3 Lagged Fibonacci Generators

Another class of random number generators is the Lagged Fibonacci generator. It is fast and has long periodicity. However, there is a possibility that the sequence could have hidden correlations and one needs to apply it with care. The generator can be written in the general form

$$X_n = (X_{n-p} \circ X_{n-q}) \text{MOD}(m) \quad (4.38)$$

where m, n, p and q are constants and \circ can be any of the operations plus, minus, multiplication or XOR. The choice of the constants is crucial to producing random numbers of good quality.

4.7 Test of Quality

The quality of random numbers generated from a given random number generator can be tested using: Frequency test, Correlation test, Parking lot test, etc. We will briefly discuss these tests here for detailed discussion one may consult Ref.[6].

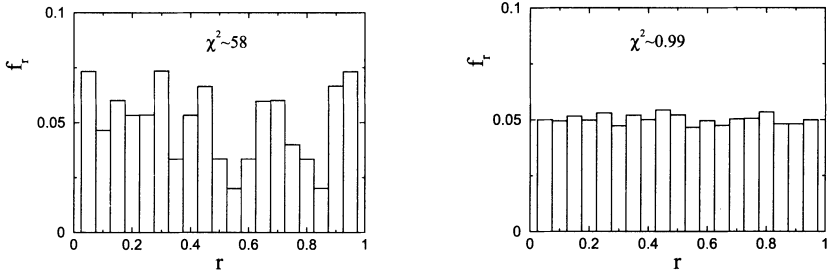


Figure 4.1: 10000 random numbers are distributed over 20 equal bins of width 0.05 generated from two random number generators. The generator with $\chi \approx 0.99$ is a good generator.

4.7.1 Frequency Test

This test verifies the uniformity of the random numbers. The interval $[0 - 1]$ is divided into N_{bin} number of bins and total N random numbers are distributed. If n_j times the random numbers appear in the j th bin, the χ^2 is defined as

$$\chi^2 = \frac{1}{N_{bin} - 1} \sum_{j=1}^{N_{bin}} \frac{(n_j - Nw)^2}{Nw}, \quad w = 1/N_{bin} \quad (4.39)$$

$\chi^2 \approx 1$ corresponds to good random number. Thus, in the figures below the generator with $\chi \approx 0.99$ is a good generator.

4.7.2 Correlation Test

The aim is to find out whether there is a tendency for each random number to be followed by another of a particular type. For example, a large number is always followed by a small number or a large number. To check this, a correlation coefficient between a sequence of N random numbers r_1, r_2, \dots, r_N can be defined as

$$C = \frac{N(\sum_{i=1}^N r_{i-1} r_i) - (\sum_{i=1}^N r_i)^2}{N \sum_{i=1}^N r_i^2 - (\sum_{i=1}^N r_i)^2} \quad (4.40)$$

where r_0 in the first term of the numerator can be taken as r_N . The value of C for an uncorrelated sequence is expected to be in the range $[\mu_N - 2\sigma_N, \mu_N + 2\sigma_N]$ where

$$\mu_N = -\frac{1}{N-1} \quad \sigma_N = \frac{1}{N-1} \sqrt{\frac{N+1}{N(N-3)}}. \quad (4.41)$$

4.7.3 Parking Lot Test

Carry out a ‘parking lot’ test on two different random number generators. Consecutive pairs of random numbers can be taken as x - and y -coordinates. Plotting the coordinates one should not find any pattern as shown in Figure 4.2.

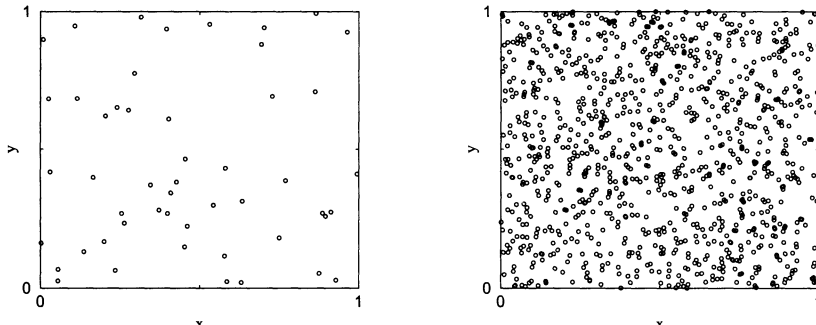


Figure 4.2: 1000 points are plotted using consecutive pairs of random numbers as x - and y -coordinates. At the left is a picture of a ‘bad’ generator and at the right are the results of a ‘good’ generator.

Problem: (i) Generate a sequence of random numbers using congruential method assuming the computer is of 4-bit word. What is the cycle of the sequence?

(ii) Generate a sequence of random numbers using congruential method with $c = 111$, $N_{max} = 23767$ and $X_0 = 99999999$. Perform the frequency and parking lot test for the sequence.

(iii) Generate a sequence of random numbers using *ran2* given in Numerical Recipes by W. H. Press *et al* with a large negative integer as seed. Compare with the generator given in (ii) by performing the same quality tests.

4.8 Monte Carlo Technique for Physical Systems

We will be presenting here Monte Carlo (MC) simulation [3, 4, 7, 8, 9] as a numerical technique to calculate macroscopic observable quantities of a thermodynamic system at equilibrium. A thermodynamic system is composed of large number of interacting particles. The microstates of these particles are either represented by their canonically conjugate position and momentum (q, p) defined by the Hamilton’s canonical equations or by the wave function obtained as a stationary state solution of the Schrödinger equation if the particle’s dynamics is represented by classical or quantum mechanics respectively. We will be considering the classical problem here. MC technique for quantum systems will be discussed in a later chapter. For a classical system described by the Hamiltonian function \mathcal{H} , the microstates are represented by points (q_i, p_i) , $i = 1, N$ in a $6N$ -dimensional phase space. Systems of interacting particles with discrete energy states can also be treated classically if they are localized, *i.e*; distinguishable. A macroscopic observable quantity is an average of that physical quantity or property over all such microstates of a system. MC technique we will be developing here will be applicable to thermodynamic systems like ferromagnet, binary alloy, fluid system, polymers in solution, disordered systems,

percolation, etc which are related to phase transition and critical phenomena. The macroscopic quantities of interest in these systems are magnetization, specific heat, susceptibility, compressibility, size of a polymer, correlation length, etc.

The difficulties one usually encounter are primarily limited computer time and memory and secondly statistical and other errors. To encounter these difficulties, one may begin with a relatively simple program using relatively small system size and modest running time. The simulation can be performed for special parameter values for which exact results may be available. The parameter range, system size and computer time then can be optimized to obtain reasonable result with less error.

Let us consider a macroscopic system at thermodynamic equilibrium with a heat bath at temperature T . Hence, we will be developing the MC technique here in the frame work of canonical ensemble. As per statistical mechanics (discussed in chapter-1), if the system is described by a Hamiltonian function \mathcal{H} , the expectation value of a macroscopic quantity A is given by

$$\langle A \rangle = \frac{1}{Z} \int \int A(p, q) \exp \{-\beta \mathcal{H}(p, q)\} d^{3N} q d^{3N} p \quad (4.42)$$

where the canonical partition function Z is given by

$$Z = \frac{1}{h^{3N}} \int \int \exp \{-\beta \mathcal{H}(p, q)\} d^{3N} q d^{3N} p, \quad (4.43)$$

whereas if system described by discrete energy state, energy $\{E_s\}$ corresponding to the state s , the expectation value of a macroscopic quantity A is then given by

$$\langle A \rangle = \frac{1}{Z} \sum_s A_s \exp(-E_s/k_B T) \quad (4.44)$$

where $Z = \sum_s \exp(-E_s/k_B T)$ is the canonical partition function. Note that the partition function Z involves either evaluation of summation over all possible states, an infinite series or an integration over a $6N$ dimensional space. The partition function gives the exact description of a system. However, in most of the cases, it is not possible to evaluate the partition function analytically or even exactly numerically. The difficulty is not only in evaluating the integral or summation over $6N$ degrees of freedom but also handling the complex interaction appearing in the exponential. In general, it is not possible to evaluate the summation over such a large number of state or the integral in such a high dimensional space interacting systems. However, it is always possible to take average over a finite number of states, a subset of all possible states, if one knows the correct Boltzmann weight of the states and the probability with which they are picked up. This can be realized MC simulation technique. In MC simulation techniques, usually only $10^6 - 10^8$ states are considered for making average. Say, N states (s_1, s_2, \dots, s_N) , a small subset of all possible

states, are chosen at random with certain probability distribution p_s . So the best estimate of the physical quantity A will be

$$A_N = \frac{\sum_{s=1}^N A_s p_s^{-1} \exp(-E_s/k_B T)}{\sum_{s=1}^N p_s^{-1} \exp(-E_s/k_B T)}. \quad (4.45)$$

Note that the Boltzmann probability of each state is normalized by the probability of choosing the state. As the number of sample N increases, the estimate will be more and more accurate. Eventually, as $N \rightarrow \infty$, $A_N \approx \langle A \rangle$.

Now, the problem is how to specify p_s so that the chosen N states will lead to right $\langle A \rangle$. Depending on the nature of a physical problem, the choice of p_s in MC averaging may differ. The physical problems can be categorized in two different groups: non-thermal non-interacting and thermal interacting systems. For non-thermal non-interacting systems ‘simple sampling MC’ and for thermal interacting systems ‘importance sampling MC’ are found suitable respectively. The specification of p_s in these sampling techniques will be described below.

4.9 Simple Sampling Monte Carlo

In the simple sampling MC averaging, all states are picked with equal probability p , the simplest choice for p_s . The best estimate of a physical quantity A then reduces to

$$\begin{aligned} A_N &= \frac{\sum_{s=1}^N A_s p_s^{-1} \exp(-E_s/k_B T)}{\sum_{s=1}^N p_s^{-1} \exp(-E_s/k_B T)} = \frac{\sum_{s=1}^N A_s p^{-1} \exp(-E_s/k_B T)}{\sum_{s=1}^N p^{-1} \exp(-E_s/k_B T)} \\ &= \frac{\sum_{s=1}^N A_s \exp(-E_s/k_B T)}{\sum_{s=1}^N \exp(-E_s/k_B T)}, \end{aligned} \quad (4.46)$$

as p cancels out from the numerator and denominator.

As it is mentioned already, such an averaging procedure is generally suitable for non-thermal non-interacting systems. For non-thermal average, the temperature T is taken as constant and usually in the high temperature limit, *i.e.*, $\exp(-E_s/k_B T) \approx 1$. In absence of any interaction, all configurations have exactly the same statistical weight and the best estimate is given by

$$\langle A \rangle \approx A_N = \frac{1}{N} \sum_{i=1}^N A_i. \quad (4.47)$$

This is to say that all the points on the phase space are contributing equally to the averaging. So, picking up points randomly over the phase space upto a reasonable number N (much smaller than the total number of states) is good enough for the averaging.

Examples:

1. Random walk: The average root mean square *end-to-end* distance $R_t = \sqrt{\langle R_t^2 \rangle}$ of a random walk with time t (the number of steps N) on a $2d$ square lattice increases as $R_t \sim t^\nu$ with $\nu = 1/2$ [10]. We will verify this result by simple sampling MC technique developed above.

The exact partition function for the random walk of N steps is $Z_N = z^N$, where $z = 4$ is the coordination number here. Thus, for 100 step walk, the number of configuration is 4^{100} , approximately 10^{60} . Definitely such a large number of sampling average is not possible even in a modern computer in a reasonable time. Therefore, one obviously take a small subset of such large number configurations randomly and make an average. It would be interesting to see the value of ν obtained from simple sampling MC considering only a very few configurations for averaging.

A possible algorithm to generate random walk on a square lattice is given below:

1. take the central site of the lattice as the origin $(0, 0)$.
2. call a random number r and make a move according to the rule: if $0 < r \leq 1/4$ go toward left, if $1/4 < r \leq 1/2$ go toward up, if $1/2 < r \leq 3/4$ go toward right, if $3/4 < r \leq 1$ go toward down.
3. increase time $t \rightarrow t + 1$ and change the position from $(x_t, y_t) \rightarrow (x_{t+1}, y_{t+1})$.
4. calculate the square distance at time t : $R_t^2 = x_t^2 + y_t^2$.
5. go to Step 2, as long as $t < N$, the required number of steps.
6. repeat Step 1 to Step 5 for a large number of samples N_{samp} and make the average $\langle R_t^2 \rangle = \sum_{i=1}^{N_{\text{samp}}} R_{t,i}^2 / N_{\text{samp}}$.

Consider a random walk of $2^{20} = 1048576$ steps on a $2d$ square lattice. Such a random walk has $4^{1048576}$ (approximately 10^{500000}) number of total configurations. Following the above algorithm, only 1000 random walks are generated and the rms end-to-end distance R_t has been calculated. In Figure 4.3, R_t is plotted against t (number of steps) in double logarithmic scale and from the slope the exponent ν is extracted as $\nu = 0.5000 \pm 0.0002$. Depending on the requirement of accuracy, one may tune the number of samples and obtain the appropriate result. Detailed numerical description is given in Ref.[7].

Problem: (a) Perform random walk on a $2d$ square lattice with disorder. Say, 10%, 20%, and 30% randomly chosen lattice sites are not available to the

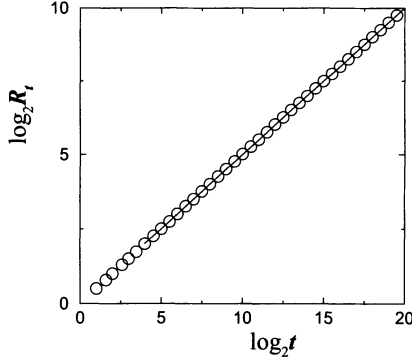


Figure 4.3: Plot of R_t against t for 2^{20} step random walk on a square lattice in double logarithmic scale. The exponent is extracted from the slope as $\nu = 0.5000 \pm 0.0002$.

random walker. Calculate the exponent ν and check that the behaviour is sub-diffusive.

(b) Perform random walk on a $2d$ square lattice in presence of a global bias E directed along left upper to right lower diagonal of the lattice. In presence of such a field, the jump probability can be given as

$$p_j = \frac{1}{4}(1 \pm E) \quad (4.48)$$

where “+” sign correspond to jumps toward down or right whereas “-” sign correspond to jumps toward up or left from the present position. The value of E changes from 0 to 1. Check that as E changes from zero to a small finite value, the exponent ν changes from $1/2$ to 1 corresponding to diffusion to drift motion.

(c) Perform part (b) in presence disorder. Check that for a given disorder, the drift velocity will not be a monotonically increasing function of E but there exists a critical field E_c above which the drift velocity will decrease[11].

2. Self-avoiding walk: In self-avoiding walk (SAW), a walker can not visit a lattice site already visited during the walk. The walk therefore depends on the whole history of the walk and consequently is non-Markovian. Such a walk can be used as a model of linear polymers in dilute solution with excluded volume effect. The number of configurations of SAWs can not be given by a simple expression as in random walk. In the asymptotic $N \rightarrow \infty$ limit, the number of configurations is approximately given by

$$Z_N \sim N^{\gamma-1} z_{eff}^N \quad \text{with} \quad z_{eff} \leq z - 1 \quad (4.49)$$

where z_{eff} is the effective coordination number of a lattice of coordination number z and γ is a critical exponent. The generating function Z_N is not exactly known even in $2d$ except for some special SAWs such as directed SAWs. MC

techniques are very useful for such walks. The effective coordination number $z_{eff} = Z_N/Z_{N-1}$ in the $N \rightarrow \infty$ limit is in general non-integer. The values of z_{eff} are obtained from extensive numerical studies as 2.638, 4.151 and 4.684 for the square, triangular and simple cubic lattices respectively [12]. The distribution function $Z_N(r)$, the number of N step SAWs of end-to-end distance r , is not Gaussian as in random walk (for random walk, $Z_N(r) \approx \exp(-r^2/N)$). Knowing the distribution function $Z_N(r)$, one can calculate the average end-to-end distance R_N as

$$\langle R_N^2 \rangle = \frac{1}{Z_N} \sum_r r^2 Z_N(r) = \frac{\sum_r r^2 Z_N(r)}{\sum_r Z_N(r)} \sim N^{2\nu} \quad (4.50)$$

where ν is a universal exponent. According to Flory theory, the value of ν is given as $\nu = 3/(2+d)$ in d dimension. Various real space renormalization and exact calculations provide $\nu = 3/4$ and $\gamma = 43/32$ in $2d$. In $3d$, $\nu \approx 0.59$ and $\gamma \approx 1.17$ as obtained in the $n \rightarrow 0$ limit of n -vector model. Details can be found in Ref.[12].

Simple sampling MC technique is very use full to generate SAWs. The algorithm of random walk has to be modified slightly. One needs to keep an array of all the lattice sites which will serve as a flag. Put the flag on (which was off initially) as soon as it is visited by the walker. In the future steps of the walk, a site of the lattice can not be occupied if the flag of that site is on.

Problem: Generate SAW of 100 steps on a $2d$ square lattice. Calculate the exponent ν and verify with the Flory exponent $\nu = 3/(d+2)$. One could vary the number of SAWs to increase the accuracy.

Thermal average can also be performed by simple sampling MC. Say, there are n nearest neighbour contacts other than those along the path of the walk in a SAW. If $-\epsilon$ is the interaction energy for each such nearest neighbour contacts then they will appear with a Boltzmann weight $\exp(n\epsilon/k_B T)$. Thus, instead of $Z_N(r)$ on needs to construct a distribution function $Z_N(n, r)$ of N step walk with n nearest neighbour contacts and r end-to-end distance. The average end-to-end distance then can be calculated as

$$\langle R_N^2 \rangle_T = \frac{\sum_{n,r} r^2 Z_N(n, r) e^{n\epsilon/k_B T}}{\sum_{n,r} Z_N(n, r) e^{n\epsilon/k_B T}} \sim N^{2\nu_T} \quad (4.51)$$

where ν_T is a temperature dependent exponent. It is found that there exists a critical temperature $T = \theta$ below which the SAWs have a compact globular structure and above which they remain as flexible chains forming a solution phase. The estimates of θ -points for different lattices are know as: $k_B\theta/\epsilon = 1.54 \pm 0.07$ for the square lattice, 2.66 ± 0.79 for the triangular lattice and 2.00 ± 0.10 for the simple cubic lattice. The exponent ν at the θ -point is obtained as $\nu_\theta = 4/7$ and $1/2$ for $d = 2$ and 3 dimensions respectively.

3. Percolation: In percolation processes a continuous path which spans the entire system is generated by the random addition of a number of objects [13, 14, 15, 16, 17, 18, 19]. The percolation model is defined here on a square lattice of linear size L in 2 dimensions ($2d$). There are two versions of the model, namely site and bond percolation. The site percolation model is described in the following. Initially the lattice is empty, *i.e.* none of the sites are occupied. Sites are then randomly occupied with a probability p or remains unoccupied with a probability $q = 1 - p$. A site is randomly occupied means that its occupation is independent of whether its nearest neighbors are occupied or empty. Occupied sites form clusters. A cluster of occupied sites is a collection of a number of occupied sites connected by nearest neighbor bonds. The smallest cluster can then be a single site if none of the nearest neighbor sites are occupied. For small values of p , only small clusters of occupied sites are generated. Since only small isolated clusters exist, there is no connection from one edge of the lattice to the opposite edge. The average size of the clusters increases with increasing value of p . On the other hand, for $p = 1$ all the sites are occupied and there is only one large cluster of size L^2 . As p increases from a small value, there exists a particular value of p between 0 and 1 at which a cluster of occupied sites spanning from left to right or top to bottom appears for the first time in the system. The percolation threshold p_c is equal to this particular value of p , below which there is no spanning cluster and above which there is always a spanning cluster present in the system. This is called percolation transition.

For an infinitely large lattice, p_c has a sharp and unique value determined by the lattice structure and the dimension d of the lattice. In Figure 4.4, four realizations on a square lattice of size $2^7 \times 2^7$ are shown for $p = 0.55, 0.58, 0.59274621$ and 0.65 . The largest cluster is shown by darker gray scale. A spanning cluster appears in the system for the first time at $p = 0.59274621$. This is the percolation threshold p_c on the square lattice for site percolation.

A geometrical phase transition is thus occurring at $p = p_c$. In order to establish percolation as critical phenomena, one should identify relevant geometrical quantities which exhibit critical behaviour at the percolation threshold p_c in similarity with that of thermodynamic phase transition. The most relevant geometrical quantity in percolation is cluster size distribution $n_s(p)$, the number of s -sited clusters per lattice site at a site occupation probability p . The total number of finite clusters per lattice site is then given by

$$\sum_s' n_s(p) \sim |p - p_c|^{2-\alpha} \quad (4.52)$$

where α is a critical exponent. This is analogous to the free energy per site in the case of magnetic phase transition. The order parameter P_∞ of the percolation transition, defined as the probability that a site belongs to the spanning cluster, is given by

$$P_\infty = p - \sum_s' s n_s(p). \quad (4.53)$$

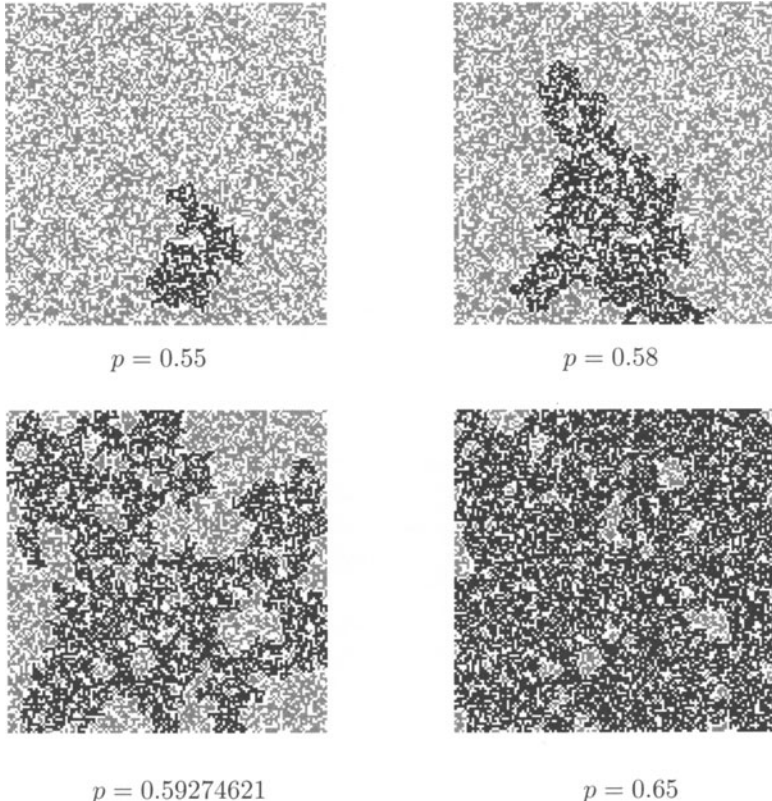


Figure 4.4: Percolation clusters generated at different site occupation probabilities on a square lattice of size 128×128 . The largest clusters are shown by dark black dots.

The order parameter $P_\infty = 0$ for $p < p_c$ as $\sum'_s sn_s(p) = p$. At $p = 1$, $\sum'_s sn_s(p) = 0$ and thus $P_\infty = 1$. As p is decreased from a large value above p_c , P_∞ continuously goes to zero from $p = p_c$ with an exponent β defined as

$$P_\infty \sim (p - p_c)^\beta. \quad (4.54)$$

The scaling behaviour of P_∞ is similar to that of the spontaneous magnetization M , the order parameter in the case of para to ferromagnetic transition. Another important geometrical quantity is the average cluster size χ defined as

$$\chi = \frac{\sum'_s s^2 n_s(p)}{\sum'_s sn_s(p)} \sim |p - p_c|^{-\gamma} \quad (4.55)$$

where γ is a critical exponent.

Different geometrical quantities like order parameter, average cluster size etc. are then just different moments of the cluster size distribution function $n_s(p)$, as thermodynamic quantities are different derivatives of the free energy function. It is then important to know the scaling function form of the cluster size distribution function $n_s(p)$ and derive all the critical exponents in terms of the exponents related to $n_s(p)$. The free energy function becomes a generalized homogeneous function in the critical regime of thermodynamic phase transition. A function of two variables x and y will be a generalized homogeneous function if it can be written as

$$f(x, y) = x^{1/a} F(y/x^{1/b}) \quad (4.56)$$

where a and b are two exponents. The cluster size distribution function $n_s(p)$ is then expected to be a generalized homogeneous function of two variables, *i.e.*; the inverse cluster size $1/s$ and $(p - p_c)$ in the critical regime of percolation. Note that, as $p \rightarrow p_c$ both of the variables approach zero. The scaling function form of $n_s(p)$ is then given by

$$\begin{aligned} n_s(p) &= (1/s)^\tau f[(p - p_c)/(1/s)^\sigma] \\ &= s^{-\tau} f[s^\sigma(p - p_c)]. \end{aligned} \quad (4.57)$$

The critical exponents associated with different geometrical quantities then can be obtained in terms of the exponents τ and σ and the scaling relations among the critical exponents such as $\alpha + 2\beta + \gamma = 2$ can also be established following the same procedure of thermodynamic phase transition.

The spin fluctuation in all possible length scales and the long range correlations in magnetic phase transition at the critical point is demonstrated by the divergence of correlation length. In the geometrical model like percolation, the linear size of the finite clusters, below and above p_c , is characterized by the connectivity length ξ which is similar to the correlation length in thermodynamic phase transition. Here ξ is defined as the root mean square distance between two sites on the same finite cluster and averaged over all finite clusters. It can be calculated by measuring the radius of gyration of a cluster

$$R_s^2 = \frac{1}{s} \sum_{i=1}^s |\mathbf{r}_i - \mathbf{r}_0|^2 \quad (4.58)$$

where $\mathbf{r}_0 = \sum_{i=1}^s \mathbf{r}_i / s$ is the position of the center of mass of the cluster and \mathbf{r}_i is the position of i th site of the cluster. The connectivity length is the average radius of gyration over all finite clusters and given by

$$\xi^2 = \frac{2 \sum'_s R_s^2 s^2 n_s(p)}{\sum'_s s^2 n_s(p)}. \quad (4.59)$$

At p_c , clusters of all possible sizes, starting from a single sited cluster up to the cluster of system size, appear in the system and correspondingly there is a huge fluctuation in the cluster size. Due to the appearance of large finite clusters at

the critical point, the connectivity length diverges as $p \rightarrow p_c$ with an exponent ν given by

$$\xi \sim |p - p_c|^{-\nu}. \quad (4.60)$$

The connectivity length exponent ν is also found related to the moment exponents of $n_s(p)$ via hyper scaling relation. The infinite cluster at $p = p_c$ contains holes of all possible sizes and the percolation cluster is found to be self similar and fractal. A hyperscaling relation $\gamma + 2\beta = d\nu$ is also found to be satisfied between the scaling exponents.

The exact values of the critical exponents for $2d$ percolation model was obtained by mapping the model onto the q -state Potts model in limit $q \rightarrow 1$ [14, 20]. The values of some of the exponents are listed in Table 4.1.

Table 4.1: The values of the critical exponents of the ordinary percolation in $2D$ obtained by mapping it onto q -state Potts model in the limit $q \rightarrow 1$.

Order parameter exponent β	$5/36$
Average cluster size exponent γ	$43/18$
Connectivity length exponent ν	$4/3$
Fractal dimension d_f	$91/48$

The values of the critical exponents are found to be the same on different lattices in the same space dimension. The critical exponents do not depend the site or the bond percolation problem on the same lattice in the same space dimension. This defines the universality class of the percolation model.

Percolation cluster generation algorithm: Two algorithms are generally used to generate percolation clusters, Hoshen-Kopelman algorithm and Leath algorithm. In Hoshen-Kopelman algorithm, the whole lattice is populated in every run whereas in Leath algorithm a single cluster is grown at a time. Below, the algorithms are described briefly on $2d$ square lattice for site percolation.

Hoshen-Kopelman algorithm:

1. Take an array $LATTICE(L \times L)$, where L is the lattice dimension. Set $LATTICE(L \times L) = 0$ initially to represent all sites are empty.
2. Consider the lattice site i , varies from 1 to L^2 . Start from one corner of the lattice and end at the opposite corner.
3. For each site, call a random number z , uniformly distributed between $[0, 1]$, using a random number generator. Compare z with the site occupation probability p . If $z \leq p$, then make $LATTICE(i) = 1$, means it is occupied.
4. If $z > p$, increment i to $i + 1$. If $i \leq L^2$ goto Step 2.
5. Cluster identification: Go through each row of the lattice in turn and labeling each site which is connected to a nearest neighbor with a number.



Figure 4.5: Cluster identification by Hoshen-Kopelman algorithm.

Thus the cluster label $L_{ij} = n$ for each occupied site, where n is the cluster number which is assigned when looking to see if previously inspected sites are nearest neighbors or not. This process is shown for the first row of a square lattice in Fig. 4.5. The difficulty arises at a point whose nearest neighbors are initially assigned to different labels but they essentially belong to the same cluster. In Fig. 4.5, cluster 1 and cluster 2 actually belong to the same cluster. The mislabeling is corrected by introducing another set of variables known as the ‘labels of the labels’, N_n . The ‘label of the label’ keeps track of situations in which two clusters actually belong to the same cluster, i.e. that an occupied site has two nearest neighbors which have already been assigned different cluster numbers. When this happens the ‘label of the label’ which is larger is set to the negative of the value of the smaller one (called the ‘proper’ label) so that both ‘clusters’ are identified as actually belonging to the same cluster and the proper label is set equal to the total size of the cluster. Thus in Fig. 4.5, after third row has been completed, $N_1 = 7$, and $N_2 = -1$.

Leath algorithm: The Leath algorithm is explained in Figure.4.6 over a small lattice. Stepwise algorithm is given below.

1. Take an array $LATTICE(L \times L)$, where L is the lattice dimension. Set $LATTICE(L \times L) = 0$ initially to represent all sites are empty.

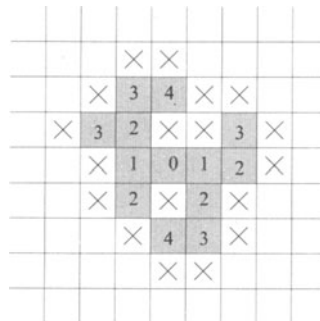


Figure 4.6: Demonstration of Leath algorithm. The central site labeled as 0 is occupied with unit probability. Other labels represent the occupied neighbours of the lower label. The cross represents the sites which are rejected.

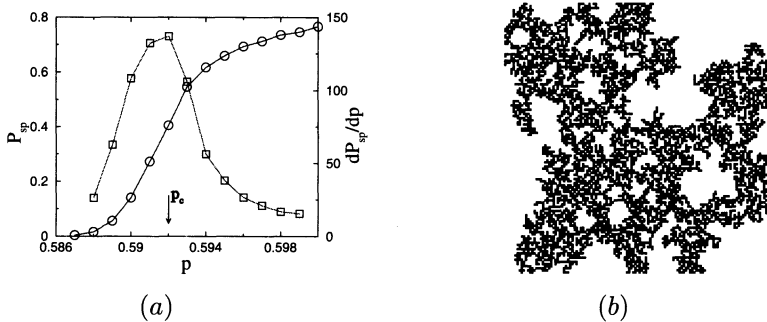


Figure 4.7: (a) Plot of P_{sp} and dP_{sp}/dp versus p . p_c corresponds to maximum slope. (b) A typical spanning cluster. The cluster contains holes of all possible sizes.

2. Occupy the central site with unit probability.
3. Make a list of nearest neighbours (eligible for occupation in the next step) of the occupied site(s) if their status $LATTICE(k) = 0$ and keep them in an array $LIST(j)$. A counter JN could represent the number of entries in the array $LIST$.
4. Call the $LIST(j)$ from $j = 1$ to JN . For each entry, call a random number z , uniformly distributed between $[0, 1]$, using a random number generator. Compare z with the site occupation probability p . If $z \leq p$, then make $LATTICE(i) = 1$, means it is occupied otherwise make $LATTICE(i) = 2$, means it is rejected.
5. Go back to Step.3 as long as JN not equal to zero.
6. Repeat Steps 1 – 4, for the desire number of clusters.

Determination of percolation threshold and critical exponents: Demonstration here is made generating clusters by Leath algorithm. Clusters are generated on a $2d$ square lattice of size 1024×1024 . Total number of clusters generated is $N_{tot} = 10,000$. In Leath method, the cluster size distribution is given by $P_s(p) = n_s/N_{tot}$, the probability to have an s -sited cluster.

Percolation threshold is determined by calculating the probability to have a spanning cluster $P_{sp} = N_{sp}/N_{tot}$, where N_{sp} is the number of spanning clusters out of total N_{tot} clusters. The threshold corresponds to the maximum change in P_{sp} and it is found as $p_c = 0.592 \pm 0.001$.

Critical exponents related to different moments of cluster size distribution have been estimated by calculating

$$\chi_q = \sum_s' s^q P_s(p) \sim |p - p_c|^{-\gamma_q}, \quad q = 1, 2, \dots \quad (4.61)$$

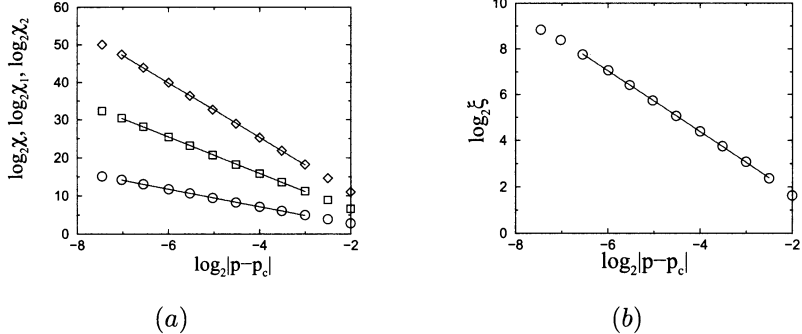


Figure 4.8: (a) Plot of χ_q against $|p - p_c|$ in double logarithmic scale. Slopes correspond to the respective exponents. (b) Plot of ξ against $|p - p_c|$ in double logarithmic scale. The exponent ν is extracted from the slope.

where $q = 1$ corresponds to average cluster size. The moments are plotted in Figure 4.8(a) against $|p - p_c|$. The exponents are extracted from the slopes. In Figure 4.8(b), the correlation length ξ is plotted against $|p - p_c|$ and the exponent ν is extracted from the slope. The values of the critical exponents can be found in Ref.[21].

In order to verify, the scaling function form of the cluster size distribution function

$$P_s(p) = s^{-\tau+1} f[s^\sigma(p - p_c)], \quad (4.62)$$

the scaled probability $P_s(p)/P_s(p_c)$ is plotted in Figure 4.9 against the scaled variable $z = s^\sigma(p - p_c)$. Data collapse onto a single curve for different values of s and p reasonably.

Percolation model has wide applications and well discussed in Ref.[22].

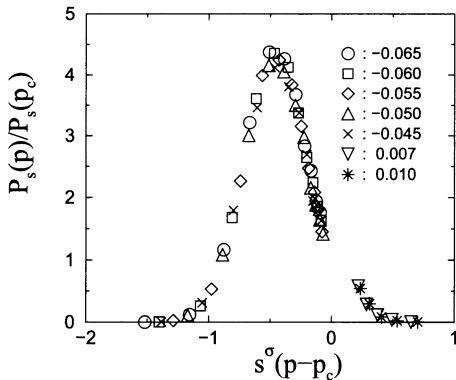


Figure 4.9: Plot of $P_s(p)/P_s(p_c)$ against the scaled variable $z = s^\sigma(p - p_c)$. A reasonable data collapse is observed.

Percolation under external bias: The universality among widely different systems is a remarkable observation in critical phenomena. It is observed that the values of the critical exponents of a system depend only on the dimensionality of the space, number of components in the order parameter and do not depend on the underlying lattice structure or type of interaction. Two widely different systems, Ising magnet and liquid gas system in 3D with scalar order parameters, belong to the same universality class with the critical exponents having the same magnitude. However, application of external bias field on the percolation model leads to new universality classes. The effect of two different external bias fields on the percolation model are extensively studied. First is a global directional bias and the second is a local rotational bias. These external bias fields are implemented on the percolation model by assigning appropriate constraint on the occupation of lattice sites. The directional bias corresponds to a directional constraint and the rotational bias corresponds to a rotational or a spiral constraint. The percolation models under these external constraints are known as directed percolation (DP) [23] and spiral percolation (SP) [26] respectively. An example of directional constraint is the motion of a charged particle in the direction of applied electric field. Similarly, the motion of a charged particle in a plane in the presence of a magnetic field perpendicular to the plane of motion is an example of spiral constraint. Percolation models under these external biases and also under the combination of these two biases are now presented briefly.

Directed percolation (DP): In directed percolation [23], a global directional constraint restricts the growth of the percolation cluster in a particular direction. Say, if the directional constraint is in the top left to bottom right diagonal of the lattice, sites are allowed to occupy only in these two preferred directions, towards right or bottom. The model is illustrated in Fig. 4.10(a). Since the clusters grow in the preferred direction, they become highly anisotropic in nature as shown in Fig. 4.10(b). Consequently, unlike the ordinary percolation, there are two lengthscales appear and the system behaves differently in the two directions. There are then two connectivity lengths, ξ_{\parallel} along the preferred direction and ξ_{\perp} in the direction perpendicular to that, which diverge with two different connectivity exponents ν_{\parallel} and ν_{\perp} respectively as $p \rightarrow p_c$. This leads to anisotropic scaling and direction-dependent critical behaviour. All the critical exponents [24] in this model are different than those of OP. Thus the DP model belongs to a new universality class other than OP.

The DP model has a lot of applications in different fields like self-organized criticality, reaction diffusion systems, nonlinear random resistor networks, polymers and many more [25].

Spiral percolation (SP): In spiral percolation [26], a rotational constraint, say clockwise, present in the percolating system. In this model cluster can be grown starting from the central site of the lattice following a rotational rule. Due to the clockwise rotational constraint present in the system, empty sites in the forward direction and in the clockwise rotational direction are eligible for

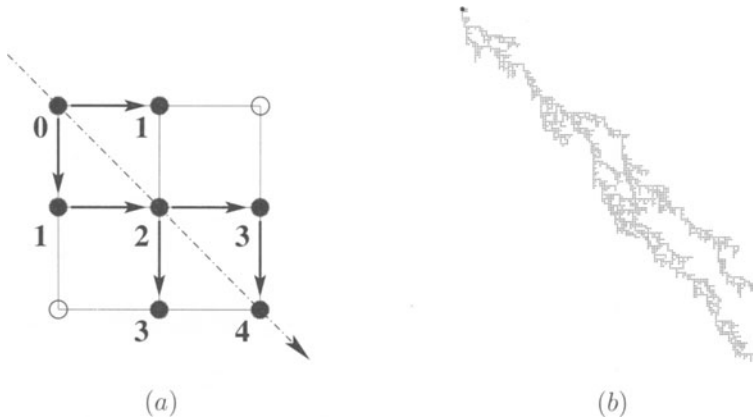


Figure 4.10: (a) Growth of cluster in directed percolation. As the directional constraint is along the top left to right bottom diagonal, indicated by the dotted arrow, sites in the right or bottom are allowed to occupy. The numbers indicate the time steps at which they are occupied. (b) Spanning DP cluster generated on a 256×256 square lattice at the percolation threshold $p_c = 0.705489$.

occupation. The forward direction is the direction from which the present site is occupied and the sense of rotational direction is defined with respect to the forward direction. This is illustrated in Fig. 4.11(a). The eligible sites are then occupied with probability p and the clusters grow isotropically on the lattice. In this model, due to the presence of rotational constraint, an occupied site can be reoccupied from different directions but forbidden for occupation from the same direction. Consequently, loops are an essential feature of the spirally grown clusters which make the clusters highly compact than those of OP or DP. Unlike DP, the clusters are isotropic here similar to OP, but they are much more compact. As a consequence, critical properties of the SP model [27] are found different than that of the OP and DP model.

The SP model has been applied in studying forest fire, pinning of interfaces and diffusion under rotational bias in disordered systems [28].

Directed spiral percolation (DSP): In order to study the electro-magnetic properties of disordered systems in the presence of both the electric and magnetic fields, a site percolation model called directed spiral percolation (DSP) model can be constructed by imposing both the directional and rotational constraints simultaneously on the ordinary percolation model [29]. If both the fields are present perpendicular to each other in a material system, due to Lorentz force the electron will get deflected and a Hall field will appear in the system perpendicular to both the fields. This is known as Hall effect. The DSP model then can also be applied to study the Hall effect in such systems.

In generating a DSP cluster, the directional and rotational constraints determine the eligibility of the empty nearest neighbours for occupation. In the

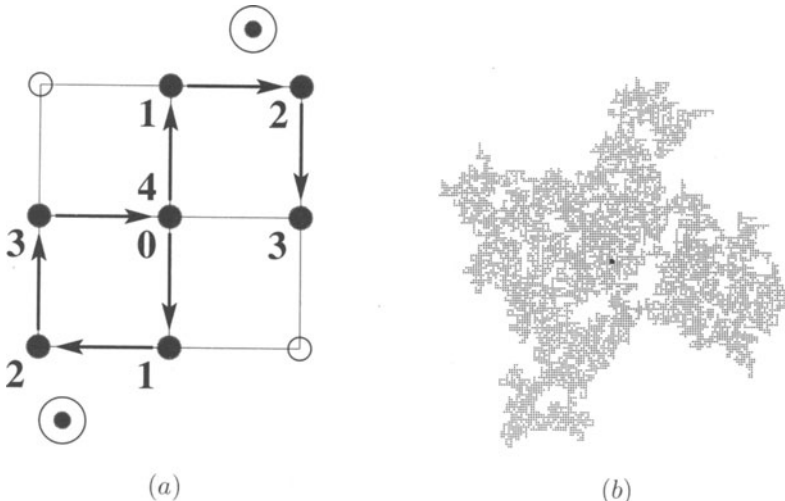


Figure 4.11: (a) Growth of a cluster in spiral percolation starting from the central site (0). As the spiral constraint is in the clockwise direction, indicated by the encircled dot, sites in the forward and in the clockwise directions are allowed to occupy. (b) Spanning SP cluster generated on a 256×256 square lattice at the percolation threshold $p_c = 0.712$.

single cluster growth algorithm, the central site of the lattice is occupied with unit probability. The nearest neighbours of the central site are occupied with equal probability p in the first MC time step. As soon as a site is occupied, the direction from which it was occupied is assigned to it. Lists of eligible sites for occupation in the next MC time steps are then prepared. Due to the directional constraint from left to right, an empty site on the right of an occupied site is always eligible for occupation. Due to the clockwise rotational constraint, empty sites in the forward direction and in the clockwise rotational direction (with respect to the forward direction) of an occupied site are eligible for occupation. However, a site index appears only once in the list of eligible sites at any time step. The eligible sites are then occupied with probability p . A typical spanning DSP cluster on the square lattice of linear size $L = 2^8$ at $p = p_c$ is shown in Figure 4.12. The cluster generated is highly anisotropic in geometry similar to the DP cluster but different from isotropic SP cluster. The growth of the cluster is along the upper left to the lower right diagonal of the lattice and it is not along the applied directional field E as in the DP cluster. If one considers clustering of classical charged particles in the presence crossed electric field (directional constraint) and magnetic field perpendicular to the plane of motion (rotational constraint), then there will be a magnetic force E_H , shown in Figure 4.12, on the positively charged particle perpendicular to both the fields. Consequently, an effective field E_{eff} will develop in the system

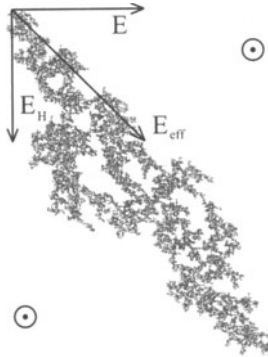


Figure 4.12: Spanning DSP clusters on the square lattice of size $2^8 \times 2^8$ generated at the percolation threshold $p_c = 0.6550$.

along the upper left to the lower right diagonal of the lattice. It is interesting to notice that the DSP cluster is growing along this effective direction rather than along the applied directional constraint. However, geometrically the DSP cluster is very different from a DP cluster shown in Figure 4.10. It is to be noted that, in a material, during the transport of charged particles under crossed electric and magnetic fields, a Hall field develops perpendicular to both the fields. The deflection of charged particles in the transverse direction stops as soon as the Hall field becomes equal to the magnetic force on the particle. In the DSP model, it seems that a fictitious Hall field opposite to E_H appears in the system which in effect stops the growth of the cluster.

A comparison between the values of the critical exponents obtained in different percolation models is made here in Table 4.2. It can be seen that the values of the critical exponents obtained in different models are very different. The external constraints then lead the percolation model to belong to new universality classes.

Problem: (a) Generate percolation clusters using Leath algorithm on a $2d$ square lattice of size, say 1000×1000 . Determine the percolation threshold p_c . Calculate the average cluster size χ and correlation length ξ as a function $|p - p_c|$ taking p below p_c and determine the corresponding critical exponents γ and ν .

(b) Consider the percolation problem under a directed bias, say, a bias is directed from upper left corner to lower right corner. Due to the bias, the site on the right and below of an occupied site can only be occupied. Check that the clusters generated are anisotropic. Calculate p_c and determine the exponents γ , $\nu_{||}$ and ν_{\perp} .

(c) Consider the percolation problem under a rotational bias. Due to this bias, the site in the forward direction and towards right with respect to the direction from which the present site is occupied are eligible for occupation.

Table 4.2: Comparison of the values of the critical exponents β , γ , τ , σ , ν and d_f in the case of ordinary (OP)[21], directed (DP)[24], spiral (SP)[27] and directed spiral (DSP)[29] percolation models on the square lattice. The values of the critical exponents are found different in different percolation models.

Percolation Models	β	γ	τ	σ	ν	d_f
OP	5/36	43/18	187/91	36/91	4/3	91/48
DP	0.277 ±0.002	2.2772 ±0.0003	2.108 ±0.001	0.3915 ±0.0004	$\nu_{\perp} = 1.0972$ $\nu_{\parallel} = 1.733$ ±0.001	1.765
SP	0.048 ±0.011	2.19 ±0.07	2.022 ±0.004	0.447 ±0.014	1.116 ±0.003	1.957 ±0.009
DSP	0.31 ±0.01	1.85 ±0.01	2.16 ±0.20	0.459 ±0.004	$\nu_{\perp} = 1.12$ $\nu_{\parallel} = 1.33$ ±0.01	1.733 ±0.005

Check that the clusters generated are isotropic. Calculate p_c and determine the exponents γ and ν .

(d) Consider the percolation problem under both the directed and rotational biases present simultaneously. Check that the clusters generated are anisotropic. Calculate p_c and determine the exponents γ , ν_{\parallel} and ν_{\perp} .

4.10 Importance Sampling Monte Carlo

In this section we will discuss MC algorithm for thermodynamic interacting systems. The expectation value of a physical quantity of a thermodynamic system at equilibrium at temperature T with a heat bath (canonical ensemble) is given by

$$\langle A \rangle = \frac{1}{Z} \sum_s A_s \exp(-E_s/k_B T) \quad (4.63)$$

as per the theory of statistical mechanics where the sum is over all possible states, generally enormously large. On the other hand, at low temperature the system spends almost all its time sitting in the ground state or one of the lowest excited states. Thus, an extremely restricted part of the phase space should contribute to the average. Accordingly, the sum should be over a few low energy states because at low temperature there is not enough thermal energy to lift the system into the higher excited states. Thus, picking up points randomly over the phase space as in simple sampling is no good here. In other words, if the sums appearing in the MC estimator are dominated by small number of

states and the contribution by all other states, the majority, are negligible then the simple sampling will not be effective.

Therefore, a method is needed that will lead us automatically in the important region of phase space. One could sample points preferentially from the region which is populated by the appropriate states. Such a method is realizable via the importance sampling MC scheme. In such a scheme, a state s is picked up with a probability p_s proportional to the Boltzmann factor. A MC estimator then can be defined for a subset of N microstates (much smaller than all possible states) as

$$A_N = \frac{\sum_{s=1}^N A_s p_s^{-1} \exp(-E_s/k_B T)}{\sum_{s=1}^N p_s^{-1} \exp(-E_s/k_B T)} \quad (4.64)$$

where each state is picked up with a probability p_s . A simple choice of $p_s = p$ for all state (as it has been made in the simple sampling method) will lead the estimator

$$A_N = \sum_{s=1}^N A_s \exp(-E_s/k_B T) / \sum_{s=1}^N \exp(-E_s/k_B T) \quad (4.65)$$

as that was obtained in simple sampling. Instead of picking N states randomly with equal probability, pick them with a probability $p_s = \exp(-E_s/k_B T)/Z$, the correct Boltzmann weight. Then the expectation value of a quantity will be given by

$$\begin{aligned} A_N &= \frac{\sum_{s=1}^N A_s p_s^{-1} \exp(-E_s/k_B T)}{\sum_{s=1}^N p_s^{-1} \exp(-E_s/k_B T)} \\ &= \frac{\sum_{s=1}^N A_s \exp(-E_s/k_B T) Z / \exp(-E_s/k_B T)}{\sum_{s=1}^N \exp(-E_s/k_B T) Z / \exp(-E_s/k_B T)} \end{aligned} \quad (4.66)$$

which simply reduces to

$$A_N = \frac{1}{N} \sum_{s=1}^N A_s \quad (4.67)$$

where each state s is picked with the correct Boltzmann probability $p_s = \exp(-E_s/k_B T)/Z$ (not randomly selected states with equal probability as in

simple sampling). This averaging is called ‘importance sampling’ average. However, it is not an easy task to pick up states which appear with its correct Boltzmann weight.

It is possible to realize importance sampling with the help of Markov chain. As already discussed, a Markov chain is a sequence of states each of which depends only on the preceding one.

$$[n] \xrightarrow{\mathcal{H}} [m] \xrightarrow{\mathcal{H}} [o] \quad (4.68)$$

The transition probability W_{nm} from state n to m should not vary over time and depends only on the properties of current states (n, m) . Moreover, $W_{nm} \geq 0$ and $\sum_m W_{nm} = 1$. The Markov chain has the property that average over successive configurations

$$\langle A \rangle_n = \langle A \rangle + O(1/\sqrt{n}) \quad (4.69)$$

as $n \rightarrow \infty$, if the states are weighted by Boltzmann factor. However, for this to happen two conditions on Markov chain have to be satisfied. They are: (i) ergodicity and (ii) detailed balance.

Ergodicity: It should be possible in Markov process to reach any state of the system starting from any other state in long run. This is necessary to achieve a state with its correct Boltzmann weight. Since each state m appears with some non-zero probability p_m in the Boltzmann distribution, and if that state is inaccessible from another state n , then the probability to find the state m starting from state n is zero. This is in contradiction with Boltzmann distribution which demands the state should appear with a probability p_m . This means that there must be at least one path of non-zero transition probabilities between any two states. One should take care in implementing MC algorithms that it should not violate ergodicity.

Detailed balance: In the steady state, the probability flux out of a state n is equal to the probability flux into the state n and the steady state condition is given by the “global balance” equation

$$\sum_m W_{nm} p_n(t) = \sum_m W_{mn} p_m(t). \quad (4.70)$$

Since $\sum_m W_{nm} = 1$, one has

$$p_n(t) = \sum_m W_{mn} p_m(t). \quad (4.71)$$

It can also be written in the matrix form as

$$\mathbf{p}(t) = \mathbf{p}(t) \cdot \mathbf{W} \quad (4.72)$$

where t represents the steps of a Markov process and \mathbf{W} is the one step transition matrix. It is expected that for any \mathbf{W} , the probability distribution p_n

should represent the equilibrium dynamics of the Markov process. However, the above condition is not sufficient to guarantee that the probability distribution will tend to p_n after a long evolution of a Markov chain starting from any state. In this way, it is also possible to reach dynamical equilibrium in which the probability distribution p_n circles around a number of different values. Such rotation is called a limit cycle. In those situations there is no guarantee that the actual states generated will have anything like the desired probability distribution. Such a situation can be ruled out by applying an additional condition, the condition of “detailed balance”, to the transition probabilities:

$$W_{nmp_n}(t) = W_{mnp_m}(t) \quad (4.73)$$

with the requirement that all entries of \mathbf{W} are positive. The condition of detailed balance then tells us that on an average the system should go from state n to state m is equal to that it goes from m to n . In a limit cycle, in which the probability of occupation of some of the states changes in a cyclic fashion, there must be states for which this condition is violated on any step of the Markov chain in order to satisfy a pre-determined occupation probability of a state. The condition of detailed balance forbids dynamics with limit cycle.

Let the equilibrium distribution to be the Boltzmann distribution, the probability of the n th state is then $p_n(t) = \exp(-E_n/k_B T)/Z$ where $Z = \sum_n \exp(-E_n/k_B T)$ is the canonical partition function. The detailed balance condition then tell us that the transition probabilities should satisfy

$$\frac{W_{nm}}{W_{mn}} = \frac{p_m}{p_n} = e^{-(E_m - E_n)/k_B T} \quad (4.74)$$

along with $\sum_m W_{nm} = 1$. If these conditions as well as the condition of ergodicity are satisfied, then the equilibrium distribution of states in a Markov process will be Boltzmann distribution.

The probability p_n is usually not known exactly because in most of the cases the canonical partition function $Z = \sum_n \exp(-E_n/k_B T)$ is extremely difficult to calculate exactly. To avoid the difficulty one uses the Markov process to generate a state directly from the preceding one following Metropolis algorithm.

Metropolis algorithm: If the m th state is produced from the n th state only, the relative probability is the ratio of the individual probabilities $p_n/p_m = \exp\{-(E_n - E_m)/k_B T\}$. As a result, only the energy difference between the two states matter, i.e.; $\Delta E = E_n - E_m$. Any transition rate which satisfies detailed balance is acceptable. The following is considered by Metropolis:

$$\begin{aligned} W_{nm} &= e^{-\Delta E/k_B T} && \text{if } \Delta E > 0 \\ &= 1 && \text{if } \Delta E \leq 0. \end{aligned} \quad (4.75)$$

Problem: Check that the Metropolis transition probability satisfies the detailed balanced condition.

The Ising Model: In this section, importance sampling Monte Carlo techniques will be used for the study of phase transitions at finite temperature. We shall discuss details, algorithms, and potential sources of difficulty using the Ising model as a paradigm. However, virtually all of the discussion of the application to the Ising model is relevant to other models as well. The Ising model is one of the simplest lattice models which one can imagine, and its behavior has been well studied. The simple Ising model consists of spins which are confined to the sites of a lattice and which may have only the values +1 or -1. If there are N spins on the lattice, then the system can be in 2^N states. The energy of a state is given by the Ising Hamiltonian:

$$\mathcal{H} = -J \sum_{\langle i,j \rangle} \sigma_i \sigma_j - h \sum_i \sigma_i \quad (4.76)$$

where J is the interaction energy between nearest neighbour spins $\langle i,j \rangle$, h is the external magnetic field in units of energy, and $\sigma_i = \pm 1$. The Ising model has been solved exactly in one dimension and as a result it is known that there is no phase transition. In two dimensions, the model is exactly solved in zero field situation which showed that there is a second order phase transition. The critical temperature is obtained from the condition

$$2 \tanh^2 \frac{2J}{k_B T_c} = 1, \quad (4.77)$$

as $k_B T_c/J = 2.269185$. The phase transition is characterized by the divergences in the specific heat, susceptibility, and correlation length. The critical exponents obtained are: $\alpha = 0$ (logarithmic), $\beta = 1/8$, $\gamma = 7/4$, $\nu = 1$. The Ising model in higher dimensions can be solved following mean field approach. The mean field exponents are: $\alpha = 0$ (discontinuity), $\beta = 1/2$, $\gamma = 1$, $\nu = 1/2$. In order to satisfy the scaling relation $2 - \alpha = d\nu$, one has $d = 4$, the upper critical dimension.

Metropolis importance sampling scheme:

1. Choose an initial state assigning +1 or -1 corresponding to up or down spin arbitrarily to the lattice sites.
2. Choose a site j
3. Calculate the energy change $\Delta E = E_f - E_i$ which results if the spin at site j is overturned
4. Generate a uniformly distributed random number r such that $0 < r < 1$
5. If $r < \exp(-\Delta E/k_B T)$, flip the spin
6. Go to the next site and go to (3)

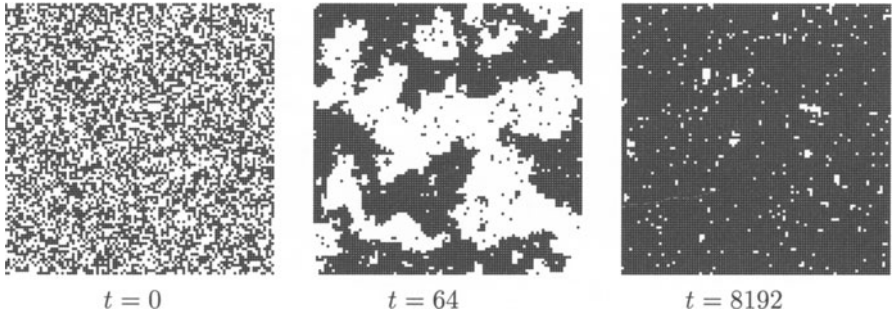


Figure 4.13: Spin configuration at temperature $k_B T/J = 2.0$, corresponds to $T < T_c$ ($k_B T_c/J \approx 2.27$). t is the MC time step per spin.

Spin configurations of a 2d zero field spin-1/2 Ising model on the square lattice are obtained using single spin flip Metropolis algorithm at a temperatures T below T_c in Figure 4.13 and above T_c in Figure 4.14. The spin configurations shown in the figures below are obtained on a 100×100 square lattice. Note that in absence of the field, the model has up-down symmetry so that overturning all the spins produces a degenerate state. At high temperature all the clusters of like spins are small, near the transition there is a broad distribution of clusters, and at low temperatures there is a single large cluster of ordered spins and a number of small clusters of oppositely directed spins.

Equilibrium: Any measurement of macroscopic property has to be made on the states at thermodynamic equilibrium of the system at a given temperature T . Equilibrium means that the average probability of finding a state n is proportional to the Boltzmann weight $e^{-\beta E_n}$ of that state. How to know that our system has reached that situation? One can calculate a macroscopic quantity, say magnetization M , as a function of MC time step t starting from

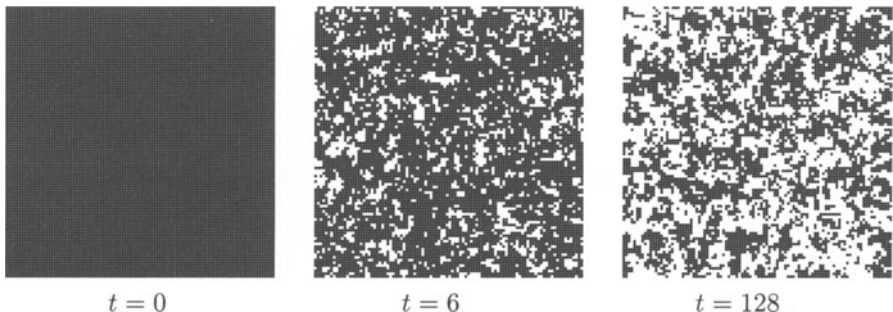


Figure 4.14: Spin configuration at $k_B T/J = 3.0$, corresponds to $T > T_c$ ($k_B T_c/J \approx 2.27$). t is the MC time step per spin.

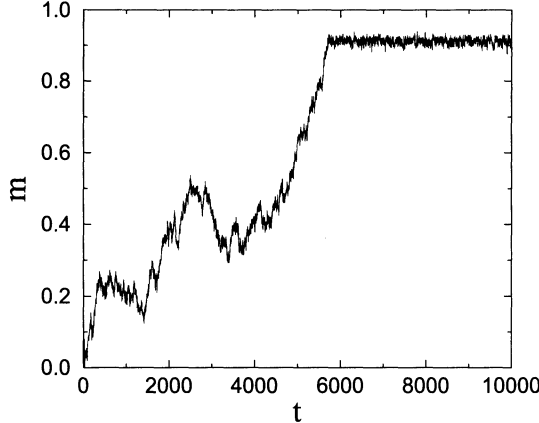


Figure 4.15: Plot of spontaneous magnetization against time t at temperature $T = 2.0$ starting from a random configuration ($T \approx \infty$).

an arbitrary configuration. As $t \rightarrow \infty$, the macroscopic quantity should reach a constant value or fluctuate slightly around a constant value. For a system of size 100×100 , magnetization, the number of up spins, are measured as a function of MC time step t and plotted in Figure 4.15. One could see that, it starts from zero as expected and reaches a steady value after 6000 time steps.

In many cases it is possible for the system to get stuck in some metastable region of its state space for a while, giving roughly constant value of the macroscopic quantities and so appearing to have reached equilibrium. In terms of statistical Mechanics, there can be a local energy minimum in which the system can remain temporarily, and one should not mistake this as a global energy minimum, which is the region of phase space corresponds to the system in equilibrium. One may verify this by calculating a macroscopic quantity as a function of MC time steps starting from two widely different initial situation and different random number seeds.

Some of the equilibrium spin configurations at different temperatures are shown below:

Measurements: Simulations are performed on a $2d$ square lattice of size 100×100 . Measurements are done after $t = 10^4$ time steps and averaged over 10^4 configurations.

The magnetization m per spin in a state n is given by

$$m_n = \frac{1}{L^2} \sum_i^{L^2} \sigma_i^n. \quad (4.78)$$

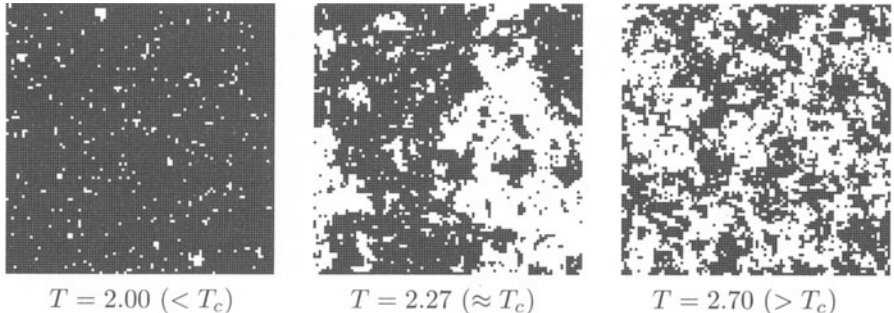


Figure 4.16: Equilibrium spin configuration at different temperatures around T_c after 8000 Monte Carlo time step per spin.

Since only one spin k flips at a time in the Metropolis algorithm, so the change in magnetization is given by

$$\Delta M = M_m - M_n = \sum_i \sigma_i^m - \sum_i \sigma_i^n = \sigma_k^m - \sigma_k^n = 2\sigma_k^m. \quad (4.79)$$

One can then calculate the magnetization at the beginning of the simulation and then use the following equation

$$M_m = M_n + \Delta M = M_n + 2\sigma_k^m \quad (4.80)$$

for every spin flip. As soon as the magnetization is obtained, one could calculate the per spin susceptibility as

$$\chi = N\beta(\langle m^2 \rangle - \langle m \rangle^2). \quad (4.81)$$

m and χ are obtained as a function temperature T and are plotted in Figure 4.17.

The energy E_n of a state n can be obtained as

$$E_n = -J \sum_{\langle i,j \rangle} \sigma_i^n \sigma_j^n \quad (4.82)$$

setting $J = 1$. However, in Metropolis algorithm we calculate the energy difference $\Delta E = E_m - E_n$ in going from state n to state m . Thus, one can calculate energy of a state m as

$$E_m = E_n + \Delta E. \quad (4.83)$$

Knowing the value of energy E , one may calculate the per spin specific heat as

$$c_V = \beta^2(\langle E^2 \rangle - \langle E \rangle^2) \quad (4.84)$$

assuming $k_B = 1$. E and c_V is plotted as a function of temperature T in Figure 4.18.

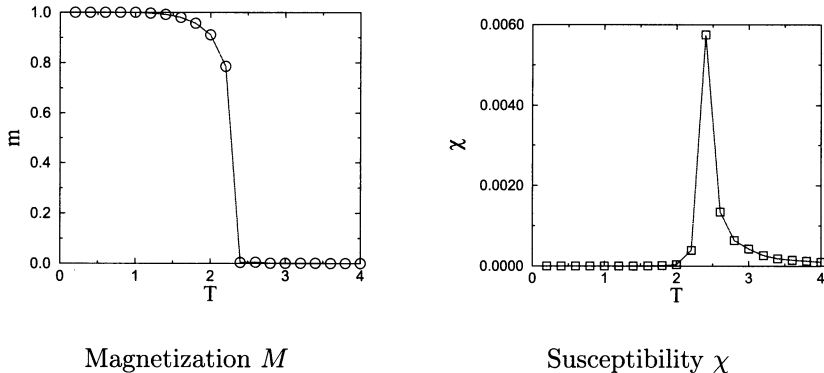


Figure 4.17: Plot of magnetization M and susceptibility χ against temperature T (in units of J/k_B).

In order to take average of a physical quantity, we have presumed that the states over which the average has been made are independent. Thus to make sure that the states are independent, one needs to measure the “correlation time” τ of the simulation. The time auto correlation $C_m(t)$ of magnetization is defined as

$$C_m(t) = \sum_{t'} [m(t') - \langle m \rangle][m(t' + t) - \langle m \rangle] = \sum_{t'} m(t')m(t' + t) - \langle m \rangle^2. \quad (4.85)$$

The auto correlation $C_m(t)$ is expected to fall off exponentially at long time

$$C_m(t) \sim e^{-t/\tau}. \quad (4.86)$$

Thus, at $t = \tau$, $C_m(t)$ drops by a factor of $1/e$ from the maximum value at $t = 0$. For independent samples, one should draw them at an interval greater

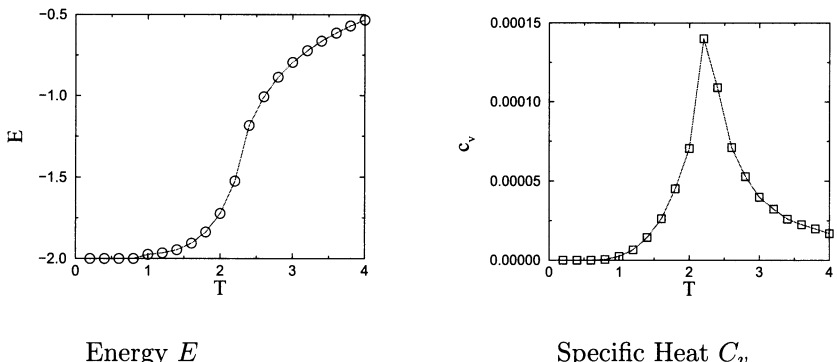


Figure 4.18: Plot of internal energy E and specific heat C_V against temperature T (in units of J/k_B).

than τ . In most of the definitions of statistical independence, the interval turns out to be 2τ .

Problem: Simulate the zero field spin-1/2 Ising model on a $2d$ square lattice employing Metropolis algorithm. Calculate per spin magnetization and susceptibility of the system as a function of T . Determine T_c .

Application of Monte Carlo technique in different fields of condensed matter could be found in Ref.[30].

4.11 Error Analysis

There are two types of error in Monte Carlo simulation: statistical error and systematic error. Statistical error arises as a result of random changes in the simulated system from measurement to measurement and can be eliminated by generating a large number of independent samples. Systematic error is due to the procedure adopted to make a measurement and that affect the whole simulation.

4.11.1 Statistical Error

Suppose a quantity x is distributed according to a Gaussian distribution with mean value $\langle x \rangle$ and width σ . Consider N independent observations $\{x_i\}$ of this quantity x . An unbiased estimator of the mean $\langle x \rangle$ of this distribution is

$$\langle x \rangle = \frac{1}{N} \sum_{i=1}^N x_i \quad (4.87)$$

and the standard error of this estimate is

$$\text{error} = \sigma / \sqrt{N}. \quad (4.88)$$

In order to estimate the standard deviation σ itself from the observations, consider the deviation $\delta x_i = x_i - \langle x \rangle$. Trivially we have $\langle \delta x \rangle = 0$. Thus we are interested in mean square deviation

$$\langle (\delta x)^2 \rangle = \frac{1}{N} \sum_{i=1}^N (x_i - \langle x \rangle)^2 = \langle x^2 \rangle - \langle x \rangle^2. \quad (4.89)$$

The square of standard deviation is the variance and it is given by

$$\sigma^2 = \text{var}(x_1 \cdots x_N) = \frac{1}{N-1} \sum_{i=1}^N (x_i - \langle x \rangle)^2 \approx \langle x^2 \rangle - \langle x \rangle^2 \quad (4.90)$$

Thus, the error in the estimation of mean $\langle x \rangle$ is given by

$$\text{error} = \sqrt{\frac{1}{N(N-1)} \sum_{i=1}^N (x_i - \langle x \rangle)^2} \quad (4.91)$$

4.11.2 Systematic Error

Since the systematic errors do not appear in the fluctuations of the individual measurement, they are more difficult to estimate than statistical errors. The main source of systematic error in the Ising Model simulation is the choice of finite number of MC time steps to equilibrate the system. There is no good general method for estimating systematic errors. Each source of such error has to be considered separately and a strategy has to be identified.

4.12 Finite Size Scaling analysis

We will now discuss how to tackle the problems that arise from the limitations that one has with a computer. Even modern day powerful computers have limited memory and limited speed. It is not possible to handle a system with large number of particles ($\sim 10^{23}$, the Avogadro's number) in a simulation nor a system which has an infinitely large correlation time or relaxation time. Both these problems become acute at phase transitions or near a critical point. Near a critical point, the correlation length is large. To get the correct results one needs to simulate a large system much larger than the correlation length. Near the critical point, the relaxation time also diverges and equilibration of a system in simulation becomes extremely demanding.

In the following two chapters, we will discuss how the physics behind scaling can be used to extract the results for infinite systems in the thermodynamic limit from the simulation results of finite systems in a systematic way. We would like to start our discussion with the following problem:

Problem: Find the change in the magnetization, susceptibility and the specific heat as a function of temperature in Ising model on a finite size lattice with periodic boundary condition.

The effect of finiteness of the system on the simulation results of a phase transition is dramatic. The singular behaviors of several thermodynamic quantities that one expects at phase transitions are realizable only in the thermodynamic limit of very large system sizes. In finite systems, the transition is generally completely smeared out. Spontaneous symmetry breaking occurs in the thermodynamic limit only. In finite systems, spontaneous magnetization is defined by taking the thermodynamic limit $L \rightarrow \infty$ first and then letting $h_0 \rightarrow 0$: $M_{sp} \equiv \lim_{h_0 \rightarrow 0} \lim_{L \rightarrow \infty} M_{h_0}$. Here, L is the size of the system and h_0 is the

applied magnetic field. The issue is that we want results which correspond to the realistic infinitely large thermodynamic systems from simulation of systems of finite sizes (few thousand particles or spins!). Here, we will discuss how to extract definite information regarding a phase transition (the nature of the transition, transition point, critical exponents in second order transitions etc.) from simulations of finite systems by a systematic finite size scaling analysis.

General principle: From above we see that one possibility is to study a system for various sizes and try to do the approximate double-limiting procedure for example for M_{h_0} numerically. But below T_c , magnetization $\pm M$ is metastable for long observation time if the system is sufficiently large and the determination of the average of any thermodynamic variable like M_{h_0} becomes highly nontrivial. This is specially so close to phase transition and at low temperatures. Also, from the knowledge of M_{sp} or any thermodynamic variable alone it is difficult to extract the information about phase transitions. To study a phase transition, we first need to know the transition temperature or critical point and then the nature of the transition or the critical exponents around critical points. So, one needs to do a two-parameter fit and both these parameters (the transition temperature and the critical exponents) depend crucially on the system size. As we will discuss now that instead of the magnetization, the knowledge of the full order parameter distribution $P(M)$ in the case of second order phase transitions and equivalently energy distribution $P(E)$ in first order transitions and the changes in the distributions as the system passes through a transition provide a precise formula to study phase transitions unambiguously. Above T_c , the magnetization of the system will fluctuate around zero with some typical amplitude δM which will depend on the system size (see fig. 4.19a). Below T_c , the magnetization in a finite system will fluctuate in a regime $\pm M \pm \delta M$, while close to T_c , δM becomes comparable to M (see fig. 4.19b). This is the central idea behind the finite size analysis of phase transitions.

To make the above statement more precise, we note that for $T > T_c$ and $L \gg \xi$ (the correlation length), the distribution function of the magnetization M is a Gaussian centered at zero:

$$P_L(M) = \frac{1}{\sqrt{2\pi}\sigma} [e^{-M^2/2\sigma^2}] \quad (4.92)$$

where the standard deviation is given by $\sigma = \sqrt{\frac{k_B T \chi(L)}{L^d}}$. For $T < T_c$ and for $L \gg \xi$, the distribution is peaked near $\pm M_L$ and near these values, the distribution can again be described by Gaussians:

$$P_L(M) = \frac{1}{2\sqrt{2\pi}\sigma} [e^{-(M-M_L)^2/2\sigma^2} + e^{-(M+M_L)^2/2\sigma^2}]. \quad (4.93)$$

Fluctuation dissipation theorem tells us that $k_B T \chi = \lim_{L \rightarrow \infty} L^d (\langle M^2 \rangle - \langle M \rangle^2)$. It is clear that the parameter χ_L which determines the width of each of the Gaussians in eqn. 4.93 will tend to χ as $L \rightarrow \infty$. At finite L ,

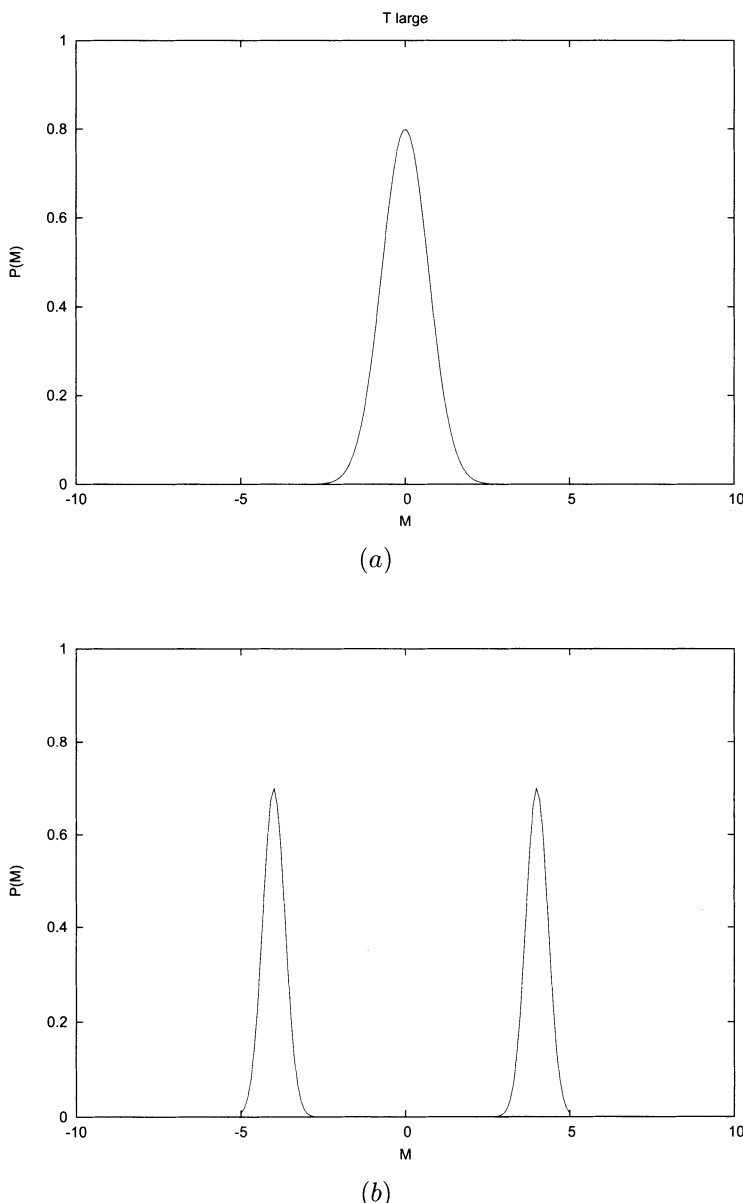


Figure 4.19: (a) Magnetization distribution function $P(M)$ versus M at high temperature $T \gg T_c$. (b) Magnetization distribution function $P(M)$ versus M at temperature $T \ll T_c$.

the Gaussians are not well separated, they always have some overlap and there is a finite probability for the system to go from one phase to the other ($-M_L$ to $+M_L$) and total symmetry breaking does not occur: $P_L(M)$ close to $M = 0$ may be small but still non-zero. However, the time taken for the transition from one phase to the other can be very large for reasonably large system. The system spends a large amount of time close to $\pm M_L$ and does not sample the full distribution for which $\langle M \rangle_L = \int_{-\infty}^{\infty} M P_L(M) dM = 0$. Rather, over the observation time the system experiences only one-half of the distributions for which the restricted average $\langle M \rangle'_L = \int_0^{\infty} M P_L(M) dM / \int_0^{\infty} P_L(M) dM = M_L$. In that case,

$$\lim_{L \rightarrow \infty} M_L = \lim_{L \rightarrow \infty} \langle M \rangle'_L = M_{sp}. \quad (4.94)$$

The susceptibility can be determined as :

$$\lim_{L \rightarrow \infty} \langle M^2 \rangle_L - \frac{L^d}{k_B T} = \lim_{L \rightarrow \infty} P_L^{-2}(0) \frac{L^d}{2\pi k_B T} = \chi, \quad T > T_c, \quad (4.95)$$

being the half-width of the distribution, and,

$$\lim_{L \rightarrow \infty} (\langle M^2 \rangle_L - \langle M \rangle_L^2) \frac{L^d}{k_B T} = \lim_{L \rightarrow \infty} P_L^{-2}(M_L) \frac{L^d}{8\pi k_B T} = \chi, \quad T < T_c. \quad (4.96)$$

So far we have considered the general idea of the order parameter distribution, and how does this distributions may look like at $T > T_c$ and $T < T_c$ and for system size $L \gg \xi$. One can , in principle, use these ideas to extrapolate the results to larger system sizes. But the extrapolation process will not at all be simple. First of all, at finite L , the $P(M)$ will not be perfect Gaussian, and, M_L (the peak position), $\langle M^2 \rangle_L^{1/2}$ and M_{sp} may deviate distinctly from each other for finite L . Also, one should have some idea of the correlation length ξ at different temperatures to ensure that $L \gg \xi$. For that one needs to know the correlation function $\langle s_i s_j \rangle$ and its decay with distance between the spins at i and at j . With finite size scaling theory these problems are handled very effectively. We will now discuss the finite size scaling theory applied to critical points and second order phase transitions and then we will discuss the same for first order phase transitions.

4.12.1 Finite Size Scaling in Second Order Phase Transitions

The power-law variations of various observables like magnetization (M), susceptibility (χ), specific heat (C_v) with $\epsilon = |T - T_c|$ and the power-law variation of correlation length ξ with ϵ suggest that ξ is a length scale which is important in determining the critical behavior of the system. Any function $f(x, y)$ where $x \sim \xi^a$ and $y \sim \xi^b$ can be written in terms of a scaling function of dimensionless variables $x' = x/\xi^a$ and $y' = y/\xi^b$. In fact, the critical behavior of a system in the thermodynamic limit can be extracted from the scaling of the singular part of the free energy $F(T, M)$ as:

$$F(T, M) = F_{\text{regular}}(T, M) + \xi^{-(2-\alpha)/\nu} \tilde{f}(\epsilon \xi^{1/\nu}, M \xi^{\beta/\nu}). \quad (4.97)$$

In a finite system of size L , the correlation length ξ which diverges as $\sim |\Delta T|^{-\nu}$ as the transition is approached is limited by the system size L . In that case L scales with ξ and L/ξ should then be the relevant scale. According to the finite size scaling theory [3, 31]

$$F(T, M, L) = F_{\text{regular}} + L^{-(2-\alpha)/\nu} \tilde{f}(\epsilon L^{1/\nu}, ML^{\beta/\nu}). \quad (4.98)$$

The finite size scaling holds good only when $L \ll \xi$. In the scaling form of free energy above, instead of $L/\xi = \epsilon^\nu L$ we have chosen the scaling variable as $\epsilon L^{1/\nu}$. The choice has the advantage that F is now an analytic function of its variables since for a finite L , F is analytic in T . The scaling function $\tilde{f}(x, y)$ behaves as $\tilde{f}(x, 0) \sim x^{(2-\alpha)}$ for large x and $\tilde{f}(x, c)$ attains a constant value for constant $y = c$ and for $x \ll 1$. This is justified as at $T = T_c$ or $x = 0$, correlation length is infinite and any size L of the system will show the scale invariance and the power-law behavior: $F \sim L^{-(2-\alpha)/\nu}$. Similarly for other variables we have the scaling form:

$$\begin{aligned} M &= L^{-\beta/\nu} \phi(\epsilon L^{1/\nu}) \\ \chi &= L^{\gamma/\nu} \tilde{\chi}(\epsilon L^{1/\nu}) \\ C_v &= L^{\alpha/\nu} \tilde{S}(\epsilon L^{1/\nu}) \end{aligned} \quad (4.99)$$

where ϕ , $\tilde{\chi}$ and \tilde{S} are scaling functions. It should be noted that the scaling ansatz is valid only for large L and close to T_c so that $\epsilon L^{1/\nu}$ has a finite cutoff value $\approx \xi |\Delta T|^\nu$. For very small system sizes or T much away from T_c , correction to the scaling term appears. At $T = T_c$, the scaling functions become constant:

$$\begin{aligned} M &= L^{-\beta/\nu} \\ \chi &= L^{\gamma/\nu} \\ C_v &= L^{\alpha/\nu}. \end{aligned} \quad (4.100)$$

It is to be noted that the scaling functions are also universal like the critical exponents. The finite size scaling relations as in above can be used to extract the values of the ratio of critical exponents. The drawback in this method is that we need to know the critical point T_c quite accurately and T_c depends on L . Since for finite L , $T_c(L)$ corresponds to the correlation length $\xi \simeq L$, we can write $L \sim |T_c(L) - T_c|^{-\nu}$, or,

$$T_c(L) = T_c + aL^{-1/\nu} \quad (4.101)$$

where a is a constant. We have here three unknown parameters: T_c , a and ν . We need lots of data and careful analysis to extract out the value of T_c or that of ν .

A convenient method to determine T_c and ν accurately from finite size system data is to employ Binder's cumulant method [32]:

$$g = 1 - \frac{1}{3}u = 1 - \frac{1}{3} \frac{\langle M^4 \rangle}{\langle M^2 \rangle^2}. \quad (4.102)$$

This is the reduced fourth order cumulant of the order parameter and the above expression holds good for example for Ising model in zero field for which all odd moments disappear by symmetry. The cumulant g checks the Gaussian character of the distribution. For a single Gaussian $u = 3$ and as the system size $L \rightarrow \infty$, $g \rightarrow 0$ for $T > T_c$. On the other hand, for two separated Gaussians as it occurs for $T < T_c$ and L large, $u = 1$ and $g \rightarrow 2/3$ as $T \rightarrow 0$ and $L \rightarrow \infty$. If we now incorporate the scaling form of the order parameter distribution $P(T, M, L) = L^{\beta/\nu} \tilde{P}(\epsilon L^{1/\nu}, ML^{\beta/\nu})$, the prefactor cancels out in the ratio in u and we end up with the scaling form of g as:

$$g(T, L) = \tilde{g}(\epsilon L^{1/\nu}). \quad (4.103)$$

This reduces the complexity of the problem to a remarkable extent. We see that at $T = T_c$, $g(T_c, L) = \tilde{g}(0) = \text{constant}$, the function g does not have any scale dependence. So all the curves $g(T)$ versus T for different system sizes L should intersect at the common point T_c . Here L should not be very small, otherwise corrections to scaling form will appear. But even then the correction terms can be analyzed. Once we know T_c , we can estimate ν using the scaling form of $g(T, L)$. If we plot $g(T, L)$ for different T and L against the scaled temperature $\epsilon L^{1/\nu}$, the data will collapse on a single master curve in the scaling regime near T_c . Once we get T_c and ν other exponents can be determined using the appropriate scaling form.

Problem: Find the transition temperature and the correlation exponent ν for a two-dimensional Ising model on a square lattice using Binder's cumulant analysis.

4.12.2 Finite Size Scaling in First Order Phase Transitions

We first need to figure out how the size of a system can affect a first order phase transition.

Problem: Consider an Ising magnet on a square lattice of sizes $L = 20$ and $L = 100$ at a temperature T much lower than the transition temperatures for these system sizes and under an applied magnetic field $-h_0$, where h_0 is large. Now cross the phase boundary by sweeping the magnetic field from $-h_0$ to h_0 . Find the change in the magnetization M with the field h_0 .

The magnetization curves are shown schematically in the Fig. 4.20. In finite systems, the magnetization changes smoothly from $-M$ to M as given by the continuous solid curve. As the system size increases the jump in the magnetization becomes sharper and in infinite system the magnetization is expected to change discontinuously at $h_0 = 0$ from a value $-M_s$ to M_s [33]. One can analyze the finite size behavior by considering the magnetization distribution by two Gaussians centered at M_s and $-M_s$ in the case of an Ising ferromagnet below T_c . The spreads of the Gaussians are related to the susceptibility χ . In the absence of an applied field the Gaussians are symmetrical and the

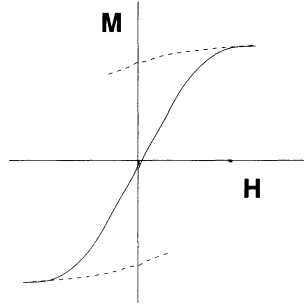


Figure 4.20: Change in the magnetization M with applied field H in a first order phase transition.

probability distribution $P_L(M)$ for the magnetization M is:

$$P_L(M) = \frac{1}{2\sqrt{2\pi}\sigma} [e^{-(M-M_s)^2/2\sigma^2} + e^{-(M+M_s)^2/2\sigma^2}] \quad (4.104)$$

where the standard deviation is given by $\sigma = \sqrt{\frac{k_B T \chi}{L^d}}$. The symmetry in the two Gaussians is broken when a magnetic field h_0 is applied. The magnetization will be shifted to $\pm M_s + \chi h_0$. The relative weights of the two peaks are no longer equal and are proportional to $e^{h_0 M_s L^d / k_B T}$ and $e^{-h_0 M_s L^d / k_B T}$ respectively. In this case the distribution becomes:

$$P_L(M) = A [e^{h_0 M_s L^d / k_B T} e^{-(M-M_s-\chi h_0)^2/2\sigma^2} + e^{-h_0 M_s L^d / k_B T} e^{-(M+M_s-\chi h_0)^2/2\sigma^2}] \quad (4.105)$$

Here $A = \frac{1}{2} \frac{L^{d/2}}{\sqrt{2\pi}\sigma [\cosh(h_0 M_s L^d / k_B T)]}$ is the normalization constant.

The first moment $\langle M \rangle_L$ is obtained as:

$$\langle M \rangle_L = \int M P_L(M) dM = \chi h_0 + M_s \tanh \left[\frac{h_0 M_s L^d}{k_B T} \right]. \quad (4.106)$$

We see that

$$\begin{aligned} \langle M \rangle_L &\approx \chi h_0 + M_s & \text{for } h_0 M_s L^d / k_B T \gg 1 \\ \langle M \rangle_L &\approx \chi h_0 + h_0 M_s^2 L^d / k_B T & \\ &\cong h_0 M_s^2 L^d / k_B T & \text{for } h_0 M_s L^d / k_B T \ll 1. \end{aligned} \quad (4.107)$$

These results corroborate to the rounding of the first order jump in Fig. 4.20. It follows that the width Δh_0 over which the transition is rounded is of the order of

$$\Delta h_0(\text{round}) \approx k_B T / M_s L^d, \quad (4.108)$$

as h_0 has to exceed this value to find the behavior characteristic of the infinite system. The susceptibility of the finite system is :

$$\chi_L = \chi + M_s^2 L^d / \left[k_B T \cosh^2 \left[\frac{h_0 M_s L^d}{k_B T} \right] \right], \quad (4.109)$$

which shows that the δ -function singularity of the susceptibility at $h_0 = 0$ has now a smooth peak of height proportional to L^d . So, if we have χ -values for different h_0 and L , we can get data collapse by rescaling χ by χ/L^d and h_0 by $h_0 L^d/k_B T$ [34].

In many cases the first order transition involves states which are not related by any particular symmetry. An example is the two dimensional q -state Potts model for $q > 4$ in which there is a temperature driven first order transition. At the transition the disordered state has the same energy as the q -fold degenerate ordered state. At high temperature, one can again describe the states by a Gaussian in the distribution of the internal energy per lattice site E of the system:

$$P_L(E) = \frac{A}{\sqrt{C}} \exp \left[-\frac{(E - E_0)^2 L^d}{2k_B T^2 C} \right], \quad (4.110)$$

where C is the infinite lattice specific heat and A is a normalization constant. The distinctive feature of a first-order transition is phase coexistence. So, at the transition $P_L(E)$ should be a superposition of two Gaussians (for two coexisting phases) centered at E_+ and E_- . If $\Delta T = T - T_c$, the Gaussians are centered at $E_+ + C_+ \Delta T$ and $E_- + C_- \Delta T$. The distribution can be written as:

$$P_L(E) = Ae^{\frac{-[E-(E_++C_+\Delta T)]^2}{2k_B T^2 C_+}} + Be^{\frac{-[E-(E_-+C_-\Delta T)]^2}{2k_B T^2 C_-}} \quad (4.111)$$

where A and B are the normalization constants. E_+ , E_- and C_+ , C_- are the internal energies and specific heats of the high and low temperature phases respectively right at the transition point [35]. It should be noted that while the Gaussian approximation is justifiable for simulations of a single phase, the double Gaussian would need correction terms for the regions between the two peaks. The interfaces between domains of the various phases plays an important role and a significant deviation from the Gaussian behavior may occur.

Once $P_L(E)$ is obtained, other quantities of interest such as internal energy or specific heat can be obtained by taking suitable moments of the distribution. Like that in second order transition, one can define here the fourth order cumulant of the energy:

$$V_L = 1 - \frac{1}{3} \frac{\langle E^4 \rangle_L - \langle E^2 \rangle_L^2}{\langle E^2 \rangle_L^2}. \quad (4.112)$$

There is no symmetry breaking transition here. Away from the transition ($T \neq T_c$), $P_L(E)$ is described by a single Gaussian, so that the $\langle E^4 \rangle = U_\pm^4$ and $\langle E^2 \rangle = U_\pm^2$ where $U_\pm = E_\pm + C_\pm \Delta T$. So, $V_L = 2/3$ for $T \neq T_c$. At the transition temperature $T_c(L)$, the double-gaussian approximation leads to

$$V_L = 1 - \frac{2(E_+^4 + E_-^4)}{3(E_+^2 + E_-^2)^2} \quad (4.113)$$

which at $L \rightarrow \infty$ gives a well-defined minima at the transition temperature $T_c(L)$. Both the minima of V_L and the temperature $T_c(L)$ scales with the system size as L^{-d} .

4.13 Critical Slowing Down and Cluster Algorithm

In this and the subsequent chapters we will discuss how to study a system in simulation near a phase transition or critical point where the relaxation time of the system diverges and the system takes enormously long time to equilibrate.

4.13.1 Relaxation Effects

Near a phase transition relaxation time diverges. In Metropolis algorithm the probability of finding a state at some $(n+1)$ th step in the evolution process strongly depends on the state at the n th step. It will then be useless to evaluate any observable X in two successive configurations separated only by a single spin flip. The values we will get for X will not be statistically independent. Ideally, we should measure X after a time gap during which any memory of the previous step is lost from the system. This time gap is typically the relaxation time τ of the system.

One way to decide how often in a run one should evaluate X is to calculate the auto-correlation function of X along the path through configuration space:

$$C(k) = \frac{\langle X_j X_{j+k} \rangle - \langle X_j \rangle^2}{\langle X_j^2 \rangle - \langle X_j \rangle^2}, \quad (4.114)$$

where X_j is the value of X at the j -th step of the simulation and $\langle \dots \rangle$ is the average taken over a particular evolution path of the system through configuration space. $C(0)$ is normalized to be 1 when the value of X is completely correlated and $C(k)$ decays to 0 at large k when the values of X are completely uncorrelated. In collecting the values of X we should evaluate X in the interval of large k -steps only to have the statistical independence of the data [37].

4.13.2 Critical Slowing Down

If one measures the auto-correlation function $C(k)$ of the internal energy or magnetization along a path through configuration space, one will find that as the critical temperature is approached the characteristic time or number of steps τ required for the auto-correlation to disappear increases rapidly. This phenomena is called the *critical slowing down*. It is found that the divergence of the decorrelation time τ at the vicinity of the critical point is coupled with the divergence of the correlation length ξ :

$$\tau \sim \xi^z, \quad (4.115)$$

where z is yet another critical exponent called the ‘dynamical critical exponent’. For the Ising model, $z \approx 2$ for the Metropolis algorithm or in any other Markov equilibration process in which the spins are flipped one at a time. This constitutes what is called the ‘dynamic universality’. In a system of finite but large size L , the relaxation time $\tau \sim L^z$. This has very serious consequences in the simulation study of large systems in the regime close to the critical point. We need different techniques consisting of multispin flipping processes instead of a single spin flip at a time as in Metropolis algorithm. We will study two such algorithms - Swendsen Wang algorithm [38] and Wolff algorithm [40].

4.14 Fortuin-Kasteleyn Mapping

To understand the multispin flip algorithms we need to discuss the Fortuin-Kasteleyn mapping which connects a spin model to the percolation problem. Fortuin and Kasteleyn showed that it is possible to map a ferromagnetic q -state Potts model

$$H = -J \sum_{ij} \delta_{\sigma_i, \sigma_j} \quad (4.116)$$

onto a percolation problem at the limit $q \rightarrow 1$ [13]. Here $\sigma_i = 1, 2, \dots, q$. The observation is very important as in the percolation problem, the states are produced by occupying sites or bonds with a certain probability and there is no notion of critical slowing down. In contrast, in Potts model there is critical slowing down and even for large q when the transition is of first order, the time scales can become very long. Fortuin-Kasteleyn Transformation maps a problem with slow critical relaxation into one where critical slowing down is almost absent.

We would like to see the Fortuin-Kasteleyn mapping in the case of nearest neighbor Ising model defined by the Hamiltonian

$$H = -J \sum_{\langle ij \rangle} (s_i s_j - 1), \quad (4.117)$$

where J is the interaction energy between any two nearest neighbor Ising spins s_i and s_j . If the spins s_i and s_j are aligned in the same direction, the energy over the bond connecting the two spin is 0 and if the two spins are antiparallel the energy is $2J$. The total energy of the system (lattice) ranges from 0 (when all the neighboring spins are parallel) to $2JN_E$, where N_E is the total number of bonds in the lattice. In terms of these energies, one can write the Hamiltonian as $H = 2J(N_E - B)$, where B is the number of *satisfied bonds*. The *satisfied bonds* are those bonds which connect identically aligned spins. The partition function of the system is:

$$Z = \sum e^{-\beta H} = \sum_B e^{-2J\beta(N_E - B)} = \sum_B q^{(N_E - B)} \quad (4.118)$$

where the sum is over all possible combination of B -bonds in the system and $q = e^{-2J\beta}$. Let us define $p = 1 - q = 1 - e^{-2J\beta}$.

Now, out of B satisfied bonds let b bonds are occupied with probability p . Number of ways b bonds can be arranged out of B number of bonds is $\Omega(B, b) = \frac{B!}{b!(B-b)!}$. The probability of occupation of b bonds in total of B number of bonds is $P(B, b) = \Omega(B, b)p^b(1-p)^{B-b}$. It is to be noted that $\sum_{b=0}^B P(B, b) = (p+q)^B = 1$. Canonical partition function then becomes,

$$\begin{aligned} Z &= \sum_B q^{N_E-B}(p+q)^B = \sum_B q^{N_E-B} \sum_{b=0}^B \Omega(B, b)p^b(1-p)^{B-b} \\ &= \sum_B \sum_{b=0}^B \Omega(B, b)p^b q^{N_E-b} \end{aligned} \quad (4.119)$$

where the second summation is over the b -bonds which are present with the probability p over the B bonds and so their number can go from 0 to B at the most. The first sum is over the B bonds which arise as the bonds that connect the likely aligned neighboring spins and so their number and their arrangement over the lattice is dependent on the configuration of the spins. The clusters formed by the B bonds can be thought of as a graph G and we can write the above sum as the sum on all possible varieties of these graphs. it is to be noted that the spins on a cluster formed by the b bonds must all have the same alignment. The partition sum can be written as:

$$Z = \sum_{\{G\}} p^b q^{N_E-b} 2^{N_C(G)} \quad (4.120)$$

where $N_C(G)$ is the number of clusters that constitute the graph G and the summation is on all possible graphs. We see that if we drop $2^{N_c(G)}$ which arise from the two orientations of the Ising spins, the partition sum of the Ising model is equivalent to the sum of the weights of all possible graphs of a bond percolation problem where the bonds are present with a probability $p = 1 - e^{-2\beta J}$. The correspondence between the spin problem and the bond percolation problem is listed below [9]:

Spontaneous magnetization	Percolation probability
Magnetic susceptibility	Average number of bonds per cluster
Energy	Number of bonds
Specific heat	Fluctuation in the number of bonds
Correlation length	Mean linear size of the cluster

4.15 Swendsen-Wang Algorithm

The mapping of the spin problem to a bond percolation problem is utilized in the Swendsen-Wang algorithm whereby the relaxation time is dramatically

reduced. In the mapping above, we note that the orientation of the spins on a cluster formed by the b bonds can be either up or down with equal probability. There is no transition probability associated with the flipping of a spin or a cluster. The Boltzmann weight factor appears in the occupation probability p of the bonds connecting the neighboring identically aligned spins. That is why it is possible to flip all the spin simultaneously in a cluster formed by the b -bonds. This helps the system to reach equilibrium fast and to come out from metastable states. The Swendsen-Wang cluster updating rules are as below;

Algorithm:

1. Start with a random spin configuration.
2. Put bonds between parallel neighboring spins with probability $p = 1 - e^{-2\beta J}$.
3. Apply Hoshen-Kopelman algorithm to identify clusters of connecting bonds.
4. Choose a cluster.
5. Flip the spins of the cluster with probability $\frac{1}{2}$.
6. Choose another cluster and go to (5).
7. When all clusters are considered, one Monte Carlo step is over and go to (2).

In Swendsen-Wang algorithm there is no energetics or energy dependent transition rate as such. The flipping of cluster is a stochastic event. The energetics appear in the occupation probability $p = 1 - e^{-2\beta J}$ of the bonds. The procedure satisfies accessibility criterion, as any bond between two like spins can be present, in principle any state can be reached from any other state in a single step. Consider a pair of configurations C and C' which are transformed into each other in a single Swendsen-Wang step via a particular bond pattern as shown in the Fig. 4.21. One can as well come back from C' to C passing through the same bond pattern and flipping the spins. But in each time we are not occupying all the b bonds. Some bonds remain unoccupied with probability $q = e^{-2\beta J}$. Number of such bonds in the configuration C is $n_1 = 5$ and in C' is $n_2 = 11$ in our example in Fig. 4.21. The number $n_1 - n_2$ is exactly the number of neighboring pairs of spins aligned in C minus the corresponding number in C' . The energy difference between the configurations C and C' is $E_C - E_{C'} = 2J(n_1 - n_2)$. The ratio of the forward and backward transition probabilities through a particular route is, therefore, $e^{-\beta(E_C - E_{C'})}$ just as required by the detailed balance condition. All the possible forward and backward moves can be argued in this way, so that the total transition probabilities also satisfy detailed balance condition. The algorithm, accordingly, is guaranteed to take the system towards equilibrium.

The algorithm reduces the relaxation time drastically. In Ising model on a lattice of size 512×512 , the relaxation time can be 10,000 times smaller

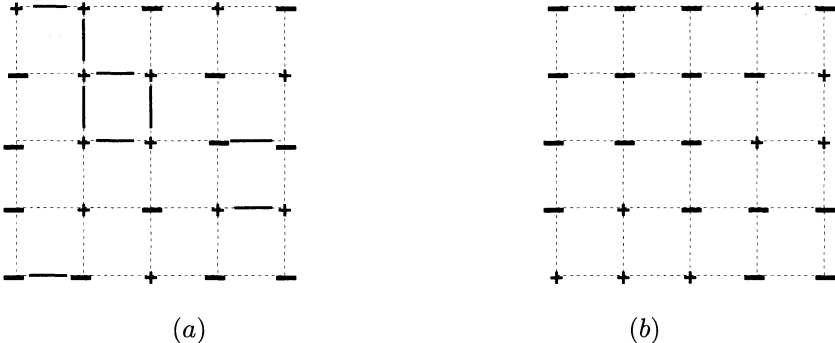


Figure 4.21: Swendsen-Wang algorithm is shown here. (a) Neighboring parallel spins are connected by bonds (thick short lines) with a probability p (step 2 of the algorithm). (b) All the spins in the clusters are flipped and the bonds are removed (steps 5, 6 and 7 of the algorithm).

than that for the single spin flip Metropolis algorithm. Numerical tests show that the relaxation times still satisfy eqn. 4.115 with $z \approx 0$ ($\sim \log$) in two dimension and ~ 0.35 in 3 dimensions instead of 2 that one finds in conventional Metropolis algorithm. The connection between the cluster configurations and the spin configurations raises many issues which has been studied in details [39]. A shortcoming of the Swendsen-Wang method is that significant effort is expended in determining the clusters which include small and big clusters. The small clusters, however, do not contribute to the critical slowing down. So their contribution does not contribute in accelerating the programme. This problem has been taken care of in Wolff algorithm described below.

4.16 Wolff Algorithm

Wolff algorithm generates a single cluster starting from a spin as the source and flips it. The performance of the algorithm generally exceeds that of Swendsen-Wang algorithm. The relaxation time follows eqn. 4.115 with z almost equal to zero (\log dependence).

Algorithm:

1. Start with a random spin configuration.
2. Choose a spin randomly.
3. Put bonds to the nearest neighbor parallel spins with probability $p = 1 - e^{-2\beta J}$.
4. From the new sites repeat the step (3) until no more bonds can be placed.

5. Flip all the spins in the cluster.
6. One Monte Carlo step is over and go to (2).

As in Swendsen-Wang algorithm, the Wolff algorithm also satisfies the accessibility criterion. There is always a non-zero probability that the cluster will contain a single spin and by flipping a sequence of single spins any configurations can be reached. The procedure also satisfies the microreversibility criterion. Consider two spin configurations C and C' in which the spins take the values s_i and s'_i which can be transformed into each other by reversing a single cluster of spins. The change in energy due to the flipping of the spins will come only from the spin interactions along the boundary of the cluster. Here we assume the invariance of the Ising Hamiltonian under the spin reversal. The ratio of the transition probabilities in going from C to C' and vice versa is:

$$\frac{P(C \rightarrow C')}{P(C' \rightarrow C)} = \exp[2\beta J \sum_{i,j} s_i s_j] = \exp[-\beta(E_{C'} - E_C)]. \quad (4.121)$$

In the above expression the spin s_i belong to the cluster C or C' and the neighboring spins S_j do not belong to the cluster. The above expression is exactly the factor required for detailed balance condition. Wolff extended his idea for generalised Heisenberg model where spins can orient in any direction.

The advantage in Wolff algorithm is that in this algorithm only one cluster is grown at a time and one can generate large number of statistically independent clusters to get good statistics in the data. But near the critical point, a connected cluster can be very large and number of operations to find the growth sites in a single step can go up drastically. It takes long time to generate each such critical cluster from seed spins.

References

- [1] E. Atlee Jacson, *Equilibrium statistical Mechanics*, (Dover Publications, Inc., Mineola, New York, 1968).
- [2] R. Y. Rubinsteing and D. P. Kroese, *Simulation and Monte Carlo Method*, (John Wiley & Sons, Inc., Hoboken, New Jersey, 2008).
- [3] D. P. Landau and K. Binder, *A Guide to Monte Carlo simulations in Statistical Physics*, (Cambridge university Press, Cambridge, 2005).
- [4] M. E. J. Newman and G. T. Barkema, *Monte Carlo Methods in Statistical Physics*, (Clarendon Press, Oxford, 2001).
- [5] W. H. Press, S. A. Teukolsky, W. T. Vellerling, B. P. Flannery, *Numerical Recipes*, (Cambridge university Press, Cambridge, 1998).
- [6] S. S. M. Wong, *Computational Methods in Physics and Engineering*, (World Scientific, Singapore, 1997).

- [7] K. Binder and D. W. Heermann, *Monte Carlo Simulation in Statistical Physics*, (Springer, Berlin, 1997).
- [8] D. Frenkel and B. Smit, *Understanding Molecular Simulation*, (Academic Press, San Diego, 2002).
- [9] K. P. N. Murthy, *Monte Carlo Methods in Statistical Physics*, University Press, Hyderabad (2004).
- [10] D. Ben-Avraham and S. Havlin, *Diffusion and Reactions in Fractals and Disordered Systems*, (Cambridge University Press, UK, 2000).
- [11] S. R. White and M. Barma, *J. Phys. A*: **17**, 2995 (1984).
- [12] D. S. McKenzie, *Phys. Rep.* **27**, 35 (1976); A. J. Guttman, in *Phase Transition and Critical Phenomena*, vol.**13**, Edited by C. Domb and J. L. Lebowitz, (Academic Press, London, 1989); K. Barat and B. K. Chakrabarti, *Phys. Rep.* **258**, 377 (1995).
- [13] D. Stauffer and A. Aharony, *Introduction to Percolation Theory*, (Taylor and Francis, London, 2nd edition, 1994).
- [14] A. Bunde and S. Havlin, *Fractals and Disordered Systems*, (Springer-Verlag, Berlin, 1991).
- [15] N. R. Moloney and K. Christensen, *Complexity and Criticality*, (Imperial College Press, 2005).
- [16] B. Bollobás and O. Riordan, *Percolation*, (Cambridge University Press, 2006).
- [17] G. R. Grimmett, *Percolation*, (Springer-Verlag, New York, 1999).
- [18] J. Feder, *Fractals*, (Plenum Press and New York and London, 1998).
- [19] J. F. Gouyet, *Physics and Fractal Structures*, (Springer-Verlag, Berlin, New York, 1996).
- [20] F. Y. Wu, *Rev. Mod. Phys.* **54**, 235 (1982).
- [21] D. Stauffer, *Phys. Rep.* **54**, 1 (1979); M. P. M. den Nijs, *J. Phys. A* **12**, 1857 (1997); B. Nienhuis, *J. Phys. A* **15**, 199 (1982); R. M. Ziff and B. Sapoval, *J. Phys. A* **19**, L1169 (1987).
- [22] R. Zallen, *The Physics of Amorphous Solids*, (Wiley, New York, 1983); M. Sahimi, *Applications of Percolation Theory*, (Taylor and Francis, London, 1994).
- [23] S. P. Obukhov, *Physica A* **101**, 145 (1980); H. Hinrichsen, *Brazilian Journal of Physics* **30**, 69 (2000).
- [24] J. K. Williams and N. D. Mackenzie, *J. Phys. A: Math. Gen.* **17**, 3343 (1984); J. W. Essam, A. J. Guttman and K. DéBell, *J. Phys. A: Math. Gen.* **21**, 3815 (1988); J. W. Essam, K. DéBell, J. Adler and F. M. Bhatti,

- Phys. Rev. B **33**, 1982 (1986); W. Kinzel and J. M. Yeomans, J. Phys. A: Math. Gen. **14**, L163 (1981); K. DéBell and J. W. Essam, J. Phys. A: Math. Gen. **16**, 385 (1983); B. Hede, J. Kertész and T. Vicsek, J. Stat. Phys. **64**, 829 (1991).
- [25] H. Hinrichsen, Adv. Phys. **49**, 815 (2000).
 - [26] P. Ray and I. Bose, J. Phys. A **21**, 555 (1988); S. B. Santra and I. Bose, J. Phys. A **24**, 2367 (1991).
 - [27] S. B. Santra and I. Bose, J. Phys. A **25**, 1105 (1992).
 - [28] S. B. Santra and I. Bose, Z. Phys. B **89**, 247 (1992); S. B. Santra, A. Patterson and S. Roux, Phys. Rev. E **53**, 3867 (1996); S. B. Santra and W. A. Seitz, Int. J. Mod. Phys. C **11**, 1357 (2000).
 - [29] S. B. Santra, Eur. Phys. J. B **33**, 75 (2003); Int. J. Mod. Phys. B **17**, 5555 (2003); S. Sinha and S. B. Santra, Eur. Phys. J. B **39**, 513 (2004).
 - [30] K. Binder (Edt.), *The Monte Carlo Method in Condensed Matter Physics*, (Springer-Verlag, Heidelberg, 1992).
 - [31] V. Privman (Edt.), *Finite Size Scaling and Numerical Simulation of Statistical Systems*, World Scientific, Singapore (1990).
 - [32] K. Binder, Z. Phys. B **43**, 119 (1981).
 - [33] K. Binder, Rep. Prog. Phys. **50**, 783 (1987).
 - [34] K. Binder and D. P. Landau, Phys. Rev. B **30**, 1477 (1984).
 - [35] M. S. S. Challa, D. P. Landau and K. Binder, Phys. Rev. B **34**, 1841 (1986).
 - [36] J. J. Binney et. al., *The Theory of Critical Phenomena*, Oxford University Press, Oxford, (1992).
 - [37] O. Narayan and A. P. Young, Phys. Rev. E **64**, 021104 (2001).
 - [38] R. H. Swendsen and J. S. Wang, Phys. Rev. Lett **58**, 86 (1987).
 - [39] M. De Meo, M. D'Onorio, D. Heermann and K. Binder, J. Stat. Phys. **60**, 585 (1990).
 - [40] U. Wolff, Nucl. Phys. B **300**, 501 (1988).

Chapter 5

Kinetics of Phase Transitions: Numerical Techniques and Simulations

Sanjay Puri

5.1 Introduction

There has been intense research interest in the study of *phase transitions*, which occur when the external parameters of a system [e.g., temperature (T), pressure (P), etc.] are changed. Consider a fluid which can exist in three phases, viz., liquid, solid and gas. In Fig. 5.1, we show the phase diagram of this fluid in the (T, P) -plane. The phase which arises at a particular (T, P) -value is the one with the lowest Gibbs potential $G(T, P)$. This phase diagram is characterized by many significant features, e.g., lines of first-order phase transitions, a second-order critical point, a triple point, etc. We have gained a thorough understanding of the equilibrium aspects of phase transitions through many important works, starting with the contributions of Van der Waals [1].

There is also a fascinating class of problems involving the *kinetics of phase transitions*, i.e., the evolution of a system which is rendered thermodynamically unstable by a change of parameters. In the context of Fig. 5.1, suppose the fluid in the solid phase is rapidly heated to a temperature where the preferred state is the liquid phase. Clearly, the solid will convert to liquid on some time-scale, but what are the dynamical processes whereby the solid converts to liquid. These processes play a crucial role in our daily life. Over the years, our understanding of the kinetics of phase transitions has improved greatly [2, 3, 4, 5, 6]. Numerical simulations of appropriate models have played a crucial role in the growth of our

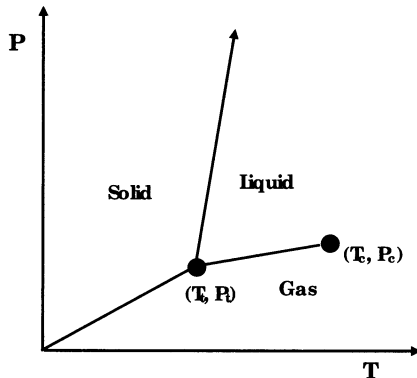


Figure 5.1: Phase diagram of a fluid in the (T, P) -plane. The system can exist in either of three phases – liquid, gas or solid. The solid lines denote lines of first-order phase transitions. At the triple point (T_t, P_t) , all three phases coexist. The point labeled (T_c, P_c) is the critical point of the system.

understanding in this area. This chapter provides an overview of the analytical and numerical techniques used to study the kinetics of phase transitions.

Let us consider two other problems which serve as paradigms for understanding the kinetics of phase transitions. First, consider a ferromagnet whose phase diagram in the (h, T) -plane is shown in Fig. 5.2. Focus on the case with zero magnetic field ($h = 0$). At high temperatures, the magnet is in a disordered or paramagnetic state. If the temperature is suddenly quenched to $T < T_c$, this

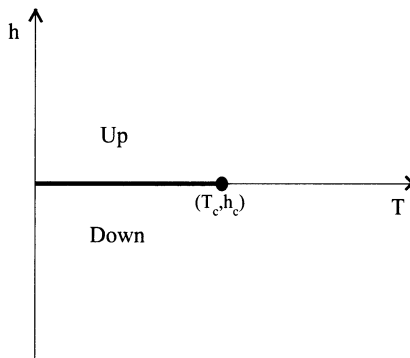


Figure 5.2: Phase diagram of a ferromagnet. The system parameters are the temperature (T) and the magnetic field (h). The point $(T_c, h_c = 0)$ is a second-order critical point. The line $(T < T_c, h = 0)$ corresponds to a line of first-order transitions. At low temperatures ($T < T_c$), the system can be in either of two phases, up or down, depending on the orientation of the magnetic spins.

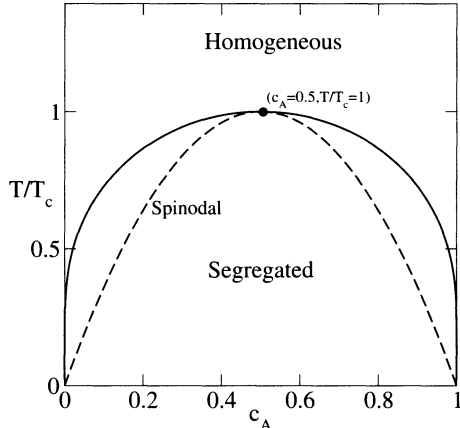


Figure 5.3: Phase diagram of a binary (AB) mixture. The system parameters are the concentration of A ($c_A = 1 - c_B$) and the temperature (T). The point ($c_A = 0.5, T/T_c = 1$) corresponds to a second-order critical point. Above the coexistence curve (solid line), the system is in a homogeneous or disordered state. Below the coexistence curve, the system is in a segregated or phase-separated state, characterized by A-rich and B-rich regions. The dashed lines denote spinodal curves. The homogeneous system is metastable between the coexistence and spinodal curves, and unstable below the spinodal lines.

system now prefers to be in the magnetized state with spins pointing in the “up” or “down” directions. The evolution of the system is characterized by the emergence and growth of domains enriched in either up or down spins. As time $t \rightarrow \infty$, the system approaches a spontaneously magnetized state. Second, consider a binary (AB) mixture whose phase diagram is shown in Fig. 5.3. The system is homogeneous at high temperatures. At time $t = 0$, the mixture is suddenly quenched below the *coexistence curve*. This system now prefers to be in the segregated or phase-separated state, and proceeds to its equilibrium state via the growth of A-rich and B-rich domains. The nonequilibrium dynamics of the magnet or binary mixture is usually referred to as *domain growth* or *coarsening* or *phase ordering kinetics*.

There have been many studies of the kinetics of phase transitions. Problems in this area arise in diverse contexts, ranging from *clustering dynamics in the early universe* to the *growth of nanostructures*. This chapter provides an overview of developments in this area, and is organized as follows. In Sec. 5.2, we introduce the Ising model for two-component mixtures. Then, we study kinetic versions of the Ising model and their coarse-grained counterparts. In Sec. 5.3, we discuss Monte Carlo (MC) techniques to study domain growth problems. In Sec. 5.4, we discuss the numerical solution of coarse-grained (continuum) models for the kinetics of phase transitions. Finally, Sec. 5.5 concludes this chapter with a summary and discussion.

5.2 Kinetic Ising Models and their Coarse-Grained Counterparts

5.2.1 Introduction

The simplest model of an interacting many-body system is the Ising model [7], which was first introduced as a model for phase transitions in magnetic systems. However, with suitable generalizations, it has wide applications to diverse problems in condensed matter physics.

Consider a set of N spins $\{S_i\}$, which are fixed on the sites $\{i\}$ of a lattice. The two-state (spin-1/2) Ising Hamiltonian has the following form:

$$H = -J \sum_{\langle ij \rangle} S_i S_j, \quad S_i = \pm 1, \quad (5.1)$$

where J is the strength of the exchange interaction between spins. We consider the case with nearest-neighbor interactions only, denoted by the subscript $\langle ij \rangle$ in Eq. (5.1).

Although the Hamiltonian in Eq. (5.1) is formulated for a magnetic system, it is clear that a similar description applies for any interacting two-state system, as the two states can be mapped onto $S = +1$ or -1 . A well-known example is the lattice gas or binary (AB) mixture [7]. We can describe this system in terms of occupation-number variables $n_i^\alpha = 1$ or 0 , depending on whether or not a site i is occupied by species α (A or B). Clearly, $n_i^A + n_i^B = 1$ for all sites. A more convenient description is obtained in terms of spin variables $S_i = 2n_i^A - 1 = 1 - 2n_i^B$. We associate an interaction energy $-\epsilon_{\alpha\beta}$ between species α and β , located at neighboring sites i and j , respectively. The corresponding Hamiltonian is

$$\begin{aligned} H &= - \sum_{\langle ij \rangle} [\epsilon_{AA} n_i^A n_j^A + \epsilon_{BB} n_i^B n_j^B + \epsilon_{AB} (n_i^A n_j^B + n_i^B n_j^A)] \\ &= - \left(\frac{\epsilon_{AA} + \epsilon_{BB} - 2\epsilon_{AB}}{4} \right) \sum_{\langle ij \rangle} S_i S_j - \frac{q(\epsilon_{AA} - \epsilon_{BB})}{4} \sum_{i=1}^N S_i \\ &\quad - \frac{Nq}{8} (\epsilon_{AA} + \epsilon_{BB} + 2\epsilon_{AB}). \end{aligned} \quad (5.2)$$

In Eq. (5.2), q denotes the coordination number of a lattice site. The second term on the RHS is constant because $\sum_i S_i = N_A - N_B$, where N_α is the fixed number of α -atoms in the system. Further, the third term on the RHS is also a constant. The Hamiltonian in Eq. (5.2) is analogous to that in Eq. (5.1) if we identify

$$J = \frac{\epsilon_{AA} + \epsilon_{BB} - 2\epsilon_{AB}}{4}. \quad (5.3)$$

The Ising model and its variants are not restricted to two-state systems, and can be easily generalized to the case of multiple-state systems. Thus, three-state systems can be mapped onto a spin-1 Hamiltonian; four-state systems

onto a spin-3/2 Hamiltonian, etc. In general, higher-spin models have a larger number of possible interaction terms (and parameters) in the Hamiltonian.

We next consider the issue of *kinetics of Ising models*. For simplicity, we restrict our discussion to the spin-1/2 model described by Eq. (5.1). The generalization to higher-spin models is straightforward. The Ising spin variables do not have intrinsic dynamics, as is seen by constructing the relevant Poisson bracket. In order to associate kinetics with the Ising model, we assume that it is placed in contact with a heat bath which generates stochastic spin-flips ($S_i \rightarrow -S_i$) in the system [5]. The resultant *kinetic Ising model* is referred to as the spin-flip or Glauber model [8], and is appropriate for describing the nonconserved kinetics of the paramagnetic \rightarrow ferromagnetic transition. The probability of a jump depends on the spin configuration and the heat-bath temperature, in general.

Next, consider the case where the Ising model describes a lattice gas or a binary (AB) mixture. The appropriate microscopic kinetics involves the diffusion of atoms, e.g., atomic jumps to vacant sites in the lattice gas, or A \leftrightarrow B interchanges in the binary mixture. Thus, the heat bath causes spin-exchanges rather than spin-flips, e.g., S_i jumps from $+1 \rightarrow -1$ while a neighbor S_j *simultaneously* jumps from $-1 \rightarrow +1$. This process mimics phonon-induced atomic jumps. The resultant model is referred to as the spin-exchange or Kawasaki model [9, 10].

It should be emphasized that transition probabilities in both the Glauber and Kawasaki models must satisfy the *detailed-balance condition* [11], which will be discussed shortly. Thus, although the two models describe different time-dependent behavior, the equilibrium state is *unique*. As $t \rightarrow \infty$, we recover properties calculable from the *equilibrium* statistical mechanics of the Ising model in an appropriate ensemble.

5.2.2 The Spin-Flip Glauber Model

In the Glauber model, the heat bath induces fluctuations in the system in the form of single-spin-flip processes [8]. The Glauber model describes nonconserved kinetics because the spin-flip processes make the total magnetization $M = \sum_{i=1}^N S_i$ time-dependent. Let us examine the evolution of the probability distribution for the spin configuration $\{S_i\}$ of a system with N spins. In this context, we introduce the conditional probability $P(\{S_i^0\}, 0 | \{S_i\}, t)$, which is the probability that the i^{th} spin is in state S_i ($i = 1 \rightarrow N$) at time t , given that it was in state S_i^0 ($i = 1 \rightarrow N$) at time $t = 0$. The evolution of P is described by the master equation [11]:

$$\begin{aligned} \frac{d}{dt} P(\{S_i\}, t) &= - \sum_{j=1}^N W(S_1, \dots, S_j, \dots, S_N | S_1, \dots, -S_j, \dots, S_N) P(\{S_i\}, t) \\ &\quad + \sum_{j=1}^N W(S_1, \dots, -S_j, \dots, S_N | S_1, \dots, S_j, \dots, S_N) P(\{S'_i\}, t), \end{aligned} \quad (5.4)$$

where we suppress the argument $(\{S_i^0\}, 0)$, for compactness. The first term on the RHS of Eq. (5.4) corresponds to the *loss of probability* for the state $\{S_i\}$ due to the spin-flip $S_j \rightarrow -S_j$. The second term on the RHS denotes the *gain of probability* for the state $\{S_i\}$ due to a spin-flip $S'_j \rightarrow -S'_j$ in a state $\{S'_i\}$ with

$$\begin{aligned} S'_i &= S_i \quad \text{for } i \neq j, \\ S'_j &= -S_j. \end{aligned} \quad (5.5)$$

Equation (5.4) assumes that the underlying stochastic process is Markovian. The essential physical input is provided by the modeling of the *transition matrix* $W(\{S_i\}|\{S'_i\})$ for the change $\{S_i\} \rightarrow \{S'_i\}$. The choice of W must be such that the ensemble approaches the equilibrium distribution $P_{\text{eq}}(\{S_i\})$ as $t \rightarrow \infty$:

$$P_{\text{eq}}(\{S_i\}) = \frac{1}{Z(T, h, N)} \exp [-\beta(H - hM)], \quad (5.6)$$

where $\beta = (k_B T)^{-1}$. Here, Z is the partition function which is defined as

$$Z(T, h, N) = \sum_{\{S_i\}} \exp [-\beta(H - hM)]. \quad (5.7)$$

To ensure this, the transition probability $W(\{S_i\}|\{S'_i\})$ should obey the *detailed-balance condition* [11]:

$$W(\{S_i\}|\{S'_i\})P_{\text{eq}}(\{S_i\}) = W(\{S'_i\}|\{S_i\})P_{\text{eq}}(\{S'_i\}). \quad (5.8)$$

Clearly, in the equilibrium ensemble, this guarantees that the number of systems making the transition from $\{S_i\} \rightarrow \{S'_i\}$ is balanced by the number of systems making the reverse transition $\{S'_i\} \rightarrow \{S_i\}$. Thus, the probability distribution P_{eq} is independent of time, as expected. Further, an arbitrary distribution $P(\{S_i\}, t) \rightarrow P_{\text{eq}}(\{S_i\})$ as $t \rightarrow \infty$ under Eq. (5.4), provided that W obeys the detailed-balance condition. For the proof of this, we refer the reader to the book by Van Kampen [11].

It is evident that there are many choices of W which satisfy the condition in Eq. (5.8). We choose the Suzuki-Kubo form [12]:

$$W(\{S_i\}|\{S'_i\}) = \frac{\lambda}{2} \left\{ 1 - \tanh \left[\frac{\beta \Delta(H - hM)}{2} \right] \right\}, \quad (5.9)$$

where λ^{-1} sets the time-scale of the nonequilibrium process. Here, $\Delta(H - hM)$ denotes the enthalpy difference between the final state $\{S'_i\}$ and the initial state $\{S_i\}$. It is straightforward to confirm that this form of W satisfies the detailed-balance condition.

For the spin-flip Ising model, the states $\{S'_i\}$ and $\{S_i\}$ differ only in one spin, i.e., $S'_j = -S_j$. Then

$$\begin{aligned}(H - hM)_{\text{initial}} &= -JS_j \sum_{L_j} S_{L_j} - hS_j + \text{other terms}, \\ (H - hM)_{\text{final}} &= JS_j \sum_{L_j} S_{L_j} + hS_j + \text{other terms},\end{aligned}\quad (5.10)$$

where L_j denotes the nearest neighbors (nn) of j . Thus

$$\Delta(H - hM) = 2JS_j \sum_{L_j} S_{L_j} + 2hS_j, \quad (5.11)$$

and

$$\begin{aligned}W(\{S_i\}|\{S'_i\}) &= \frac{\lambda}{2} \left[1 - \tanh \left(\beta JS_j \sum_{L_j} S_{L_j} + \beta hS_j \right) \right] \\ &= \frac{\lambda}{2} \left[1 - S_j \tanh \left(\beta J \sum_{L_j} S_{L_j} + \beta h \right) \right].\end{aligned}\quad (5.12)$$

In Eq. (5.12), we can bring S_j outside the argument of the tanh-function because it only takes the values $+1$ or -1 . We replace the form of W from Eq. (5.12) in Eq. (5.4) to obtain the explicit form of the master equation:

$$\begin{aligned}\frac{d}{dt} P(\{S_i\}, t) &= -\frac{\lambda}{2} \sum_{j=1}^N \left[1 - S_j \tanh \left(\beta J \sum_{L_j} S_{L_j} + \beta h \right) \right] P(\{S_i\}, t) \\ &\quad + \frac{\lambda}{2} \sum_{j=1}^N \left[1 + S_j \tanh \left(\beta J \sum_{L_j} S_{L_j} + \beta h \right) \right] P(\{S'_i\}, t).\end{aligned}\quad (5.13)$$

We can use this master equation to obtain the evolution of the magnetization:

$$\langle S_k \rangle = \sum_{\{S_i\}} S_k P(\{S_i\}, t). \quad (5.14)$$

We multiply both sides of Eq. (5.13) by S_k and sum over all configurations to obtain

$$\begin{aligned}\frac{d}{dt} \langle S_k \rangle &= -\frac{\lambda}{2} \sum_{j=1}^N \sum_{\{S_i\}} S_k \left[1 - S_j \tanh \left(\beta J \sum_{L_j} S_{L_j} + \beta h \right) \right] P(\{S_i\}, t) \\ &\quad + \frac{\lambda}{2} \sum_{j=1}^N \sum_{\{S_i\}} S_k \left[1 + S_j \tanh \left(\beta J \sum_{L_j} S_{L_j} + \beta h \right) \right] P(\{S'_i\}, t) \\ &\equiv A + B.\end{aligned}\quad (5.15)$$

In the second term on the RHS of Eq. (5.15), we redefine $S_j = -\overline{S_j}$. Clearly, the sum $\sum_{S_j=\pm 1}$ is equivalent to the sum $\sum_{\overline{S_j}=\pm 1}$. Therefore, the terms in A and B cancel with each other, except for the case $j = k$. This yields the following evolution equation for the magnetization:

$$\begin{aligned}\lambda^{-1} \frac{d}{dt} \langle S_k \rangle &= - \sum_{\{S_i\}} S_k \left[1 - S_k \tanh \left(\beta J \sum_{L_k} S_{L_k} + \beta h \right) \right] P(\{S_i\}, t) \\ &= -\langle S_k \rangle + \left\langle \tanh \left(\beta J \sum_{L_k} S_{L_k} + \beta h \right) \right\rangle,\end{aligned}\quad (5.16)$$

where we have used $S_k^2 = 1$.

Mean-Field Approximation

Unfortunately, the exact time-dependent equation (5.16) is analytically intractable in $d \geq 2$. (For the $d = 1$ solution, see the work of Glauber [8].) The main obstacle is that the second term on the RHS of Eq. (5.16) yields a set of higher-order correlation functions, as can be seen by expanding the tanh-function. These dynamical equations can be rendered tractable by invoking the MF approximation, which truncates the hierarchy by neglecting correlations between different sites, i.e., the average of the product of spin operators is replaced by the product of their averages. The result of such a random-phase decoupling is that the angular brackets denoting the statistical average can be taken inside the argument of the tanh-function [13, 14]. Thus, we obtain

$$\lambda^{-1} \frac{d}{dt} \langle S_k \rangle = -\langle S_k \rangle + \tanh \left(\beta J \sum_{L_k} \langle S_{L_k} \rangle + \beta h \right). \quad (5.17)$$

For time-independent effects in equilibrium, the LHS of Eq. (5.17) is identically zero. Thus, we have (as $t \rightarrow \infty$)

$$\langle S_k \rangle^{\text{eq}} = \tanh \left(\beta J \sum_{L_k} \langle S_{L_k} \rangle^{\text{eq}} + \beta h \right). \quad (5.18)$$

Notice that Eq. (5.17) is nonlinear because of the presence of the tanh-function, and is only tractable numerically. These equations are often referred to as *mean-field dynamical models* in the literature [15, 16, 17, 18]. A further simplification can be effected by expanding the tanh-function and retaining only leading terms. For simplicity, we consider the case of zero magnetic field, i.e., $h = 0$. We can then expand various terms on the RHS of Eq. (5.17) as follows:

$$\sum_{L_k} \langle S_{L_k} \rangle \simeq q\psi(\vec{r}_k, t) + a^2 \nabla_k^2 \psi(\vec{r}_k, t) + \text{higher-order terms}, \quad (5.19)$$

where a is the lattice spacing. Further,

$$\begin{aligned} \tanh \left(\beta J \sum_{L_k} \langle S_{L_k} \rangle \right) &\simeq \beta J \sum_{L_k} \langle S_{L_k} \rangle - \frac{1}{3} \left(\beta J \sum_{L_k} \langle S_{L_k} \rangle \right)^3 \\ &\quad + \text{higher-order terms} \\ &\simeq \frac{T_c}{T} \psi(\vec{r}_k, t) - \frac{1}{3} \left(\frac{T_c}{T} \right)^3 \psi(\vec{r}_k, t)^3 + \frac{T_c}{qT} a^2 \nabla_k^2 \psi(\vec{r}_k, t) \\ &\quad + \text{other terms,} \end{aligned} \quad (5.20)$$

where we have used Eq. (5.19) to obtain the second expression. Therefore, the order-parameter equation for the Glauber-Ising model simplifies as

$$\lambda^{-1} \frac{\partial}{\partial t} \psi(\vec{r}, t) = \left(\frac{T_c}{T} - 1 \right) \psi - \frac{1}{3} \left(\frac{T_c}{T} \right)^3 \psi^3 + \frac{T_c}{qT} a^2 \nabla^2 \psi + \text{other terms,} \quad (5.21)$$

where we have dropped the subscript k for the position variable.

At this stage a few remarks are in order. Firstly, Eq. (5.21) is referred to as the *time-dependent Ginzburg-Landau* (TDGL) equation. We will discuss the general formulation of the TDGL equation in the next subsection. Secondly, the approximation of neglecting the higher-order terms in Eq. (5.21) is justifiable only for $T \simeq T_c$, where the order parameter is small. However, it is generally believed that the TDGL equation is valid even for deep quenches ($T \ll T_c$), at least in terms of containing the correct physics.

5.2.3 Phase Ordering Dynamics: Nonconserved Kinetics

In Fig. 5.2, we had shown the phase diagram for a ferromagnet. The corresponding ordering problem considers a paramagnetic system at $T > T_c, h = 0$ for time $t < 0$. At $t = 0$, the system is rapidly quenched to $T < T_c$, where the preferred equilibrium state is spontaneously magnetized. The *far-from-equilibrium* disordered system evolves towards its new equilibrium state by separating into domains which are rich in either up or down spins (see Fig. 5.4). These domains coarsen with time and are characterized by a growing length scale $L(t)$. A finite system becomes ordered in either of the two equivalent states (up or down) as $t \rightarrow \infty$.

At the microscopic level, this evolution can be described by an Ising model with Glauber spin-flip kinetics, as discussed in Sec. 5.2.2. At the coarse-grained level, the appropriate order parameter to describe the system is the local magnetization $\psi(\vec{r}, t)$. In Sec. 5.2.2, we used the Glauber-Ising model to derive the TDGL equation (5.21) which governs the evolution of the order parameter. More generally, the TDGL equation models the dissipative (over-damped) relaxation of a ferromagnetic system to its free-energy minimum:

$$\frac{\partial}{\partial t} \psi(\vec{r}, t) = -\Gamma \frac{\delta G[\psi]}{\delta \psi} + \theta(\vec{r}, t). \quad (5.22)$$

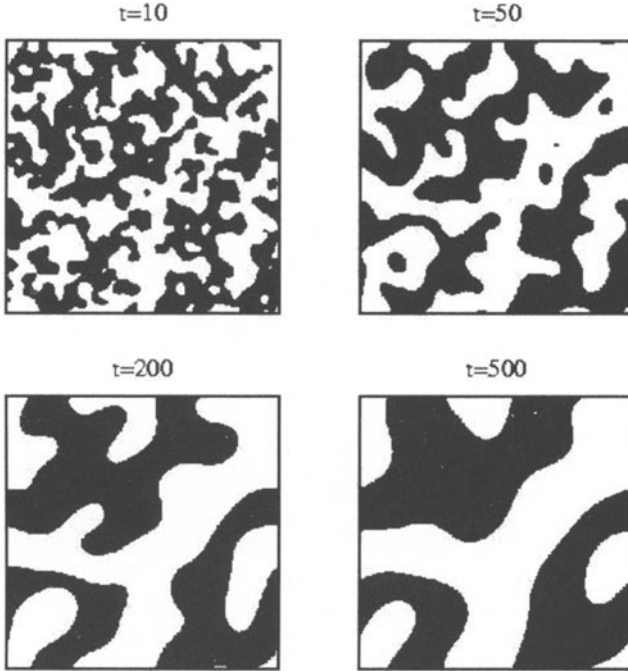


Figure 5.4: Evolution of a disordered ferromagnet, which is quenched to $T < T_c$ at time $t = 0$. These pictures were obtained from an Euler-discretized version of the dimensionless TDGL equation (5.29) with $h = 0$ and no thermal fluctuations ($\epsilon = 0$). The discretization mesh sizes were $\Delta t = 0.1$ and $\Delta x = 1$ in time and space, respectively. The initial condition $\psi(\vec{r}, 0)$ consisted of small-amplitude fluctuations about $\psi = 0$. The lattice size was 256^2 , and periodic boundary conditions were applied in both directions. Regions with up spins ($\psi > 0$) and down spins ($\psi < 0$) are marked black and white, respectively.

In Eq. (5.22), Γ denotes the inverse damping coefficient; and $\delta G/\delta\psi$ is the functional derivative of the free-energy functional:

$$G[\psi] = \int d\vec{r} \left[g(\psi) + \frac{1}{2} K(\vec{\nabla}\psi)^2 \right]. \quad (5.23)$$

The first term on the RHS of Eq. (5.23) is the local free energy. The second term accounts for surface tension due to inhomogeneities in the order parameter. The parameter K (> 0) measures the strength of the surface tension.

The noise term in Eq. (5.22) is also space- and time-dependent, and satisfies the fluctuation-dissipation relation:

$$\begin{aligned} \overline{\theta(\vec{r}, t)} &= 0, \\ \overline{\theta(\vec{r}', t')\theta(\vec{r}'', t'')} &= 2\Gamma k_B T \delta(\vec{r}' - \vec{r}'') \delta(t' - t''), \end{aligned} \quad (5.24)$$

where the bars denote an average over the Gaussian noise ensemble. The presence of the noise term ensures that the system equilibrates to the correct Boltzmann distribution at temperature T . Equations (5.22)-(5.24) are also referred to as *Model A* of order-parameter kinetics, as discussed by Hohenberg and Halperin [19] in the context of critical dynamics.

Recall the TDGL equation (5.21) which was derived in Sec. 5.2.2. We identify it as the deterministic version of Eq. (5.22) with the damping coefficient $\Gamma = \beta\lambda$, where λ is the inverse time-scale of Glauber spin-flips. The form of the free-energy functional which gives rise to Eq. (5.21) is

$$\beta G[\psi] = \int d\vec{r} \left[-\frac{1}{2} \left(\frac{T_c}{T} - 1 \right) \psi^2 + \frac{1}{12} \left(\frac{T_c}{T} \right)^3 \psi^4 + \frac{T_c}{2qT} a^2 (\vec{\nabla}\psi)^2 \right]. \quad (5.25)$$

For our subsequent discussion, we use the general form of the ψ^4 -free energy:

$$G[\psi] = \int d\vec{r} \left[-\frac{a(T_c - T)}{2} \psi^2 + \frac{b}{4} \psi^4 - h\psi + \frac{K}{2} (\vec{\nabla}\psi)^2 \right], \quad (5.26)$$

where we have introduced the parameters $a, b > 0$ and a term proportional to the magnetic field; and neglected terms of $O(\psi^6)$ and higher. The parameters a, b can be identified by a comparison with the explicit form of the free energy in (say) Eq. (5.25). However, it is more appropriate to think of them as phenomenological parameters, without any reference to an underlying microscopic model.

For the ψ^4 -free energy in Eq. (5.26), the TDGL equation (5.22) has the form:

$$\frac{\partial}{\partial t} \psi(\vec{r}, t) = \Gamma [a(T_c - T)\psi - b\psi^3 + h + K\nabla^2\psi] + \theta(\vec{r}, t). \quad (5.27)$$

The parameters in Eq. (5.27) can be absorbed into the definitions of space and time by introducing the rescaled variables (for $T < T_c$)

$$\begin{aligned} \psi' &= \frac{\psi}{\psi_0}, & \psi_0 &= \sqrt{\frac{a(T_c - T)}{b}}, \\ t' &= a(T_c - T)\Gamma t, \\ \vec{r}' &= \sqrt{\frac{a(T_c - T)}{K}} \vec{r}, & \xi_b &= \sqrt{\frac{2K}{a(T_c - T)}}, \\ h' &= \frac{h}{a(T_c - T)\psi_0}, \\ \theta' &= \frac{\theta}{a(T_c - T)\Gamma\psi_0}. \end{aligned} \quad (5.28)$$

Dropping primes, we obtain the dimensionless TDGL equation:

$$\frac{\partial}{\partial t} \psi(\vec{r}, t) = \psi - \psi^3 + h + \nabla^2\psi + \theta(\vec{r}, t), \quad (5.29)$$

where

$$\begin{aligned}\overline{\theta(\vec{r}, t)} &= 0, \\ \overline{\theta(\vec{r}', t')\theta(\vec{r}'', t'')} &= 2\epsilon\delta(\vec{r}' - \vec{r}'')\delta(t' - t''), \\ \epsilon &= \frac{k_B T b [a(T_c - T)]^{(d-4)/2}}{K^{d/2}}.\end{aligned}\quad (5.30)$$

We will focus on the case with $h = 0$ (shown in Fig. 5.4), where the system evolves into two competing states. (In Sec. 5.4.2, we will discuss the numerical solution of the TDGL equation.) There is a *domain boundary* or *interface* which separates regions enriched in the two states. Our understanding of domain growth problems is based on the dynamics of these interfaces, which is governed by the Allen-Cahn equation of motion [20]. For this, we compute various terms in Eq. (5.29) in terms of the interfacial coordinates (n, \vec{a}) . We have

$$\vec{\nabla}\psi = \frac{\partial\psi}{\partial n} \Big|_t \hat{n}, \quad (5.31)$$

where \hat{n} is the unit vector normal to the interface in the direction of increasing ψ . Further

$$\nabla^2\psi = \frac{\partial^2\psi}{\partial n^2} \Big|_t \hat{n} \cdot \hat{n} + \frac{\partial\psi}{\partial n} \Big|_t \vec{\nabla} \cdot \hat{n}. \quad (5.32)$$

Finally, we use the identity

$$\frac{\partial\psi}{\partial t} \Big|_n \frac{\partial t}{\partial n} \Big|_\psi \frac{\partial n}{\partial\psi} \Big|_t = -1 \quad (5.33)$$

to obtain (from the TDGL equation)

$$\begin{aligned}-\frac{\partial\psi}{\partial n} \Big|_t \frac{\partial n}{\partial t} \Big|_\psi &= \psi - \psi^3 + \frac{\partial^2\psi}{\partial n^2} \Big|_t + \frac{\partial\psi}{\partial n} \Big|_t \vec{\nabla} \cdot \hat{n} \\ &\simeq \frac{\partial\psi}{\partial n} \Big|_t \vec{\nabla} \cdot \hat{n}.\end{aligned}\quad (5.34)$$

In the above simplification, we have used the fact that the interfaces are locally equilibrated to a static kink profile. We recognize that $\partial n/\partial t|_\psi = v(\vec{a})$, the normal interfacial velocity in the \hat{n} -direction. This yields the Allen-Cahn equation:

$$v(\vec{a}) = -\vec{\nabla} \cdot \hat{n} = -K(\vec{a}), \quad (5.35)$$

where K denotes the local curvature of the interface.

It is useful to examine the evolution of a droplet of (say) $\psi = -1$ immersed in a matrix of $\psi = +1$. We consider the 3-d case of a spherical droplet with radius R . The normal unit vector at a point (x, y, z) on the surface of the sphere is

$$\hat{n} = \frac{x}{R}\hat{i} + \frac{y}{R}\hat{j} + \frac{z}{R}\hat{k}, \quad (5.36)$$

so that

$$\begin{aligned} \vec{\nabla} \cdot \hat{n} &= \frac{1}{R} - \frac{x^2}{R^3} + \frac{1}{R} - \frac{y^2}{R^3} + \frac{1}{R} - \frac{z^2}{R^3} \\ &= \frac{2}{R}. \end{aligned} \quad (5.37)$$

Further, $v(\vec{a}) = dR/dt$, and Eq. (5.35) becomes

$$\frac{dR}{dt} = -\frac{2}{R}, \quad (5.38)$$

with the solution

$$R(0)^2 - R(t)^2 = 4t. \quad (5.39)$$

Thus, the droplet collapses on a time-scale $t_c \sim R(0)^2$. In arbitrary dimensions d , the corresponding form of Eq. (5.38) is

$$\frac{dR}{dt} = -\frac{(d-1)}{R}. \quad (5.40)$$

More generally, we can use Eq. (5.35) to obtain the growth law for the domains in Fig. 5.4. For a domain of characteristic size L , we have $v \sim dL/dt$ and curvature $K \sim 1/L$. This yields the diffusive growth law $L(t) \sim t^{1/2}$, which is valid for nonconserved scalar fields in $d > 1$. The case with $d = 1$ does not obey these general arguments and we discuss it separately here. For domain scales $L(t) \gg \xi_b$, there is only an exponentially-decaying interaction of order e^{-L/ξ_b} between domain walls. This results in a logarithmic growth law $L(t) \sim \xi_b \ln t$ [21].

Before proceeding, it is important to consider the role of thermal fluctuations in the dynamics shown in Fig. 5.4. It turns out that thermal noise is asymptotically irrelevant for ordering in systems which are free of disorder. This is because fluctuations only affect the interfacial profile. However, the fixed length scale of the interface becomes irrelevant in comparison to the diverging domain scale [22]. An equivalent argument is due to Bray [23], who used a renormalization-group (RG) approach to demonstrate that domain growth is driven by a fixed point at $T = 0$.

Correlation Function and Structure Factor

Now, if the system is characterized by a single length scale, the morphology of the domains does not change with time, apart from a scale factor. Therefore, the *order-parameter correlation function* exhibits a dynamical-scaling property [24]:

$$\begin{aligned} C(\vec{r}, t) &\equiv \frac{1}{V} \int d\vec{R} \left[\langle \psi(\vec{R}, t) \psi(\vec{R} + \vec{r}, t) \rangle - \langle \psi(\vec{R}, t) \rangle \langle \psi(\vec{R} + \vec{r}, t) \rangle \right] \\ &= g\left(\frac{r}{L}\right), \end{aligned} \quad (5.41)$$

where V is the system volume, and the angular brackets denote an averaging over independent initial conditions and thermal fluctuations. This equal-time correlation function is a nonequilibrium quantity as domain growth is a nonequilibrium process. In Eq. (5.41), $g(x)$ is a time-independent scaling function.

Actually, most experiments (e.g., neutron or light scattering) probe the time-dependent *structure factor*, which is the Fourier transform of the real-space correlation function

$$S(\vec{k}, t) = \int d\vec{r} e^{i\vec{k} \cdot \vec{r}} C(\vec{r}, t), \quad (5.42)$$

where \vec{k} is the wave-vector of the scattered beam. The corresponding dynamical-scaling form for $S(\vec{k}, t)$ is

$$S(\vec{k}, t) = L^d f(kL), \quad (5.43)$$

where the scaling function $f(p)$ is obtained as

$$f(p) = \int d\vec{x} e^{i\vec{p} \cdot \vec{x}} g(x). \quad (5.44)$$

The scaling functions $g(x)$ and $f(p)$ characterize the morphology of the ordering system. In experiments or simulations of domain growth, one usually attempts to obtain the functional forms of $g(x)$ and $f(p)$. In Fig. 5.5, we show the scaled correlation functions [$C(r, t)$ vs. r/L] and the scaled structure factors [$L^{-d} S(k, t)$ vs. kL] for the ordering ferromagnet. The presence of interfacial defects results in a Porod tail for the scaled structure factor, $f(p) \sim p^{-(d+1)}$ as $p \rightarrow \infty$; and a singular short-distance behavior of the correlation function [6]. In Fig. 5.6, we show the time-dependence of the domain length scale.

5.2.4 The Spin-Exchange Kawasaki Model

We mentioned earlier that the Glauber model, which assumes single-spin-flip processes, is appropriate for nonconserved kinetics. The Glauber model is not applicable when the Ising model describes either phase separation ($J > 0$) or order-disorder ($J < 0$) transitions in an AB mixture [7]. For a binary mixture, the Ising spin variable models the presence of an A- or B-atom on a lattice site. Thus, the appropriate microscopic dynamics should involve random exchanges

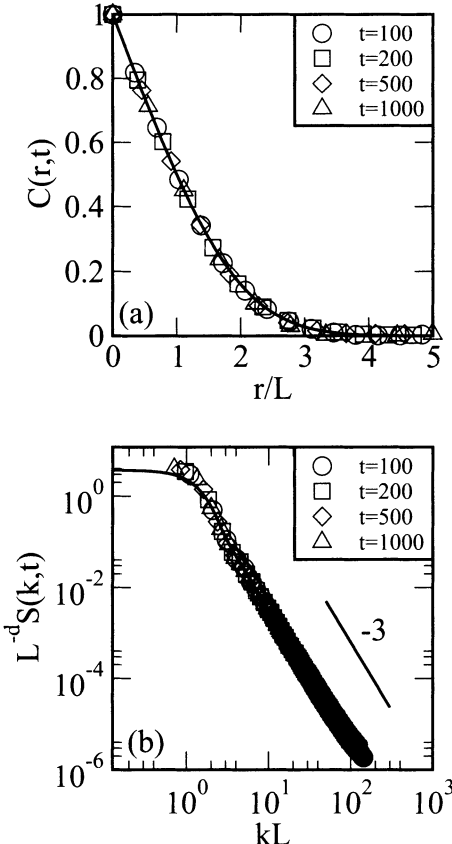


Figure 5.5: (a) Scaled correlation function [$C(r,t)$ vs. r/L] for the evolution depicted in Fig. 5.4. The numerical data is obtained as an average over 5 independent runs for systems of size 1024^2 . The length scale $L(t)$ is defined as the distance over which the correlation function falls to half its maximum value. We show data for times 100, 200, 500, 1000 – denoted by the specified symbols. The solid line denotes the Ohta-Jasnow-Kawasaki (OJK) function [53], scaled in the same manner as the numerical data. (b) Scaled structure factor [$L^{-d}S(k,t)$ vs. kL], corresponding to the data in (a). In this case, we plot the data on a log-log scale. The solid line denotes the Fourier transform of the OJK function. The line with slope -3 corresponds to the Porod tail.

of A- and B-atoms at neighboring sites, with their individual numbers being fixed. In practice, these jumps are actually mediated by vacancies [25, 26, 27] and the system should be described as a ternary (ABV) mixture [17, 18, 28]. However, when the vacancy concentration is small, it is reasonable to ignore vacancies and assume that the underlying stochastic process is a spin-exchange. As stated earlier, this corresponds to the Kawasaki model, which is based on

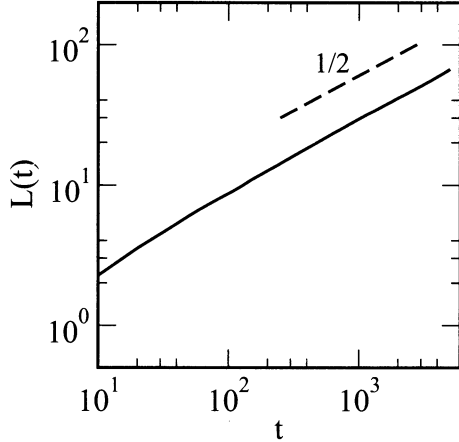


Figure 5.6: Domain growth law for the evolution depicted in Fig. 5.4. The numerical details are the same as in Fig. 5.5. We plot the data on a log-log scale. The dashed line denotes the Allen-Cahn growth law, $L(t) \sim t^{1/2}$.

a stationary Markov process involving a spin-exchange mechanism [9, 10]. The resultant master equation is as follows:

$$\begin{aligned} \frac{d}{dt} P(\{S_i\}, t) = & - \sum_{j=1}^N \sum_{k \in L_j} W(S_1, \dots, S_j, S_k, \dots, S_N | S_1, \dots, S_k, S_j, \dots, S_N) P(\{S_i\}, t) \\ & + \sum_{j=1}^N \sum_{k \in L_j} W(S_1, \dots, S_k, S_j, \dots, S_N | S_1, \dots, S_j, S_k, \dots, S_N) P(\{S'_i\}, t). \end{aligned} \quad (5.45)$$

The first term on the RHS is the loss of probability for the state $\{S_i\}$ due to the spin-exchange $S_j \leftrightarrow S_k$. We consider only nearest-neighbor exchanges, where site $k \in L_j$, i.e., the nearest-neighbors of j . The second term on the RHS corresponds to the gain of probability for the state $\{S_i\}$ due to an exchange $S'_j \leftrightarrow S'_k$ in a state $\{S'_i\}$. The state $\{S'_i\}$ differs from the state $\{S_i\}$ in only two spins:

$$\begin{aligned} S'_i &= S_i \quad \text{for } i \neq j, k, \\ S'_j &= S_k, \\ S'_k &= S_j. \end{aligned} \quad (5.46)$$

As in the Glauber case, the transition probability $W(\{S_i\} | \{S'_i\})$ must obey the detailed-balance condition. The binary mixture is described by an ensemble with fixed (T, M, N) , where the “magnetization” $M = \sum_{i=1}^N S_i = N_A - N_B$. The

corresponding equilibrium distribution is

$$P_{\text{eq}}(\{S_i\}) = \frac{1}{Z(T, M, N)} \exp(-\beta H) \delta_{\sum_i S_i, M}, \quad (5.47)$$

where the Kronecker delta confines the distribution to configurations with $\sum_{i=1}^N S_i = M$. The appropriate partition function is

$$Z(T, M, N) = \sum_{\{S_i\}} \exp(-\beta H) \delta_{\sum_i S_i, M}. \quad (5.48)$$

Again, we choose the Suzuki-Kubo form for the transition probability in Eq. (5.45):

$$W(\{S_i\} | \{S'_i\}) = \frac{\lambda}{2} \left[1 - \tanh\left(\frac{\beta \Delta H}{2}\right) \right], \quad (5.49)$$

where ΔH is the change in energy due to the spin-exchange $S_j \leftrightarrow S_k$. For the Ising model,

$$\begin{aligned} H_{\text{initial}} &= -JS_j \sum_{L_j \neq k} S_{L_j} - JS_k \sum_{L_k \neq j} S_{L_k} - JS_j S_k + \text{other terms}, \\ H_{\text{final}} &= -JS_k \sum_{L_j \neq k} S_{L_j} - JS_j \sum_{L_k \neq j} S_{L_k} - JS_j S_k + \text{other terms}. \end{aligned} \quad (5.50)$$

Thus, the change in energy resulting from the spin exchange is

$$\Delta H = J(S_j - S_k) \sum_{L_j \neq k} S_{L_j} - J(S_j - S_k) \sum_{L_k \neq j} S_{L_k}, \quad (5.51)$$

and

$$\begin{aligned} W(\{S_i\} | \{S'_i\}) &= \frac{\lambda}{2} \left\{ 1 - \tanh \left[\frac{\beta J}{2} (S_j - S_k) \sum_{L_j \neq k} S_{L_j} - \frac{\beta J}{2} (S_j - S_k) \sum_{L_k \neq j} S_{L_k} \right] \right\} \\ &= \frac{\lambda}{2} \left\{ 1 - \frac{(S_j - S_k)}{2} \tanh \left[\beta J \left(\sum_{L_j \neq k} S_{L_j} - \sum_{L_k \neq j} S_{L_k} \right) \right] \right\}. \end{aligned} \quad (5.52)$$

In Eq. (5.52), we have used the fact that $(S_j - S_k)/2 = 0, \pm 1$ to factor it out of the argument of the tanh function. Therefore, the master equation has the

form

$$\begin{aligned} \frac{d}{dt} P(\{S_i\}, t) = & -\frac{\lambda}{2} \sum_{j=1}^N \sum_{k \in L_j} \left\{ 1 - \frac{(S_j - S_k)}{2} \tanh \left[\beta J \left(\sum_{L_j \neq k} S_{L_j} - \sum_{L_k \neq j} S_{L_k} \right) \right] \right\} P(\{S_i\}, t) \\ & + \frac{\lambda}{2} \sum_{j=1}^N \sum_{k \in L_j} \left\{ 1 + \frac{(S_j - S_k)}{2} \tanh \left[\beta J \left(\sum_{L_j \neq k} S_{L_j} - \sum_{L_k \neq j} S_{L_k} \right) \right] \right\} P(\{S'_i\}, t). \end{aligned} \quad (5.53)$$

We can obtain an evolution equation for the order parameter by multiplying both sides of Eq. (5.53) with S_n and summing over all configurations:

$$\begin{aligned} \frac{d}{dt} \langle S_n \rangle = & -\frac{\lambda}{2} \sum_{\{S_i\}} \sum_{j=1}^N \sum_{k \in L_j} S_n \left\{ 1 - \frac{(S_j - S_k)}{2} \tanh \left[\beta J \left(\sum_{L_j \neq k} S_{L_j} - \sum_{L_k \neq j} S_{L_k} \right) \right] \right\} P(\{S_i\}, t) \\ & + \frac{\lambda}{2} \sum_{\{S_i\}} \sum_{j=1}^N \sum_{k \in L_j} S_n \left\{ 1 + \frac{(S_j - S_k)}{2} \tanh \left[\beta J \left(\sum_{L_j \neq k} S_{L_j} - \sum_{L_k \neq j} S_{L_k} \right) \right] \right\} P(\{S'_i\}, t). \end{aligned} \quad (5.54)$$

In the second term on the RHS of Eq. (5.54), we redesignate $S_j = \bar{S}_k$ and $S_k = \bar{S}_j$. This leads to a large-scale cancellation between the first and second terms. The only remaining terms are

$$\begin{aligned} \frac{d}{dt} \langle S_n \rangle = & -\frac{\lambda}{2} \sum_{\{S_i\}} \sum_{k \in L_n} S_n \left\{ 1 - \frac{(S_n - S_k)}{2} \tanh \left[\beta J \left(\sum_{L_n \neq k} S_{L_n} - \sum_{L_k \neq n} S_{L_k} \right) \right] \right\} P(\{S_i\}, t) \\ & + \frac{\lambda}{2} \sum_{\{S_i\}} \sum_{k \in L_n} S_k \left\{ 1 + \frac{(S_k - S_n)}{2} \tanh \left[\beta J \left(\sum_{L_n \neq k} S_{L_n} - \sum_{L_k \neq n} S_{L_k} \right) \right] \right\} P(\{S_i\}, t) \\ = & -\frac{\lambda}{2} \left\langle \sum_{k \in L_n} (S_n - S_k) \left\{ 1 - \frac{(S_n - S_k)}{2} \tanh \left[\beta J \left(\sum_{L_n \neq k} S_{L_n} - \sum_{L_k \neq n} S_{L_k} \right) \right] \right\} \right\rangle. \end{aligned} \quad (5.55)$$

Some algebra yields the exact evolution equation

$$\begin{aligned} 2\lambda^{-1} \frac{d}{dt} \langle S_n \rangle = & -q \langle S_n \rangle + \sum_{L_n} \langle S_{L_n} \rangle \\ & + \sum_{k \in L_n} \left\langle (1 - S_n S_k) \tanh \left[\beta J \left(\sum_{L_n \neq k} S_{L_n} - \sum_{L_k \neq n} S_{L_k} \right) \right] \right\rangle. \end{aligned} \quad (5.56)$$

This equation is analogous to Eq. (5.16), obtained in the context of Glauber kinetics.

Although the Kawasaki model is usually associated with conserved kinetics, we should make a clarifying remark. In the context of binary mixtures, a *ferromagnetic* interaction ($J > 0$) results in phase separation, i.e., the equilibrium system consists of domains of A-rich and B-rich phases. The appropriate order parameter is the difference in densities of A and B, and is locally conserved by Kawasaki kinetics. The length scale over which the order parameter is conserved increases if we allow *long-ranged* exchanges rather than only *nearest-neighbor* exchanges. In the limit where the spin exchanges are *infinite-ranged*, the Kawasaki model has *global conservation* rather than *local conservation*. In this case, the Kawasaki model is essentially equivalent to the Glauber model [29, 30].

It is also of great interest to consider the binary mixture with *antiferromagnetic* interactions, $J < 0$. In this case, there is a phase transition from a high-temperature disordered phase to a low-temperature ordered phase, where the A- and B-atoms order on alternate sub-lattices. The appropriate order parameter is now the *staggered magnetization*, which is the difference between the two sub-lattice *magnetizations*. This quantity is not conserved by Kawasaki kinetics, though the overall concentration is conserved. For the AB alloy with equal fractions of A and B, the antiferromagnetic case with Kawasaki kinetics is equivalent to the ferromagnetic Ising model with Glauber kinetics [31]. For asymmetric compositions, novel features arise due to the conserved concentration variable.

Mean-Field Approximation

As in the Glauber case, Eq. (5.56) is the first of a hierarchy of equations involving higher-order correlations of the spin variable. This hierarchy can be truncated by invoking the MF approximation, i.e., by replacing the expectation value of a function of spin variables by the function of the expectation values of the spin variables. The resultant MF dynamical model is

$$\begin{aligned} 2\lambda^{-1} \frac{d}{dt} \langle S_n \rangle &= -q \langle S_n \rangle + \sum_{L_n} \langle S_{L_n} \rangle \\ &\quad + \sum_{k \in L_n} (1 - \langle S_n \rangle \langle S_k \rangle) \tanh \left[\beta J \left(\sum_{L_n} \langle S_{L_n} \rangle - \sum_{L_k} \langle S_{L_k} \rangle \right) \right]. \end{aligned} \quad (5.57)$$

Notice that the restrictions on the summations inside the tanh-function have been dropped in the MF approximation. This is necessary for Eq. (5.57) to contain the correct MF solution in Eq. (5.18) [13]. Recall the MF solution for

the $h = 0$ case:

$$\langle S_k \rangle^{\text{eq}} = \tanh \left(\beta J \sum_{L_k} \langle S_{L_k} \rangle^{\text{eq}} \right). \quad (5.58)$$

If we replace this in the RHS of Eq. (5.57), we obtain

$$\begin{aligned} \text{RHS} &= -q \langle S_n \rangle^{\text{eq}} + \sum_{L_n} \langle S_{L_n} \rangle^{\text{eq}} + \sum_{k \in L_n} (1 - \langle S_n \rangle^{\text{eq}} \langle S_k \rangle^{\text{eq}}) \times \\ &\quad \left[\frac{\tanh \left(\beta J \sum_{L_n} \langle S_{L_n} \rangle^{\text{eq}} \right) - \tanh \left(\beta J \sum_{L_k} \langle S_{L_k} \rangle^{\text{eq}} \right)}{1 - \tanh \left(\beta J \sum_{L_n} \langle S_{L_n} \rangle^{\text{eq}} \right) \tanh \left(\beta J \sum_{L_k} \langle S_{L_k} \rangle^{\text{eq}} \right)} \right] \\ &= -q \langle S_n \rangle^{\text{eq}} + \sum_{L_n} \langle S_{L_n} \rangle^{\text{eq}} + \sum_{L_n} (\langle S_n \rangle^{\text{eq}} - \langle S_{L_n} \rangle^{\text{eq}}) \\ &= 0, \end{aligned} \quad (5.59)$$

as expected.

Finally, let us derive a continuum equation for the order parameter. This is the conserved counterpart of the TDGL equation we derived for the magnetization in Sec. 5.2.2. We can simplify the RHS of Eq. (5.57) by using the identity

$$\begin{aligned} \tanh(X - Y) &= \frac{\tanh X - \tanh Y}{1 - \tanh X \tanh Y}, \quad \text{where} \\ X &= \beta J \sum_{L_n} \langle S_{L_n} \rangle, \\ Y &= \beta J \sum_{L_k} \langle S_{L_k} \rangle. \end{aligned} \quad (5.60)$$

We are interested in the late-stage dynamics, where the system has equilibrated locally and Eq. (5.58) applies. Then, we make the approximation:

$$(1 - \langle S_n \rangle \langle S_k \rangle) \left(\frac{\tanh X - \tanh Y}{1 - \tanh X \tanh Y} \right) \simeq \tanh X - \tanh Y. \quad (5.61)$$

Therefore, we can rewrite Eq. (5.57) as

$$\begin{aligned} 2\lambda^{-1} \frac{d}{dt} \langle S_n \rangle &\simeq \sum_{L_n} (\langle S_{L_n} \rangle - \langle S_n \rangle) \\ &\quad + \sum_{k \in L_n} \left[\tanh \left(\beta J \sum_{L_n} \langle S_{L_n} \rangle \right) - \tanh \left(\beta J \sum_{L_k} \langle S_{L_k} \rangle \right) \right] \\ &= \Delta_D \left[\langle S_n \rangle - \tanh \left(\beta J \sum_{L_n} \langle S_{L_n} \rangle \right) \right], \end{aligned} \quad (5.62)$$

where Δ_D denotes the discrete Laplacian operator. We can use the Taylor expansion in Eq. (5.20) to obtain the coarse-grained version of Eq. (5.62) as

$$\begin{aligned} 2\lambda^{-1} \frac{\partial}{\partial t} \psi(\vec{r}, t) = & -a^2 \nabla^2 \left[\left(\frac{T_c}{T} - 1 \right) \psi - \frac{1}{3} \left(\frac{T_c}{T} \right)^3 \psi^3 + \frac{T_c}{qT} a^2 \nabla^2 \psi \right] \\ & + \text{other terms.} \end{aligned} \quad (5.63)$$

Equation (5.63) is known as the Cahn-Hilliard (CH) equation [32] and is the standard model for phase separation driven by diffusion. In the next subsection, we will derive the CH equation using phenomenological arguments.

5.2.5 Phase Ordering Dynamics: Conserved Kinetics

A typical phase diagram for an AB mixture was shown in Fig. 5.3. In Fig. 5.7, we show the evolution of a binary mixture subsequent to a quench from above the coexistence curve (homogeneous phase) to below the coexistence curve (segregated phase). The initially homogeneous system separates into A-rich and B-rich domains, denoted as black and white regions in Fig. 5.7. In contrast to the nonconserved case, the evolution in this case must satisfy the constraint that numbers of A and B are constant, i.e., the order parameter is conserved. In the corresponding kinetic Ising model in Sec. 5.2.4, recall that the conservation law was implemented via Kawasaki spin-exchange kinetics.

Experimentalists distinguish between *shallow quenches* (just below the coexistence curve) and *deep quenches* (far below the coexistence curve). For shallow quenches, in the region between the coexistence line and the spinodal lines in Fig. 5.3, the homogeneous system is metastable and decomposes by the *nucleation and growth* of droplets. For deep quenches, into the region below the spinodal lines, the homogeneous system spontaneously decomposes into A-rich and B-rich regions, a process referred to as *spinodal decomposition*. However, there is no sharp physical distinction between the *nucleation and growth* and *spinodal decomposition* regions of the phase diagram [3].

For simplicity, let us focus on the kinetics of phase separation in a binary mixture where hydrodynamic effects are not relevant, e.g., binary alloys. In this case, the primary mechanism for phase separation is diffusion and aggregation. As in the nonconserved case, we introduce a space-time-dependent order parameter $\psi(\vec{r}, t) = n^A(\vec{r}, t) - n^B(\vec{r}, t)$, where $n^\alpha(\vec{r}, t)$ is the local density of species α . The evolution of ψ is described by the continuity equation:

$$\frac{\partial}{\partial t} \psi(\vec{r}, t) = -\vec{\nabla} \cdot \vec{J}(\vec{r}, t), \quad (5.64)$$

where $\vec{J}(\vec{r}, t)$ denotes the current. Further, since the current is driven by concentration fluctuations, we expect

$$\vec{J}(\vec{r}, t) = -D \vec{\nabla} \mu(\vec{r}, t), \quad (5.65)$$

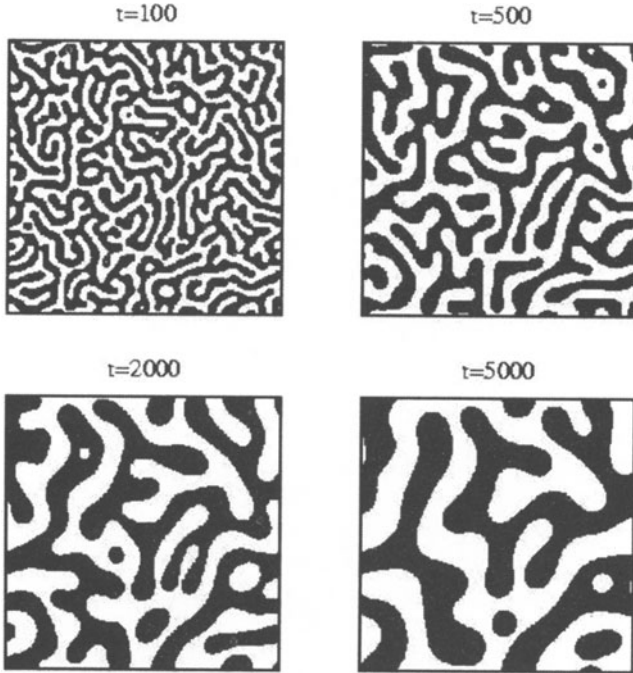


Figure 5.7: Evolution of a homogeneous binary (AB) mixture, which is quenched below the coexistence curve at time $t = 0$. These pictures were obtained from a numerical solution of the CHC equation (5.72) with $\epsilon = 0$. The discretization mesh sizes were $\Delta t = 0.01$ and $\Delta x = 1$, and the lattice size was 256^2 . The random initial condition consisted of small-amplitude fluctuations about $\psi = 0$, corresponding to a mixture with equal amounts of A and B (critical composition). Regions with $\psi > 0$ (A-rich) and $\psi < 0$ (B-rich) are marked in black and white, respectively.

where D is the diffusion coefficient and $\mu(\vec{r}, t)$ is the chemical potential. Finally, the chemical potential is determined as

$$\mu(\vec{r}, t) = \frac{\delta F[\psi]}{\delta \psi}, \quad (5.66)$$

where F refers to the Helmholtz potential, which is the appropriate thermodynamic potential for the binary mixture. This is obtained from Eq. (5.23) with $g(\psi)$ replaced by $f(\psi)$.

Combining Eqs. (5.64)-(5.66), we obtain the CH equation for the phase separation of a binary mixture:

$$\frac{\partial}{\partial t} \psi(\vec{r}, t) = D \nabla^2 \left(\frac{\delta F[\psi]}{\delta \psi} \right). \quad (5.67)$$

In Sec. 5.2.4, we had derived such an equation from the Kawasaki-Ising model [cf. Eq. (5.63)]. Notice that Eq. (5.67) corresponds to the case of a constant diffusion coefficient. There have also been studies of systems where the diffusion coefficient depends on the local order parameter [33].

The effects of thermal fluctuations can be incorporated in the CH equation by including a Gaussian noise term in the definition of the current in Eq. (5.65) [34]. The resultant model is the Cahn-Hilliard-Cook (CHC) equation:

$$\frac{\partial}{\partial t} \psi(\vec{r}, t) = \vec{\nabla} \cdot \left\{ D \vec{\nabla} \left(\frac{\delta F[\psi]}{\delta \psi} \right) + \vec{\theta}(\vec{r}, t) \right\}. \quad (5.68)$$

The vector noise $\vec{\theta}$ satisfies the usual fluctuation-dissipation relation:

$$\begin{aligned} \overline{\vec{\theta}(\vec{r}, t)} &= 0, \\ \overline{\theta_i(\vec{r}', t') \theta_j(\vec{r}'', t'')} &= 2Dk_B T \delta_{ij} \delta(\vec{r}' - \vec{r}'') \delta(t' - t''). \end{aligned} \quad (5.69)$$

Equations (5.68)-(5.69) are also referred to as *Model B* in the classification scheme of Hohenberg and Halperin [19].

For the ψ^4 -form of the free-energy functional [Eq. (5.26) without the magnetic field term], the CHC equation has the following form:

$$\frac{\partial}{\partial t} \psi(\vec{r}, t) = \vec{\nabla} \cdot \left\{ D \vec{\nabla} [-a(T_c - T)\psi + b\psi^3 - K\nabla^2\psi] + \vec{\theta}(\vec{r}, t) \right\}. \quad (5.70)$$

In analogy with the TDGL equation (5.27), we rescale variables as follows (for $T < T_c$):

$$\begin{aligned} \psi' &= \frac{\psi}{\psi_0}, \quad \psi_0 = \sqrt{\frac{a(T_c - T)}{b}}, \\ t' &= \frac{Da^2(T_c - T)^2}{K} t, \\ \vec{r}' &= \sqrt{\frac{a(T_c - T)}{K}} \vec{r}, \quad \xi_b = \sqrt{\frac{2K}{a(T_c - T)}}, \\ \vec{\theta}' &= \frac{\sqrt{bK}}{Da^2(T_c - T)^2} \vec{\theta}. \end{aligned} \quad (5.71)$$

We then drop primes to obtain the dimensionless CHC equation:

$$\frac{\partial}{\partial t} \psi(\vec{r}, t) = \vec{\nabla} \cdot \left[\vec{\nabla} (-\psi + \psi^3 - \nabla^2\psi) + \vec{\theta}(\vec{r}, t) \right], \quad (5.72)$$

where

$$\begin{aligned} \overline{\vec{\theta}(\vec{r}, t)} &= 0, \\ \overline{\theta_i(\vec{r}', t') \theta_j(\vec{r}'', t'')} &= 2\epsilon \delta_{ij} \delta(\vec{r}' - \vec{r}'') \delta(t' - t''), \\ \epsilon &= \frac{k_B T b [a(T_c - T)]^{(d-4)/2}}{K^{d/2}}. \end{aligned} \quad (5.73)$$

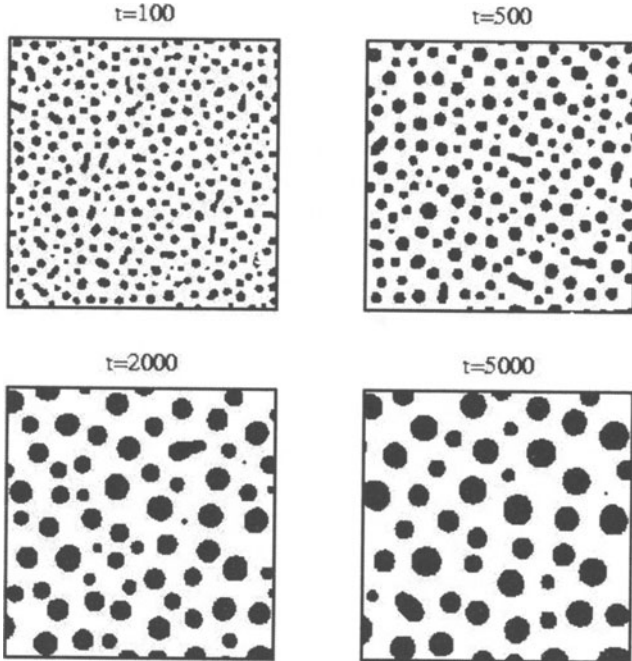


Figure 5.8: Analogous to Fig. 5.7, but for the case of an off-critical binary mixture. The initial condition consisted of small-amplitude fluctuations about $\psi = -0.4$, corresponding to a mixture with 30% A and 70% B.

The evolution depicted in Fig. 5.7 is obtained from a numerical solution of the dimensionless CHC equation with a disordered initial condition, which mimics the homogeneous state prior to the quench. (We will discuss the numerical solution of the CHC equation in Sec. 5.4.2.) Regions which are A-rich ($\psi = +1$) are marked black, and regions which are B-rich ($\psi = -1$) are not marked. The mixture has a critical composition with 50% A–50% B, i.e., the average value of the order parameter $\psi_0 = V^{-1} \int d\vec{r} \psi(\vec{r}, 0) = 0$. This composition is maintained during the evolution due to the conservation constraint. As in the TDGL equation, thermal noise is asymptotically irrelevant for the CHC equation – the evolution shown in Fig. 5.7 corresponds to the deterministic case with $\epsilon = 0$. In Fig. 5.8, we show the evolution for an off-critical composition with 30% A and 70% B, i.e., $\psi_0 = -0.4$. This composition still lies inside the spinodal curve in Fig. 5.3, so the evolution corresponds to spinodal decomposition. However, the morphology is characterized by the growth of A-rich (minority phase) droplets in a B-rich (majority phase) background.

Before we proceed, it is relevant to discuss the applicability of the CHC model to real binary alloys. Typically, lattice parameter mismatches in alloys can set up large strain fields in the intermediate and late stages of phase separation. These strain fields drastically modify the results we quote below, and

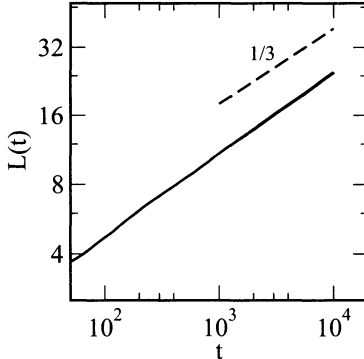


Figure 5.9: Domain growth law for the evolution depicted in Fig. 5.7. The numerical data was obtained as an average over 10 independent runs for systems of size 512^2 . The data is plotted on a log-log scale. The dashed line denotes the Lifshitz-Slyozov growth law, $L(t) \sim t^{1/3}$.

must be accounted for in any realistic description of phase separation in alloys [35, 36, 37].

In the absence of strain effects, the phase-separating system is characterized by a unique length scale, $L(t) \sim t^{1/3}$ in $d \geq 2$. This power-law behavior was first derived by Lifshitz and Slyozov (LS) [38] for extremely off-critical systems, where one of the components is present in a vanishing fraction, and the evolution proceeds via the nucleation and growth of minority droplets. Huse [39] demonstrated that the same law is applicable to spinodal decomposition, where there are approximately equal fractions of the two components and the coarsening structure is bi-continuous. Typically, the chemical potential on the surface of a domain of size L is $\mu \sim \sigma/L$, where σ is the surface tension. The concentration current is obtained as $D|\vec{\nabla}\mu| \sim D\sigma/L^2$, where D is the diffusion constant. Therefore, the domain size grows as $dL/dt \sim D\sigma/L^2$, or $L(t) \sim (D\sigma t)^{1/3}$. In Fig. 5.9, we show the domain growth law for the case with $\psi_0 = 0$ (shown in Fig. 5.7) – the asymptotic growth law is seen to be consistent with the LS law.

As in the nonconserved case, the quantities which characterize the evolution morphology in Figs. 5.7 and 5.8 are the correlation function and the structure factor. The existence of a characteristic length scale results in the dynamical scaling of these quantities. For the critical quench shown in Fig. 5.7, we demonstrate the dynamical scaling of the correlation function and structure factor in Fig. 5.10. As in Fig. 5.5, the presence of sharp defects yields a Porod tail for the structure factor.

The above properties are common to the nonconserved and conserved cases. There are some additional features due to the conservation law. For example, the conservation constraint dictates the sum rule:

$$\int d\vec{r} C(\vec{r}, t) = 0, \quad \text{or} \quad S(0, t) = 0. \quad (5.74)$$

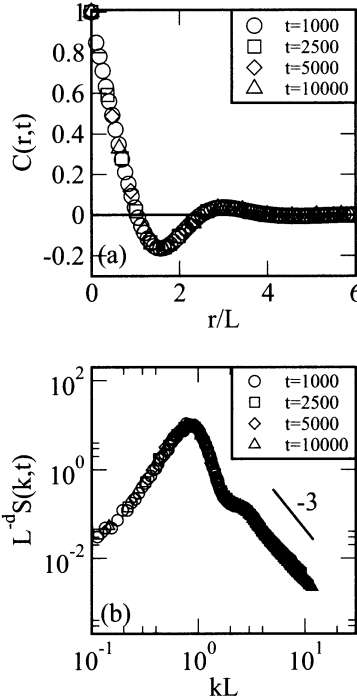


Figure 5.10: Analogous to Fig. 5.5, but for the evolution depicted in Fig. 5.7. The numerical data was obtained as an average over 10 independent runs for systems of size 512^2 .

Furthermore, the conservation law also fixes the $p \rightarrow 0$ behavior of the scaled structure factor as $f(p) \sim p^4$ [40, 41].

Clearly, we have a good understanding of various general features of the morphology. There have been extensive simulations of phase-separation kinetics, which have provided detailed results for the late-time behavior. These studies are based on *cell dynamical system* (CDS) models [42]; discrete simulations of the CHC equation [43]; and Monte Carlo (MC) simulations of the Kawasaki-Ising model [44, 45]. These techniques are described in detail in Secs. 5.3 and 5.4. However, inspite of many attempts [46, 47, 48], there is still no theory for the scaling form of the correlation function. A major analytical obstacle in this regard is the strongly correlated motion of interfaces, resulting from the conservation law.

Let us next discuss some of the numerical approaches which are used to study domain growth problems. Broadly speaking, there are three classes of numerical techniques applied to study the kinetics of phase transitions:

- (a) Monte Carlo (MC) techniques;
- (b) Molecular dynamics (MD) methods;

- (c) Simulation (or solution) of coarse-grained models, e.g., partial differential equation models.

In this chapter, we will focus on (a) and (c) above. Readers interested in MD methods will find many relevant details in Ref. [49]. We merely remark that, as the name suggests, MD methods involve direct integration of the equations of motion for a large number of microscopic particles with appropriate interactions.

5.3 Monte Carlo Techniques

Let us first discuss the application of Monte Carlo (MC) techniques. Typically, MC methods are applied to systems described by microscopic Hamiltonians. (There are also applications to systems described by coarse-grained Hamiltonians, but these are fewer in number.) MC methods can be used for both equilibrium and nonequilibrium problems, and we will elaborate on these applications shortly. The purpose of these lectures is not to provide an exhaustive survey of the MC approach, which is already the subject of many books [50]. Rather, we will try to rapidly take the reader to a level where he can generate a simple MC code.

5.3.1 Equilibrium Systems

A thermodynamic system typically consists of microscopic elements (labeled by i , say) which are described by coordinates (say, \vec{x}_i). The constituent elements could be spins as in the Ising model (in which case the coordinates will take discrete values), or molecules (in which case the coordinates will be position and momentum vectors), etc. Let us consider a spin system described by a generalized version of the Ising Hamiltonian in Eq. (5.1):

$$H\{S_i\} = - \sum_{j>i} J_{ij} S_i S_j, \quad (5.75)$$

where J_{ij} is the strength of the interaction between spins i and j . This Hamiltonian describes many physical situations, and the nature of the system is reflected in the form of J_{ij} , viz., whether it is long-ranged or short-ranged; whether it is uniform or site-dependent; etc.

The basic problem of equilibrium statistical physics is to obtain (a) the partition function Z (in an appropriate ensemble) for a given Hamiltonian; and (b) the expectation value of an operator $A\{S_i\}$, which is some functional of the system variables. Thus, for a ferromagnet in a magnetic field h , we are

interested in quantities like

$$\begin{aligned} Z &= \sum_{\{S_i\}} \exp \left[-\beta \left(H\{S_i\} - h \sum_{i=1}^N S_i \right) \right], \\ \langle A \rangle &= \frac{1}{Z} \sum_{\{S_i\}} A\{S_i\} \exp \left[-\beta \left(H\{S_i\} - h \sum_{i=1}^N S_i \right) \right]. \end{aligned} \quad (5.76)$$

Some particularly interesting forms of A are $A = S_i$ (which yields $\langle S_i \rangle$, the single-spin expectation value or magnetization); and $A = S_i S_j$ (which gives $\langle S_i S_j \rangle$, the spin-spin correlation function). For most systems, it is difficult to compute Z or $\langle A \rangle$ analytically. Thus, one has to resort to a sequence of approximations to make analytical progress. Numerically, one has no such problem, regardless of how complicated the Hamiltonian $H\{S_i\}$ or operator $A\{S_i\}$ are. Thus, we can set up a discrete lattice on the computer with some initial configuration of spins $\{S_i^0\}$. New configurations can then be generated by flipping spins at random – this is the reason for using the term “Monte Carlo”, which is associated with games of chance. The averages in Eq. (5.76) can be computed numerically as a sum over these configurations. In the limit of infinite system size and an infinite number of configurations, we are guaranteed to obtain exact values of Z and $\langle A \rangle$. Of course, computational constraints do not permit an infinite system size or an infinite number of configurations. However, one can obtain good approximate values of Z and $\langle A \rangle$ in a reasonable simulation.

The MC procedure described above is simple and easily implemented on the computer, but is not particularly useful in statistical physics. This is because the phase space is often very large and purely random sampling results in the system spending a lot of time in energetically unphysical regions of phase space. To circumvent this problem, Metropolis et al. [51] introduced a novel MC scheme, based on a preferential sampling of statistically important regions of phase space, i.e., regions of low free energy. This scheme is based on the stochastic evolution described in Secs. 5.2.2 and 5.2.4 as follows:

- (a) Start off with an ensemble of M systems having some initial distribution of spin configurations $P(\{S_i\}, 0)$. Focus on a particular configuration, say $\{S_i\}$.
- (b) Make a random change in this configuration by some specified procedure (e.g., flip a randomly-chosen single spin or a fixed fraction of the spins). Call this the target configuration $\{S'_i\}$.
- (c) Choose a transition probability $W(\{S_i\} | \{S'_i\})$ for $\{S_i\} \rightarrow \{S'_i\}$, which satisfies the detailed-balance condition. One possibility is the Suzuki-Kubo probability in Eq. (5.9) with rate $\lambda = 1$. Another commonly used transition probability is

$$\begin{aligned} W(\{S_i\} | \{S'_i\}) &= \exp[-\beta \Delta(H - hM)] \quad \text{if } \Delta(H - hM) > 0, \\ &= 1 \quad \text{if } \Delta(H - hM) \leq 0. \end{aligned} \quad (5.77)$$

- (d) Generate a random number $p \in [0, 1]$. Compare the transition probability with this random number to determine whether this transition should be

made. Thus, if $W(\{S_i\}|\{S'_i\}) > p$, take $\{S'_i\}$ as the new configuration of the system. Otherwise, the old configuration remains unchanged.

(e) All systems in the ensemble are updated via the above procedure. After some transient regime, the ensemble settles into an equilibrium distribution with the appropriate Boltzmann weight. The quantity $\langle A \rangle$ in Eq. (5.76) is calculated as an average over this ensemble:

$$\langle A \rangle = \frac{1}{M} \sum_{j=1}^M A\{S_i^j\}, \quad (5.78)$$

where the superscript j labels the configurations. There is no Boltzmann weight factor in Eq. (5.78) because the generated states sample phase space proportionally to the Boltzmann weight.

(f) If the system is ergodic (which is often the case), the ensemble average in Eq. (5.78) can be replaced by a time-average over a single system evolving as described above.

We stress that there are an infinite number of possibilities for $W(\{S_i\}|\{S'_i\})$ which satisfy the detailed-balance condition. The ones we have mentioned merely constitute two forms frequently used in the MC literature.

Thus, it is now clear how the improved MC scheme works. If we start off with an ensemble of systems, it is rapidly driven into an equilibrium ensemble. A simple average over this equilibrium ensemble as in Eq. (5.78) corresponds to the correct statistical average. Of course, in many applications, one actually works with a single system. Under the prescription in (b)-(d), the evolving system (after an initial equilibration time) will wander around in phase space, tracing an equilibrium ensemble. If the system is ergodic, the time-average of quantities for this single system is the same as the equilibrium ensemble average. Thus, given reasonable system sizes and simulation times, we can obtain accurate numerical values for statistical quantities.

5.3.2 Nonequilibrium Systems

In general, nonequilibrium systems are considerably harder to study than equilibrium systems. Typically, there are two classes of nonequilibrium problems:

(a) Systems which are rendered *far-from-equilibrium* by a rapid change of parameters and evolve towards a new equilibrium state. Recall that this is the typical scenario in problems involving the kinetics of phase transitions.

(b) Systems which are in a *steady state* (i.e., macroscopic variables do not change with time) but in a nonequilibrium state due to flow of currents.

The MC technique has been applied to systems in both classes above. In this chapter, we focus on far-from-equilibrium problems.

The prescription for MC dynamics in this case is a simple extension of the equilibrium MC procedure described in Sec. 5.3.1. After all, the transition probabilities we considered drive an ensemble with some initial distribution

$P(\{S_i\}, 0)$ to the equilibrium ensemble $P_{\text{eq}}(\{S_i\})$. In Sec. 5.3.1, we ignored the relaxation of the initial ensemble to equilibrium and computed statistical quantities as averages over the equilibrium ensemble, or equivalently, as time-averages for a single system. In the nonequilibrium case, our interest is in the relaxation to equilibrium.

We should stress that MC dynamics differs from the equilibrium prescription [i.e., (a)-(f) in Sec. 5.3.1] in three important respects:

- (1) The initial ensemble $P(\{S_i\}, 0)$ must be carefully chosen to reflect the far-from-equilibrium state of interest. In phase ordering dynamics, the initially disordered state corresponds to a set of configurations in which spins are randomly oriented with no correlation between different spins.
- (2) We must be careful about how we make random changes to the configuration $\{S_i\}$ as the stochastic dynamics must reflect the underlying physics of the problem. Thus, for the ordering of a ferromagnet in Sec. 5.2.2, one considers configuration changes occurring via Glauber or spin-flip kinetics. On the other hand, the segregation dynamics of a mixture in Sec. 5.2.4 is modeled by Kawasaki or spin-exchange kinetics, which preserves the overall magnetization. In equilibrium MC, we can use any means of changing the configuration because we are interested only in the equilibrium ensemble – this is independent of the dynamics of configuration change.
- (3) In the nonequilibrium case, it is more convenient to work with an ensemble of systems and evolve them according to the MC prescription in Sec. 5.3.1 with the modifications (1)-(2) above. The expectation value of an operator $A\{S_i\}$ can be obtained by averaging over this time-dependent probability distribution as

$$\langle A \rangle(t) = \frac{1}{M} \sum_{j=1}^M A\{S_i^j\} \simeq \sum_{\{S_i\}} A\{S_i\} P(\{S_i\}, t). \quad (5.79)$$

This is in contrast to the equilibrium case, where we can invoke ergodicity of the system (which holds in many cases of interest) to compute the expectation value of an operator as the time-average of a single evolving system.

Before we proceed, we should warn the reader that the stochastic MC dynamics may not be consistent with the actual physical evolution equations of some systems, which may be described by deterministic kinetic equations (e.g., the Heisenberg ferromagnet). In such cases, the MC kinetics actually misses important components of the dynamics. Fortunately, for the kinetic Ising models we have described above, the MC dynamics is a reasonably accurate description of real dynamics for a wide range of physical systems.

There have been extensive MC simulations of phase ordering dynamics in both the cases with nonconserved and conserved order parameters. As discussed in Sec. 5.2.3, the quantities of interest are usually the correlation function $C(\vec{r}, t)$; the structure factor $S(\vec{k}, t)$; and the length scale $L(t)$, which characterizes the growing domains. MC simulations of the case with nonconserved order parameter [50] clearly establish the dynamical scaling of the correlation function [cf. Eq. (5.41)] and the structure factor [cf. Eq. (5.43)]. These MC

simulations have also demonstrated that $L(t) \sim t^{1/2}$, in conformity with the Allen-Cahn growth law.

The case with conserved order parameter has proved less amenable to MC simulations because of the extremely long times needed to access the asymptotic regime and the large system sizes needed to avoid finite-size effects. An extensive MC simulation of the Kawasaki-Ising model is due to Amar et al. [44]. This simulation established the dynamical scaling of the structure factor. In this case, domain growth obeys the LS growth law, $L(t) \sim t^{1/3}$. The MC simulations of Amar et al. [44] yielded this asymptotic growth law only after an extrapolation of the numerical data. Marko and Barkema [45] have used an accelerated MC algorithm to clearly demonstrate that the LS growth law describes the asymptotic growth regime for the Kawasaki-Ising model.

5.4 Simulation of Coarse-Grained Models

In Secs. 5.2.3 and 5.2.5, we have shown results obtained from the simulation (or solution) of coarse-grained partial differential equation models of phase ordering systems. Let us now discuss some numerical techniques for solution of these models.

We will consider dynamical equations which describe an evolution from some initial condition, i.e., we focus on nonequilibrium problems. As far as the simulation of ordinary differential equations is concerned, this is a well-studied subject and we do not go into it here. Many good numerical schemes and a brief description of the underlying theory are available in Ref. [52]. We will focus on the simulation of partial differential equations in this section, with special reference to equations of phase ordering dynamics. We will also briefly discuss cell dynamical system (CDS) models [42], which are discrete space-time models, and have become popular as alternative coarse-grained descriptions of many important phenomena.

5.4.1 The Diffusion Equation

Let us start with a familiar example, viz., the 1-*d* diffusion equation:

$$\frac{\partial}{\partial t} u(x, t) = \frac{\partial^2}{\partial x^2} u(x, t), \quad (5.80)$$

where $u(x, t)$ is (say) the temperature of a bar at point x and time t . We have rescaled the units of space and time to put the equation in a dimensionless form. Equation (5.80) must be supplemented with one initial condition and boundary conditions at the end of the bar (if it is finite). We can solve the initial-value problem for this equation analytically, but its numerical implementation will illustrate a number of important points.

A typical numerical scheme for Eq. (5.80) discretizes space (with mesh size Δx) and time (with mesh size Δt). We can approximate the derivatives by

using a simple Euler formula as

$$\begin{aligned}\frac{\partial}{\partial t} u(x, t) &\simeq \frac{u(x, t + \Delta t) - u(x, t)}{\Delta t}, \\ \frac{\partial^2}{\partial x^2} u(x, t) &\simeq \frac{u(x + \Delta x, t) - 2u(x, t) + u(x - \Delta x, t)}{(\Delta x)^2}.\end{aligned}\quad (5.81)$$

We can use more sophisticated discretizations involving a larger number of points to approximate the derivatives better. However, for purposes of illustration, the simple discretization in Eq. (5.81) will suffice. If we replace Eq. (5.81) in Eq. (5.80), we have the finite-difference equivalent of the diffusion equation as:

$$u(x, t + \Delta t) = u(x, t) + \alpha[u(x + \Delta x, t) - 2u(x, t) + u(x - \Delta x, t)], \quad (5.82)$$

where $\alpha = \Delta t / (\Delta x)^2$. Thus, we can numerically solve the diffusion equation for any initial condition by putting $u(x, 0)$ on the LHS of Eq. (5.82) to obtain $u(x, \Delta t)$. We can then use $u(x, \Delta t)$ as the initial condition to obtain $u(x, 2\Delta t)$ and so on. Clearly, we want the solution of Eq. (5.82) to replicate the solution of Eq. (5.80) with some accuracy. For this to happen, it is necessary (though not sufficient) to satisfy what is known as the *stability criterion*. This is derived by demanding that the physics of the finite-difference equation (5.82) should be the same as that of the partial differential equation (5.80).

The physics of the diffusion equation is rather simple, viz., arbitrary fluctuations about a flat background decay to zero. Let us see what happens to small fluctuations in Eq. (5.82). We put $u(x, t) = u_0 + \delta u(x, t)$ to obtain

$$\delta u(x, t + \Delta t) = \alpha \delta u(x + \Delta x, t) + (1 - 2\alpha) \delta u(x, t) + \alpha \delta u(x - \Delta x, t). \quad (5.83)$$

If we multiply both sides of Eq. (5.83) by e^{ikx} and sum over x , we get the corresponding equation for the Fourier transform of the fluctuation:

$$\begin{aligned}\delta u(k, t + \Delta t) &= [\alpha e^{-ik\Delta x} + (1 - 2\alpha) + \alpha e^{ik\Delta x}] \delta u(k, t) \\ &= \left[1 - 4\alpha \sin^2\left(\frac{k\Delta x}{2}\right) \right] \delta u(k, t) \\ &= \lambda(k) \delta u(k, t),\end{aligned}\quad (5.84)$$

where we have assumed periodic boundary conditions. The evolution of the fluctuations is determined by the eigenvalues $\lambda(k)$. In particular, a mode with wavevector k will grow if $|\lambda(k)| > 1$. All $\lambda(k) < 1$, so there is no danger of divergence from that end of the spectrum. However, it is possible that $\lambda(k) < -1$, and this will lead to an unphysical divergence (known as a *subharmonic bifurcation*) in Eq. (5.82). This happens for $k = \pi / \Delta x$ when $\alpha > 1/2$. To avoid this unphysical situation, we must satisfy the stability criterion

$$\alpha = \frac{\Delta t}{(\Delta x)^2} \leq 1/2. \quad (5.85)$$

As we have mentioned earlier, the stability criterion is necessary but not sufficient condition for the numerical solution of Eq. (5.82) to closely approximate the actual solution of Eq. (5.80). This is because of the errors associated with the discretization. We do not want to discuss these errors here, though we point out that the classification and reduction of these errors is a matter of concern to numerical analysts. For our purposes, the crucial point is that, once the stability criterion is satisfied, we can use fairly large mesh sizes for t and x and get a qualitatively reasonable (though not quantitatively precise) solution for the partial differential equation. For the physicist's applications, this is often sufficient.

The discrete numerical scheme in Eq. (5.82) can be made *unconditionally* (or always) stable by introducing an implicit difference scheme, which discretizes the diffusive term at the later time ($t + \Delta t$). The corresponding finite-difference equation is

$$u(x, t + \Delta t) = u(x, t) + \alpha [u(x + \Delta x, t + \Delta t) - 2u(x, t + \Delta t) + u(x - \Delta x, t + \Delta t)]. \quad (5.86)$$

The numerical implementation of Eq. (5.86) requires solution of a matrix equation at each time step, but this is not a major problem because the system is tridiagonal. If we carry out the same stability analysis as before, we find

$$\lambda(k) = \frac{1}{1 + 4\alpha \sin^2(k\Delta x/2)}, \quad (5.87)$$

so that $|\lambda(k)| \leq 1$ for all k and there is never a stability problem.

5.4.2 Domain Growth Models

Recall the continuum models which describe phase ordering systems. The case with nonconserved order parameter (e.g., ordering of a ferromagnet) is usually described by the TDGL equation (5.29):

$$\frac{\partial}{\partial t} \psi(\vec{r}, t) = \psi - \psi^3 + \nabla^2 \psi + \theta(\vec{r}, t), \quad (5.88)$$

where we have set $h = 0$. The case with conserved order parameter (e.g., segregation of a binary mixture) is usually described by the CHC equation (5.72), which we reproduce here for convenience:

$$\frac{\partial}{\partial t} \psi(\vec{r}, t) = \nabla^2 (-\psi + \psi^3 - \nabla^2 \psi) + \vec{\nabla} \cdot \vec{\theta}(\vec{r}, t). \quad (5.89)$$

The dynamics represented by Eqs. (5.88) and (5.89) locally drives the system to homogeneous order parameter values $\psi = +1$ or -1 , corresponding to domains which are rich in up or down spins. These dissipative nonlinear partial differential equations are analytically intractable and can only be solved numerically. In Sec. 5.2.3, we argued that thermal noise is irrelevant for domain growth problems. Therefore, we will consider only the deterministic versions of

Eqs. (5.88) and (5.89). (Of course, for a general problem, noise is not irrelevant and must be carefully incorporated in a simulation.)

First, consider the deterministic version of the TDGL equation:

$$\frac{\partial}{\partial t}\psi(\vec{r},t) = \psi - \psi^3 + \nabla^2\psi. \quad (5.90)$$

As in the case of the diffusion equation, we can construct a finite-difference scheme for Eq. (5.90) by simple Euler discretization in space and time. The scheme is

$$\psi(\vec{r}, t + \Delta t) = \psi(\vec{r}, t) + \Delta t [\psi(\vec{r}, t) - \psi(\vec{r}, t)^3] + \alpha \Delta_D \psi(\vec{r}, t), \quad (5.91)$$

where Δ_D denotes the discrete Laplacian operator, and $\alpha = \Delta t / (\Delta x)^2$. As before, the stability criterion is fixed by demanding that the finite-difference equation respect the same physics as the original partial differential equation. The crucial physics in Eq. (5.90) is that, once the domains saturate to their equilibrium values of $+1$ or -1 , the bulk is stable against fluctuations around these values. To check on the corresponding behavior of Eq. (5.91), we set $\psi(\vec{r}, t) = 1 + \delta\psi(\vec{r}, t)$ and linearize in $\delta\psi(\vec{r}, t)$ to obtain

$$\delta\psi(\vec{r}, t + \Delta t) = (1 - 2\Delta t)\delta\psi(\vec{r}, t) + \alpha \Delta_D \delta\psi(\vec{r}, t). \quad (5.92)$$

Multiply both sides of Eq. (5.92) by $e^{i\vec{k} \cdot \vec{r}}$ and sum over \vec{r} to obtain

$$\begin{aligned} \delta\psi(\vec{k}, t + \Delta t) &= \{1 - 2\Delta t - 2\alpha [2 - \cos(k_x \Delta x) - \cos(k_y \Delta x)]\} \delta\psi(\vec{k}, t) \\ &= \lambda(\vec{k}) \delta\psi(\vec{k}, t). \end{aligned} \quad (5.93)$$

Here, we consider the 2-d case and apply periodic boundary conditions in both directions. It is clear that $\lambda(\vec{k}) < 1$ for all \vec{k} so there is no instability at that end of the spectrum. As before, the danger to stability is from a subharmonic bifurcation when $\lambda(\vec{k}) < -1$. To avoid this, we must have $\lambda(\vec{k}) \geq -1$, which holds when

$$\frac{(\Delta x)^2}{(\Delta x)^2 + 4} \geq \Delta t. \quad (5.94)$$

In the d -dimensional case, the factor 4 in the denominator of Eq. (5.94) is replaced by $2d$.

In similar fashion, we can construct a finite-difference scheme for the deterministic CHC equation (5.89). A similar stability analysis about the homogeneous solutions, $\psi = +1$ or -1 , can also be done for this scheme. The corresponding stability condition (i.e., the requirement for the finite-difference scheme to have the same physics as the CHC equation) is more stringent than Eq. (5.94):

$$\frac{(\Delta x)^4}{4d[(\Delta x)^2 + 2d]} \geq \Delta t. \quad (5.95)$$

Recall that numerical errors grow as we increase the mesh sizes, and one intuitively expects that rather small values of Δt and Δx are required to get

numerically accurate results. Fortunately, as for the diffusion equation, it is reasonable to use rather large mesh sizes if one is only interested in statistical properties (e.g., correlation functions, structure factors, growth laws) of phase ordering systems. Thus, even though the discrete model with large mesh sizes does not have the same solution as the continuum model, it lies in the same *dynamical universality class*. This dynamical universality has been exploited by Oono and Puri [42] to formulate computationally efficient, discrete space-time models (called CDS models) for phase ordering dynamics. These CDS models can be considered as stand-alone models of physical phenomena, without reference to underlying partial differential equations. This understanding has led to much research activity in the CDS modeling of a wide range of physical systems, e.g., hydrodynamic flows, crystal growth, biological dynamics, chemical turbulence, etc.

5.5 Summary and Discussion

Let us conclude this chapter with a summary and discussion. We have presented a broad overview of the *kinetics of phase transitions* and numerical simulations of problems in this area. There are two typical domain growth problems: (a) the ordering of a ferromagnet, which is an example of the *case with nonconserved order parameter*; and (b) the phase separation of a binary mixture, which is an example of the *case with conserved order parameter*.

We have a good understanding of the morphologies and growth laws which characterize domain-growth kinetics. The domain size $L(t)$ usually grows as a power-law in time, $L(t) \sim t^\phi$, where the growth exponent ϕ depends on (a) the nature of conservation laws, (b) the defects which drive the ordering process, and (c) the relevance of flow fields. The morphology is characterized by the *correlation function* or the *structure factor*. There is a good theoretical understanding of systems having nonconserved dynamics with both scalar and vector order parameters. Unfortunately, our understanding of the conserved problem is not so good. Thus, we know the various limiting behaviors of the correlation function or structure factor. However, the overall functional form is not well-understood, and this remains one of the outstanding problems in this area.

Numerical simulations of appropriate models have contributed greatly to our understanding of domain growth problems. In this chapter, we have described simulations of both microscopic models (based on spin variables or molecular positions) and coarse-grained continuum models (based on order parameters) of phase ordering dynamics. At this stage, a comparison between microscopic and coarse-grained methods is appropriate. In this author's opinion, microscopic approaches usually do not give as conclusive results as coarse-grained approaches. There are various reasons for this. Firstly, one needs much larger system sizes to avoid finite-size effects at the microscopic level. Secondly, noise terms are larger at the microscopic level than at the continuum

level, and these fluctuations are often reflected in the quality of the numerical data. Finally, relaxation times are often much larger at the microscopic level so longer simulations are necessary to obtain asymptotic results with microscopic systems. Given a physical problem, it is often straightforward to set up a microscopically accurate model and simulate it. In contrast, the coarse-grained level of description is not always apparent. However, this author would rather go to the effort of formulating the appropriate continuum model (by using some standard coarse-graining procedure on the microscopic model) because our experience indicates that much better results are obtained from simulations of coarse-grained models.

References

- [1] H.E. Stanley, *Introduction to Phase Transitions and Critical Phenomena*, Oxford University Press, Oxford (1971).
- [2] A.J. Bray, Adv. Phys. **43**, 357 (1994).
- [3] K. Binder and P. Fratzl, in *Materials Science and Technology Vol. 5*, G. Kostorz (ed.), Wiley-VCH, Weinheim (2001).
- [4] A. Onuki, *Phase Transition Dynamics*, Cambridge University Press, Cambridge (2002).
- [5] S. Dattagupta and S. Puri, *Dissipative Phenomena in Condensed Matter Physics*, Springer-Verlag, Heidelberg.
- [6] S. Puri and V.K. Wadhawan (eds.), *Kinetics of Phase Transitions*, CRC Press, Boca Raton, Florida (2009).
- [7] M. Plischke and B. Bergersen, *Equilibrium Statistical Physics*, Second Edition, World Scientific, Singapore (1994).
- [8] R.J. Glauber, J. Math. Phys. **4**, 294 (1963).
- [9] K. Kawasaki, in *Phase Transitions and Critical Phenomena*, Vol. 2, C. Domb and M.S. Green (eds.), Academic Press, London (1972).
- [10] K. Kawasaki, Phys. Rev. **145**, 224 (1966).
- [11] N.G. Van Kampen, *Stochastic Processes in Physics and Chemistry*, North-Holland, Amsterdam (1981).
- [12] M. Suzuki and R. Kubo, J. Phys. Soc. Jpn. **24**, 51 (1968).
- [13] K. Binder, Z. Phys. **267**, 313 (1974).
- [14] K. Binder, Phys. Rev. B **15**, 4425 (1977).
- [15] J.-F. Gouyet, Europhys. Lett. **21**, 335 (1993);
Phys. Rev. E **51**, 1695 (1995).
- [16] M. Plapp and J.-F. Gouyet, Phys. Rev. E **55**, 45 (1997).

- [17] S. Puri, Phys. Rev. E **55**, 1752 (1997).
- [18] S. Puri and R. Sharma, Phys. Rev. E **57**, 1873 (1998).
- [19] P.C. Hohenberg and B.I. Halperin, Rev. Mod. Phys. **49**, 435 (1977).
- [20] S.M. Allen and J.W. Cahn, *Acta Metall.* **27**, 1085 (1979).
- [21] T. Nagai and K. Kawasaki, *Physica A* **134**, 483 (1986).
- [22] S. Puri and Y. Oono, J. Phys. A **21**, L755 (1988).
- [23] A.J. Bray, Phys. Rev. Lett. **62**, 2841 (1989).
- [24] K. Binder and D. Stauffer, Phys. Rev. Lett. **33**, 1006 (1974).
- [25] J.R. Manning, *Diffusion Kinetics for Atoms in Crystals*, Van Nostrand, Princeton (1968).
- [26] C.P. Flynn, *Point Defects and Diffusion*, Clarendon, Oxford (1972).
- [27] K. Yaldram and K. Binder, Acta Metall. **39**, 707 (1991);
J. Stat. Phys. **62**, 161 (1991).
- [28] K. Tafa, S. Puri and D. Kumar, Phys. Rev. E **63**, 046115 (2001);
Phys. Rev. E **64**, 056139 (2001).
- [29] A.J. Bray, Phys. Rev. Lett. **66**, 2048 (1991).
- [30] J.F. Annett and J.R. Banavar, Phys. Rev. Lett. **68**, 2941 (1992).
- [31] M.K. Phani, J.L. Lebowitz, M.H. Kalos and O. Penrose, Phys. Rev. Lett. **45**, 366 (1980).
- [32] J.W. Cahn and J.E. Hilliard, J. Chem. Phys. **28**, 258 (1958);
J. Chem. Phys. **31**, 688 (1959).
- [33] S. Puri, A.J. Bray and J.L. Lebowitz, Phys. Rev. E **56**, 758 (1997).
- [34] H.E. Cook, Acta Metall. **18**, 297 (1970).
- [35] H. Nishimori and A. Onuki, Phys. Rev. B **42**, 980 (1990);
A. Onuki and H. Nishimori, Phys. Rev. B **43**, 13649 (1991).
- [36] F. Langmayr, P. Fratzl, G. Vogl and W. Miekeley, Phys. Rev. B **49**, 11759 (1994).
- [37] P. Fratzl, O. Penrose and J.L. Lebowitz, J. Stat. Phys. **95**, 1429 (1999).
- [38] I.M. Lifshitz and V.V. Slyozov, J. Phys. Chem. Solids **19**, 35 (1961).
- [39] D.A. Huse, Phys. Rev. B **34**, 7845 (1986).
- [40] C. Yeung, Phys. Rev. Lett. **61**, 1135 (1988).
- [41] H. Furukawa, Phys. Rev. B **40**, 2341 (1989).

- [42] Y. Oono and S. Puri, Phys. Rev. Lett. **58**, 836 (1987);
Phys. Rev. A **38**, 434 (1988);
S. Puri and Y. Oono, Phys. Rev. A **38**, 1542 (1988).
- [43] T.M. Rogers, K.R. Elder and R.C. Desai, Phys. Rev. B **37**, 9638 (1988).
- [44] J. Amar, F. Sullivan and R.D. Mountain, Phys. Rev. B **37**, 196 (1988).
- [45] J.F. Marko and G.T. Barkema, Phys. Rev. E **52**, 2522 (1995).
- [46] T. Ohta and H. Nozaki, in *Space-Time Organization in Macromolecular Fluids*, F. Tanaka, M. Doi and T. Ohta (eds.), Springer-Verlag, Berlin (1989).
- [47] H. Tomita, Prog. Theor. Phys. **90**, 521 (1993).
- [48] G.F. Mazenko, Phys. Rev. E **50**, 3485 (1994);
G.F. Mazenko and R. Wickham, Phys. Rev. E **51**, 2886 (1995);
G.F. Mazenko, Phys. Rev. E **62**, 5967 (2000).
- [49] M.P. Allen and D.J. Tildesley, *Computer Simulations of Liquids*, Clarendon, Oxford (1987); and references therein.
- [50] K. Binder (ed.), *Monte Carlo Methods in Statistical Physics*, Springer-Verlag, Berlin (1986);
K. Binder and D.W. Heermann, *Monte Carlo Simulations in Statistical Physics: An Introduction*, Springer-Verlag, Berlin (1988);
K. Binder (ed.), *The Monte Carlo Method in Condensed Matter Physics*, Springer-Verlag, Berlin (1992).
- [51] N. Metropolis, A.W. Rosenbluth, M.N. Rosenbluth, A.H. Teller and E. Teller, J. Chem. Phys. **21**, 1087 (1953).
- [52] W.H. Press, S.A. Teukolsky, W.T. Vetterling and B.P. Flannery, *Numerical Recipes: The Art of Scientific Computing*, Cambridge University Press, Cambridge (1992).
- [53] T. Ohta, D. Jasnow and K. Kawasaki, Phys. Rev. Lett. **49**, 1223 (1982).
- [54] The author's understanding of the problems discussed here has grown through many fruitful collaborations. He would like to thank his research collaborators for many stimulating interactions and inputs. He is also grateful to Anupam Mukherjee for assistance in preparing the figures.

Chapter 6

Introduction to Molecular Dynamics Simulation

Hemant Kumar and Prabal K Maiti

6.1 Introduction

Laplace vision

... An intelligence which could, at any moment, comprehend all the forces by which nature is animated and respective positions of the beings of which it is composed, and moreover, if this intelligence were far-reaching enough to subject these data to analysis, it would encompass in that formula both the movements of the largest bodies in the universe and those of the lightest atom: to it nothing would be uncertain, and the future, as well as the past would be present to its eyes. The human mind offers us, faint sketch of this intelligence [1].

Molecular dynamics (MD) can be termed as Laplace's vision of Newtonian mechanics on supercomputers. Molecular dynamics is the term used to describe the solution of the classical equation of motion (Newton's equations) for a set of molecules. In MD particles move at constant velocity between perfectly elastic collisions, and it is possible to solve the dynamic problem without making any approximations, within the limits imposed by machine accuracy. Computer simulation has been very powerful tool to attack many body problems in Statistical physics, Physical chemistry and Biophysics. Although the theoretical description of complex system in the framework of statistical physics is rather well developed and experimental techniques for detailed microscopic are sophisticated, it is often possible to study specific aspect of those system in great details via simulation only. There are only handfuls of non-trivial, exactly

soluble problem in statistical mechanics, 2-D Ising model and ideal gas being example. Some problems in statistical mechanics, while not being exactly soluble, are analyzed based on straightforward approximation scheme. Problem is that for many problems of interest these “straightforward approximations” do not work. For many systems it may not be even clear that how to begin constructing an approximate theory. In all such cases computer simulation can help a lot by providing sufficient input about microscopic properties of complex systems of interest. Computer simulations provide “exact” results for the problems which otherwise only be soluble by approximate methods, or might be quite intractable. Thus computer simulations can be used to test approximate theories. Results of computer simulations can also be compared with real experiment than it can be used to test underlying model. Simulation offers insights to experimentalist to interpret new result on the basis of microscopic details of system.

Computer simulations act as a bridge between microscopic world and macroscopic world of laboratory. We provide microscopic input about system (masses of constituent atoms and interaction between them), we get macroscopic properties measurable in experiments, like equation of state, diffusion constant, correlation functions to name a few as simulation output. Simulation are also used to study properties under extremes of temperature and pressure, which may be difficult or impossible to carry out experimentally, however can provide details useful for lot of technological applications as well as for academic interest. Simulation has also been used to improve our understanding of phase transition and behavior at interfaces. Before we go into the details of computer simulation technique we give a brief history of the development of this field.

6.1.1 History Of Simulation

In 1953 Metropolis et. al.[2] did the first molecular simulation using Monte Carlo method (MC) to calculate the equation of state of rigid sphere in two dimension. This was followed by the celebrated numerical work by Fermi, Pasta and Ulam [3] to test ergodicity in a system of coupled oscillators. The first MD simulation was subsequently performed by Alder and Wainwright [4] in the year 1957 in the context of phase transition in a system of hard sphere. This was followed by the radiation damage study in copper by Vineyard et. al. [5] in 1960. In 1964 Rahman [6] made the first successful attempt to simulate a molecular system with realistic potential using MD like the phase behavior of Lennard-Jones particles. Since then, the properties of the Lennard-Jones model have been thoroughly investigated [7, 8]. Later he also studied the properties of liquid argon and water using MD simulation[6, 9]. After that diatomic molecules was modeled using molecular dynamics by Harp and Berne[10]. In the recent years MD simulation has been used to study problems in areas such as biophysics (proteins and DNAs), polymer, liquid crystal (both thermotropic and lyotropic), nanoscince (nanotube, grapheme, bucky-ball) as well as many

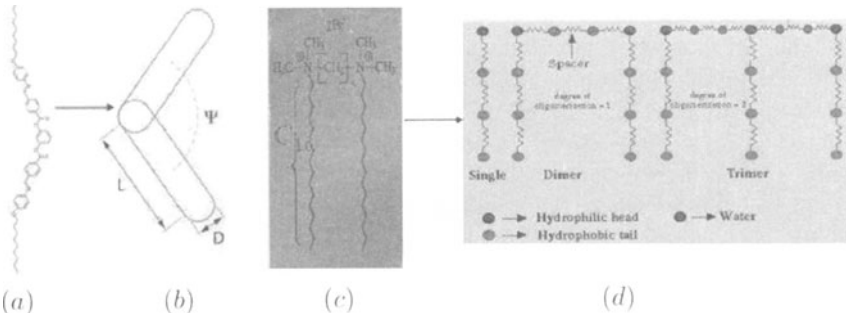


Figure 6.1: Examples of molecular models at various levels. (a) Atomistic model of a class of banana liquid crystal (b) coarse-grained representation of the banana molecules using spherocylinder of aspect ratio L/D (c) atomistic model of a two-tail surfactant (d) coarse-grained representation of various class of surfactants using simple bead-spring model.

other condensed matter systems. Computer simulation has also advanced to non-equilibrium system, stochastic dynamics and incorporation of quantum effects. This article is by no means a exhaustive treatment of the subject. There exist several excellent text books[11, 13] which give a very comprehensive understanding of the various advanced concepts of the simulation methodology. The reader is referred to these for further details.

The rest of the article is organized as follows: In section 2 we describe the model building, in section 3 we describe the basic of Hamiltonian dynamics as a basis for the equation of motion and will discuss various schemes for integration used in simulations. Section 4 is about various complexities arising during simulation and way of dealing with those complexities. In Section 5 simulation techniques for different ensembles has been discussed. Finally we conclude this article by giving two case studies with MD simulations.

6.2 Building Model

Before we can study the properties of a system via computer simulation we need to develop a microscopic model of the system. In fact appropriate model building for a given system is one of the key challenges in the whole area of molecular simulation and requires great efforts and intuition. The ingredients and details of the model depend on the properties to be studied and length scale and time scale to be explored. Depending on the access to the level computational resources, details of the molecular models can vary. Model can be as simple as representing molecule by rigid rods, hard/soft sphere (beads), and sphere/beads connected through spring (bead spring model) or other geometrical shapes. Or we can have fully atomistic model of the molecules. Figure 6.1 below shows some examples of various level of model building:

In Fig.6.1(a) we show the molecular model at full atomic detail of a banana liquid crystal which exhibits various Liquid crystalline phases. The LC phases of this molecule can be simulated using this atomistic description but is computationally very expensive. Many LC phases of this molecule can also be simulated using a more coarse-grained model as shown in Fig.6.1(b) where we consider the rigid core part of the molecule in Fig.6.1(a) and represent using hard spherocylinder where we consider only excluded volume interaction. In Fig.6.1(c) we represent molecular model of lipid molecule which exhibits micellar, lamellar and bilayer phases. Again another appropriate coarse-grained molecular model can be developed as shown in Fig.6.1(d) which can capture many of the phases

In principle we should consider all atomic details while dealing with molecular systems including bond formation and breakage mechanism taking into account all quantum effects, but it turns out to be too difficult to perform in practice. Moreover for many problems of interest these approximate simple models seem to be adequate enough. With the power of modern computer and recent algorithm development it is possible to take care of all quantum effects. To describe molecular charge, a set of fictitious charges are distributed in such a way that this distribution reproduce known multipole moments.

Microscopic state of a system may be specified in terms of the positions and momenta (assuming classical description is adequate) of constituent set of particles. Within adiabatic approximation, we neglect electronic motion and consider only nucleic motion. This approximation is excellent for a wide range of system but is unsuitable for reaction involving electronic rearrangement such as bond formation and cleavage, polarization and chemical bonding of metal ions. Quantum approaches are used for such studies.

For a classical system, specifying the instantaneous positions and momenta of all the particles constituting the system can specify the microstate at any time t . For N particles there are $3N$ coordinates q_1, q_2, \dots, q_{3N} and $3N$ conjugate momenta p_1, p_2, \dots, p_{3N} . The Hamiltonian of the system can be written in term of these q_i 's and p_i 's as follows

$$\begin{aligned} H(q, p) &= K(p) + V(q) \\ q &= (q_1, q_2, \dots, q_N) \\ p &= (p_1, p_2, \dots, p_N) \end{aligned} \quad (6.1)$$

K and V being kinetic and potential energy respectively. q is the generalized coordinate, it may be Cartesian coordinate of each nucleus or Cartesian coordinate of each center of mass (COM) with orientation parameter in case of molecules and rigid bodies p is conjugate momenta.

Kinetic energy is defined as

$$K = \sum_{i=1}^N \sum_{\alpha} p_{i\alpha}^2 / 2m_i \quad (6.2)$$

where i stands for particle number and α represents various components of momenta. Potential energy V depends on intermolecular interaction. We will

describe various potential for different kind of systems.

$$V = \sum_i v_1(r_i) + \frac{1}{2} \sum_i \sum_{i>j} v_2(r_i, r_j) + \sum_i \sum_{j>i} \sum_{k>j>i} v_3(r_i, r_j, r_k) + \dots \quad (6.3)$$

where v_1 represents effect of external field on individual atoms, v_2 is pair potential, and is most important in computer simulation. In general we consider only pair potential.

Once we have information of Hamiltonian, we have equations of motion given by

$$\frac{d^2\vec{r}}{dt^2} = -\nabla V(\vec{r}) \quad (6.4)$$

This governs the evolution of the system and is at the heart of Molecular dynamics simulation. Numerically there are various schemes to solve the above differential equation. In the next section we will discuss few of them. A major challenge in the field of molecular dynamics is to describe the inter-atomic potential $V(r)$ (inter and intra-molecular potential in case of molecular systems). The accuracy and validity of the simulation results critically depends on the quality of the potential $V(r)$. There exist several well-known empirical force-fields which give forms as well as parameters for a variety of intra and inter-molecular potential. Below we discuss those.

6.2.1 Discussion on Force Fields

The inter and intra-molecular interaction can be modeled by empirical forms and the total potential energy is given as follows:

$$E_{total} = E_{vdW} + E_{elec} + E_{bond} + E_{angle} + E_{torsion} \quad (6.5)$$

Where E_{total} , E_{vdW} , E_{elec} , E_{bond} , E_{angle} , and $E_{torsion}$ are the total energy, the van der Waals, electrostatic, bond stretching, angle bending, and torsion energy components, respectively.

The van der Waals interaction is given by the 12 – 6 LJ interaction of the following form

$$E_{vdW}(R) = D_0 \left\{ \left(\frac{R_0}{R} \right)^{12} - 2 \left(\frac{R_0}{R} \right)^6 \right\} \quad (6.6)$$

where D_0 is the strength of the interaction and R_0 is the range of interaction. These constants can be found either by first principle quantum calculation or by experimental input. In general these parameters are available for various atom types from various well known force fields such as Dreiding, AMBER and CHARMM. Interaction parameters between different kind of atom types (like between C & O) are calculated by taking either arithmetical mean or geometrical mean. Other commonly used form of non-bond interaction is the

so-called Buckingham potential and has the following form

$$E_{Buckingham} = \sum_{\substack{\text{nonbonded} \\ \text{pairs}}} \left(A \exp(-cr_{ik}) - \frac{B}{r_{ik}^6} \right) \quad (6.7)$$

Again constants appearing in these potential are given in available force fields.

In case one needs to maintain special coordination using non-bond interaction Morse potential is the choice and has the following form

$$E_{Morse} = \sum_{\substack{\text{nonbonded} \\ \text{pairs}}} D_o \left(1 - e^{-\alpha(R-R_o)} \right)^2 \quad (6.8)$$

where D_o , R_o and α are constants.

Electrostatic interaction between charged particles can be computed using Coulomb's law and given by

$$E_{Coulomb} = \sum_{\substack{\text{nonbonded} \\ \text{pairs}}} \frac{q_i q_k}{\epsilon r_{ik}} \quad (6.9)$$

q_i 's being charge on each atom and ϵ being dielectric constant. In fact computationally this is the most expensive calculation because of its long range character. In Complexity of force calculation section, we will discuss various algorithms to compute Coulomb's interaction efficiently.

Apart from these various non-bond interactions discussed above for molecular systems we have also the following bonded interaction (as shown in Fig.6.2) present in the systems to maintain molecular topology.

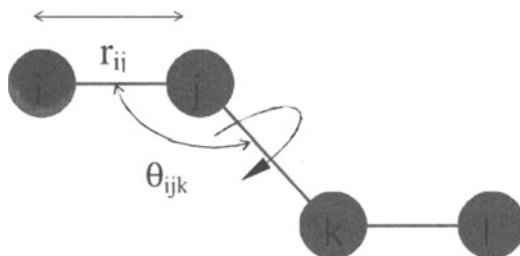


Figure 6.2: Different intra-molecular interactions.

The intra-molecular interaction corresponding to the bond stretching potential can be described by the harmonic potential of the following form

$$E_{bond}(r_{ij}) = \frac{1}{2}K_b(r_{ij} - r_0)^2 \quad (6.10)$$

The harmonic potential is adequate only for small deviations from reference value. For large deviations **Morse potential** is the choice. This is particularly useful for maintaining specific coordination in a given geometry. This has functional form:

$$E_{Morse} = \sum_{1,2 pairs} D_b \{1 - \exp[-K_m(r - r_0)]\} \quad (6.11)$$

Where the parameters D_b and K_m characterize the well depth and well width respectively.

Similarly angle bending potential can be described by the following harmonic form

$$E_{angle}(\theta_{ijk}) = \frac{1}{2}K_\theta(\theta_{ijk} - \theta_0)^2 \quad (6.12)$$

Many available force fields however use a cosine harmonic form rather than simple theta harmonic as given above. In case of cosine harmonic theta the angle bending potential has the following form

$$E_{angle}(\theta_{ijk}) = \frac{1}{2}K'_\theta (\cos \theta_{ijk} - \cos \theta_0)^2 \quad (6.13)$$

Apart from the bond stretching and angle bending potential to maintain certain topology of the molecular system torsional potentials are included. Mainly two types of torsional potentials are used: dihedral angle potential and improper torsions. The dihedral angle potential is mostly used to constrain the rotation around a bond and involves four consecutive bonded atoms (i-j-k-l) as shown in Fig.6.2. Improper torsion is used to maintain planarity of certain atoms and involves four atom which are not bonded in the same sequence as i-j-k-l. Out-of-plane bending is incorporated through the improper torsion potential. In many force fields instead of improper torsion an inversion potential is used. One of the most commonly used dihedral potential is the cosine form given by

$$E(\phi_{ijkl}) = \sum_n \frac{V_n}{2} [1 + \cos(n\phi_{ijkl} - \phi_0)] \quad (6.14)$$

Where n is an integer. For each such rotational sequence described by torsion angle ϕ , n denotes the periodicity of the rotational barrier, and V_n is the associated barrier height. ϕ_0 is reference torsion angle.

Commonly used improper torsion is harmonic in nature and is described by following functional form

$$E(\varphi_{ijkl}) = k_{ijkl}^I (\varphi_{ijkl} - \varphi_0)^2 \quad (6.15)$$

Where k_{ijkl}^I is the force constant.

6.3 Various Schemes of Integration

Main idea of simulation is to generate various snapshots of the system in certain ensemble to get average thermodynamic properties or to get time evolution of system. The evolution is governed by equation (6.4). Position of constitute atoms of system on next time step can be found by integrating equation (6.4). This can be integrated in many ways. The choice of the integration scheme will largely depend on the following criteria:

1. Newton's Equations are time reversible so should be integrator.
2. Hamiltonian dynamics preserve the magnitude of volume element in phase space and so our algorithm should have this area preserving property.
3. It should be fast and require little memory
4. It should be able to produce real classical trajectory as close as possible
5. It should be easy to code
6. It should permit large time step
7. It should be stable i.e. energy should be conserved in long term

There are many integration algorithm available satisfying these criteria. Most adapted algorithm is due to Verlet which we will describe in details now.

6.3.1 Verlet Algorithm

Taylor Expansion for position around time t is

$$r(t + \delta t) = r(t) + v(t)\delta t + 1/2a(t)\delta t^2 + b(t)\delta t^3 + O\delta t^4 \quad (6.16)$$

If we reverse the time we have

$$r(t - \delta t) = r(t) - v(t)\delta t + 1/2a(t)\delta t^2 - b(t)\delta t^3 + O\delta t^4 \quad (6.17)$$

Adding the above two equations and keeping terms up to δt^2 we get-

$$r(t + \delta t) = 2r(t) - r(t - \delta t) + a(t)\delta t^2 + O\delta t^4 \quad (6.18)$$

This is the update equation for position. Similarly for velocity update we have

$$v(t) = r(t + \delta t) - r(t - \delta t)/2\delta t \quad (6.19)$$

Equation (6.18) and (6.19) are the update equations in Verlet algorithm[8]. Thus Verlet algorithm takes position and acceleration at time t and position at previous time step as input. Note that for Verlet integrator we need position at "previous time step" which can be obtained by simple approximation as follows

$$r(t_0 - \delta t) = r(t_0) - v(t_0)\delta t \quad (6.20)$$

It is easy to see that Verlet integrator indeed satisfies the above listed criteria.

Time Reversible

Forward time step equation

$$r(t + \delta t) = 2r(t) - r(t - \delta t) + \frac{1}{m} F(t) \delta t^2 \quad (6.21)$$

Reverse time step (replace dt with $-dt$)

$$r(t + (-\delta t)) = 2r(t) - r(t - (-\delta t)) + \frac{1}{m} F(t) (-\delta t)^2 \quad (6.22)$$

$$r(t - \delta t) = 2r(t) - r(t + \delta t) + \frac{1}{m} F(t) \delta t^2 \quad (6.23)$$

Thus we have same algorithm to move system backward with same force and same position.

Accuracy

Verlet algorithm calculates position accurate up to order of δt^4 and velocities are accurate up to δt^2 . However it is not very accurate in terms of numerical precision as it adds large and small numbers in same equation.

$$r(t + \delta t) - r(t) = r(t) - r(t - \delta t) + \frac{1}{m} F(t) \delta t^2 \quad (6.24)$$

Here term on left hand side is of order δt while on right hand side first term is of the order of δt^0 second term of δt^1 and third term is of δt^2 .

Memory usage and efficiency

It requires $9N$ ($3N$ position of previous step and $6N$ for current step) words of memory so it is compact. Verlet algorithm is simple and easy to implement in a MD code.

Area preserving property

This algorithm preserves area in phase which is essential criteria for an integrator[14]. It has excellent energy conservation even at large time step.

6.3.2 Leap-Frog Algorithm-

Leap-Frog algorithm can be obtained by simple algebraic manipulation of the Verlet integrator. It eliminates one of the major disadvantage of the Verlet algorithm namely the addition of small numbers $O(\delta t^2)$ to differences in large ones $O(\delta t^0)$. In this scheme first velocity at half time-step is calculated which in turn is used to update the position at full time step. The equations for Leap-Frog algorithm is as follows

$$r(t + \delta t) = r(t) + v(t + \frac{1}{2}\delta t)\delta t \quad (6.25)$$

$$v(t + \frac{1}{2}\delta t) = v(t - \frac{1}{2}\delta t) + \frac{1}{m} F(t) \delta t \quad (6.26)$$

The Leap-Frog algorithm is equivalent to the Verlet algorithm as can be seen easily as follows. Substituting equation (6.26) in equation (6.25) we have

$$r(t + \delta t) = r(t) + [v(t - \frac{1}{2}\delta t) + \frac{1}{m}F(t)\delta t] \delta t \quad (6.27)$$

From equation (6.25), we can also get $r(t)$ evaluated at previous time step as follows

$$r(t) = r(t - \delta t) + v(t - \frac{1}{2}\delta t)\delta t$$

Substituting the value of $v(t - \frac{1}{2}\delta t)$ from above equation in into equation (6.26), we get

$$\begin{aligned} r(t + \delta t) &= r(t) + [(r(t) - r(t - \delta t)) + \frac{1}{m}F(t)\delta t^2] \\ &\doteq 2r(t) - r(t - \delta t) + \frac{1}{m}F(t)\delta t^2 \end{aligned} \quad (6.28)$$

Equation (6.28) is equivalent to the original Verlet equation as given by equation (6.18). Note that for Leap-Frog algorithm we need to have velocity at the previous time step which can be obtained by simple approximation as follows

$$v(t_0 - \delta t) = v(t_0) - \frac{1}{m}F(t_0)\frac{1}{2}\delta t \quad (6.29)$$

Velocity at current time step can be obtained using simple interpolation like

$$v(t) = (v(t + \frac{1}{2}\delta t) + v(t - \frac{1}{2}\delta t))/2 \quad (6.30)$$

One of main advantage of the Leap-Frog integration scheme is that we need not add numbers which are different order in δt .

6.3.3 Velocity-Verlet Algorithm

Both in the position Verlet and Leap-Frog integration scheme velocity is not treated accurately. To handle velocity in satisfactorily manner another form of Verlet scheme (known as Velocity -Verlet algorithm) has been proposed which can be obtained as follows

$$r(t + \delta t) = r(t) + v(t)\delta t + \frac{1}{2m}F(t)\delta t^2 \quad (6.31)$$

$$v(t + \delta t) = v(t) + \frac{1}{2m}[F(t) + F(t + \delta t)]\delta t \quad (6.32)$$

Basic Verlet Scheme can be recovered from these equations by eliminating velocity. This algorithm also requires storage of 9N words i.e. position, velocity and acceleration at current time step. Although it is not implemented same as above, it involves one intermediate step. First position is updated with equation (6.18) and velocities at mid step are computed using

$$v(t + \frac{1}{2}\delta t) = v(t) + \frac{1}{2m}[F(t)]\delta t \quad (6.33)$$

The force and acceleration at time $t + \delta t$ are then computed and velocity move is computed with

$$v(t + \delta t) = v(t + \frac{1}{2}\delta t) + \frac{1}{2m}[F(t + \delta t)]\delta t \quad (6.34)$$

Due to stability, accuracy and simplicity this is the most preferred choice of integrator.

6.3.4 Higher Order Integrator

To achieve better accuracy both in position and velocity higher order integration scheme can be employed. Such schemes allow one to use larger time step without compromising on energy accuracy. But one of the major drawbacks of such algorithm is that they are not time reversible and do not have area preserving property. Also implementation wise they require more storage. As an example we will discuss the predictor-corrector algorithm. The basic idea behind the predictor-corrector[15] algorithm is as follows:

1. **Predictor:** use the position and its first n derivatives at time t (velocity, acceleration etc.) to find the position and its first n derivatives (velocity, acceleration etc.) at time $t + \delta t$.
2. **Force evaluation:** Use the predicted position to compute the force and acceleration at the predicted positions. The resulting acceleration will be in general different from the “predicted acceleration” in previous step.
3. **Corrector:** use the new acceleration to correct the predicted position, velocities and acceleration.

Use the Taylor expansion of the position at time $t + dt$

$$r(t + \delta t) = r(t) + v(t) \delta t + \frac{\delta t^2}{2} a(t) + \frac{\delta t^3}{6} b(t) + \frac{\delta t^4}{24} c(t) + \dots \quad (6.35)$$

Where v is the velocity, a is the acceleration, b is the third derivative of position, c is the fourth derivative etc.

Using the Taylor expansion for velocity, acceleration etc. we have

$$v(t + \delta t) = v(t) + a(t)\delta t + \frac{\delta t^2}{2} b(t) + \frac{\delta t^3}{6} c(t) + \dots \quad (6.36)$$

$$a(t + \delta t) = a(t) + b(t)\delta t + \frac{\delta t^2}{2} c(t) + \dots \quad (6.37)$$

$$b(t + \delta t) = b(t) + c(t)\delta t + \dots \quad (6.38)$$

The difference between the predicted (step 1) and calculated (step 2) acceleration is given by

$$\Delta a(t + \delta t) = a^c(t + \delta t) - a(t + \delta t) \quad (6.39)$$

and is used to correct the positions and velocities in the correction step as follows

$$r^c(t + \delta t) = r(t + \delta t) + c_0 \Delta a(t + \delta t) \quad (6.40)$$

$$v^c(t + \delta t) = v(t + \delta t) + c_1 \Delta a(t + \delta t) \quad (6.41)$$

$$a^c(t + \delta t) = a(t + \delta t) + c_2 \Delta a(t + \delta t) \quad (6.42)$$

$$b^c(t + \delta t) = b(t + \delta t) + c_3 \Delta a(t + \delta t) \quad (6.43)$$

The values of the coefficients depend on the order of the Taylor series expansion. Gear[15] has suggested the best values of the set of coefficients c_0, c_1, c_2, c_3 .

6.3.5 Hamilton Dynamics

In the preceding section we have discussed some of the most commonly used integration scheme used in literature. In this section we will give a more formal derivation of the Verlet integration scheme using the formulation of Hamiltonian dynamics. First we will show that Hamilton dynamics is equivalent of Newton's Dynamics. Then we will show that Hamilton dynamics preserves area in phase space and is time reversible.

For a classical system, specifying the instantaneous positions and momenta of all the particles constituting the system can specify the microstate at any time t . For N particles there are $3N$ coordinates q_1, q_2, \dots, q_{3N} and $3N$ conjugate momenta p_1, p_2, \dots, p_{3N} . The equations of motion are first order differential equations and are given by

$$\dot{q}_i = \frac{\partial H(q_i, p_i)}{\partial p_i} \quad \dot{p}_i = -\frac{\partial H(q_i, p_i)}{\partial q_i} \quad (6.44)$$

Let us consider a simple one-particle system in one dimension with a Hamiltonian.

$$H = \frac{p^2}{2m} + U(x) \quad (6.45)$$

The equations of motion are

$$\dot{q} = \frac{p}{m} \quad \dot{p} = -\frac{dU}{dx} = F(x) \quad (6.46)$$

Now Liouville's theorem states that any phase space function $A(x, p)$ evolves according to the following equation

$$\frac{dA}{dt} = \{A, H\} \quad (6.47)$$

Where $\{A, H\}$ is the Poisson bracket and is given by

$$\{A, H\} = \frac{\partial H}{\partial p} \frac{\partial A}{\partial x} - \frac{\partial H}{\partial x} \frac{\partial A}{\partial p} \quad (6.48)$$

The evolution equation (6.47) gives back Hamilton's equation of motion: To see this consider $A(x, p) = x$. Then

$$\begin{aligned} \frac{dx}{dt} &= \dot{x} = \{x, H\} \\ \{x, H\} &= \frac{p}{m} \frac{\partial x}{\partial x} - \frac{dU}{dx} \frac{\partial x}{\partial p} = \frac{p}{m} \quad \text{since } \frac{\partial x}{\partial p} = 0 \end{aligned} \quad (6.49)$$

So we have $\dot{x} = p/m$ $\dot{x} = p/m$.

Similarly if we consider $A(x, p) = p$, we have the equation of motion for p as

$$\begin{aligned}\frac{dp}{dt} &= \dot{p} = \{p, H\} \\ \{p, H\} &= \frac{p}{m} \frac{\partial p}{\partial x} - \frac{dU}{dx} \frac{\partial p}{\partial p} = -\frac{dU}{dx} = F(x) \\ \dot{p} &= F(x)\end{aligned}\quad (6.50)$$

Thus we get same equations of motion as in equation (6.46).

Now define a two-dimensional phase space vector $\Gamma = (x, p)$. Hamilton's equation of motion for Γ is given by

$$\frac{d\Gamma}{dt} = \{\Gamma, H\} \quad (6.51)$$

We define Liouville operator L such that $iL\Gamma = \{\Gamma, H\}$

The equation of motion given by equation (6.51) in Liouville operator form is given by,

$$\frac{d\Gamma}{dt} = iL\Gamma \quad (6.52)$$

Solution of this equation of motion is given by

$$\Gamma(t) = e^{iLt}\Gamma(0) \quad (6.53)$$

The operator $\exp(iLt)$ is called the classical propagator and acts as phase space evolution operator. Notice that the presence of i allows one to make an analogy with the QM propagator $\exp(-iHt/\hbar)$.

In general it is difficult to evaluate $\exp(iLt)$ because of the following reason. iL can be written as

$$iL = \frac{p}{m} \frac{\partial}{\partial x} + F(x) \frac{\partial}{\partial p} = iL_1 + iL_2 \quad (6.54)$$

Where, $iL_1 = \frac{p}{m} \frac{\partial}{\partial x}$ and $iL_2 = F(x) \frac{\partial}{\partial p}$

The difficulty in any computation arises from the fact that iL_1 and iL_2 do not commute: $[iL_1, iL_2] \neq 0$.

Since they don't commute,

$$e^{(iL_1+iL_2)t} \neq e^{iL_1 t} e^{iL_2 t} \quad (6.55)$$

Trotter Theorem helps us to evaluate evolution operator in the following way:

$$e^{(iL_1+iL_2)t} = \lim_{M \rightarrow \infty} \left[e^{iL_2 t/2M} e^{iL_1 t/M} e^{iL_2 t/2M} \right]^M \quad (6.56)$$

For large but finite M above equation can be approximated as

$$e^{(iL_1+iL_2)t} = \left[e^{iL_2 t/2M} e^{iL_1 t/M} e^{iL_2 t/2M} \right]^M \quad (6.57)$$

This implies:

$$e^{(iL_1+iL_2)t/M} \approx e^{iL_2t/2M} e^{iL_1t/M} e^{iL_2t/2M} \quad (6.58)$$

The expression on the left looks like approximate propagation of the system up to time t by M application of the operator in the bracket. If we interpret t/M as single time step, δt , then we have

$$e^{iL\delta t} = e^{(iL_1+iL_2)\delta t} \approx e^{iL_2\delta t/2} e^{iL_1\delta t} e^{iL_2\delta t/2} \quad (6.59)$$

This is the propagator $U(\delta t)$ for time step δt . $U(\delta t)$ is unitary and preserve the time reversibility of the dynamics.

$$U^+(\delta t)U(\delta t) = I \quad (6.60)$$

The unitarity of the propagator implies time reversal symmetry in the equations of motion. If the system is propagated forward in time up to a time t and then the clock is allowed to run backwards for a time $-t$, the system will evolve according to the same equations of motion but the direction of the velocities will be reversed, so that the system will simply return to its initial condition. To see this we note that $U(-t) = \exp(-iLt)$

Now apply $U(t)$ on $\Gamma(0)$ to get $\Gamma(t)$ followed by $U(-t)$:

$$\Gamma(t) = U(t)\Gamma(0)$$

Operating $U(-t)$ will give back the

$$U(-t)U(t)\Gamma(0) = e^{-iLt}e^{iLt}\Gamma(0) = \Gamma(0)$$

So we have

$$U(-t)U(t) = I \quad (6.61)$$

Equation (6.61) implies time reversibility. Another important property of the unitary operator $U(t)$ is that its determinant is one. This is consistent with the fact that volume in phase space remains conserved under Hamilton's equation. So we have demonstrated that evolution propagator $U(\delta t)$ satisfies two fundamental criteria of the Newton's equation of motion namely the time reversibility and the area preserving property. So equation of motion derived from such evolution operator will have these properties in-built. Now we will demonstrate that evolution operator gives back the original Verlet equation as given in equation(6.19)-(6.20).

To see this we first apply equation (6.59) on x , the position of particle at time t to get position $x(t+dt)$

$$\begin{aligned} U(\delta t)x &= e^{\frac{\delta t}{2}F(x)\frac{\partial}{\partial p}} e^{\delta t\frac{p}{m}\frac{\partial}{\partial x}} e^{\frac{\delta t}{2}F(x)\frac{\partial}{\partial p}}x \\ &= e^{\frac{\delta t}{2}F(x)\frac{\partial}{\partial p}} e^{\delta t\frac{p}{m}\frac{\partial}{\partial x}}x \\ &= e^{\frac{\delta t}{2}F(x)\frac{\partial}{\partial p}}(x + \frac{\delta t}{m}p) \\ &= x + \frac{\delta t}{m}(p + \frac{\delta t}{2}F(x)) \end{aligned}$$

So we have the update equation for the position given by

$$x(t + \delta t) = x(t) + \frac{\delta t}{m} p(t) + \frac{\delta t^2}{2m} F(x, t) \quad (6.62)$$

Similarly when we apply equation (6.59) on p , the velocity of particle at time t , we get velocity of the particle at time $t+\delta t$ to as follows

$$\begin{aligned} U(\delta t)p &= e^{\frac{\delta t}{2}F(x)\frac{\partial}{\partial p}}e^{\delta t\frac{p}{m}\frac{\partial}{\partial x}}e^{\frac{\delta t}{2}F(x)\frac{\partial}{\partial p}}p \\ &= e^{\frac{\delta t}{2}F(x)\frac{\partial}{\partial p}}e^{\delta t\frac{p}{m}\frac{\partial}{\partial x}}(p + \frac{\delta t}{2}F(x)) \\ &= e^{\frac{\delta t}{2}F(x)\frac{\partial}{\partial p}}(p + \frac{\delta t}{2}F(x + \frac{\delta t}{m}p)) \\ &= p + \frac{\delta t}{2}F(x) + \frac{\delta t}{2}F(x) + \frac{\delta t}{m}(p + \frac{\delta t}{2}F(x)) \end{aligned}$$

So we have the velocity update equation as follows

$$\begin{aligned} p(t + \delta t) &= p(t) + \frac{\delta t}{2}[F(x, t) + F(x + \frac{\delta t}{m}p + \frac{\delta t^2}{2m}F(x))] \\ &= p(t) + \frac{\delta t}{2}[F(x(t)) + F(x(t + \delta t))] \end{aligned} \quad (6.63)$$

Equations (6.62) and (6.63) are same as the Verlet equation as given by equation (6.18) and (6.19). So Verlet equations have both the time reversible and area preserving properties.

6.3.6 Dealing with Molecules: SHAKE Algorithm

At this point we discuss the optimum choice of the integration time step for a numerically stable integrator as well as better energy conservation. In a molecular system, the choice of time step is limited by the various time scales associated with vibrational degrees of freedom such as bond vibration, angle stretching or torsional mode. In table I we list time scales associated with various vibrational mode of the system. In general the bonds involving hydrogen atoms have the fastest vibrational mode and they limit the time step of integration to 1 fs.

Table I: Typical time scale associated with various vibrational modes in molecular system. The table is based on the values given in reference 13.

Vibrational mode	Wave number ($1/\lambda$) cm^{-1}	Period T_p (λ/c) fs	$T_p/2\pi$ (fs)
O-H, N-H stretch	3200-3600	9.8	3.1
C-H stretch	3000	11.1	3.5
CC, CN stretch	2100	15.9	5.1
C=C stretch	1700	19.6	6.2
H-O-H bend	1600	20.8	6.4
O-C-O bend	700	47.6	15

So for simulation of systems having hydrogen bond we can use 1 fs time step without having any problem with energy conservation. Another solution to this problem is to restrain these fast degrees of freedoms while solving the un-constrained degrees of freedom. Bonds involving H have highest frequency hence they are constrained during dynamics so that larger time step can be used. Several algorithms exist for this purpose. The SHAKE algorithm for bond constraints was introduced by Ryckaert *et al*[16]and is widely used in molecular simulation. A full description of SHAKE algorithm is outside the scope of this article. The reader is referred to the original article for further details.

Basic idea of SHAKE is to use Lagrange multiplier formalism to enforce bonds distances constant. Suppose we have N_c such constrained given by

$$\alpha_k = r_{k_1 k_2}^2 - R_{k_1 k_2}^2 = 0, \quad \text{where } k = 1, 2, 3, \dots, N_c$$

$R_{k_1 k_2}$ being constrained distant between atoms k_1 and k_2 atoms. This leads to modified constrained equation of motion

$$m_i \frac{d^2 r_i(t)}{dt^2} = -\frac{\partial}{\partial r_i} [V(r_1, \dots, r_N) + \sum_{k=1}^{N_c} \lambda_k(t) \alpha_k(r_1, \dots, r_N)] \quad (6.64)$$

Where m_i is mass of i^{th} particle and λ_k is the Lagrange multiplier(unknown) for k^{th} constraint. This equation can be solved for unknown multiplier by solving N_c quadratic coupled equations. And we get the following equation of motion

$$\begin{aligned} r_{k_1}(t + \Delta t) &= r_{k_1}^{uc}(t + \Delta t) - 2(\Delta t)^2 m_{k_1}^{-1} \lambda_k(t) r_{k_1 k_2}(t) \\ r_{k_2}(t + \Delta t) &= r_{k_2}^{uc}(t + \Delta t) - 2(\Delta t)^2 m_{k_2}^{-1} \lambda_k(t) r_{k_1 k_2}(t) \end{aligned} \quad (6.65)$$

Where r_{uc} is position updates with unconstrained force only. This procedure is repeated till defined tolerance τ given as

$$\frac{|r_{k_1 k_2}(t + \Delta t) - R_{k_1 k_2}|}{R_{k_1 k_2}} \leq \tau \quad (6.66)$$

6.3.7 Boundary Condition

Due to computational constraint one is forced to simulate small system with few thousands of particles in the simulation box. Thermodynamic properties calculated from such small system when used to study bulk properties become a problem. In such situation proper boundary condition is very critical for studying macroscopic properties of system using a smaller system size. There exist several ways to treat the boundary condition in molecular dynamics simulation. The widely used method is to use periodic boundary condition (PBC). In the case of PBC simulation cell is replicated in all direction to form an infinite lattice as shown in Fig.6.3. During simulation particles in the central cell are only considered and when a particle moves in the central cell, its periodic image in each of the neighboring cell also moves in the same fashion. If a particle moves away from the central cell, its periodic images appear from the opposite face.

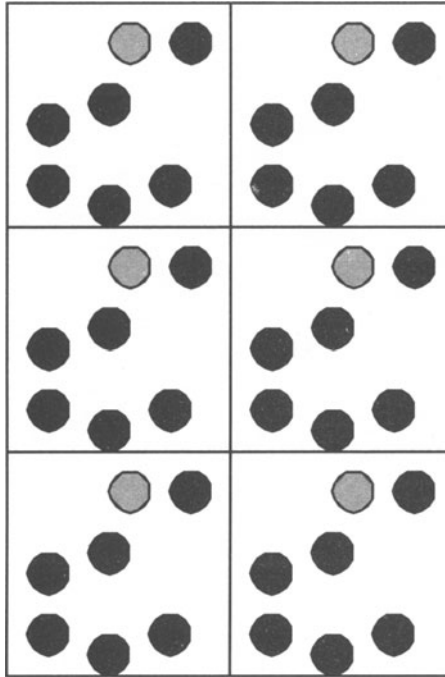


Figure 6.3: In periodic boundary condition central simulation cell is replicated in all direction to form an infinite lattice.

This implies that there is no rigid boundary wall and the number of particles in the central simulation cell is conserved during the course of simulation. One of the major drawbacks of using PBC is that it suppresses fluctuation that have wavelength greater than the length of the central simulation cell. This could be problem near critical point where fluctuation plays dominant role. Also PBC can introduce new artificial correlations length in the simulation. It can also affect the rate at which a simulated liquid nucleates and forms a solid or glass when rapidly cooled [17]. However, artifact of PBC can be determined by performing simulations using a variety of cell sizes and shape.

The use of PBC has also important implication the way one computes the interaction energy and hence forces. To illustrate the difficulty in calculating the energy and hence forces consider the evaluation of energy for particle **A** in the simulation cell as shown in Fig.6.4. Assuming pair wise interaction we should include interaction of atom A with all other atoms in the simulation box. There are $N - 1$ such term. However, we must also include interaction coming from images lying in the surrounding boxes.

That is an infinite number of terms and it is not feasible to include interactions with all images. For short-range interaction this problem is resolved by invoking what is called minimum image convention. In this case we construct a

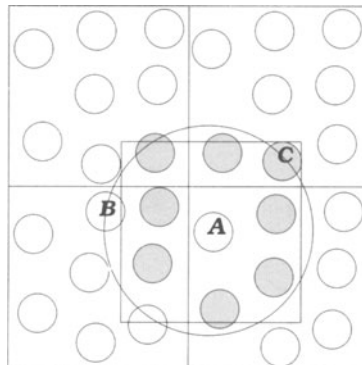


Figure 6.4: Illustration of minimum image convention. Atom A interacts with atoms (gray shaded) within the box drawn by assuming atom A is at the center. Although atoms B and C are the same distance away, atom A does not interact with atom B as it is out of the box.

simulation box of same size as the original box with atom A at its center. Now minimum image convention says that atom A interacts with those atoms which lie in this region, that is with the closest periodic images of the other $N - 1$ atoms (see Fig.6.4).

6.4 Complexity of Force Calculation

For a system with pair wise additive interactions with minimum image convention we have to evaluate $N(N - 1)/2$ pair interactions at each MD step. So the time needed for computation of energy/force scales as N^2 . Even for a moderate system size this computation is very expensive. For short range interaction like LJ potential, major contribution comes from the neighbors close to the atom of interest. One of the simplest way to reduce the computation cost is to truncate the interaction at some cut-off using a spherical cut-off to reduce the number of pair computation. This technique was first used in simulations by Metropolis².

While truncating potential following points should be remembered

1. The cutoff distance should be smaller than $L/2$, where L is the minimum of the box dimension in any periodic direction.
2. Thermodynamic properties are different for a truncated potential compared to non-truncated case. However, we can apply long range correction to get back approximately the non-truncated properties.
3. Cutoff introduces discontinuity in the force and energy computation. This has serious consequence on the energy conservation and stability of the simulation

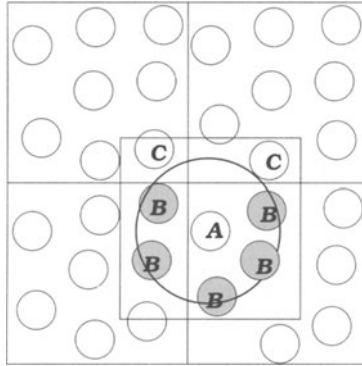


Figure 6.5: The number of pair computations can be reduced by introducing a spherical cut-off. Here atom A only interacts with particles within cutoff sphere namely the B particles. Although particles C are within the minimum image convention box, interaction with them has been ignored since they lie beyond the cut-off distance.

6.4.1 Shifted Potential and Force

Simply truncating potential at some cut-off distance r_c , introduces discontinuity in both the potential energy and force at $r = r_c$. This leads to serious problem in the energy conservation during MD simulations. There exist several solutions to this problem. Simplest way is to shift the potential by the value of the potential at cut-off $u(r_c)$ at all distance. Mathematically this can be written as

$$u_s(r) = \begin{cases} u(r) - u(r_c) & r \leq r_c \\ 0 & r > r_c \end{cases} \quad (6.67)$$

This additional term is constant and does not affect the force and hence equation of motion of the system. However, the force is still discontinuous at or near cut-off. This can cause numerical instability in the numerical solution of the differential equations. To avoid this one can use shifted-force potential[18] where a linear term is added to the potential, so that its derivative is zero at the cutoff. The form of the potential with the shifted force is given as follows

$$u_{sf}(r) = \begin{cases} u(r) - u(r_c) - \left(\frac{du}{dr}\right)_{r=r_c} (r - r_c) & r \leq r_c \\ 0 & r > r_c \end{cases} \quad (6.68)$$

The discontinuity now appears in the gradient, not in the force itself. The force goes smoothly to zero at cutoff. But this shift makes the potential deviate from the true potential, so the calculated thermodynamics properties will be changed. However, the thermodynamic properties of the system interacting with

un-shifted potential can be recovered from shifted-force potential simulation result using perturbation scheme. But it is difficult to do so and is rarely used in simulation.

6.4.2 Switching Function

To avoid discontinuities due the truncation of the potential, other alternative approach is to use a switching function to taper the potential between two cut-off values. Potential energy is multiplied by a switching function (usually by a polynomial function) which smoothly goes to zero at cut-off

$$u_s(r) = u(r)S(r) \quad (6.69)$$

The switching function $S(r)$ gradually tapers the potential between two cutoffs: it smoothly changes its value from 1 at a cut-off distance r_l (lower cutoff) to a value of 0 at cutoff distance r_u (upper cutoff) and satisfies the following criteria

$$\begin{aligned} S_{r=r_l} &= 1.0 & \left(\frac{dS}{dr}\right)_{r=r_l} &= 0 & \left(\frac{d^2S}{dr^2}\right)_{r=r_l} &= 0 \\ S_{r=r_u} &= 0 & \left(\frac{dS}{dr}\right)_{r=r_u} &= 0 & \left(\frac{d^2S}{dr^2}\right)_{r=r_u} &= 0 \end{aligned} \quad (6.70)$$

Zero first derivatives ensure that the force approaches to zero smoothly at the cutoffs. A continuous second derivative ensures the stability of the integration algorithm. The lowest order polynomial which satisfies the above criteria is the third order polynomial (or cubic spline) and given by

$$\begin{aligned} S(r) &= (r_u^2 - r^2)^2 \frac{2}{\gamma^3} [\frac{3\gamma}{2} - (r_u^2 - r^2)] & \text{where } \gamma &= r_u^2 - r_l^2 \\ &= c_0(r_u^2 - r^2) + c_1(r_u^2 - r^2)^2 + c_2(r_u^2 - r^2)^3 \end{aligned} \quad (6.71)$$

For better accuracy higher order polynomial can also be used for switching function. For example we can use 5th order polynomial of the following form

$$\begin{aligned} S(r) &= c_0 + c_1 \left[\frac{r-r_l}{r_u-r_l} \right] + c_2 \left[\frac{r-r_l}{r_u-r_l} \right]^2 + c_3 \left[\frac{r-r_l}{r_u-r_l} \right]^3 \\ &\quad + c_4 \left[\frac{r-r_l}{r_u-r_l} \right]^4 + c_5 \left[\frac{r-r_l}{r_u-r_l} \right]^5 \end{aligned} \quad (6.72)$$

The coefficients can be obtained using the boundary condition given in equation (6.70) and are given as follows $c_0 = 1, c_1 = 0, c_2 = 0, c_3 = -10, c_4 = 15, c_5 = -6$. We can use higher order polynomial also.

6.4.3 Verlet List

In the cut-off scheme for force calculation, we still need to check distance between all pairs of molecules to see whether they are really within cutoff distance.

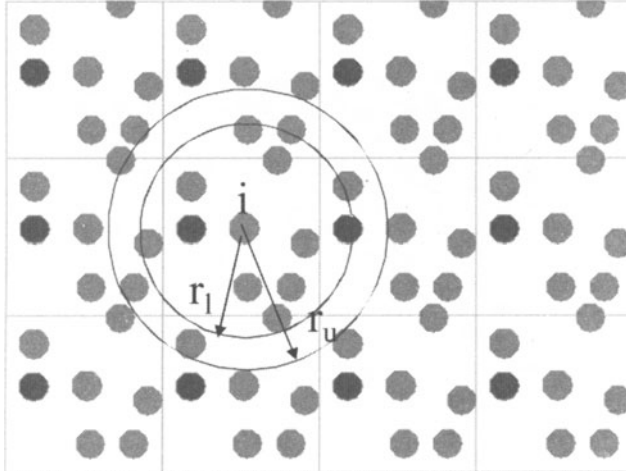


Figure 6.6: Scheme for constructing Verlet list for non-bond computation.

This distance calculation is still of the order of N^2 and is costly. To save time from this costly operation, Verlet suggested[8] the following scheme:

A second cutoff, upper cutoff r_u is introduced in addition to original cutoff r_l as shown in Fig.6.6. List of all particles within a radius r_u of particle i is made. As long as maximum displacement of particle is less than $(r_u - r_l)$, we have to consider only particles in this list for force computation. Hence, depending on the value $r_u - r_l$, we do not need to scan all the particles at each MD time steps. These lists are updated after few steps. When the value of $r_u - r_l$ is smaller, list has to be updated very frequently, on the other hand if value of $r_u - r_l$ is larger, then update frequency will be low but force calculation will take larger time due to large number of particles within the cut-off. Value of $r_u - r_l$ and update frequency has to be optimized keeping these factors in mind. Typically neighbour lists are updated after 10 – 20 steps. For number of particles more than few thousands Verlet neighbour list improves simulation efficiency drastically. During MD simulation it is sufficient to have a Verlet list with half the number of particles for each particle as long as interaction $i-j$ is accounted for in either the list of particle i or that of j . However as the system size increases neighbour list for each particle uses a lot of memory and becomes too large to store easily. Also to scan every pair in system becomes inefficient. This is resolved by making the Verlet list using Cell list as described below.

6.4.4 Cell Lists or Linked List

For larger systems (more than few thousands particles) to cell list [19] method is commonly used. Simulation box is divided in cells with size equal to or greater than cutoff distance. Each particle is assigned a cell index depending on its position. This kind of sorting is easy and order N operation only. Each particle

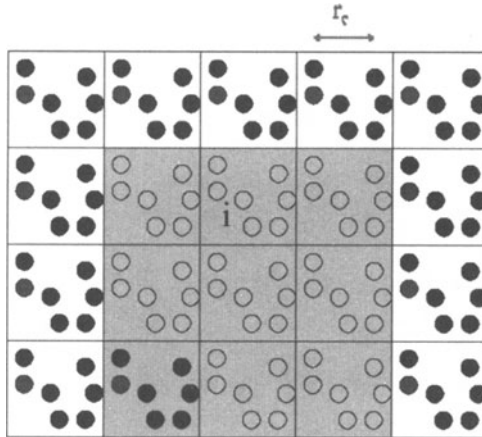


Figure 6.7: Scheme to construct Cell list

interacts with the particle in the same cell and its neighboring cell. Now every particle interacts with particle either in the same cell or in the neighbour cell. Cell list can be created using the method of Linked list. For details reader is referred to chapter 3 of Allen and Tildesley¹¹.

6.4.5 Long Range Interactions: Ewald Sum

Above mentioned techniques for efficient force calculation work well for short-range interactions but do not work for long range interactions like Coulomb interaction. Hence special techniques are employed to handle long range interactions. Ewald summation[20] is one of the most widely used techniques to treat long range interaction in periodic system. Below we briefly outline the main points of this method.

Main idea of Ewald sum is to consider a charge distribution of opposite sign on every charge site; this extra charge distribution screens the interaction between neighboring atoms. This screened interaction is now short-range and can be accurately taken care of using the cut-off scheme discussed above for short range interaction. To compensate the additional charge distribution equal charge distribution having opposite sign (i.e. having same sign as original point charge) is added and summed in reciprocal space. This is illustrated in Fig.6.8 below.

Using the above mentioned scheme the electrostatic potential has now following three contributions:

1. Potential due to original point charge q_i
2. Potential due to Gaussian screening charge cloud with charge $-q_i$
3. Potential due to compensating charge cloud with charge q_i

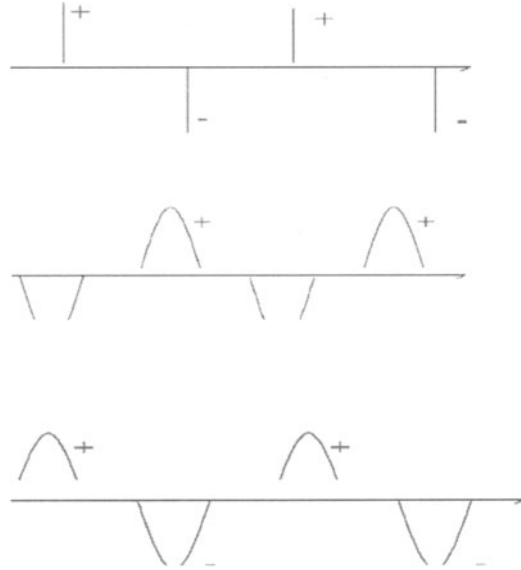


Figure 6.8: (a) the original charge distribution, (b) A Gaussian charge distribution of opposite sign is added at every charge site, (c) another Gaussian charge distribution of Scheme for Ewald summation.

The contribution to the electrostatic potential at point r_i due to a set of screened charges can easily be computed by direct summation because the electrostatic potential due to screened charge is a rapidly decaying function of r . A Gaussian charge distribution of following form is commonly used

$$\rho(r) = \frac{q_i \alpha^3}{\pi^{3/2}} \exp(-\alpha^2 r^2) \quad (6.73)$$

α controls the width of the distribution. Using the solution of Poisson's equation either in real space or in Fourier space potential for the above three cases can be computed.

One thing should be noted here, in the above mentioned recipe interaction of cancelling distribution centered at a site with itself is also included. Hence it should be subtracted from the above mentioned sum. This is termed as the self correction. Another correction comes from smeared nature of charge.

Thus total potential energy due to Long range Coulomb interaction is given by the expression

$$U_c = U_q(\alpha) - U_{self}(\alpha) + \Delta U(\alpha) \quad (6.74)$$

The first term $U_q(\alpha)$ represents the reciprocal sum due to compensating charge cloud with charge q_i and is given by

$$\begin{aligned} U_q &= \frac{1}{2} \sum_i q_i \phi(r_i) \\ &= \frac{1}{2} \sum_{k \neq 0} \frac{4\pi V}{k^2} e^{-k^2/4\alpha} \sum_{i,j} \frac{q_i q_j}{V^2} e^{ik \cdot (\mathbf{r}_i - \mathbf{r}_j)} \\ &= \frac{1}{2} \sum_{k \neq 0} \frac{4\pi V}{k^2} e^{-k^2/4\alpha} |\rho(\mathbf{k})|^2 \end{aligned} \quad (6.75)$$

$U_{self}(\alpha)$ is the self correction term and is given by

$$\begin{aligned} U_{self} &= \frac{1}{2} \sum_j q_j \phi(0) \\ &= \left(\frac{\alpha}{\pi}\right)^{1/2} \sum_j q_j^2 \end{aligned} \quad (6.76)$$

And finally $\Delta U(\alpha)$ is the potential in the real space due to the interaction between the original charges q_i plus the Gaussian screening charge cloud with charge $-q_i$ and is given by

$$\begin{aligned} \Delta U &= \frac{1}{2} \sum_n \sum_{i \neq j} q_i \Delta \phi_j(r_{ij}) \\ &= \frac{1}{2} \sum_n \sum_{i \neq j} \frac{q_i q_j}{r_{ij}} \text{erfc}(\sqrt{\alpha} r_{ij}) \end{aligned} \quad (6.77)$$

Where error function, denoted erf is defined as follows

$$\text{erf}(x) = \frac{2}{\sqrt{\pi}} \int_0^x \exp(-u^2) du \quad (6.78)$$

And the complementary error function erfc is defined as follows

$$\begin{aligned} \text{erfc}(x) &= 1 - \text{erf}(x) \\ &= \frac{2}{\sqrt{\pi}} \int_x^\infty \exp(-u^2) du \end{aligned} \quad (6.79)$$

Larger the value of α , sharper the distribution hence large number of K summation has to be included for better accuracy. On the other hand, large value of α reduces range of screened potential hence we can use smaller cutoff radius. Hence value of α is optimized between these two factors to give better accuracy and efficiency. Note that Ewald summation as presented above scales as N^2 only. However, with suitable choice of α and k-space summation cut-off K, Finchman[21] was able to optimize the summation which scales as $N^{3/2}$. The optimized values for α and k-space summation cut-off K is given by

$$\begin{aligned} \bar{\alpha} &= \pi/\bar{R} \\ \bar{K} &= \bar{\alpha} \end{aligned} \quad (6.80)$$

Where $\bar{R} = \frac{R}{L}$; $\bar{\alpha} = \alpha L$; $\bar{K} = \frac{KL}{2\pi}$ and R and L are the real space cut-off (same as r_c as discussed above) and the simulation box length respectively.

Ewald summation can further be optimized through the use of Fast Fourier transform (FFT) in evaluating the reciprocal summation. This goes in the name of Particle Mesh Ewald (PME)[22]. Particle Mesh based approaches rely on the use of fixed cutoff on the direct space sum together with an FFT based approximation for the reciprocal space sum that scales as $N \log(N)$.

6.5 Thermostat and Barostat

The algorithm framework discussed so far is appropriate for Micro canonical ensemble (NVE ensemble), where total energy of the system is a constant of motion. However, in many cases we require simulating systems in canonical ensemble which requires either constant temperature (NVT) or constant pressure and constant temperature (NPT). For simulation in canonical ensemble we need to solve constrained Hamiltonian equation of motion to have desired ensemble. Nose and Hoover formulated an extended system Hamiltonian dynamics[23] to do the simulation in NVT and NPT ensembles. In general constrained Hamiltonian dynamics is difficult and requires complicated coding and beyond the scope of this article. Interested reader can consult the original article or the discussion in Frenkel and Smit [12]. Below we discuss two very commonly used schemes for doing simulation in canonical ensemble namely velocity rescaling method and the weak coupling method of Berendsen [24].

6.5.1 Velocity Rescaling Method

Temperature of the system during the simulation is calculated from the kinetic energy using equi-partition theorem and is given by

$$E_{KE} = \frac{3}{2} N k_B T \quad (6.81)$$

Simplest way to maintain a constant T is to rescale the velocities consistent with the desired temperature. Suppose at time t temperature is $T(t)$ and the desired temperature is $T_{desired}$. If the velocities are multiplied by a factor λ , the change in temperature is given by

$$\begin{aligned} \Delta T &= \frac{1}{2} \sum_{i=1}^N \frac{2}{3} \frac{m_i (\lambda v_i)^2}{N k_B} - \frac{1}{2} \sum_{i=1}^N \frac{2}{3} \frac{m_i v_i^2}{N k_B} \\ &= (\lambda^2 - 1) T(t) \end{aligned}$$

So we have

$$\lambda = \sqrt{T_{desired}/T(t)} \quad (6.82)$$

At each time step the velocities are multiply by λ and $T(t)$ is calculated from the KE at time t .

This drastic approach, however, implies rapid energy transfer to, from and among the various degrees of freedom in the system. In particular it can be shown that velocity rescaling leads to an artificial pumping of energy into low frequency modes. This does not represent any statistical ensemble. However this algorithm is simple and easy to implement.

6.5.2 Berendsen Weak Coupling method

Berendsen algorithm [24] mimics weak coupling to an external heat bath to maintain constant temperature during simulation. Such a coupling can be accomplished by adding a stochastic and friction term in equation of motion as

follows

$$m_i \dot{v}_i = F_i - m_i \gamma_i v_i + R(t) \quad (6.83)$$

where γ_i is the damping constant which determines the strength of coupling with the heat bath. For simplicity we consider $\gamma_i = g$ (friction constant equal for all particles). $R(t)$ is a Gaussian stochastic variable satisfying following relation:

$$\langle R_i(t)R_j(t+\tau) \rangle = 2m_i\gamma_i kT\delta(\tau)\delta_{ij} \quad (6.84)$$

Time dependence of the total kinetic energy is given by;

$$\frac{dE_k}{dt} = \lim_{\Delta t \rightarrow 0} \left[\left\{ \sum_{i=1}^{3N} \frac{1}{2} m_i v_i^2(t + \Delta t) - \sum_{i=1}^{3N} \frac{1}{2} m_i v_i^2(t) \right\} / \Delta t \right] \quad (6.85)$$

N being the total number of particles

From equation (6.83) we have the the change Δv_i of the velocity over a time interval of $t = 0$ Δt is give by (assuming Δt small) difference in velocity in two time step given by

$$\begin{aligned} \Delta v_i &= v_i(t + \Delta t) - v_i(t) \\ &= \frac{1}{m_i} \int_t^{t+\Delta t} [F_i(t') - m_i \gamma v_i(t') + R_i(t')] dt \end{aligned} \quad (6.86)$$

Since R is Gaussian noise, using equation (6.84) we get,

$$\sum_{i=1}^{3N} \int_t^{t+\Delta t} dt' \int_t^{t+\Delta t} dt'' R_i(t') R_i(t'') = 6N m \gamma k T_0 \Delta t \quad (6.87)$$

Using this relation in equation (6.85) get

$$\frac{dE_k}{dt} = \sum_{i=1}^{3N} v_i F_i + 2\gamma \left(\frac{3N}{2} k T_0 - E_k \right) \quad (6.88)$$

First term on the right hand side is equal to minus of the time derivative of potential energy and is related to the effect of systematic force which will have no effect of the imposed thermostat. Hence the coupling to the heat bath is represented by the second term and can be associated with the time dependence of the system temperature

$$\frac{dT}{dt} = 2\gamma (T_0 - T) \quad (6.89)$$

where the time constant for heat bath coupling τ_T is equal to $2\gamma^{-1}$. So the temperature deviation decays exponentially with time with time constant τ_T and the equation of motion can be written as

$$m_i \dot{v}_i = F_i - m_i \gamma \left(\frac{T_0}{T} - 1 \right) v_i \quad (6.90)$$

In the Berendsen weak coupling scheme coupling to the heat bath and subsequent temperature control is achieved by appropriate rescaling of the velocities by a time dependent scaling factor λ during the integration of equation of motion. In the following we show the scaling factor in the context of leap-frog integrator equ. (6.26).

$$\begin{aligned}\dot{\mathbf{r}}_i\left(t + \frac{\Delta t}{2}\right) &= \lambda(t)\dot{\mathbf{r}}'_i\left(t + \frac{\Delta t}{2}\right) \\ &= \lambda(t) \left[\dot{\mathbf{r}}_i\left(t - \frac{\Delta t}{2}\right) + m_i^{-1}\mathbf{F}_i(t)\Delta t \right]\end{aligned}\quad (6.91)$$

To achieve temperature variation consistent with equ.(6.89) the scaling factor λ can be found by imposing [42]

$$\mathcal{T}\left(t + \frac{\Delta t}{2}\right) = \mathcal{T}\left(t - \frac{\Delta t}{2}\right) + \tau_T^{-1}\Delta t \left[T_0 - \mathcal{T}\left(t - \frac{\Delta t}{2}\right) \right] \quad (6.92)$$

Using equation (6.91) and (6.92) we have

$$\lambda^2(t)\mathcal{T}'\left(t + \frac{\Delta t}{2}\right) = \mathcal{T}\left(t - \frac{\Delta t}{2}\right) + \tau_T^{-1}\Delta t \left[T_0 - \mathcal{T}\left(t - \frac{\Delta t}{2}\right) \right] \quad (6.93)$$

solving this for $\lambda(t)$ gives;

$$\begin{aligned}\lambda(t; \Delta t) &= \left\{ \frac{\mathcal{T}(t - \frac{\Delta t}{2})}{\mathcal{T}'(t + \frac{\Delta t}{2})} + \tau_T^{-1}\Delta t \frac{T_0 - \mathcal{T}(t - \frac{\Delta t}{2})}{\mathcal{T}'(t + \frac{\Delta t}{2})} \right\}^{1/2} \\ &\approx \left\{ 1 + \tau_T^{-1}\Delta t \left[\frac{T_0}{\mathcal{T}'(t + \frac{\Delta t}{2})} - 1 \right] \right\}^{1/2}\end{aligned}\quad (6.94)$$

So the temperature is controlled by scaling the velocities of the particle as each time step with a time dependent constant given by,

$$\lambda = \left[1 + \frac{\Delta t}{\tau_T} \left(\frac{T_0}{T} - 1 \right) \right]^{1/2} \quad (6.95)$$

If τ_T is large, then the coupling will be weak. If τ_T is small, the coupling will be strong and when the coupling parameter equal to integration time step ($\tau_T = \delta t$) then this algorithm is equivalent to simple velocity rescaling method. A good value of τ_T is $0.5 - 1$ ps when integration time step $\delta t = 1$ fs.

Advantage

1. Strength of the coupling can be varied and adapted to the use requirement
2. Very easy to code
3. Very efficient to bring the system to a desired temperature.

Disadvantage

1. Does not represent a true canonical ensemble. Velocity rescaling artificially prolongs any temperature difference among components of the system, which can lead to the phenomena of ‘hot solvent’ and ‘cold solute’, even though the temperature of the system is at its desired value. This can be avoided by having separate temperature coupling to the solute and solvent, but this leads to the unequal distribution of energy among various components.

6.5.3 Weak Coupling Barostat for Constant P

From the above discussion it is clear that, coupling to a bath is obtained by adding an extra term to equation of motion for relevant variable. Similarly coupling to constant pressure bath can be obtained by adding an extra term to the equation of motion that controls pressure change. In analogy with equation (6.89), the equation of motion for pressure can be written as

$$\frac{dP}{dt} = \frac{P_0 - P}{\tau_P} \quad (6.96)$$

The pressure is given by the expression

$$P = \frac{2}{3V} (E_k - \Xi) \quad (6.97)$$

where

$$\Xi = -\frac{1}{2} \sum_{i < j} r_{ij} \cdot F_{ij} \quad (6.98)$$

is the internal virial for pair additive potential. F_{ij} is the force on particle i , due to particle j and V is the volume of the simulation cell. During the simulation pressure can be changed by changing the virial which can be accomplished by scaling inter-particle distances. Constant pressure simulation is achieved by scaling the coordinates along with appropriate volume scaling. At each time step particle coordinate x is scaled to μx and box length l to μl where μ is given by

$$\mu = [1 - \frac{\delta t}{\tau_p} (P - P_0)]^{1/3} \quad (6.99)$$

For further details of the Berendsen weak coupling method the reader is referred to the original paper.

6.6 Example of MD Simulation

As mentioned in the introduction, variety of problems can be solved using MD simulation. They offer great microscopic insight to the problems and in many

cases gives an alternative route where experiments are difficult to perform. Below we give two examples of the current research problems done by Molecular dynamics simulation in our group [25, 26].

1. Dynamics of Water in Confined System

2. Elastic Properties of Boron-Nitiride Nanotube

6.6.1 Structure and Dynamics of water in Confined Systems

Structure and dynamics of water confined in the narrow pore of carbon nanotube (CNT) has received lots of attention in recent years. Single chain of water inside narrow carbon nanotube serves as the model system which has direct relevance in proton transfer, flow in biological channels and nano-devices. We have studied the structure and various reorientational dynamics of water wire inside nanotube and nanoring using MD simulation.

Carbon nanotube is generated by folding a graphene sheet. First an armchair nanotube of chirality (6,6) having 24 unit cells (diameter 8.02Å) and length 57Å is immersed in a bath of TIP3P water using xleap module of AMBER[27]. The box dimensions were chosen in order to ensure a 10Å solvation shell around the dendrimer structure. This procedure resulted in solvated structures, containing 3027 water molecules. MD simulation was performed using the AMBER7⁴² software suite, using the AMBER force field [28]. TIP3P is a rigid water model (Fig.6.9(a)) with HOH bond angle and both OH bonds fixed during simulation. HOH angle is fixed to a value of 104.5° and OH bond length is fixed to 0.9572Å using harmonic potentials as described in previous section with force constants $\mathbf{K}_q = 120\text{Kcal/mol}$ and $\mathbf{K}_b = 553\text{Kcal/mol}$. Partial positive atomic charge on hydrogen (+0.4170e) is balanced by negative charge on oxygen (-0.8340e). Intermolecular force between two water molecules is described by Lennard-Jones potential with a single interaction site centered on oxygen atom with potential depth of $\varepsilon = 0.6364 \text{ KJ/mol}$ and range of $\sigma = 3.1506$. In CNT C-C bond distance length $r_0 = 1.43\text{\AA}$ and C-C-C angel is fixed to $\theta_0 = 2\pi/3$. Interaction of water molecules with carbon atom is described by Lennard-Jones potential having potential depth $\varepsilon = 0.1143 \text{ Kcal/mol}$ and range $\sigma = 3.275\text{\AA}$. The solvated structures were subjected to 1000 steps of steepest descent minimization of potential energy, followed by another 2000 steps of conjugate gradient minimization. During this minimization the nanotube structure was kept fixed in their starting conformations using a harmonic constraint with a force constant of 500 kcal/mol/Å. This allowed the reorganization of the water molecules to eliminate bad contacts with the nanotube. The minimized structure was then subjected to 45 ps of MD, with 2 fs time step. During the dynamics, the system was gradually heated from 0 to 300 K with harmonic constraints on the solute using the SHAKE method. This was followed by 200 ps constant volume – constant temperature (NVT) dynamics with a temperature-coupling constant of 0.5–1.0ps on the solute. Finally, 20-30 ns NPT production dynamics was carried out with a time constant

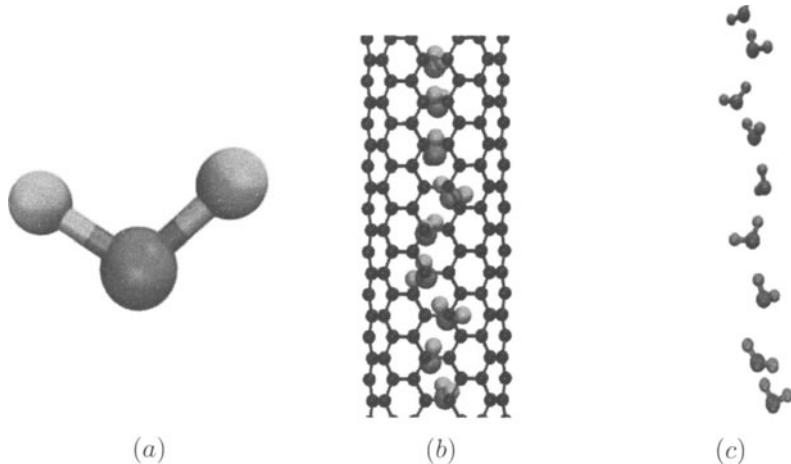


Figure 6.9: (a) TIP3P model of water (b) Water inside carbon nanotube (c) typical ordering of water inside CNT

for heat bath coupling of 1ps. The electrostatics interactions were evaluated with the Particle Mesh Ewald [20] (PME) method, using a real space cut off of 9Å. Again during this production runs nanotube was held fixed to its starting configuration using a force constant of 500 kcal/mol/Å². The trajectory was saved forevery 1 ps interval and was used for data analysis.

Results

Despite of hydrophobic nature of carbon nanotubes, water spontaneously goes inside CNT in quantitative agreement with earlier works[29]. Water enters from one end of the tube and leave from other end. Water molecules inside the tube are arranged in a single file with all dipole either pointing up or down as shown in Fig.6.9(b) & (c).

Figure 6.10 shows the typical trajectories of four neighbouring, confined water molecules in the single file chain. The extreme correlation among the trajectories is apparent. To quantify the positional ordering of the water molecules inside the nanotube we have calculated the pair-correlation function for the water molecules inside the nanotube using

$$g(z) = \frac{1}{N} \sum_{i=1}^N \sum_{j=1, j \neq i}^N \langle \delta(z - z_{ij}) \rangle \quad (6.100)$$

where z_{ij} is the axial separation between the i^{th} and the j^{th} water molecules, N is the number of water molecules inside the nanotube and the angular brackets indicate an average over time.

We have also looked at the reorientational dynamics of the confined water. The water molecules are tightly packed inside a nanotube due to hydrogen

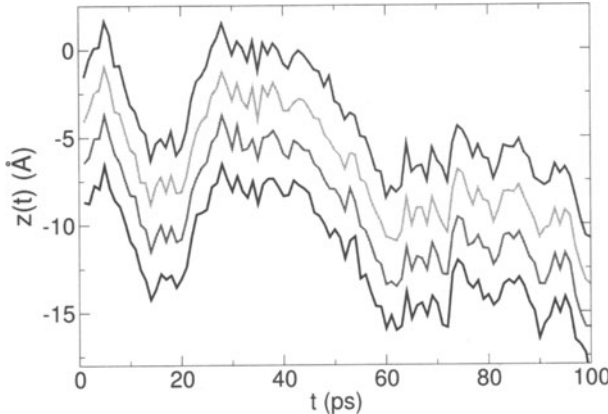


Figure 6.10: The z coordinates of four confined, neighbouring water molecules as a function of time.

bonding, with the average density almost four times that of bulk water. The dipole moments of all the confined water molecules are almost always aligned, pointing either “up” (along $+z$ direction, see Fig.6.9b & 6.9c) or “down” (along $-z$ direction). Their orientation changes by cooperative “flips” that take them from one of these states to the other. Fig.6.11 shows the time-dependence of the axial component of the average dipole moment, $M_z(t)$ of the confined water molecules, defined by

$$M_z(t) = \frac{1}{N(t)} \sum_{i=1}^{N(t)} \vec{p}_i(t) \cdot \vec{n} \quad (6.101)$$

Where $N(t)$ is the total number of water molecules inside the tube at time t and $\vec{p}_i(t)$ is the dipole moment of i th water molecules inside tube at time t and \vec{n} represents axis of the tube.

Figures 6.11(a) and 6.11(b) show data for water confined inside 14\AA and 28\AA along nanotubes, respectively. The average number of confined water molecules is 5 and 10 inside the 14\AA and 28\AA nanotubes, respectively. The net dipole moment of the chain of water molecules makes collective flips between the “up” and “down” states. The mean time interval between successive flips increases with the length of the tube. The red curve in Fig.6.11(b) shows the time-dependence of the axial component of the average dipole moment of the water molecules in bulk water outside the nanotube. This clearly shows that confinement leads to ordering of the dipole moments of the water molecules.

Further details about these interesting reorientational dynamics can be found in our original works [26, 30].

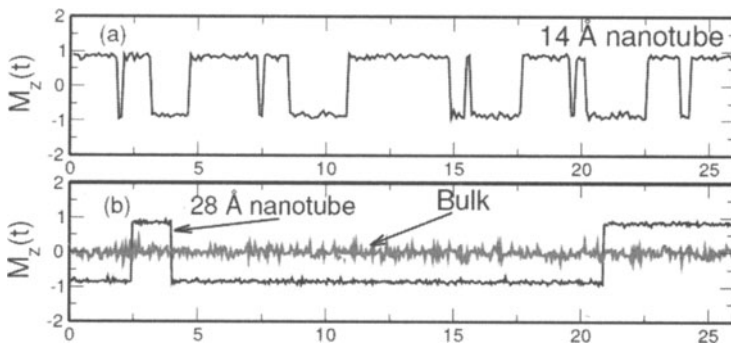


Figure 6.11: (a) and (b) show the average dipole moment of the water molecules confined inside the 14 \AA and 28 \AA nanotubes respectively. The 14 \AA and 28 \AA tubes accommodate 5 and 10 water molecules on an average. The dipole moments of the water molecules inside the nanotube are mostly aligned in either “up” or “down” states, with cooperative flips between these two states. The flips become rarer as the length of the water chain increases. The red curve in 11(b) shows the axial component of the average dipole moment of the water molecules in the bulk, where there is no orientational order.

6.6.2 Elastic Properties of Boron-Nitride Nanotube

Nanotubes have remarkable mechanical properties. This makes them most desirable candidate for many applications. Mechanical properties of CNT have been studied extensively and they are suggested to be very strong substance. Boron -Nitride nanotube (BNNT) has same structure as CNT except that they have alternating boron and nitrogen atoms in graphite like network and are strongly polar in nature due to large charge on boron and nitrogen atoms. Mechanical properties of BNNTs have been studied using tight binding molecular dynamics simulation (TBD)[31] and ab-initio molecular dynamics simulation [32]. Classical Force Field (FF) based calculation (molecular mechanics or molecular dynamics) of mechanical properties of BNNTs are not common due to unavailability of force field interaction parameters for boron and nitrogen in most of the available classical FF. Among the existing set of classical FF, only Universal force field (UFF) [33] and DREIDING FF [34] have interaction parameters set for boron and nitrogen. Recently Moon and Hwang [35] have used UFF to study the structure and energetics of BNNTs. Recently we have investigated the mechanical properties of BNNTs using molecular mechanics calculation [36]. We have used DREIDING [34], a generic force field for macromolecular simulations for our molecular mechanics calculations of SWNTs of chirality (5, 5)(7, 7)(10, 10)(12, 12)(15, 15)(20, 20)(25, 25)(30, 30)(35, 35)(40, 40) and (45, 45) for both the CNTs and the BNNTs. For BNNTs we have considered the following set of charges on boron and nitrogen respectively: $\pm 0e$, $\pm 0.41e$, $\pm 0.68e$, $\pm 1e$ and $\pm 1.41e$. We also performed molecular mechanics

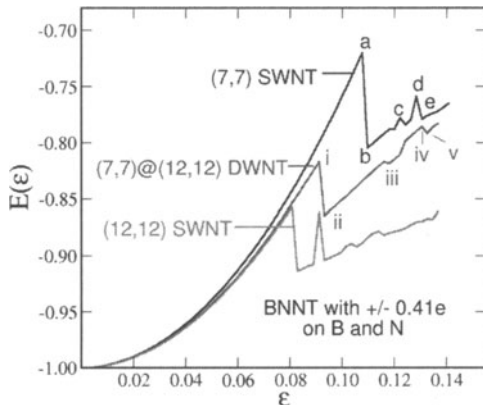


Figure 6.12: Energy versus strain for BNNTs for single wall nanotube (SWNT) and double wall nanotube (DWNT) of different chiralities.

calculations on double-walled nanotubes (DWNTs) of chirality $(5,5)\alpha(10,10)$, $(7,7)\alpha(12,12)$, $(10,10)\alpha(15,15)$, $(15,15)\alpha(20,20)$ and $(20,20)\alpha(25,25)$. All these tubes were taken to be twenty unit cells long (~ 4.8 nm), and the inter tube gap is 0.34 nm 37. For DWNT, the inner tube was rotated in steps of 1° and the minimum energy configuration was taken to be the starting configuration for the molecular mechanics calculation. In the minimum energy configuration, boron (nitrogen) in inner layer lies on top of nitrogen (boron) in the outer layer. For the compression of the nanotubes, the atoms at both ends of the unit cells in the tube were moved in small steps of 0.05 Å along the tube axis and then the whole structure was minimized by conjugate - gradient minimization method while keeping the end atoms fixed. Similarly, for the torsion one end of the tube was fixed and atoms at the other end were rotated in small steps of 1° and the structure was minimized.

When the tube is under axial compression, we define the strain energy as the ratio of the energy of the compressed tube to the energy without compression. For small strain e , the strain energy $E(e)$ is $E(e) = \frac{1}{2}ke^2$; where k is a constant. In Fig.6.12, we plot $E(e)$ as a function of e for single wall and double wall BNNTs with $\pm 0.41e$ charge on B/N atoms, respectively. Energy for SW has discontinuities at a,b,c,d,e which corresponds to snaps in Fig.6.13 respectively, other energy curves are for SW $(12,12)$ and DW $(7,7)\alpha(12,12)$.

The elastic properties of the C/BN nanotubes arise due to the strength of in plane C-C/B-N bonds in comparison with the ease of out of plane deformation. The strength of the tube is reflected in the high Young modulus. Young modulus is calculated from the second derivative of the strain energy,

$$Y = \frac{1}{V_0} \left. \frac{\partial^2 E(\varepsilon)}{\partial \varepsilon^2} \right|_{\varepsilon=0} \quad (6.102)$$

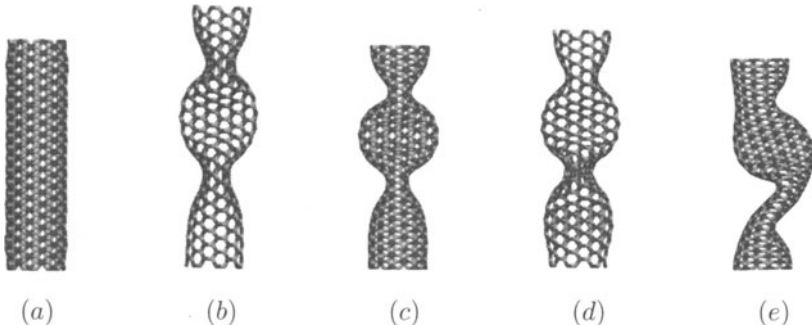


Figure 6.13: Snapshots of (7,7) single wall BNNT under compression, snapshots correspond to discontinuities in Fig.6.12.

Where V_0 is the equilibrium volume of the nanotube, given by $V_0 = \pi [(R + h)^2 - R^2] L$; where L is the length, R is the radius and h is the shell thickness. The values of h used [38, 39] are 0.066 nm[38] and 0.34 nm[39]. Empirical force constant model [39] and non-orthogonal tight binding calculation [40] suggest that h should be 0.34 nm, a value used by us. The values of Young modulus of DWNTs show that there is not much significance of inter-wall van der Waal interaction on the Young modulus.

In Fig.6.14 we show the variation of Young modulus as a function of tube radius for different charge scheme on B/N atoms in BNNT. The following observations can be made. (i) BNNTs with charge $\pm 0.68e$, $\pm 1.0e$ and $\pm 1.41e$

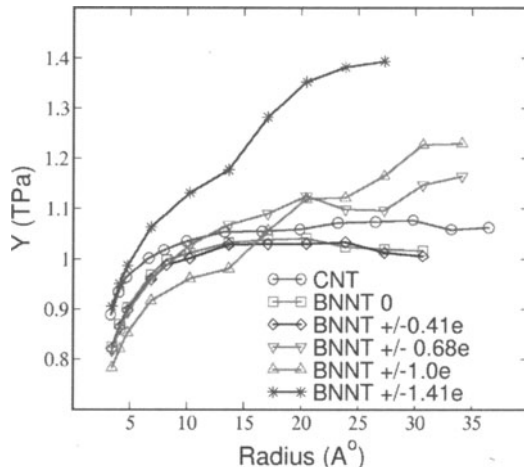


Figure 6.14: Young's modulus Y as a function of tube radius and charge on B/N atoms in BNNT.

on B and N atoms have higher Young modulus than that of CNT whereas BNNTs with charge $\pm 0e$ and $\pm 0.41e$ on B and N atoms have smaller Young modulus as compared to CNT. This difference has its origin in electrostatic interactions. (ii) Young modulus increases with the radius and asymptotically approaches the value of the flat sheet, consistent with ref. 31 and 41, but in contrast to ref. 39. Young modulus of SWNTs and DWNTs are very similar which can be explained by the fact that the elastic properties of nanotubes are determined by the strength of B-N bonds in the bent BN sheet and C-C bonds in bent Graphene and also the vdW interaction is comparatively very weak in MWNTs.

References

- [1] P. S. d. Laplace, *Theorie Analytique des Probabilités*, 3 ed. (Gauthier-Villars, Paris).
- [2] N. Metropolis, A. W. Rosenbluth, M. N. Rosenbluth, A. H. Teller, and E. Teller, Journal of Chemical Physics 21, 1087 (1953).
- [3] E. Fermi, J. Pasta, and S. Ulam, Document LA-1940 (1955).
- [4] B. J. Alder and T. E. Wainwright, J. Chem. Phys. 27, 1208 (1957).
- [5] J. B. Gibson, A. N. Goland, M. Milgram, and G. H. Vineyard, Physical Review 120, 1229 (1960).
- [6] A. Rahman, Physical Review a-General Physics 136 (2A), A405 (1964).
- [7] L. Verlet, Physical Review 165, 201 (1968).
- [8] L. Verlet, Physical Review 159, 98 (1967).
- [9] A. Rahman and F. H. Stillinger, J. Chem. Phys. 55, 3336 (1971).
- [10] G. D. Harp and B. J. Berne, Physical Review A 2, 975 (1970); G. D. Harp and B. J. Berne, Journal of Chemical Physics 49, 1249 (1968).
- [11] M. P. Allen and D. J. Tildesley, Computer Simulation of liquids. (Oxford: Clarendon, 1987).
- [12] D. Frenkel and B. Smit, Understanding Molecular Simulations. (Academic Press: San Diego 2002).
- [13] A. Leach, Molecular Modelling. (Prentice Hall 2001); T. Schlick, Molecular Modeling and Simulation - An Interdisciplinary Guide (Springer, New York, 2002).
- [14] M. Tuckerman, B. J. Berne, and G. J. Martyna, J. Chem. Phys. 97, 1990 (1992).
- [15] C. W. Gear, Report No. ANL-7126, 1966.

- [16] J. P. Ryckaert, G. Ciccotti, and H. J. C. Berendsen, *J. Comput. Phys.* 23, 327 (1977).
- [17] J. D. Honeycutt and H. C. Andersen, *J. Phys. Chem.* 90, 1585 (1986); J. D. Honeycutt and H. C. Andersen, *Chem. Phys. Letts.* 108, 535 (1984).
- [18] S. D. Stoddard, *Phys Rev A* 8, 1504 (1973).
- [19] B. Quentrec and C. Brot, *J. Comp. Phys* 13, 430 (1973).
- [20] D. M. Heyes, *Electrostatic potentials and fields in infinite point charge lattice.* (1981).
- [21] D. Fincham, *Molecular Simulation* 13, 1 (1994).
- [22] T. Darden, York D., Pedersen L., *J Chem Phys* 98, 10089 (1993); T. A. Darden, A. Toukmaji, and L. G. Pedersen, *Journal De Chimie Physique Et De Physico-Chimie Biologique* 94 (7-8), 1346 (1997).
- [23] S. Nose, *J. Chem. Phys* 81, 511 (1984); S. Nose, *Molecular Physics* 52, 255 (1984); W. G. Hoover, *Physical Review A* 31, 1695 (1985).
- [24] H. J. C. Berendsen, J. P. M. Postma, A. van Gunsteren, A. DiNola, and H. R. Haak, *J. Chem. Phys.* 81, 3684 (1984).
- [25] B. Mukherjee, P. K. Maiti, C. Dasgupta, and A. K. Sood, *J. Chem. Phys.* 126, 124704 (2007).
- [26] B. Mukherjee, P. K. Maiti, C. Dasgupta, and A. K. Sood, *Acs Nano* 2, 1189 (2008); B. Mukherjee, P. K. Maiti, C. Dasgupta, and A. K. Sood, *J. Phys. Chem. B* 113, 10322 (2009).
- [27] D. A. Case, Darden, T.A., Cheatham III, T.E., Simmerling, C.L., Wang, J., Duke, R.E., Luo, R., Merz, K.M., Wang, B., Pearlman, D.A., Cowley, M., Brozell, S., Tsui, V., Gohlke, H., Mongan, J., Hornak, V., Cui, G., Beroza, P., Schafmeister, C., Caldwell, J.W., Ross, W.S., Kollman, P.A., AMBER 8 (University of California, San Francisco., 2004).
- [28] W. D. Cornell, P. Cieplak, C. I. Bayly, I. R. Gould, K. M. Merz, D. M. Ferguson, D. C. Spellmeyer, T. Fox, J. W. Caldwell, and P. A. Kollman, *JACS* 117, 5179 (1995).
- [29] G. Hummer, J. C. Rasaiah, and J. P. Noworyta, *Nature* 414 (6860), 188 (2001); B. Mukherjee, P. K. Maiti, C. Dasgupta, and A. K. Sood, *J. Chem. Phys.* 126(2007).
- [30] B. Mukherjee, P. K. Maiti, C. Dasgupta, and A. K. Sood, *Journal of Nanoscience and Nanotechnology* 9, 5303 (2009).
- [31] E. Hernandez, C. Goze, P. Bernier, and A. Rubio, *Phys. Rev. Letts.* 80, 4502 (1998).
- [32] K. N. Kudin, G. E. Scuseria, and B. I. Yakobson, *Physical Review B* 64, (2001).

- [33] A. K. Rappe, Goddard, W. A. III, J. Phys. Chem 95, 3358 (1991).
- [34] S. L. Mayo, B. D. Olafson, and W. A. Goddard, J. Phys. Chem. 94, 8897 (1990).
- [35] W. H. Moon and H. J. Hwang, Physica E-Low-Dimensional Systems & Nanostructures 23 (1-2), 26 (2004).
- [36] M. Santosh, P. K. Maiti, and A. K. Sood, Journal of Nanoscience and Nanotechnology 9, 5425(2009).
- [37] J. F. Waters, P. R. Guduru, M. Jouzi, J. M. Xu, T. Hanlon, and S. Suresh, App. Phys. Letts. 87 (2005).
- [38] B. I. Yakobson, C. J. Brabec, and J. Bernholc, Phys. Rev. Letts. 76, 2511 (1996).
- [39] J. P. Lu, Phys. Rev. Letts., 79, 1297 (1997).
- [40] A. Rubio, J. L. Corkill, and M. L. Cohen, Phys. Rev. B 49, 5081 (1994).
- [41] C. Y. Li and T. W. Chou, Journal of Nanoscience and Nanotechnology 6, 54 (2006).
- [42] P. H. Hunenberger, Adv. Polym. Sci., 173, 105(2005).
- [43] This article is based on the set of lectures I gave in the SERC school at IIT, Guwahati in 2008. I have greatly benefitted from the excellent set of lectures on the subject by Prof. David Kofke, University at Buffalo, The State University of New York.

Chapter 7

Applications of Molecular Dynamics Simulations

Subhankur Mitra and Samrath Lal Chapat

7.1 Introduction

The aim of Molecular Dynamics (MD) simulation is to study a system by recreating it on the computer as close to nature as possible, i.e. by simulating the dynamics of a system in all microscopic detail over a physical length of time relevant to the properties of interest. MD simulation generates very detailed information at the microscopic level and the conversion of this information into macroscopic level is the province of statistical mechanics. Therefore, MD simulations act as a bridge between microscopic length and time scales and the macroscopic world of the laboratory: we provide a guess at the interactions between molecules, and obtain predictions of bulk properties. Simulations act as a bridge also between theory and experiment. We may test a theory by conducting a simulation using the same model. We may test the model by comparing with experimental results. We may also carry out simulations on the computer that are difficult or impossible in the laboratory (for example, working at extremes of temperature or pressure). Finally we may want to make direct comparisons with experimental measurements made on specific materials, in which case a good model of molecular interactions is essential. The aim of so-called *ab initio* molecular dynamics is to reduce the amount of fitting and guesswork in this process to a minimum. On the other hand, we may be interested in phenomena of a rather generic nature, or we may simply want to discriminate between good and bad theories. When it comes to aims of this kind, it is not necessary to have a perfectly realistic molecular model; one that contains the essential physics may be quite suitable.

In this article, we do not intend to discuss the basics of MD simulation [1]. Rather, our main intention will be to show how to extract the various macroscopic properties from the MD simulation data and compare those properties with that obtained from experiments. MD simulation technique has been successfully exploited in many fields including biology [2], chemistry [3], material science [4], soft condensed matter [5] and condensed mater [6]. In the few examples described here, it is of interest to compare various properties obtained from MD simulation with that obtained from neutron scattering experiments. Therefore, it is better to discuss some basic parameters involved in neutron scattering experiments before discussing few examples. Algorithms for calculating various time correlation functions from MD simulation data are also discussed in the appendix.

The combination of thermal neutron scattering experiments and molecular dynamics (MD) simulations is a powerful tool to study the structure and dynamics of complex molecular systems. Thermal neutron scattering is sensitive to time and space correlations of atomic positions on the ps time scale and the Å length scale. These are exactly the time and space domains covered by classical molecular dynamics simulations. On the length scale under consideration the neutron-target interaction can be modelled by pseudopotentials with zero range which are centered on the atomic nuclei of the targets. The coupling between neutron and target is described by so-called scattering lengths describing the strength of the neutron-nucleus interaction [7, 8]. The differential scattering cross section can be expressed in terms of quantum time correlation functions of the spatially Fourier transformed particle density. The corresponding classical time correlation function can be easily obtained from molecular dynamics simulations. This enables a direct comparison between simulated and measured neutron scattering intensities. The experimental data can be used as a gauge for the MD force field which is the central input for the simulations. Conversely, the simulated intensities allow a detailed analysis of the dynamical and structural behaviour of the system under consideration [9, 10, 11, 12].

7.2 Theoretical Background

7.2.1 Dynamic Structure Factor

The quantity of interest in neutron scattering experiments with thermal neutrons is the *dynamic structure factor*, $\mathcal{S}(\mathbf{q}, \omega)$, which is closely related to the double differential cross-section [7], $d^2\sigma/d\Omega dE$. The double differential cross section is defined as the number of neutrons which are scattered per unit time into the solid angle interval $[\Omega, \Omega + d\Omega]$ and into the energy interval $[E, E + dE]$. It is normalized to $d\Omega$, dE , and the flux of the incoming neutrons,

$$\frac{d^2\sigma}{d\Omega dE} = N \cdot \frac{k}{k_0} \mathcal{S}(\mathbf{q}, \omega). \quad (7.1)$$

Here N is the number of atoms, and $k \equiv |\mathbf{k}|$ and $k_0 \equiv |\mathbf{k}_0|$ are the wave numbers of scattered and incident neutrons, respectively; \mathbf{k} and \mathbf{k}_0 being the wave vectors along the directions of the scattered and incident neutron beam respectively. They are related to the corresponding neutron energies by $E = \hbar^2 k^2 / 2m$ and $E_0 = \hbar^2 k_0^2 / 2m$, where m is the neutron mass. The arguments of the dynamic structure factor, \mathbf{q} and ω , are the momentum and energy transfer in units of \hbar , respectively:

$$\mathbf{q} = \frac{\mathbf{k}_0 - \mathbf{k}}{\hbar}, \quad (7.2)$$

$$\omega = \frac{E_0 - E}{\hbar}. \quad (7.3)$$

The dynamic structure factor contains information about the structure and dynamics of the scattering system [13]. It can be written as

$$\mathcal{S}(\mathbf{q}, \omega) = \frac{1}{2\pi} \int_{-\infty}^{+\infty} dt \exp[-i\omega t] \mathcal{F}(\mathbf{q}, t). \quad (7.4)$$

$\mathcal{F}(\mathbf{q}, t)$ is called the *intermediate scattering function* and is defined as

$$\mathcal{F}(\mathbf{q}, t) = \sum_{\alpha, \beta} \Gamma_{\alpha\beta} \langle \exp[-i\mathbf{q} \cdot \hat{\mathbf{R}}_{\alpha}(0)] \exp[i\mathbf{q} \cdot \hat{\mathbf{R}}_{\beta}(t)] \rangle, \quad (7.5)$$

$$\Gamma_{\alpha\beta} = \frac{1}{N} \left[\overline{b_{\alpha} b_{\beta}} + \delta_{\alpha\beta} (\overline{b_{\alpha}^2} - \overline{b_{\alpha}}^2) \right]. \quad (7.6)$$

The operators $\hat{\mathbf{R}}_{\alpha}(t)$ in Eq. (7.5) are the position operators of the nuclei in the sample. The brackets $\langle \dots \rangle$ denote a quantum thermal average and the time dependence of the position operators is defined by the Heisenberg picture. The quantities b_{α} are the scattering lengths of the nuclei which depend on the isotope and the relative orientation of the spin of the neutron and the spin of the scattering nucleus. If the spins of the nuclei and the neutron are not prepared in a special orientation one can assume a random relative orientation and that spin and position of the nuclei are uncorrelated. The symbol $\overline{\dots}$ appearing in $\Gamma_{\alpha\beta}$ denotes an average over isotopes and relative spin orientations of neutron and nucleus.

Usually one splits the intermediate scattering function and the dynamic structure factor into their *coherent* and *incoherent* parts which describe collective and single particle motions, respectively. Defining

$$b_{\alpha, coh} \doteq \overline{b_{\alpha}}, \quad (7.7)$$

$$b_{\alpha, inc} \doteq \sqrt{\overline{b_{\alpha}^2} - \overline{b_{\alpha}}^2}, \quad (7.8)$$

the coherent and incoherent intermediate scattering functions can be cast in the form

$$\mathcal{F}_{coh}(\mathbf{q}, t) = \frac{1}{N} \sum_{\alpha, \beta} b_{\alpha, coh} b_{\beta, coh} \langle \exp[-i\mathbf{q} \cdot \hat{\mathbf{R}}_{\alpha}(0)] \exp[i\mathbf{q} \cdot \hat{\mathbf{R}}_{\beta}(t)] \rangle, \quad (7.9)$$

$$\mathcal{F}_{inc}(\mathbf{q}, t) = \frac{1}{N} \sum_{\alpha} b_{\alpha, inc}^2 \langle \exp[-i\mathbf{q} \cdot \hat{\mathbf{R}}_{\alpha}(0)] \exp[i\mathbf{q} \cdot \hat{\mathbf{R}}_{\alpha}(t)] \rangle. \quad (7.10)$$

The corresponding dynamic structure factors are obtained by performing the Fourier transformation defined in Eq. (7.4).

An important quantity describing *structural* properties of liquids is the *static structure factor*, which is defined as

$$\mathcal{S}(\mathbf{q}) \doteq \int_{-\infty}^{+\infty} d\omega \mathcal{S}_{coh}(q, \omega) = \mathcal{F}_{coh}(\mathbf{q}, 0). \quad (7.11)$$

If the sums over α and β in (7.9) are extended over subsets of respectively equivalent atoms, one obtains the *partial static structure factors*.

7.2.2 Classical Framework

In the classical framework the intermediate scattering functions are interpreted as classical time correlation functions. The position operators are replaced by time-dependent vector functions and quantum thermal averages are replaced by classical *ensemble averages*. It is well known that this procedure leads to a loss of the universal detailed balance relation,

$$\mathcal{S}(\mathbf{q}, \omega) = \exp[\beta \hbar \omega] \mathcal{S}(-\mathbf{q}, -\omega), \quad (7.12)$$

and also to a loss of all odd moments

$$\langle \omega^{2n+1} \rangle \doteq \int_{-\infty}^{+\infty} d\omega \omega^{2n+1} \mathcal{S}(\mathbf{q}, \omega), \quad n = 1, 2, \dots \quad (7.13)$$

The odd moments vanish since the classical dynamic structure factor is even in ω , assuming invariance of the scattering process with respect to reflections in space. The first moment is also universal. For an atomic liquid, containing only one sort of atoms, it reads

$$\langle \omega \rangle = \frac{\hbar q^2}{2M}, \quad (7.14)$$

where M is the mass of the atoms. Formula (7.14) shows that the first moment is given by the average kinetic energy (in units of \hbar) of a particle which receives a momentum transfer $\hbar\mathbf{q}$. Therefore $\langle \omega \rangle$ is called the *recoil moment*. A number of ‘recipes’ has been suggested to correct classical dynamic structure factors

for detailed balance and to describe recoil effects in an approximate way. The most popular one has been suggested by SCHOFIELD [14]

$$\mathcal{S}(\mathbf{q}, \omega) \approx \exp\left[\frac{\beta\hbar\omega}{2}\right] \mathcal{S}_{cl}(\mathbf{q}, \omega). \quad (7.15)$$

One can easily verify that the resulting dynamic structure factor fulfills the relation of detailed balance. Formally, the correction (7.15) is correct to first order in \hbar . Therefore it cannot be used for large q -values which correspond to large momentum transfers $\hbar q$. This is actually true for all correction methods which have suggested so far.

7.2.3 Elastic Incoherent Structure Factor

The elastic incoherent structure factor (EISF) is defined as the limit of the incoherent intermediate scattering function for infinite time,

$$EISF(\mathbf{q}) \doteq \lim_{t \rightarrow \infty} \mathcal{F}_{inc}(\mathbf{q}, t). \quad (7.16)$$

Using the above definition of the EISF one can decompose the incoherent intermediate scattering function as follows:

$$\mathcal{F}_{inc}(\mathbf{q}, t) = EISF(\mathbf{q}) + \mathcal{F}'_{inc}(\mathbf{q}, t), \quad (7.17)$$

where $\mathcal{F}'_{inc}(\mathbf{q}, t)$ decays to zero for infinite time. Taking now the Fourier transform it follows immediately that

$$\mathcal{S}_{inc}(\mathbf{q}, \omega) = EISF(\mathbf{q})\delta(\omega) + \mathcal{S}'_{inc}(\mathbf{q}, \omega). \quad (7.18)$$

The EISF appears as the amplitude of the *elastic* line in the neutron scattering spectrum. Elastic scattering is only present for systems in which the atomic motion is confined in space, as for solids. To understand which information is contained in the EISF we consider for simplicity a system where only one sort of atoms is visible to the neutrons. To a very good approximation this is the case for all systems containing a large amount of hydrogen atoms, as biological systems. Incoherent scattering from hydrogen dominates by far all other contributions. Using the definition of the van Hove self-correlation function $G_s(\mathbf{r}, t)$ [7],

$$b_{inc}^2 G_s(\mathbf{r}, t) \doteq \frac{1}{2\pi^3} \int d^3 q \exp[-i\mathbf{q} \cdot \mathbf{r}] \mathcal{F}_{inc}(\mathbf{q}, t), \quad (7.19)$$

which can be interpreted as the conditional probability to find a tagged particle at the position \mathbf{r} at time t , given it started at $\mathbf{r} = \mathbf{0}$, one can write:

$$EISF(\mathbf{q}) = b_{inc}^2 \int d^3 r \exp[i\mathbf{q} \cdot \mathbf{r}] G_s(\mathbf{r}, t = \infty). \quad (7.20)$$

The EISF gives the sampling distribution of the points in space in the limit of infinite time. In a real experiment this means times longer than the time which

is observable with a given instrument. The EISF vanishes for all systems in which the particles can access an infinite volume since $G_s(\mathbf{r}, t)$ approaches $1/V$ for large times. This is the case for molecules in liquids and gases.

For computational purposes it is convenient to use the following representation of the EISF [15]:

$$EISF(\mathbf{q}) = \frac{1}{N} \sum_{\alpha} b_{\alpha,inc}^2 \langle |\exp[i\mathbf{q} \cdot \mathbf{R}_{\alpha}]|^2 \rangle. \quad (7.21)$$

This expression is derived from definition (7.16) of the EISF and expression (7.10) for the intermediate scattering function, using that for infinite time the relation

$$\langle \exp[-i\mathbf{q} \cdot \mathbf{R}_{\alpha}(0)] \exp[i\mathbf{q} \cdot \mathbf{R}_{\alpha}(t)] \rangle = \langle |\exp[i\mathbf{q} \cdot \mathbf{R}_{\alpha}]|^2 \rangle \quad (7.22)$$

holds. In this way the computation of the EISF is reduced to the computation of a static thermal average. We remark at this point that the length of the MD trajectory from which the EISF is computed should be long enough to allow for a representative sampling of the conformational space.

7.2.4 Velocity Correlation Functions

The velocity autocorrelation function (VACF) of atom α in an atomic or molecular system is usually defined as

$$C_{vv;\alpha\alpha}(t) \doteq \frac{1}{3} \langle \mathbf{v}_{\alpha}(0) \cdot \mathbf{v}_{\alpha}(t) \rangle. \quad (7.23)$$

In some cases, e.g. for non-isotropic systems, it is useful to define VACFs along a given axis,

$$C_{vv;\alpha\alpha}(t; \mathbf{n}) \doteq \langle v_{\alpha}(0; \mathbf{n}) v_{\alpha}(t; \mathbf{n}) \rangle, \quad (7.24)$$

where $v_{\alpha}(t; \mathbf{n})$ is given by

$$v_{\alpha}(t; \mathbf{n}) \doteq \mathbf{n} \cdot \mathbf{v}_{\alpha}(t). \quad (7.25)$$

The vector \mathbf{n} is a unit vector defining a space-fixed axis.

The VACFs of the particles in a many body system can be related to the incoherent dynamic structure factor. It is easy to show that

$$\lim_{q \rightarrow 0} \frac{\omega^2}{q^2} S(\mathbf{q}, \omega) = G(\omega), \quad (7.26)$$

where $G(\omega)$ is the *density-of-states* (DOS). For an isotropic system it reads

$$G(\omega) = \sum_{\alpha} b_{\alpha,inc}^2 \tilde{C}_{vv;\alpha\alpha}(\omega), \quad (7.27)$$

$$\tilde{C}_{vv;\alpha\alpha}(\omega) = \frac{1}{2\pi} \int_{-\infty}^{+\infty} dt \exp[-i\omega t] C_{vv;\alpha\alpha}(t). \quad (7.28)$$

For non-isotropic systems relation (7.26) holds if the DOS is computed from the atomic velocity autocorrelation functions $C_{vv;\alpha\alpha}(t; \mathbf{n}_q)$, where \mathbf{n}_q is the unit vector in the direction of \mathbf{q} .

7.2.5 Mean-square Displacements

Another important quantity describing the dynamics of an atomic or molecular system is the mean-square displacement (MSD) of a particle. Defining

$$\mathbf{d}_\alpha(t) \doteq \mathbf{R}_\alpha(t) - \mathbf{R}_\alpha(0). \quad (7.29)$$

the MSD of particle α is given by

$$\Delta_\alpha^2(t) = \langle \mathbf{d}_\alpha^2(t) \rangle. \quad (7.30)$$

As for the VACF one can introduce a mean-square displacement with respect to a given axis:

$$\Delta_\alpha^2(t; \mathbf{n}) \doteq \langle d_\alpha^2(t; \mathbf{n}) \rangle \quad (7.31)$$

with

$$d_\alpha(t; \mathbf{n}) \doteq \mathbf{n} \cdot \mathbf{d}_\alpha(t). \quad (7.32)$$

The calculation of mean-square displacements is the standard way to obtain diffusion coefficients from MD simulations. Assuming Einstein-diffusion in the long time limit one has for isotropic systems

$$D_\alpha = \lim_{t \rightarrow \infty} \frac{1}{6t} \Delta_\alpha^2(t). \quad (7.33)$$

The mean-square displacement can be related to the incoherent intermediate scattering function via the cumulant expansion [16, 17]

$$\mathcal{F}_{inc}(\mathbf{q}, t) = \frac{1}{N} \sum_\alpha b_{\alpha, inc}^2 \exp[-q^2 \rho_{\alpha, 1}(t) + q^4 \rho_{\alpha, 2}(t) \mp \dots]. \quad (7.34)$$

The cumulants $\rho_{\alpha, k}(t)$ are defined as

$$\rho_{\alpha, 1}(t) = \frac{1}{2!} \langle d_\alpha^2(t; \mathbf{n}_q) \rangle \quad (7.35)$$

$$\rho_{\alpha, 2}(t) = \frac{1}{4!} [\langle d_\alpha^4(t; \mathbf{n}_q) \rangle - 3 \langle d_\alpha^2(t; \mathbf{n}_q) \rangle^2] \quad (7.36)$$

⋮

The vector \mathbf{n}_q is the unit vector in the direction of \mathbf{q} . In the Gaussian approximation the above expansion is truncated after the q^2 -term. For certain model systems like the ideal gas, the harmonic oscillator, and a particle undergoing Einstein diffusion, this is exact. For these systems the incoherent intermediate scattering function is completely determined by the mean-square displacement.

There exists also a well-known relation between the mean-square displacement and the velocity autocorrelation function. Writing $\mathbf{d}_\alpha(t) = \int_0^t d\tau \mathbf{v}_\alpha(\tau)$ in Eq. (7.30) one can show (see e.g. [17]) that

$$\Delta_\alpha^2(t) = 6 \int_0^t d\tau (t - \tau) C_{vv; \alpha\alpha}(\tau). \quad (7.37)$$

Using now the definition (7.33) of the diffusion coefficient one obtains the relation

$$D_\alpha = \int_0^t d\tau C_{vv;\alpha\alpha}(\tau). \quad (7.38)$$

With Eq. (7.28) this can also be written as

$$D_\alpha = \pi \tilde{C}_{vv;\alpha\alpha}(0). \quad (7.39)$$

7.2.6 Structural Quantities

The density of the particle is given by

$$\rho^{(1)}(\mathbf{r}) = \langle \rho(\mathbf{r}) \rangle = \left\langle \sum_i \delta(\mathbf{r} - \mathbf{r}_i) \right\rangle \quad (7.40)$$

In the homogeneous system, $\rho^{(1)} = \rho = N/V$. In the same way, we define the pair density function as

$$\rho^{(2)}(\mathbf{r}, \mathbf{r}') = \left\langle \sum_i \sum_{j \neq i} \delta(\mathbf{r} - \mathbf{r}_i) \delta(\mathbf{r}' - \mathbf{r}_j) \right\rangle \quad (7.41)$$

If we define, $\mathbf{R} = \mathbf{r} - \mathbf{r}'$ and assume that $\rho^{(2)}$ depends only on \mathbf{R} , then

$$\rho^{(2)}(\mathbf{R}) = \left\langle \sum_i \sum_{j \neq i} \delta(\mathbf{R} - \mathbf{r}' - \mathbf{r}_i) \delta(\mathbf{r}' - \mathbf{r}_j) \right\rangle \quad (7.42)$$

$$= \frac{1}{V} \left\langle \int d\mathbf{r}' \sum_i \sum_{j \neq i} \delta(\mathbf{R} + \mathbf{r}' - \mathbf{r}_i) \delta(\mathbf{r}' - \mathbf{r}_j) \right\rangle \quad (7.43)$$

$$= \frac{1}{V} \left\langle \sum_i \sum_{j \neq i} \delta(\mathbf{R} + \mathbf{r}_j - \mathbf{r}_i) \right\rangle \quad (7.44)$$

The pair distribution function $g_2(\mathbf{r}_j, \mathbf{r}_i)$ or $g(r)$ gives a probability of finding a pair of atoms a distance r apart, relative to the probability expected for a completely random distribution at the same density.

$$g(\mathbf{r}) = \frac{\rho^{(2)}(\mathbf{r})}{\rho^2} \quad (7.45)$$

$$= \frac{V}{N^2} \left\langle \sum_i \sum_{j \neq i} \delta(\mathbf{r} - \mathbf{r}_{ij}) \right\rangle \quad (7.46)$$

The Fourier transformed density $\rho(\mathbf{q})$ is defined as

$$\rho(\mathbf{q}) = \int d\mathbf{r} e^{-i\mathbf{q}\cdot\mathbf{r}} \sum_i \delta(\mathbf{r} - \mathbf{r}_i) \quad (7.47)$$

$$= \sum_i e^{-i\mathbf{q}\cdot\mathbf{r}_i} \quad (7.48)$$

If we consider the reciprocal lattice vector of the initial lattice for \mathbf{q} , then for a solid, $\rho(q)$ is of order unity, whereas for a liquid it oscillates, with amplitude $O(N^{-1/2})$ about zero.

The static structure factor $S(\mathbf{q})$ is defined as

$$S(\mathbf{q}) = \frac{1}{N} \langle \rho(\mathbf{q})\rho(-\mathbf{q}) \rangle \quad (7.49)$$

$$= \frac{1}{N} \left\langle \sum_i \sum_j e^{-i\mathbf{q}\cdot\mathbf{r}_i} e^{-i\mathbf{q}\cdot\mathbf{r}_j} \right\rangle \quad (7.50)$$

$$= 1 + \frac{1}{N} \left\langle \sum_i \sum_{j \neq i} \int \int d\mathbf{r} d\mathbf{r}' e^{-i\mathbf{q}\cdot(\mathbf{r}-\mathbf{r}')} \delta(\mathbf{r} - \mathbf{r}_i) \delta(\mathbf{r}' - \mathbf{r}_j) \right\rangle \quad (7.51)$$

$$= 1 + \frac{1}{N} \int \int d\mathbf{r} d\mathbf{r}' e^{-i\mathbf{q}\cdot(\mathbf{r}-\mathbf{r}')} \rho^{(2)}(\mathbf{r}, \mathbf{r}') \quad (7.52)$$

$$= 1 + \rho \int d\mathbf{r} e^{-i\mathbf{q}\cdot\mathbf{r}} g(\mathbf{r}) \quad (7.53)$$

$$S(q) = 1 + 4\pi\rho \int dr r^2 g(r) \frac{\sin qr}{qr} \quad (7.54)$$

7.3 Case Study

7.3.1 Diffusion of Hydrocarbons in Zeolitic Pores

The shape selectivity of zeolitic materials with respect to hydrocarbons for the cracking reactions has been an ongoing research field for quite some time now [18]. The catalytic properties of zeolites for cracking reactions have been known to be influenced by the way hydrocarbons are selected both on the reactant as well as the product sides by their shapes. A major contribution to this is thought to come from the diffusive properties of the adsorbed hydrocarbons [19]. These properties are further known to be affected by a variety of parameters including the temperature, the concentration of the adsorbed species and size/shape of the guest molecules as well as the host cages among others [19, 20]. Several such dependencies have been investigated. Here we shall discuss the diffusive properties of one particular hydrocarbon, propylene absorbed in two types of zeolite, e.g., Na-Y zeolite and ZSM-5 zeolite. Na-Y zeolite is characterized by a network of almost spherical supercages, which are interconnected with each other in a tetrahedral manner by 12 membered oxygen rings forming windows.

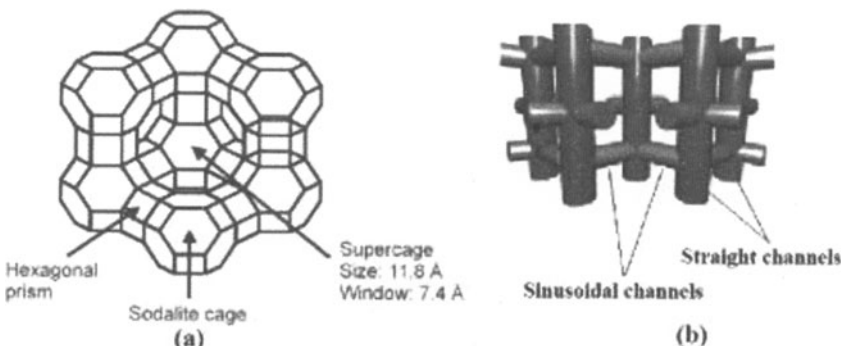


Figure 7.1: Structure of Na-Y (a) and ZSM5 (b) zeolites. The sinusoidal and straight channels in ZSM5 and almost spherical supercage in Na-Y zeolite are indicated.

The diameter of these windows is about 7.8 Å while the supercages themselves have a diameter of 11.8 Å. Na-Y has a high Si/Al ratio of more than 2.5. Another zeolite in which the dynamics of adsorbed hydrocarbons has been widely studied is the ZSM5 zeolite. The all silica form of this zeolite is called silicalite. Unlike Na-Y zeolite, this zeolite is typified by a network of intersecting channels. There are straight ellipsoidal channels with a diameter of ~ 5.5 Å running along the crystallographic axis ‘*b*’. These are intersected by sinusoidal channels in the ‘*a-c*’ plane. The free space available for the adsorbed guest molecule is thus restricted in ZSM5 as compared to that in the Na-Y zeolite. Fig. 1 shows the structures of Na-Y and ZSM5 zeolites.

Here, we shall discuss the diffusive behaviour of propylene molecule inside Na-Y and ZSM5 zeolite. Propylene molecule was assumed to be rigid and modelled as united atom as shown in Fig. 2. Atomic positions of the zeolites as reported by Fitch et al [21] for Na-Y and Koningsveld et al [22] for ZSM5 were used in the simulation. The simulation cell consisted of $(2 \times 2 \times 2)$ unit cells of ZSM5 zeolite and a $(1 \times 1 \times 1)$ unit cell for Na-Y zeolite. Intermolecular interactions were modelled by Lennard-Jones (6-12) potential. Molecule-molecule and molecule-zeolite interactions for the system of propylene in Na-Y zeolite and ZSM5 zeolite using united atom model were taken from the literature [23, 24, 25, 26].

The position vector of an interacting species of propylene molecule can be written as a sum of the position vector of the centre of mass of the molecule with respect to a space fixed reference frame, \mathbf{r}_i^{CM} and the position vector of the species with respect to the centre of mass of the molecule \mathbf{d}_i .

$$\mathbf{r}_i = \mathbf{r}_i^{CM} + \mathbf{d}_i \quad (7.55)$$

This decomposition of the position vector of an interacting species in the space fixed frame can be used to separate the two components – translational and rotational part of the molecular motion. While the evolution of position

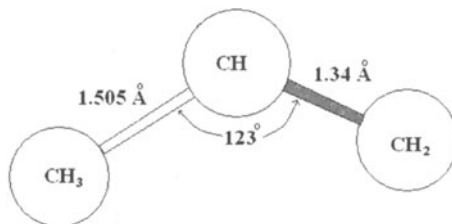


Figure 7.2: United atom model of a propylene molecule.

vector of the centre of mass of the molecules can be understood to represent the translational motion, the position vector of the species in the centre of mass frame provides information about the rotational motion. The trajectories of the centre of mass of a propylene molecule inside Na-Y and ZSM5 zeolites are plotted in figs. 3 and 4. The trajectories in the Na-Y zeolite are marked by intermittent crowding which indicates presence of pores at those positions. As can be seen in Fig. 4, the trajectories of propylene in ZSM5 zeolite indicate the existence of straight channels in y direction and sinusoidal channels in the x - z plane. Moreover, if one were to project the trajectories on the Cartesian axes, the projection can be seen to be smallest on the z axis. This indicates that the diffusivity is slowest along z direction as also revealed by MSD and VACF curves.

In a molecular dynamics simulation, several correlation functions can be calculated from the trajectories of the molecules made available by the simulation. These correlation functions reveal a lot of information about the system. For example, the translational diffusion coefficient for a molecular system can be obtained in a molecular dynamics simulation from the mean squared displacement (MSD) as discussed in section 7.2.5. Algorithm for computing MSD

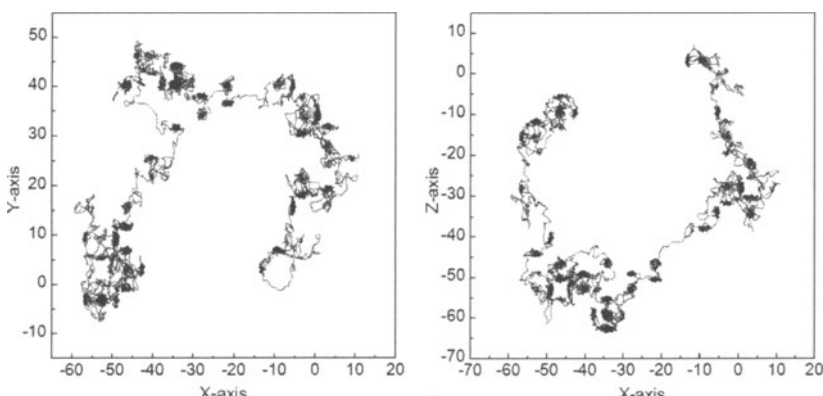


Figure 7.3: Center of mass trajectory of a single propylene molecule inside Na-Y zeolite.

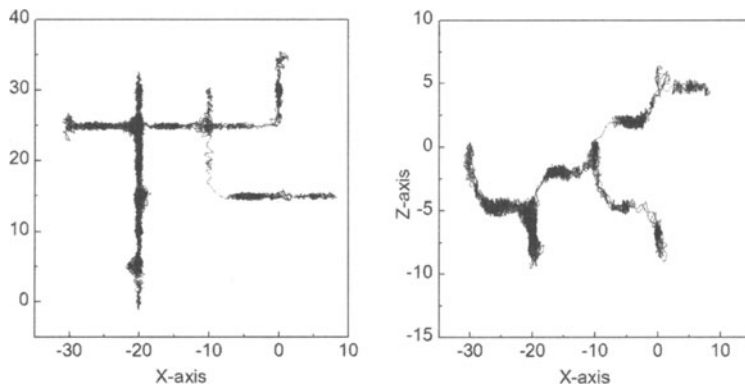


Figure 7.4: Center of mass trajectory of a single propylene molecule inside ZSM5 zeolite.

is also discussed in section 7.4.2. MSD curves obtained from a simulation of propylene in Na-Y and ZSM5 zeolites are shown in Fig. 5. It is evident that the diffusivity (calculated as described by Eq. (7.33)) of propylene is larger in Na-Y zeolite ($3.8 \times 10^{-5} \text{ cm}^2/\text{s}$) as compared to that in ZSM5 ($1.5 \times 10^{-5} \text{ cm}^2/\text{s}$). This is to be expected because of a larger void volume available in Na-Y zeolite for the propylene molecules to diffuse as compared to that in ZSM5.

Another interesting feature in the MSD behaviour is the anisotropy observed in the case of propylene adsorbed in ZSM5. As can be seen in Fig. 6 the MSD in the y direction (crystallographic axis b) is maximum and it is minimum in the z direction (crystallographic axis c). From these curves values of diffu-

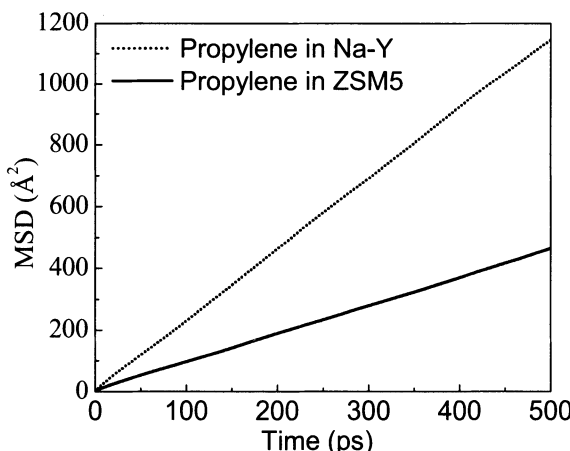


Figure 7.5: Mean squared displacement vs. time for centre of mass of propylene molecule adsorbed in Na-Y (dotted line) and ZSM5 (solid line) zeolites.

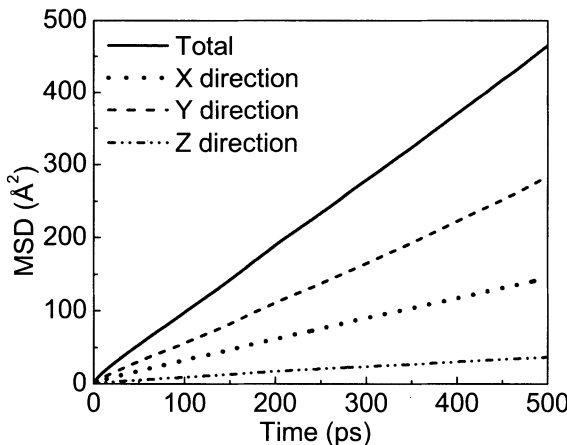


Figure 7.6: Mean squared displacement vs. time in different directions for propylene adsorbed in ZSM5 zeolite.

sivity were obtained in different directions as shown in Table I. The anisotropy in the diffusivity is to be expected because, as said earlier the zeolite topology consists of straight channels in the y direction and sinusoidal channels in the x and z directions. This means that the molecules can freely move in the y direction whereas they suffer many collisions with the sinusoidal channel walls in the x and z directions. Moreover, this constriction in the motion of propylene molecules within the sinusoidal channels is stronger in the z direction as compared to that in the x direction. This makes the diffusivity along the z direction minimum.

Table I: Diffusion coefficients obtained from MSD vs. time curve for propylene adsorbed in ZSM5 zeolite. All values quoted are in the units of $\times 10^{-5} \text{ cm}^2/\text{s}$.

Dx	Dy	Dz	Dtotal
1.424	2.941	0.3320	1.534

The velocity autocorrelation functions (as described in section 7.2.4 and the algorithm described in section 7.4.1 is used for the calculation) for propylene adsorbed in Na-Y and ZSM5 zeolites are shown in Fig. 7. A striking feature of the VACF for propylene in ZSM5 zeolite is the existence of rapid oscillations. This is because of a larger restriction put on the translational motion of propylene molecules by the zeolitic channel walls in the case of ZSM5 zeolite as compared to that in the case of Na-Y zeolite. A negative region is nevertheless seen also in the case of Na-Y zeolite indicating a rebound motion at short times. This may be caused by collisions of the propylene molecule with the surrounding propylene molecules as well as the walls of the zeolitic supercage. The anisotropy seen in the mean squared displacement for propylene adsorbed in

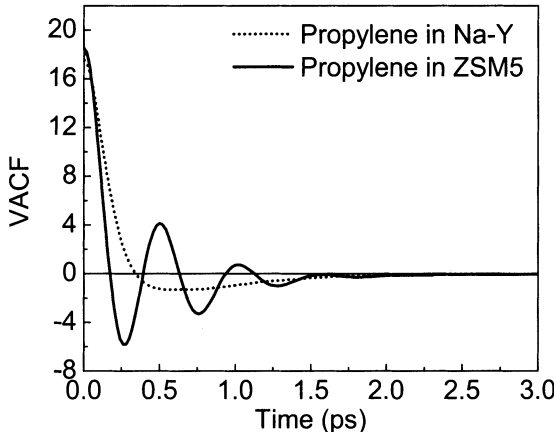


Figure 7.7: Center of mass velocity autocorrelation function for propylene adsorbed in Na-Y (dotted curve) and ZSM5 (solid curve) zeolites.

ZSM5 zeolite is reflected by the corresponding velocity autocorrelation function also. This is shown in Fig. 8. One can observe here that the oscillations in the VACF are more prominent in the z direction as compared to that in the x and y directions. This indicates frequent collision of propylene molecules with the zeolitic walls in the z direction.

To obtain the detail information about the translational motion, the incoherent intermediate scattering function (described in section 7.4.3) for center of mass $I^{CM}(Q,t)$ was calculated for propylene in both the systems for different Q

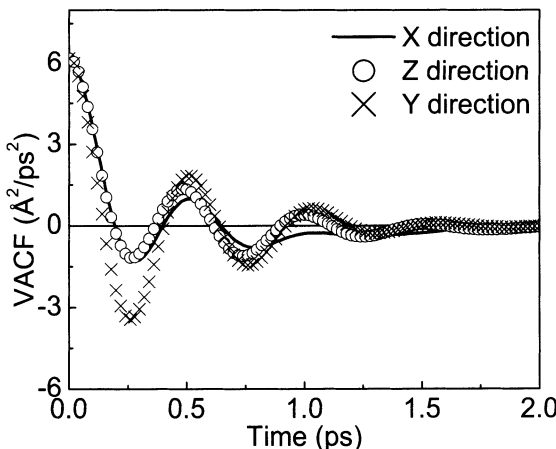


Figure 7.8: Anisotropy in the center of mass velocity autocorrelation function for propylene adsorbed ZSM5 zeolite.

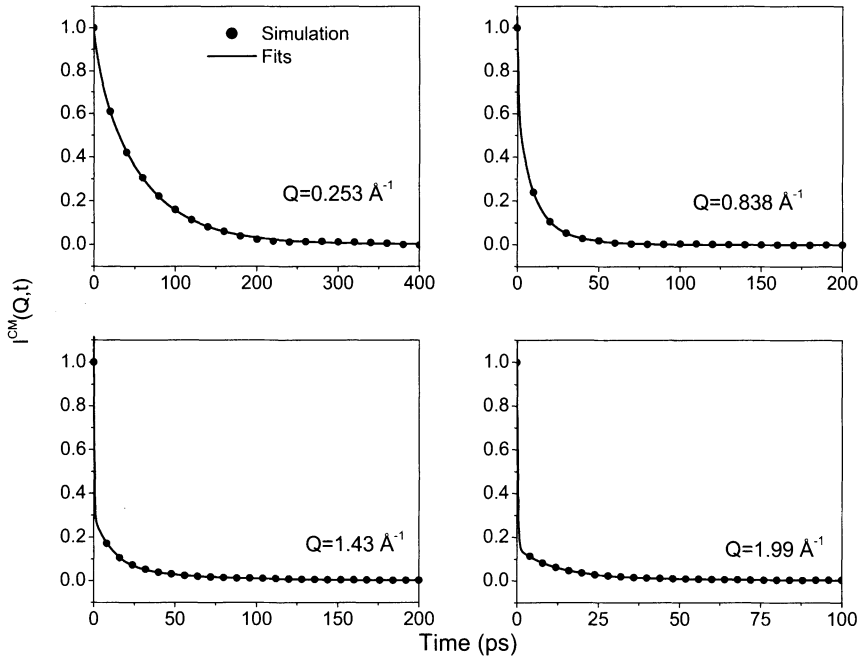


Figure 7.9: $I^{CM}(Q,t)$ functions for propylene in Na-Y zeolite fitted with the model in Eq. 56.

values. This intermediate scattering function is nothing but the Fourier transform of the dynamic scattering function $S(Q,\omega)$ obtained from any scattering experiment, e.g., inelastic neutron scattering experiment.

In case of propylene adsorbed in Na-Y zeolite, a combination of three exponential functions was found to fit these functions well over the whole range of Q and t . The $I^{CM}(Q,t)$ functions could thus be modelled as

$$I^{CM}(Q,t) = A_1(Q) \exp(-\Gamma_1(Q)t) + A_2(Q) \exp(-\Gamma_2(Q)t) + A_3(Q) \exp(-\Gamma_3(Q)t) \quad (7.56)$$

The resulting fits are shown in Fig. 9. Presence of three exponentials in the model $I^{CM}(Q,t)$ indicates the presence of three components of translational motion. The three components correspond to the motion of the propylene molecules in different regions of the zeolitic framework. The behavior of the decay constants corresponding to the three components, Γ_1 , Γ_2 and Γ_3 , are shown in Fig. 10. Also shown in Fig. 10 is the quasielastic neutron scattering (QENS) data for propylene adsorbed in Na-Y zeolite from ref. [27]. It can be noticed that, intermediate component of the translational motion (with a decay constant Γ_2) of propylene in Na-Y zeolite is found to correspond to the one observed in the QENS experiments [27]. Since the QENS spectrometer is

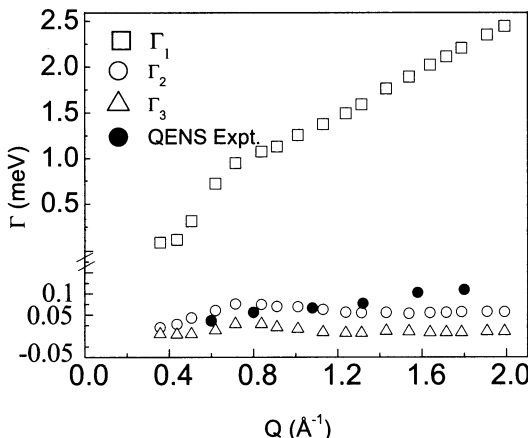


Figure 7.10: Variation of Γ of the three components of the intermediate scattering function corresponding to the translational motion of propylene in Na-Y zeolite (Eq. 56)

having a finite energy resolution, a very fast motion, such as Γ_1 or a very slow motion such as Γ_3 can not be observed through a QENS spectrometer used for this particular study. The intermediate scattering functions for rotational motion at some Q are shown in Fig. 11 for propylene in Na-Y zeolite.

As is evident these functions decay to a non-zero value at a very rapid rate. This indicates a faster rotational motion. As discussed earlier the value of these

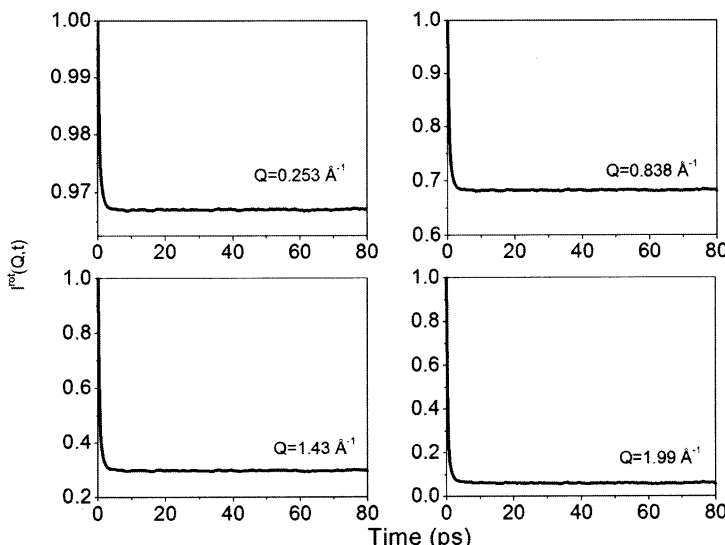


Figure 7.11: $I^{rot}(Q,t)$ functions for propylene in Na-Y zeolite.

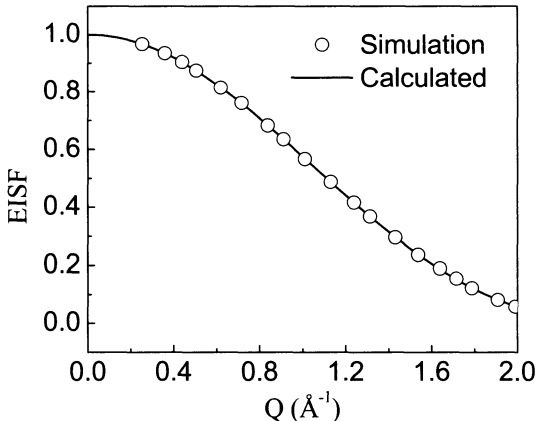


Figure 7.12: Variation of $EISF$ obtained from the simulation for propylene in Na-Y zeolite. The solid curve corresponds to the calculated variation for isotropic rotational diffusion.

functions at long enough times is identical to the elastic incoherent structure factor or $EISF$ (see section 7.2.3). To understand the behavior of the rotational motion, the variation of $EISF$ was compared with various models of rotational motion. The variation of $EISF$ is found to be described well by the isotropic rotational diffusion model (where rotation axis is isotropically distributed) as shown in Fig. 12 for propylene in Na-Y zeolite. Similar behaviour is observed in case of ZSM5 zeolite also. Trajectory of a CH_3 site with respect to centre of mass in Na-Y zeolite is also shown in Fig. 13.

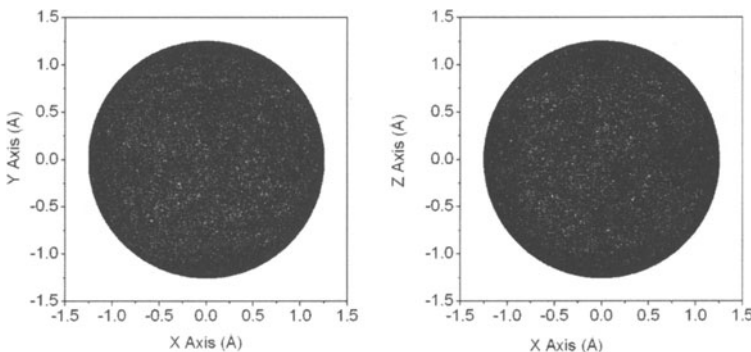


Figure 7.13: Trajectory of a CH_3 site with respect to the centre of mass of the molecule for the whole production run time of 1.3 ns in Na-Y zeolite. The trajectory is evidently a sphere in three dimensions confirming that the rotational motion indeed is isotropic.

7.3.2 Phase Transitions in MgSiO₃

Magnesium silicate in various polymorphic forms constitutes a major component of the Earth's mantle. The upper mantle, which extends to a depth of 440 km, contains olivine, pyroxene and garnet phases, whereas the lower mantle below 660 km depth is largely made of the perovskite phase [28]. Apparently, the most important difference between the upper and lower mantle silicates is that the silicon coordination changes from 4 to 6 respectively, whereas the Mg coordination also increases from 6 to 8. This kind of information is indirectly inferred from seismic observations and compositional modeling of the Earth's interior based on accurate information about the structure and thermodynamic properties of the constituent phases [29, 30, 31, 32, 33, 34]. Accurate modelling of mantle minerals is therefore of utmost importance, and simultaneously is also a major challenge in condensed matter physics.

We shall discuss here the results of MD simulations in Magnesium silicate as a function of pressure at high temperature starting from an important upper mantle phase, orthoenstatite [35]. The present studies have used well-tested interatomic potentials comprising of long-ranged Coulomb and short ranged Born-Mayer type interactions. The MD simulations were performed on systems of about 4000 atoms using macrocells of size (2a, 4b, 6c), where a, b, and c are respectively, around 18 Å, 9 Å, and 5 Å. The results have been cross-checked using macrocells of sizes (2a, 2b, 4c) and (4a, 4b, 6c) and these simulations took several weeks on a parallel supercomputer.

The wave velocities are calculated from the simulation of the dynamical structure factors $S(\mathbf{Q}, \omega)$ of fairly long wave length (of about 40 Å) acoustic phonons in several propagation directions. The structure factor $S(\mathbf{Q}, \omega)$ is the Fourier transform of the intermediate scattering function $I(\mathbf{Q}, t)$, which is described in section 4.3.

Figure 14 shows the simulated change of volume as a function of pressure at three fixed temperatures of 300 K, 900 K, and 2050 K, which clearly reveal first order transitions. The transition pressures appear to decrease with increasing temperature.

The Preliminary Reference Earth Model (PREM) estimates [29] of seismic wave velocity and density variations in the Earth's interior are also shown (squares) in the Fig. The simulations involve only one initial phase while the PREM results (based on seismic observations and estimates of the physical and thermodynamic properties of mantle forming phases) correspond to an actual mantle composition. The transition zone between the upper and lower mantle is defined by the observed seismic discontinuities at depths of about 440 km and 660 km which on a pressure scale correspond to about 13 GPa and 24 GPa, respectively.

The simulated structure factors of a typical longitudinal and transverse acoustic phonon mode in the enstatite, intermediate, and perovskite phases are shown in Figures 15. Both the longitudinal and transverse acoustic phonon frequencies shift to higher energies upon transformation from the enstatite to the

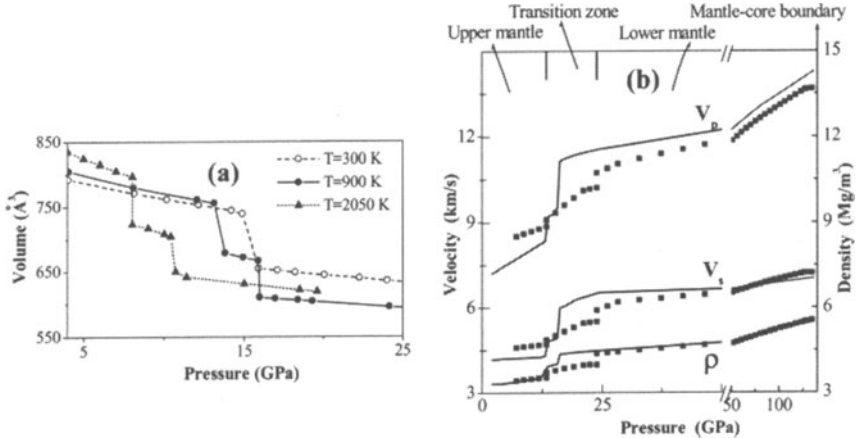


Figure 7.14: (a) The simulated volumes as a function of increasing pressure at various temperatures. (b) The solid line corresponds to the simulated longitudinal (VP) and transverse (VS) wave velocities and density (ρ) as a function of pressure upto the mantle-core boundary at $T = 900$ K. The wave velocities VP and VS are obtained by averaging over a large number of acoustic mode frequencies along various directions. The discontinuities in the simulated VP , VS and ρ represent phase transitions.

perovskite phase (via the intermediate phase). This “hardening” of frequencies in turn results in significant changes in the elastic properties, which finally manifests as discontinuities in the simulated seismic velocities (Fig. 14b).

Figures 16 shows the crystal structures of the three simulated phases. Orthoenstatite [36] is orthorhombic (having the space group $Pbca$ with 80 atoms in the unit cell) and its structure comprises of MgO_6 octahedral bands and single silicate tetrahedral chains. For clarity, only the coordination polyhedra around the Si atoms are shown, with the Mg atoms depicted as circles. In enstatite, there are two crystallographically distinct MgO_6 octahedra (which are shown as circles of varying shades) and the silicate SiO_4 tetrahedra share corners to form chains parallel to the c -axis. The perovskite structure, on the other hand comprises of a network of corner-shared SiO_6 octahedra, with the Mg atoms occupying the interstices. The coordination number of Mg in $MgSiO_3$ perovskite, depends on the degree of distortion from the cubic, varying from 12 (in the ideal cubic) to 8 (in the distorted orthorhombic). X-ray diffraction studies indicate that $MgSiO_3$ perovskite has the orthorhombic structure (with space group $Pnma$ having 20 atoms/unit cell) over a wide range of pressures and temperature [36]. The simulated structures of enstatite and perovskite are overall consistent with these experimental observations. In Figures 17, the calculated vibrational density of states (see Eq. (7.26)) in enstatite phase along with the partial contributions from the Mg, Si, and O atoms is shown. The

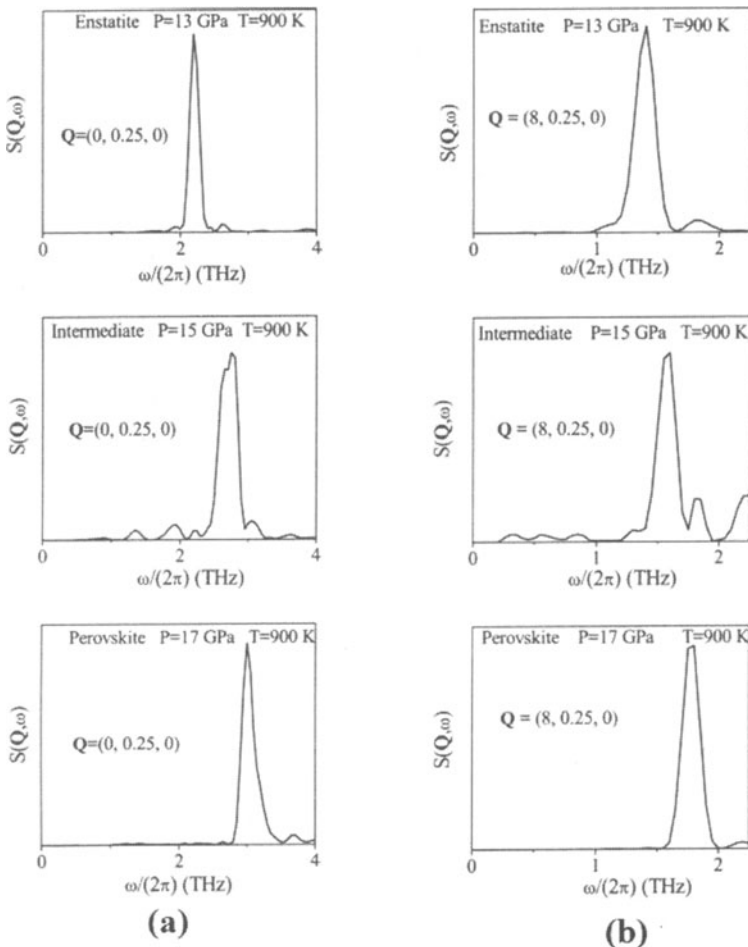


Figure 7.15: The simulated structure factor of a typical a) longitudinal acoustic phonon mode and b) transverse acoustic phonon mode in the enstatite, intermediate and perovskite phases.

simulated density of states of enstatite is found to be in overall agreement with results obtained from lattice dynamics calculations and available inelastic neutron scattering data [37].

7.3.3 Shock-induced Amorphization of Alpha-quartz

Amorphous or glassy materials are usually formed by rapid quenching of a melt. However, in case of a large number of compounds, especially those composed of polyhedral networks such as quartz, application of pressure often leads to a crystal to amorphous transition. Typically, static or shock pressures of about 2-20

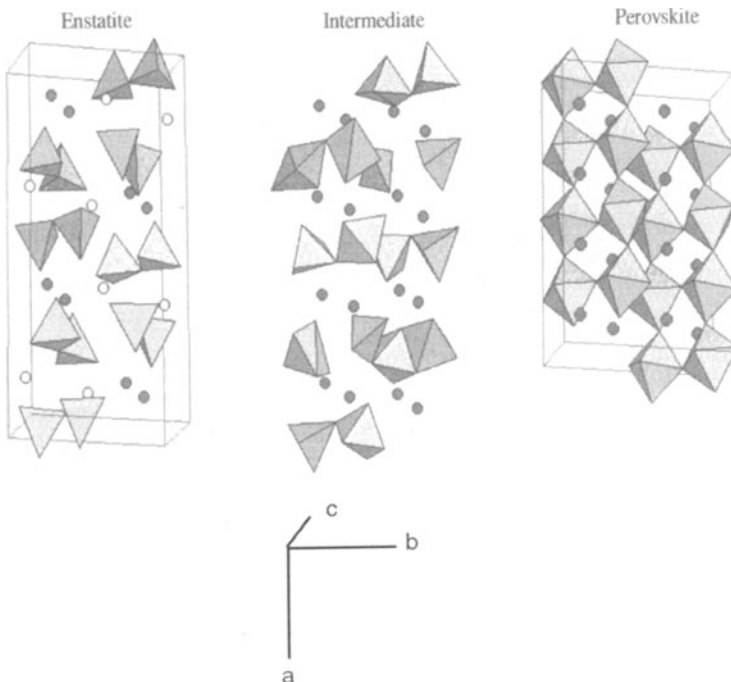


Figure 7.16: Simulated high pressure structures in the enstatite, intermediate, and perovskite phases. The Mg atoms (circles) and the coordination polyhedra around the Si atoms are displayed. The intermediate phase (characterized by 5-coordinated silicon) is an orientationally disordered crystalline phase with space group $Pmna$ where the Mg and Si atoms occupy the $2b$ and $2d$ sites, respectively.

GPa are involved. Molecular dynamics simulations are useful in understanding, and even predicting, such transformations. This example describes the results of MD simulation of shock pressure induced amorphization of alpha-quartz [38]. A very long periodic macro cell of 100-200 nm length is used along the shock direction that contains about 15000 atoms. The shock pressure front, temperature and the average coordination of the silicon atoms along the shock-axis as a function of time after the shock initiation have been monitored. Fig. 18 gives the shock front profiles at a few pressures. The shock front is expected to have one or more steps depending on whether the pressure is below the Hugoniot elastic limit, below the phase transition pressure, just above it or much above it. Split shock wave profiles have been observed in experiments on α -quartz. Fig. 18 clearly shows such a behavior. The shock front is found to be rather sharp with a width of a few nm only. The calculated equation of state for the shock along the c -axis is given in Fig. 19, which includes a comparison with shock data [39, 40]. The agreement is found to be very good.

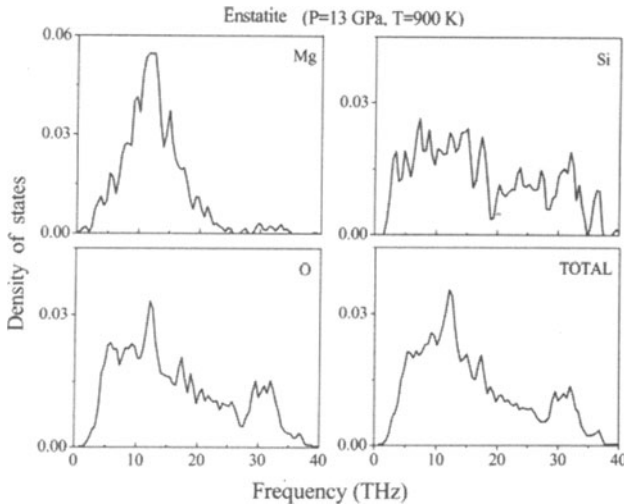


Figure 7.17: Calculated partial and total density of states (arbitrary units) of enstatite at $P = 13$ GPa and $T = 900$ K.

Snapshots of atomic positions under the shock at a few pressures are shown in Fig. 20. While the plot for 8 GPa indicates the a-quartz structure, the plot for 52 GPa indicates amorphization. After the phase transformation above 21 GPa the structure is found to be amorphous with several silicon atoms having acquired a coordination of 5 or 6 oxygen atoms with an increase in the Si-O bond lengths and very broad bond-angle distributions.

7.3.4 Diffuse Scattering from Solid Fullerene

The fullerene is a nearly spherical molecule made of sixty carbon atoms. Its surface contains 30 C=C double bonds, 60 C-C single bonds, 12 pentagons and 20 hexagons. In the crystal, the molecular center arrange in a fcc lattice. At T above 260 K, the molecules rotate nearly freely and no librations are observed. Below 260 K, in the simple cubic lattice, the molecules stay in two possible orientations of nearly equal energies, so their relative population varies from 60:40 at 250 K to 85:15 at T below 90 K. In the majority (minority) state, a double-bond centre of one molecule faces opposite a pentagon (hexagon) of a neighbouring molecule.

The intermolecular interaction in fullerene is largely of the van der Waals type since the nearest carbon atoms of the neighbouring molecules are separated by about the sum of their van der Waals radii. Using previously known vdW potential, either from the organic molecules or from graphite, it is possible to nearly predict the lattice constant, bulk modulus and the phonon dispersion relation of the rigid molecular translations. However, both the orientational structure and the librational frequencies are not explained by the vdW potential. A

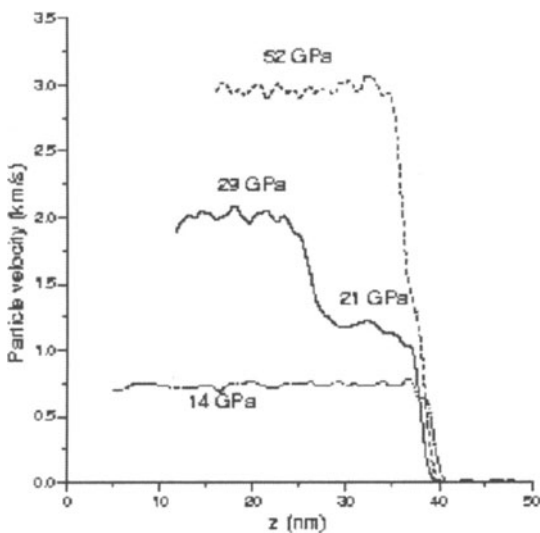


Figure 7.18: The shock front profiles after 5 ps of initiating the shock along the a-quartz c-axis at a few pressures depicting the multiple split shock. The values of the shock stress are indicated.

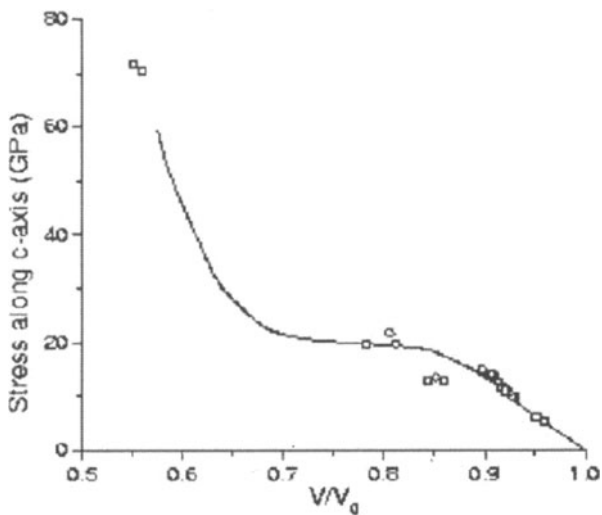


Figure 7.19: The simulated equation of state and temperature for the shock stress along the a-quartz c-axis. The experimental data are shown by squares [39] and circles [40].

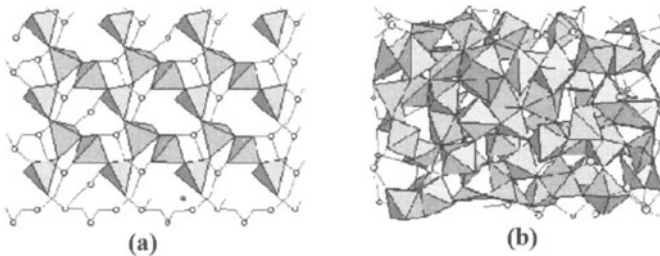


Figure 7.20: A snap shot of a layer of the structure showing some of the SiO_x ($x = 4\text{-}6$) polyhedra (c-axis horizontal, a-axis vertical) under the shock stress along the a-quartz c-axis of a) 8 and b) 52 GPa.

split-bond-charge model [41] was developed in which a small negative charge (-0.27 e) was placed at two split positions radially inwards and outwards a double-bond centre, and a compensating positive charge (0.27 e) placed on the carbon atom. Among all the available models, this model produced the best agreement with the experimental phonon dispersion relation of the external modes and the associated specific heat at low temperatures [41].

The short-range correlations in a disordered structure may be conveniently studied by the wave-vector dependence of the diffuse scattering of X-rays or neutrons from a single crystal. Above 260 K in the disordered phase, the diffuse scattering experiments [42] indicated significant short-range order of the orientations extending to several neighbours beyond 2 nm. The order was found to be much more pronounced in neutron quasi-elastic scattering than in X-ray scattering [43], which indicated its dynamical nature.

MD simulation on 256 molecular periodic cells was carried out, to understand the observed pattern of the diffuse scattering and thereby reveal the nature of the short-range order [41, 42]. Simulation using the splitbond-charge model produces the pattern of the atomic density on the molecular surface in good agreement with that derived from the diffraction experiments [44] (Fig. 21a). So also the calculated diffuse scattering from the MD simulation compares very well with the observed diffuse scattering. The simulated orientational correlations indicate preference for the double bonds on one molecule to face opposite the pentagons of the neighbouring molecules (Fig. 22). In contrast, the MD simulation using the vdW model produces an atomic density pattern in clear disagreement with experiment (Fig. 21b), and predicts preference for the double bond to hexagon correlations (Fig. 22).

7.4 Appendix

7.4.1 Computation of Time Correlation Functions

In Section 7.2 it has been outlined that most of the quantities which can be extracted from MD simulations are time correlation functions. Correlation func-

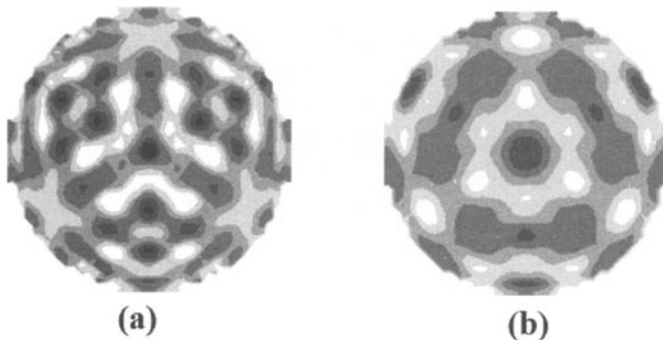


Figure 7.21: Atomic number density on the spherical surface of fullerene, shown as excess over the average density. From MD simulations [42] using the (a) split-bond-charge model and (b) the van der Waals potential model, respectively. The brighter and darker areas show excess and deficit densities, respectively.

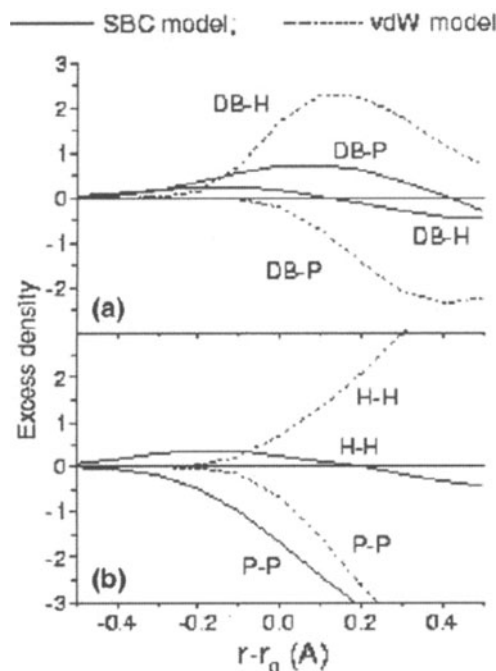


Figure 7.22: The pair correlation functions as calculated from the MD simulations [42] using (a) the split-bond-charge model and (b) the van der Waals potential model. The excess from the average pair correlation function is shown for the pairs of sites on the surface of neighbouring molecules, which reveals the dominant correlation at the nearest average contact separation of about 3 Å. DB-double bond, PG-pentagon, and HG-hexagon.

tions of discrete time series can be efficiently calculated by using the Fast Fourier Transform (FFT) [45]. The so-called Fast Correlation Algorithm (FCA) allows to reduce the number of multiplications (complexity) from $\propto N_t^2$ to $\propto N_t \log_2(N_t)$. All time correlation functions described in the tutorial sessions are computed using the FCA method which will be outlined in the following.

We consider two time series

$$a(k \cdot \Delta t), \quad b(k \cdot \Delta t), \quad k = 0 \dots N_t - 1, \quad (7.57)$$

of length $T = (N_t - 1) \cdot \Delta t$ which are to be correlated. In the following the shorthands $a(k)$ and $b(k)$ will be used. The discrete correlation function of $a(k)$ and $b(k)$ is defined as

$$c_{ab}(m) \doteq \begin{cases} \frac{1}{N_t - m} \sum_{k=0}^{N_t - m - 1} a^*(k)b(k + m), & m = 0 \dots N_t - 1, \\ \frac{1}{N_t - |m|} \sum_{k=|m|}^{N_t - 1} a^*(k)b(k - |m|), & m = -(N_t - 1) \dots - 1. \end{cases} \quad (7.58)$$

The prefactors in front of the sums ensure the proper normalization of the individual channels, $m = -(N_t - 1) \dots N_t - 1$. The asterisk denotes a complex conjugate. According to (7.58), $c_{ab}(m)$ has $2N_t - 1$ data points and obeys the symmetry relation

$$c_{ab}(m) = c_{ba}^*(-m). \quad (7.59)$$

In case that $a(k)$ and $b(k)$ are identical, the corresponding correlation function $c_{aa}(m)$ is called an *autocorrelation* function. We define now the extended, periodic time series

$$A(k) = \begin{cases} a(k) & k = 0 \dots N_t - 1 \\ 0 & k = N_t \dots 2N_t - 1 \end{cases}, \quad (7.60)$$

$$B(k) = \begin{cases} b(k) & k = 0 \dots N_t - 1 \\ 0 & k = N_t \dots 2N_t - 1 \end{cases}, \quad (7.61)$$

which have the period $2N_t$,

$$A(k) = A(k + m \cdot 2N_t), \quad B(k) = B(k + m \cdot 2N_t), \quad m = 0, \pm 1, \pm 2, \dots \quad (7.62)$$

The discrete, cyclic correlation of $A(k)$ and $B(k)$ is defined as

$$S_{AB}(m) = \sum_{k=0}^{2N_t - 1} A^*(k)B(k + m). \quad (7.63)$$

It is easy to see that

$$c_{ab}(m) = \frac{1}{N_t - |m|} S_{AB}(m), \quad -(N_t - 1) \leq m \leq N_t - 1. \quad (7.64)$$

Using the correlation theorem of discrete periodic functions [45], $S_{AB}(m)$ can be written as

$$S_{AB}(m) = \frac{1}{2N_t} \sum_{n=0}^{2N_t-1} \exp \left[2\pi i \left(\frac{mn}{2N_t} \right) \right] \tilde{A}^* \left(\frac{n}{2N_t} \right) \tilde{B} \left(\frac{n}{2N_t} \right) \quad (7.65)$$

where $\tilde{A} \left(\frac{n}{2N_t} \right)$ and $\tilde{B} \left(\frac{n}{2N_t} \right)$ are the discrete Fourier transforms of $A(k)$ and $B(k)$, respectively:

$$\tilde{A} \left(\frac{n}{2N_t} \right) = \sum_{k=0}^{2N_t-1} \exp \left[-2\pi i \left(\frac{nk}{2N_t} \right) \right] A(k), \quad (7.66)$$

$$\tilde{B} \left(\frac{n}{2N_t} \right) = \sum_{k=0}^{2N_t-1} \exp \left[-2\pi i \left(\frac{nk}{2N_t} \right) \right] B(k). \quad (7.67)$$

If the Fourier transforms of the signals $A(k)$ and $B(k)$ as well as the inverse transform in (7.65) are computed by FFT, $S_{AB}(m)$ can be computed by $\propto N_t \log_2(N_t)$ instead of $\propto N_t^2$ multiplications. It is sometimes said that the FFT method induces spurious correlations. We emphasize that this is only the case if the time series $a(k)$ and $b(k)$ are not properly extended, as indicated in Eqs. (7.60) and (7.61). The FFT method and the direct scheme (7.58) give *identical results*, apart from round-off errors.

7.4.2 Computation of Mean-square Displacements

The FCA-method described above may also be used to compute mean-square displacements. In the discrete case the mean-square displacement of a particle is given by

$$\Delta^2(m) = \frac{1}{N_t - m} \sum_{k=0}^{N_t-m-1} [\mathbf{r}(k+m) - \mathbf{r}(k)]^2, \quad m = 0 \dots N_t - 1, \quad (7.68)$$

where $\mathbf{r}(k)$ is the particle trajectory. We define now the auxiliary function

$$S(m) \doteq \sum_{k=0}^{N_t-m-1} [\mathbf{r}(k+m) - \mathbf{r}(k)]^2, \quad m = 0 \dots N_t - 1, \quad (7.69)$$

which is split as follows:

$$S(m) = S_{AA+BB}(m) - 2S_{AB}(m), \quad (7.70)$$

$$S_{AA+BB}(m) = \sum_{k=0}^{N_t-m-1} [\mathbf{r}^2(k+m) + \mathbf{r}^2(k)], \quad (7.71)$$

$$S_{AB}(m) = \sum_{k=0}^{N_t-m-1} \mathbf{r}(k) \cdot \mathbf{r}(k+m). \quad (7.72)$$

The function $S_{AB}(m)$ can be computed using the FCA method described in Section 7.4.1. For $S_{AA+BB}(m)$ the following recursion relation holds:

$$S_{AA+BB}(m) = S_{AA+BB}(m-1) - \mathbf{r}^2(m-1) - \mathbf{r}^2(N_t - m), \quad (7.73)$$

$$S_{AA+BB}(0) = \sum_{k=0}^{N_t-1} \mathbf{r}^2(k). \quad (7.74)$$

This allows to construct the following efficient scheme for the computation of mean-square displacements:

1. Compute $DSQ(k) = \mathbf{r}^2(k)$, $k = 0 \dots N_t - 1$; $DSQ(-1) = DSQ(N_t) = 0$.
2. Compute $SUMSQ = 2 \cdot \sum_{k=0}^{N_t-1} DSQ(k)$.
3. Compute $S_{AB}(m)$ using the FFT method.
4. Compute mean-square displacement $MSD(m)$ in the following loop:

```
for      $m = 0$    to    $N_t - 1$ 
         $SUMSQ \leftarrow SUMSQ - DSQ(m-1) - DSQ(N_t - m)$ 
         $MSD(m) \leftarrow (SUMSQ - 2 \cdot S_{AB}(m)) / (N_t - m)$ 
next    $m$ 
```

It should be noted that the efficiency of this algorithm is the same as for the FCA computation of time correlation functions since the number of operations in step (1), (2), and (4) grows linearly with N_t .

7.4.3 Computation of Intermediate Scattering Functions

Incoherent intermediate scattering function can be computed on a rectangular grid of equidistantly spaced points along the time- and the q -axis, respectively:

$$\mathcal{F}_{inc}(q_m, k \cdot \Delta t) = \sum_{\alpha} w_{\alpha} F_{inc,\alpha}(q_m, k \cdot \Delta t), \quad (7.75)$$

$$F_{inc,\alpha}(q_m, k \cdot \Delta t) = \overline{\langle \exp[-i\mathbf{q} \cdot \mathbf{R}_{\alpha}(0)] \exp[i\mathbf{q} \cdot \mathbf{R}_{\alpha}(t)] \rangle^q}. \quad (7.76)$$

The indices k and m run from 0 to $N_t - 1$ and from 0 to $N_q - 1$, respectively. N_t is the total number of time steps in the coordinate time series and N_q is a user-defined number of q -shells. The values for q_m are defined as $q_m = q_{min} + m \cdot \Delta q$. The symbol $\overline{\dots}^q$ in (7.76) denotes an average over q -vectors having the same modulus q_m . For each q -value and each atom an average over intermediate scattering functions $F_{inc,\alpha}(\mathbf{q}_i, k \cdot \Delta t)$ for a fixed number of vectors \mathbf{q}_i is performed. The \mathbf{q}_i are isotropically distributed. The correlation functions $F_{inc,\alpha}(\mathbf{q}_i, k \cdot \Delta t)$ are computed by using the FCA-algorithm described in Section 7.4.1. The quantities w_{α} are user-defined weights which are normalized to one, $\sum_{\alpha} w_{\alpha} = 1$, such that $\mathcal{F}_{inc}(q, 0) = 1$. From the relation $\mathcal{F}(\mathbf{q}, t) = \mathcal{F}(-\mathbf{q}, -t)$ it follows that

$\mathcal{F}_{inc}(q, t) = \mathcal{F}_{inc}(q, -t)$ is symmetric in time. Therefore, the intermediate scattering function is stored only for values on the positive time axis. Although the efficient FCA technique is used to compute the atomic time correlation functions, calculation of intermediate scattering function may consume a considerable amount of CPU-time since the number of time correlation functions to be computed equals the number of atoms times the total number of q -vectors.

7.4.4 Computation of Radial Distribution Function, $g(r)$

The radial distribution function $g(r)$ can be calculated as [1]

```
do i=1, natom-1
  do j= i+1, natom
    calculate minimum image convention
    ibin= int(rij/delr)+1
    if (ibin.le.maxbin)then
      hist(ibin)=hist(ibin)+2
    endif
  enddo
enddo
```

Here $r_{\max} = dr \times (\text{max bin})$, $r_{\max} \leq L/2$. Suppose there are τ_{run} steps on the disk. The above ‘hist’ are accumulated for all τ_{run} steps. Then the average number of atoms whose distance from a given atom is

$$n(ibin) = \text{hist}(ibin)/\text{natom}/\tau_{run} \quad (7.77)$$

The average number of atoms in an ideal gas at the same density ρ is

$$n_{ideal}(ibin) = \frac{4\pi\rho}{3} \left[(r + \delta r)^3 - r^3 \right] \quad (7.78)$$

By definition radial distribution function is

$$g \left(r + \frac{\delta r}{2} \right) = n(ibin)/n_{ideal}(ibin) \quad (7.79)$$

7.4.5 Spatial Distribution Function (SDF)

The radial distribution function (RDF) or $g(r)$ is traditionally used to analyze the structure revealed from either experimental or computer simulation studies. The RDF function $g_{ij}(r)$ describes the probability of finding a pair of atoms i and j at the distance r apart. The running integral of the RDF gives the number of atoms j in a sphere of radius r around the atom i . RDF is orientationally averaged over the angular coordinates and much of the detail information of the local structure can be lost as a result of the cancellation of contributions from regions of low and high probability at the same distance but different parts of the local structure [46]. Radial distribution functions provide

a complete structural picture for liquids of spherical particles. To overcome the limitations of RDF, the spatial distribution function (SDF) was proposed by Kusalik and Svishchev [47]. They have shown that the spatial distribution function spans both the radial and angular coordinates of the interatomic separation vector and may well describe three-dimensional density distribution of water molecules in a local coordinate system linked with the solute molecule or a part of it. However, to build a SDF around a relatively large, flexible molecule such as RNA duplexes [48] the local coordinate system should be accordingly defined. Spatial distribution functions around α -D-Manp-(1 → 3)- β -D-Glcp-OMe in methanol is also shown by Vishnyakov et. al, [49]. SDF finds many applications e.g., understanding the hydrophobic hydration and the distribution of solvent molecules around non-isotropic solute molecules etc.

References

- [1] M. P. Allen and D. J. Tildesley, *Computer Simulation of Liquids* (Oxford University Press, Oxford, 1987).
- [2] M. Karplus and J. Andrew McCammon, *Nature Structural Biology*, **9** (2002) 646; M. Karplus and G. A. Petsko, *Nature*, **347** (1990) 631.
- [3] J.-P. Perdew, Y. Wang, *Phys. Rev.* **45** (1992) 13244.
- [4] J. Schiøtz, F. D. Di Tolla, K. W. Jacobsen, *Nature* **391** (1998) 561; P. Entel, R. Meyer, K. Kadau, H.C. Herper, E. Hoffmann, *Eur. Phys. J. B* **5** (1998) 379; D. M. Beazley, P. S. Lomdahl, *Computers in Physics* **11** (1997) 230.
- [5] U. Havemann, A. G. Grivtsov, N. N. Merkulenko, *J. Phys. Chem.*, **99** (1995) 15518; S.-C. Kim, B.-S. Seong and S.-H. Suh, *J. Phys.: Condens. Matter*, **21** (2009) 035101; *Parallel molecular dynamics simulation of commercial surfactants*, Lecture Notes in Computer Science, Volume 796 (Springer Verlag, Berlin, 1994).
- [6] D. C. Rapaport, *The Art of Molecular Dynamics Simulation* (Cambridge University Press, Cambridge, 2004).
- [7] S.W. Lovesey, *Theory of Neutron Scattering from Condensed Matter*, Vol. 1 (Clarendon Press, Oxford, 1984).
- [8] M. Bee, *Quasielastic Neutron Scattering: Principles and Applications in Solid State Chemistry, Biology, and Materials Science* (Adam Hilger, Bristol, 1988).
- [9] A. Sayeed, S. Mitra, A. V. Anil Kumar, R. Mukhopadhyay, S. Yashonath, and S.L. Chaplot , *J. Phys. Chem. B* **107** (2003) 527.
- [10] R. Mukhopadhyay, A. Sayeed, S. Mitra, A. V. Anil Kumar, Mala N. Rao, S. Yashonath, and S. L. Chaplot , *Phys. Rev. E* **66** (2002) 061201.
- [11] S. Gautam, S. Mitra, R. Mukhopadhyay and S. L. Chaplot, *Phys. Rev. E* **74** (2006) 041202.

- [12] S. Gautam, S. Mitra, S. L. Chaplot, and R. Mukhopadhyay, *Phys. Rev E* **77** (2008) 061201.
- [13] L. van Hove, *Phys. Rev.* **95** (1954) 249.
- [14] P. Schofield, *Phys. Rev. Letters* **4**(5) (1960) 239.
- [15] G. R. Kneller, J. C. Smith, S. Cusack and W. Doster, *J. Chem. Phys.*, **97** (1992) 8864.
- [16] A. Rahman, K. S. Singwi, and A. Sjölander, *Phys. Rev.* **126** (1962) 986.
- [17] J.-P. Boon and S. Yip, *Molecular Hydrodynamics* (McGraw-Hill, New York, 1980).
- [18] B. Smit and T. L. Maesen, *Nature*, **451** (2008) 671.
- [19] P. Demontis and G. Suffritti, *Chem. Rev.* **97** (1997) 2845.
- [20] H. Jobic, J. Karger, M. Bee, *Phys. Rev. Lett.* **82** (1999) 4260.
- [21] A. N. Fitch, H. Jobic, and A. Renouprez, *J. Phys. Chem.* **90** (1986) 1311.
- [22] H. van Koningsveld, H. van Bekkum and J. C. Jansen, *Acta Cryst.*, **B43** (1987) 127.
- [23] P. K. Ghorai, S. Yashonath, P. Demontis and G. B. Suffritti, *J. Am. Chem. Soc.*, **125** (2003) 7116.
- [24] W. L. Jorgensen, J. D. Madura, and C. J. Swenson, *J. Am. Chem. Soc.* **106** (1984) 6638.
- [25] R. L. June, A. T. Bell, and D. N. Theodorou, *J. Phys. Chem.* **96** (1992) 1051.
- [26] J. I. Siepmann, M. G. Martin, C. Mundy and M. L. Klein, *Mol. Phys.* **90** (1997) 687.
- [27] S. Gautam, A. K. Tripathi, V. S. Kamble, S. Mitra, and R. Mukhopadhyay, *Pramana-J. Phys.* **71** (2008) 1153.
- [28] A. E. Ringwood, *Composition and petrology of the Earth's mantle* (McGraw Hill, New York 1975).
- [29] A. M. Dzeiwonski and D. L. Anderson, *Phys. of the Earth and Planetary Interiors*, **25** (1981) 297.
- [30] T. S. Duffy and D. L. Anderson, *J. of Geophysical Res.*, **94** (1989) 1895.
- [31] J. P. Poirier, *Introduction to the physics of the Earth's interior* (Cambridge University Press, Cambridge, 1991).
- [32] R. J. Hemley, (Ed.) *Ultrahigh Pressure Mineralogy-Physics and Chemistry of the Earth's Deep Interior* (Mineralogical Society of America, Washington D.C. 1998)

- [33] R. Jeanloz, *High pressure chemistry of the Earth's mantle and core*, in W.R. Peltier, Ed., *Mantle Convection: Plate Tectonics and Global Dynamics*, (Gordon and Breach, New York. 1986).
- [34] R. Jeanloz and A. B. Thompson, *Rev. of Geophys. and Sp. Phys.*, **21** (1983) 51.
- [35] S. L. Chaplot and N. Choudhury, *American Mineralogist*, **86** (2001) 752.
- [36] S. Ghose, V. Schomaker and R. K. McMullan, *Zeits. fur Kristal.* **176** (1986) 159; N. Funamori and T. Yagi, *Geophys. Res. Lett.*, **20** (1993) 387.
- [37] N. Choudhury, S. Ghose, C. P. Chowdhury, C. K. Loong, and S. L. Chaplot, *Phys. Rev. B* **58** (1998) 756.
- [38] S. L. Chaplot and S. K. Sikka, *Phys. Rev. B* **61** (2000) 11205.
- [39] J. Wackerle, *J. Appl. Phys.* **33** (1962) 922.
- [40] G. R. Fowles, *J. Geophys. Res.* **72** (1967) 5729.
- [41] L. Pintschovius, S. L. Chaplot, *Z. Phys. B* **98** (1995) 527; S. L. Chaplot, L. Pintschovius, *Fullerene Sci. Technol.* **3** (1995) 707.
- [42] L. Pintschovius, S. L. Chaplot, G. Roth, G. Heger, *Phys. Rev. Lett.* **75** (1995) 2843; L. Pintschovius, S. L. Chaplot, G. Roth, *Physica B* **219 & 220** (1996) 148; S. L. Chaplot, L. Pintschovius, *Int. J. Mod. Phys. B* **13** (1999) 217; S. L. Chaplot, P. S. Schiebel, L. Pintschovius, *Fullerene Sci. Technol.* **9** (2001) 363.
- [43] R. Moret, S. Ravy and S.-M. Godard, *J. Phys. I* **2** (1992) 1699.
- [44] P.C. Chow, X. Jiang, G. Reiter, P. Wochner, S. C. Moss, J. D. Axe, J. C. Hanson, R. K. McMullan, R. L. Meng and C. W. Chu, *Phys. Rev. Lett.* **69** (1992) 2943; P. Schiebel, K. Wulf, W. Prandl, G. Heger, R. Papoular and W. Paulus *Acta Cryst. A* **52** (1996) 176; W. I. F. David, R. M. Ibbersen and T. Matsuo, *Proc. R. Soc. (London) A* **442** (1993) 129.
- [45] E. O. Brigham, *The Fast Fourier Transform* (Prentice Hall, Englewood Cliffs, 1974).
- [46] A. Laaksonen, P.G. Kusalik, I. M. Svishchev, *J. Phys. Chem. A* **101** (1997) 5910.
- [47] P. G. Kusalik, I. M. Svishchev, *Science*, **265** (1994) 1219; P. G. Kusalik, I. M. Svishchev, *J. Chem. Phys.*, **99** (1993) 3049.
- [48] K. Kulinska, T. Kulinski, A. Lyubartsev, A. Laaksonen and R. W. Adamiak, *Computers and Chemistry*, **24** (2000) 451.
- [49] A. Vishnyakov, A. Laaksonen, and G. Widmalm, *J. Mol. Graphics Modell.*, **19** (2001) 338.

Chapter 8

The Conjugate Gradient Method for Unconstrained Minimization

Subir K. Sarkar

8.1 Introduction

Unconstrained function minimization is a rather commonly occurring numerical problem in many areas of engineering and natural sciences. Two illustrative examples are: (i) The minimization of the energy functional in *ab-initio* electronic structure calculation and (ii) The generation of the geometries of the atomic arrangements in numerical studies of the behaviour of solids based on atomistic or model potential. In both of these problems one is given a real function f of a fixed number (n) of real variables. The argument of f is thus \mathbf{r} which is a point in the n -dimensional Cartesian space denoted by \mathbb{R}^n . The function f is said to have a local minimum at a point $P \in \mathbb{R}^n$ if its value increases with any movement of its argument away from P . In general a function will have many such local minima. Out of these local minima one or more will have the property that the value of the function is nowhere below the common value at these points. Thus the value at these points represents the value of the global minimum of the function.

The Conjugate Gradient (CG) algorithm that we discuss here provides a method for searching the location of any local minimum, up to a desired level of accuracy, in the proximity of the point where the search starts. If the function under consideration has many local minima the outcome of the search will in general depend on the starting point and the actual numerical values of the adjustable parameters that appear in the computer program implementing

the algorithm. It must be understood that the method does *not* enable us to conduct a systematic search for the various local minima – except in the trivial case where the function has only one local minimum.

Historically, the CG method was introduced as a technique for solving some special cases of linear algebraic equations in a n -dimensional space. These equations are of the form $\sum_{j=1}^n A_{i,j} z_j = d_i$ for $i = 1, 2, \dots, n$. Here $\mathbf{d} \in \mathbb{R}^n$ and \mathbf{A} is a $n \times n$ real, symmetric matrix. When \mathbf{A} is also positive definite it is easy to see that the problem of solving the aforementioned linear equations is equivalent to that of finding the global (and the only) minimum of the real and quadratic function

$$F_0(\mathbf{r}) = -\mathbf{d} \cdot \mathbf{r} + (1/2)\mathbf{r} \cdot \mathbf{A}\mathbf{r} + \text{an arbitrary constant}$$

If \mathbf{A} has even one eigenvalue that is negative, the quadratic function $F_0(\mathbf{r})$ does not have a local minimum. But when \mathbf{A} is positive definite the basic theorem of the CG technique demonstrates that the location of the minimum can be reached exactly in no more than n steps (This theorem will be proved shortly).

Going beyond the quadratic function of the type just mentioned the next level of complication is when the function is globally convex and is continuously differentiable at least upto the second order. Such a function f can have only one local (and thus global) minimum. Let this minimum be at \mathbf{r}_0 . Recall that the Hessian matrix of the function f at a point \mathbf{r} is a $n \times n$ matrix of which the (i, j) element is defined to be $\partial^2 f / \partial \mathbf{r}_i \partial \mathbf{r}_j$. Denoting \mathbf{M} to be the positive definite Hessian matrix of f at \mathbf{r}_0 and expanding f in a Taylor series around \mathbf{r}_0

$$\begin{aligned} f(\mathbf{r}) &= f(\mathbf{r}_0) + (1/2)(\mathbf{r} - \mathbf{r}_0) \cdot \mathbf{M}(\mathbf{r} - \mathbf{r}_0) + \dots \\ &= (1/2)\mathbf{r} \cdot \mathbf{M}\mathbf{r} + \text{Terms linear in } \mathbf{r} + \text{Constant} + \dots \end{aligned}$$

The constant term in the last approximate expression has no bearing on the location of the minimum. The \dots at the end denote terms that are cubic or higher order in $(\mathbf{r} - \mathbf{r}_0)$. If we are in a region sufficiently close to \mathbf{r}_0 terms higher than second order can be ignored and the function, within this approximation, is a quadratic one. This is precisely the situation for which the basic theorem of conjugate gradients method is applicable. As we will see shortly the general implementation of the CG technique guarantees that one goes only downhill while searching for the location of the minimum. Thus it is plausible that after a not-too-large number of steps one does land in the close proximity of the minimum. After this the power of the basic theorem of the CG technique takes over and guarantees convergence to a point very close to the minimum (since the function is not strictly quadratic) in about n steps.

This intuitive argument, of course, overlooks some mathematical subtleties especially regarding the character of the Hessian matrix in the neighborhood of the minimum. A mathematically rigorous discussion can be found in [1]. Finally, in the most general case the function will have more than one local minimum. In these cases the application of the CG technique will lead to a minimum that depends on the starting point of the search.

In order to make the article somewhat self-contained, the steepest-descent and quasi-Newton methods for optimization are discussed briefly in the final sections.

8.2 The Conjugate Gradient Method

While considering the problem of minimization of a function f it is helpful to have a geometrical picture in mind. Imagine that you are plotting the function with f along one axis and the independent variables along axes transverse to this. The visualization naturally becomes difficult if more than two independent variables are involved. In any case, think of the value of f as the altitude variable in a topographic map (negative value of the function will create no problem once you get used to the picturization process). It is obvious that with such a picture the local minima constitute the various (locally) lowest lying points in this landscape and the process of minimization in general will mean going downhill until one cannot go down any further.

If one is dealing with a globally convex function the minimum can be “seen” from anywhere on the topographic map. So it may seem that the goal of reaching the minimum is attainable quite easily. However, a computer based algorithm has no way of “seeing” the landscape and it has to proceed on the basis of “local” calculations i.e. the algorithm must make all decisions based on the value of the function or its derivatives at a finite sequence of points. The CG algorithm is no exception and the statement of the procedure makes no distinction between the various conceivable landscapes. However the convergence of the algorithm is an issue that is indeed controlled by these landscape features.

The generic algorithm for minimizing a real function f of n real variables that we discuss here has the following structure:

Algorithm I

- (A) Select a starting point \mathbf{x}_0 as the initial guess for the search of the location of a nearby local minimum and set the value of the iteration index $k = 0$.
- (B) Calculate the gradient $\nabla f(\mathbf{x}_k)$.
- (C) If $\nabla f(\mathbf{x}_k)$ is a null vector, stop. Otherwise choose a vector \mathbf{h}_k along which the function is going downhill i.e. the scalar product $\nabla f(\mathbf{x}_k) \cdot \mathbf{h}_k$ is negative.
- (D) Starting from \mathbf{x}_k keep moving in the direction of \mathbf{h}_k until you reach the minimum of the function along that line and in that direction i.e. minimize the function $f(\mathbf{x}_k + \lambda \mathbf{h}_k)$ with respect to λ in the *positive* λ domain. Let the value of λ at the minimum be λ_k . Thus the location of the minimum along the line of search is $\mathbf{x}_k + \lambda_k \mathbf{h}_k$.
- (E) Define $\mathbf{x}_{k+1} = \mathbf{x}_k + \lambda_k \mathbf{h}_k$. Update the value of k to $k+1$ and go to step (B).

This completes the definition of the generic algorithm. Please note that the search for the minimum takes us along a connected series of directed straight lines. Steps (C) and (D) ensure that during this journey the function value always goes down. The reason the algorithm is “generic” at this stage is that we have not made the choice of \mathbf{h}_k in step (C) quite precise – except to say that this is a downhill direction for the function at \mathbf{x}_k . In fact the convergence of the iterative loop between the steps (B) and (E) depends on how \mathbf{h}_k is selected. We now introduce further specificity in the choice of \mathbf{h}_k .

Suppose we are given a $n \times n$ matrix \mathbf{W} that is real and symmetric. In such a case a series of vectors denoted by \mathbf{t}_i , with $i = 0, 1, 2, \dots$, are said to be **mutually conjugate with respect to \mathbf{W}** if $\mathbf{t}_i \cdot (\mathbf{W}\mathbf{t}_j) = 0$ whenever $i \neq j$. Having thus defined mutual conjugacy we now define a “Conjugate Directions” method of minimization to be one in which the directions \mathbf{h}_i , $i = 0, 1, 2, \dots$ (for the series of line minimizations used in the generic algorithm), are mutually conjugate with respect to some suitable matrix of the type specified above. The only such matrix which can possibly be relevant to the problem of minimization is the Hessian matrix of the function to be minimized — at any point for a quadratic function and only at a local minimum for other types of functions. That indeed turns out to be the case.

Finally, a Conjugate Directions method is called a “Conjugate Gradient” method when the information regarding the gradient of the function at appropriate points is used in constructing the various conjugate directions. As we will see later this nomenclature regarding methods of minimization in the spirit of algorithm I is meaningful only in the case of strictly quadratic functions. In other cases the nomenclature is mechanically extended on the basis of the algorithm used — even though the basis for the nomenclature no longer holds.

We now state and prove a theorem that is basic to the operation of the CG method. It forms the basis of how the CG method locates the minimum of a strictly quadratic function exactly in no more than n steps.

The fundamental theorem of the Conjugate Gradient method (FTCG theorem)

Let \mathbf{M} be a symmetric, positive definite $n \times n$ matrix and let \mathbf{g}_0 be an arbitrary non-null vector $\in \mathbb{R}^n$. Set $\mathbf{h}_0 = \mathbf{g}_0$. Now iteratively define the sequence of vector pairs $[\mathbf{g}_i, \mathbf{h}_i]$ with $i = 1, 2, \dots$ in the following manner:

$$\mathbf{g}_{i+1} = \mathbf{g}_i - \lambda_i \mathbf{M} \mathbf{h}_i \quad (8.1)$$

and

$$\mathbf{h}_{i+1} = \mathbf{g}_{i+1} + \gamma_i \mathbf{h}_i \quad (8.2)$$

Here λ_i and γ_i are chosen so that

$$\mathbf{g}_{i+1} \cdot \mathbf{g}_i = 0 \quad (8.3)$$

and

$$\mathbf{h}_{i+1} \cdot \mathbf{M} \mathbf{h}_i = 0 \quad (8.4)$$

Given the definitions (8.1) and (8.2), requirements (8.3) and (8.4) can be satisfied if the following choices are made:

$$\lambda_i = (\mathbf{g}_i \cdot \mathbf{g}_i) / (\mathbf{g}_i \cdot \mathbf{Mh}_i) \quad (8.5)$$

and

$$\gamma_i = -(\mathbf{g}_{i+1} \cdot \mathbf{Mh}_i) / (\mathbf{h}_i \cdot \mathbf{Mh}_i) \quad (8.6)$$

If the denominators in (8.5) and (8.6) vanish (and they can vanish only simultaneously), set $\lambda_i = \gamma_i = 0$.

The fundamental theorem states that:

- (I) $\mathbf{g}_i = \mathbf{h}_i = \mathbf{0}$ whenever $i > l$ - with $l \leq (n - 1)$, and
- (II) $\mathbf{g}_i \cdot \mathbf{g}_j = \delta_{ij}\mathbf{g}_i \cdot \mathbf{g}_i$ and

$$\mathbf{h}_i \cdot \mathbf{Mh}_j = \delta_{ij}\mathbf{h}_i \cdot \mathbf{Mh}_i \quad (8.7)$$

for $i, j = 0, 1, 2, \dots$. Here the Kronecker delta function δ_{ij} is 1 when $i = j$ and zero otherwise).

Content of the theorem:

Result I: The first result says that although an infinite sequence of (\mathbf{g}, \mathbf{h}) pairs can be constructed by the rules given above, all beyond the first $(l + 1)$ of them are just pairs of null vectors and the value of $(l + 1)$ cannot exceed the dimensionality n of the space (it can be less - with special choice of \mathbf{g}_0). In fact, as we shall see in the proof, for the first $(l + 1)$ pairs neither \mathbf{g} nor \mathbf{h} can be a null vector. Thus each (\mathbf{g}, \mathbf{h}) pair in the infinite sequence can be one of the following two types: For the first $(l + 1)$ pairs both \mathbf{g} and \mathbf{h} are non-null vectors. For all pairs that follow both \mathbf{g} and \mathbf{h} are null vectors.

Result II: The rules of construction guarantee that: (i) any two *consecutive* \mathbf{g} vectors are orthogonal (from Eq. (8.3)) and (ii) any two *consecutive* \mathbf{h} vectors are mutually conjugate (from Eq. (8.4)). What the second result says is that these statements relating to pairs of \mathbf{g} and \mathbf{h} are true even if they are not consecutive elements in the sequence. Obviously this result is nontrivial only when both the vectors (\mathbf{g} or \mathbf{h}) belong to the first $(l + 1)$ pairs.

Proof of a part of Result I: Suppose, during the construction of the infinite sequence of $[\mathbf{g}, \mathbf{h}]$ pairs, no null vector appears in any of the first $(p + 1)$ pairs but \mathbf{g}_{p+1} turns out to be a null vector on application of Eq. (8.1) (Since $\mathbf{g}_0 = \mathbf{h}_0$ and \mathbf{g}_0 has been taken to be a non-null vector at least one non-null pair is always guaranteed to exist at the beginning of the infinite sequence). Then, from Eqs. (8.2) and (8.6), it follows that \mathbf{h}_{p+1} is a null vector. Thus the assumption of \mathbf{g}_{p+1} being a null vector implies that \mathbf{h}_{p+1} is also a null vector. Now we prove the reverse: if \mathbf{h}_{p+1} is a null vector, \mathbf{g}_{p+1} must be a null vector.

To prove this we need to prove the following result:

$$\mathbf{h}_k \cdot \mathbf{g}_{k+1} = 0 \text{ for } k = 0, 1, 2, \dots \quad (8.8)$$

Proof: The proof is inductive in nature. Notice that the result to be proved is certainly valid for $k = 0$ since $\mathbf{h}_0 \cdot \mathbf{g}_1 = \mathbf{g}_0 \cdot \mathbf{g}_1$ (since, by choice, $\mathbf{h}_0 = \mathbf{g}_0 = 0$) = 0 (since any two consecutive \mathbf{g} vectors are orthogonal by construction). Now, in the spirit of an inductive proof, suppose that $\mathbf{h}_t \cdot \mathbf{g}_{t+1} = 0$ for some $t \in [0, 1, 2, \dots]$. We next show that the result $\mathbf{h}_{t+1} \cdot \mathbf{g}_{t+2} = 0$ follows as a consequence. Indeed,

$$\begin{aligned} & \mathbf{h}_{t+1} \cdot \mathbf{g}_{t+2} \\ &= \mathbf{h}_{t+1} \cdot (\mathbf{g}_{t+1} - \lambda_{t+1} \mathbf{M} \mathbf{h}_{t+1}) \\ &= \mathbf{h}_{t+1} \cdot \mathbf{g}_{t+1} - \lambda_{t+1} \mathbf{h}_{t+1} \cdot (\mathbf{M} \mathbf{h}_{t+1}) \\ &= (\mathbf{g}_{t+1} + \gamma_t \mathbf{h}_t) \cdot \mathbf{g}_{t+1} - \lambda_{t+1} \mathbf{h}_{t+1} \cdot (\mathbf{M} \mathbf{h}_{t+1}) \\ &= \mathbf{g}_{t+1} \cdot \mathbf{g}_{t+1} - \lambda_{t+1} \mathbf{h}_{t+1} \cdot (\mathbf{M} \mathbf{h}_{t+1}) \text{ (since, by assumption, } \mathbf{h}_t \cdot \mathbf{g}_{t+1} = 0\text{)} \\ &= 0 \text{ (see the following two lines).} \end{aligned}$$

$[\mathbf{h}_{t+1} \cdot (\mathbf{M} \mathbf{h}_{t+1}) = (\mathbf{g}_{t+1} + \gamma_t \mathbf{h}_t) \cdot (\mathbf{M} \mathbf{h}_{t+1}) = \mathbf{g}_{t+1} \cdot (\mathbf{M} \mathbf{h}_{t+1}) \text{ since } \mathbf{h}_t \cdot (\mathbf{M} \mathbf{h}_{t+1}) = \mathbf{h}_{t+1} \cdot (\mathbf{M} \mathbf{h}_t) \text{ (}} M \text{ is a symmetric matrix)} = 0 \text{ (consecutive } \mathbf{h} \text{ vectors are mutually conjugate)]}. This, combined with Eq. (8.5), leads to the last result. We have already proved that } \mathbf{h}_0 \cdot \mathbf{g}_1 = 0. By repeated application of the result just proved it follows that } \mathbf{h}_t \cdot \mathbf{g}_{t+1} = 0 \text{ for any } t.$

Now we get back to proving that \mathbf{g}_{p+1} must be a null vector if \mathbf{h}_{p+1} is given to be a null vector. For this we note that $\mathbf{g}_{p+1} \cdot \mathbf{h}_{p+1} = 0$ (since \mathbf{h}_{p+1} is a null vector) = $\mathbf{g}_{p+1} \cdot (\mathbf{g}_{p+1} + \gamma_p \mathbf{h}_p) = \mathbf{g}_{p+1} \cdot \mathbf{g}_{p+1} + \gamma_p \mathbf{g}_{p+1} \cdot \mathbf{h}_p = \mathbf{g}_{p+1} \cdot \mathbf{g}_{p+1}$ (since we have just proved that $\mathbf{g}_{p+1} \cdot \mathbf{h}_p = 0$). Since the norm of the vector \mathbf{g}_{p+1} is zero it must be a null vector.

We have proved that the first time a null vector appears during the construction of the infinite sequence of $[\mathbf{g}, \mathbf{h}]$ pairs, both the \mathbf{g} and \mathbf{h} components must be null vectors. Obviously, by the recursive rules of construction, all subsequent pairs are pairs of null vectors. However, we still have not proved that the null vectors must appear. For that we have to prove the result II first.

Proof of Result II: We are given that, for $i \leq l$ (first group), neither of \mathbf{g}_i and \mathbf{h}_i is a null vector, whereas, for $i > l$ (second group), both \mathbf{g}_i and \mathbf{h}_i are null vectors. Clearly, the contents of result II are trivially valid if either of the vectors involved in the pair (for \mathbf{g} or for \mathbf{h}) belong to the second group. Thus we need to prove the result only for the case in which both the vectors belong to the first group. The proof is again inductive. We note that, by construction, $\mathbf{g}_0 \cdot \mathbf{g}_1 = 0$ and $\mathbf{h}_0 \cdot (\mathbf{M} \mathbf{h}_1) = 0$. Hence there is nothing more to be proved if $l = 1$. So, in what follows, we assume that $l \geq 2$. Now, assume that the orthonormality of pairs of \mathbf{g} vectors and the conjugacy of pairs of \mathbf{h} vectors holds whenever they are picked from two distinct pairs out of the *first s* elements of the sequence of $[\mathbf{g}, \mathbf{h}]$ pairs – with s being less than $(l + 1)$ i. e.

$$\mathbf{g}_i \cdot \mathbf{g}_j = 0 \quad (8.9)$$

and

$$\mathbf{h}_i \cdot (\mathbf{M}\mathbf{h}_j) = 0 \quad (8.10)$$

whenever i and j are distinct and are in the range from 0 to $(s - 1)$. We have seen already that the above assumption is certainly valid when $s = 2$. We shall now show that we can increase the value of s by one (i.e. we can include one more $[\mathbf{g}, \mathbf{h}]$ pair) and the content of the assumption will still be valid for all pairs selected from the *expanded* set.

Proof: The *new* pairs of \mathbf{g} and \mathbf{h} available as a result of increasing the value of s to $s + 1$ are those for which one of the two \mathbf{g} (or \mathbf{h}) vectors belong to the pair $[\mathbf{g}_s, \mathbf{h}_s]$. Thus we need to show that the expressions of the type $\mathbf{g}_s \cdot \mathbf{g}_i$ and $\mathbf{h}_s \cdot (\mathbf{M}\mathbf{h}_i)$ vanish whenever $i < s$ ($2 \leq s \leq l$).

Calculation of $\mathbf{g}_s \cdot \mathbf{g}_i$: When $i = 0$, $\mathbf{g}_s \cdot \mathbf{g}_i = (\mathbf{g}_{s-1} - \lambda_{s-1} \mathbf{M}\mathbf{h}_{s-1}) \cdot \mathbf{g}_0 = \mathbf{g}_{s-1} \cdot \mathbf{g}_0 - \lambda_{s-1} (\mathbf{M}\mathbf{h}_{s-1}) \cdot \mathbf{h}_0$ (since, $\mathbf{g}_0 = \mathbf{h}_0$) = 0 as a consequence of the starting assumptions (Eqs. (8.9) and (8.10)).

When $i = (s - 1)$, $\mathbf{g}_s \cdot \mathbf{g}_i = \mathbf{g}_s \cdot \mathbf{g}_{s-1} = 0$ (from Eq. (8.3)). When $s = 2$ the above two cases already cover all possibilities. If, however, s is greater than two the remaining values of i are 1, 2, ..., $(s - 2)$. In these cases

$$\begin{aligned} \mathbf{g}_s \cdot \mathbf{g}_i &= (\mathbf{g}_{s-1} - \lambda_{s-1} \mathbf{M}\mathbf{h}_{s-1}) \cdot \mathbf{g}_i \\ &= -\lambda_{s-1} (\mathbf{M}\mathbf{h}_{s-1}) \cdot \mathbf{g}_i \quad (\text{from Eq. (8.9)}) \\ &= -\lambda_{s-1} (\mathbf{M}\mathbf{h}_{s-1}) \cdot (\mathbf{h}_i - \gamma_{i-1} \mathbf{h}_{i-1}) \quad (\text{from Eq. (8.2)}) \\ &= 0 \quad (\text{from Eq. (8.10)}) \end{aligned}$$

Thus we have proved that $\mathbf{g}_s \cdot \mathbf{g}_i = 0$ for all permissible values of i .

Calculation of $\mathbf{h}_s \cdot (\mathbf{M}\mathbf{h}_i)$: Similarly, when $i = (s - 1)$, $\mathbf{h}_s \cdot (\mathbf{M}\mathbf{h}_i) = 0$ (from Eq. (8.4)) and for $i = 0, 1, \dots, (s - 2)$,

$$\begin{aligned} \mathbf{h}_s \cdot (\mathbf{M}\mathbf{h}_i) &= (\mathbf{g}_s + \gamma_{s-1} \mathbf{h}_{s-1}) \cdot (\mathbf{M}\mathbf{h}_i) \quad (\text{from Eq. (8.2)}) \\ &= \mathbf{g}_s \cdot (\mathbf{M}\mathbf{h}_i) \quad (\text{from Eq. (8.10)}) \\ &= \mathbf{g}_s \cdot [(1/\lambda_i)(\mathbf{g}_i - \mathbf{g}_{i+1})] \quad (\text{from Eq. (8.1)}) \\ &= 0 \quad (\text{from Eq. (8.9)}). \end{aligned}$$

This completes the demonstration that $\mathbf{h}_s \cdot (\mathbf{M}\mathbf{h}_i) = 0$ for all allowed values of i .

Thus the assumption of the validity of Eqs. (8.9) and (8.10) with i and j in the range $[0, (s - 1)]$ leads to the consequence that the validity continues even when the ranges of i and j are expanded to $[0, s]$. Since we have already *proved* the validity for $s = 2$, validity for all higher values of s follows via induction.

Proof of the remaining part of Result I: We have just proved that all the \mathbf{g} vectors are mutually orthogonal. So if the first $(l + 1)$ of them are all non-null vectors, $(l + 1)$ cannot exceed n since the number of non-null vectors that are also mutually orthogonal cannot exceed the dimensionality of the space.

This completes the proof of the fundamental theorem underlying the Conjugate Gradient method. Its connection to the problem of minimizing a strictly quadratic real function of n real variables in no more than n steps will be demonstrated after we present the following Conjugate Gradient algorithms which concretize the generic algorithm (Algorithm I) described earlier.

Algorithm II: (Polak-Ribiere)

- (A) Select a point $\mathbf{x}_0 \in \mathbb{R}^n$ as the starting point of your search for the nearby minimum. If $\nabla f(\mathbf{x}_0) = \mathbf{0}$, stop; otherwise go to step (B).
- (B) Define $\mathbf{g}_0 = \mathbf{h}_0 = -\nabla f(\mathbf{x}_0)$ and set the iteration index k to 0.
- (C) Starting from \mathbf{x}_k keep moving in the direction of \mathbf{h}_k until you reach the minimum of the function along that line and in that direction i.e. minimize the function $f(\mathbf{x}_k + \lambda \mathbf{h}_k)$ with respect to λ in the positive λ domain. Let the value of λ at the minimum be λ_k . Thus the location of the minimum along the line of search is $(\mathbf{x}_k + \lambda_k \mathbf{h}_k)$.
- (D) Define $\mathbf{x}_{k+1} = \mathbf{x}_k + \lambda_k \mathbf{h}_k$.
- (E) Calculate $\nabla f(\mathbf{x}_{k+1})$.
- (F) If $\nabla f(\mathbf{x}_{k+1}) = \mathbf{0}$, stop; otherwise define

$$\mathbf{g}_{k+1} = -\nabla f(\mathbf{x}_{k+1}) \text{ and}$$

$$\mathbf{h}_{k+1} = \mathbf{g}_{k+1} + \gamma_k \mathbf{h}_k \text{ with}$$

$$\gamma_k = ((\mathbf{g}_{k+1} - \mathbf{g}_k) \cdot \mathbf{g}_{k+1}) / (\mathbf{g}_k \cdot \mathbf{g}_k).$$

Update the value of k to $k + 1$ and go to step (C).

This completes the statement of **Algorithm II**.

Algorithm III: (Fletcher-Reeves)

This algorithm differs from Algorithm II only in step F, where the expression is

$$\gamma_k = (\mathbf{g}_{k+1} \cdot \mathbf{g}_{k+1}) / (\mathbf{g}_k \cdot \mathbf{g}_k).$$

The FTCCG theorem and the algorithms II and III have one immediately noticeable common aspect: they all define a sequence of pairs of n -component

vectors $[\mathbf{g}_i, \mathbf{h}_i]$ with $i = 0, 1, 2, 3, \dots$. In all cases \mathbf{g}_0 is arbitrary, \mathbf{h}_0 is defined to be equal to \mathbf{g}_0 and then rules are given for constructing $[\mathbf{g}_{i+1}, \mathbf{h}_{i+1}]$ from $[\mathbf{g}_i, \mathbf{h}_i]$. We now demonstrate the following:

Suppose that the function to be minimized in algorithms II or III is the purely quadratic function $f(\mathbf{r}) = -\mathbf{d} \cdot \mathbf{r} + (1/2)\mathbf{r} \cdot \mathbf{M}\mathbf{r}$ where $\mathbf{d} \in \mathbb{R}^n$ and \mathbf{M} is a positive definite $n \times n$ matrix that is real and symmetric. Take the positive definite real symmetric matrix in the FTCG theorem to be this same \mathbf{M} . Then:

If the same \mathbf{g}_0 (and hence \mathbf{h}_0) is used for algorithm II, algorithm III and the sequence generating algorithm of the FTCG, then *all the three processes will generate exactly the same sequence of $[\mathbf{g}, \mathbf{h}]$ pairs.*

Proof: First of all we need to prove two results which are corollaries of the FTCG theorem and are valid in that context:

$$(1) \frac{(\mathbf{g}_i \cdot \mathbf{g}_i)}{(\mathbf{g}_i \cdot \mathbf{M}\mathbf{h}_i)} \text{ (Call this expression 8.A)} = \frac{(\mathbf{h}_i \cdot \mathbf{g}_i)}{(\mathbf{h}_i \cdot \mathbf{M}\mathbf{h}_i)} \text{ (\equiv expression 8.B) for } i = 0, 1, 2, \dots, l.$$

Proof: For $i = 0$ the equality holds since $\mathbf{g}_0 = \mathbf{h}_0$ by choice. For other values of i , $(\mathbf{g}_i \cdot \mathbf{g}_i)/(\mathbf{g}_i \cdot \mathbf{M}\mathbf{h}_i) = ((\mathbf{h}_i - \gamma_{i-1}\mathbf{h}_{i-1}) \cdot \mathbf{g}_i)/((\mathbf{h}_i - \gamma_{i-1}\mathbf{h}_{i-1}) \cdot \mathbf{M}\mathbf{h}_i)$ (from Eq. (8.2)) $= (\mathbf{h}_i \cdot \mathbf{g}_i)/(\mathbf{h}_i \cdot \mathbf{M}\mathbf{h}_i)$ (from Eqs. (8.4) and (8.8)).

$$(2) -\frac{(\mathbf{g}_{i+1} \cdot \mathbf{M}\mathbf{h}_i)}{(\mathbf{h}_i \cdot \mathbf{M}\mathbf{h}_i)} \text{ (\equiv expression 8.C)} = \frac{(\mathbf{g}_{i+1} \cdot \mathbf{g}_{i+1})}{(\mathbf{g}_i \cdot \mathbf{g}_i)} \text{ (\equiv expression 8.D)} = \frac{((\mathbf{g}_{i+1} - \mathbf{g}_i) \cdot \mathbf{g}_{i+1})}{(\mathbf{g}_i \cdot \mathbf{g}_i)} \text{ (\equiv expression 8.E) for } i = 0, 1, 2, \dots, l.$$

$$\begin{aligned} \text{Proof: Now, expression 8.C} &= -\frac{(\mathbf{g}_{i+1} \cdot \mathbf{M}\mathbf{h}_i)}{(\mathbf{h}_i \cdot \mathbf{M}\mathbf{h}_i)} \\ &= -\frac{((\mathbf{g}_{i+1} - \mathbf{g}_i) \cdot \mathbf{g}_{i+1})}{((\mathbf{g}_{i+1} - \mathbf{g}_i) \cdot \mathbf{h}_i)} \text{ (from Eq. (8.1))} \\ &= \frac{(\mathbf{g}_{i+1} \cdot \mathbf{g}_{i+1})}{(\mathbf{g}_i \cdot \mathbf{h}_i)} \text{ (from Eqs. (8.3) and (8.8))} \\ &= \frac{(\mathbf{g}_{i+1} \cdot \mathbf{g}_{i+1})}{(\mathbf{g}_i \cdot (\mathbf{g}_i + \gamma_{i-1}\mathbf{h}_{i-1}))} \text{ (from Eq. (8.2))} \\ &= \frac{(\mathbf{g}_{i+1} \cdot \mathbf{g}_{i+1})}{(\mathbf{g}_i \cdot \mathbf{g}_i)} \text{ (from Eq. (8.8))} \\ &= \text{Expression 8.D} \\ &= \frac{((\mathbf{g}_{i+1} - \mathbf{g}_i) \cdot \mathbf{g}_{i+1})}{(\mathbf{g}_i \cdot \mathbf{g}_i)} \text{ (from Eq. (8.3))} \\ &= \text{Expression 8.E.} \end{aligned}$$

In the FTCG theorem one constructs the sequence $[\mathbf{g}_i, \mathbf{h}_i]$ for $i = 0, 1, 2, \dots$ by taking an arbitrary \mathbf{g}_0 , setting $\mathbf{h}_0 = \mathbf{g}_0$ and then using the recursive definitions given by the Eqs. (8.1) and (8.2). These equations contain λ_i and γ_i as parameters which are defined in Eqs. (8.5) and (8.6). Expressions 8.A and 8.C are nothing but these formulae for λ_i and γ_i , respectively. Hence, in view of the equivalences established above, if we replace the expression for λ_i in Eq. (8.5) by the expression 8.B and the expression for γ_i in Eq. (8.6) by either expression 8.D (Case A) or 8.E (Case B) exactly the same sequence of $[\mathbf{g}, \mathbf{h}]$ pairs will be generated. Thus we get two modified FTCG theorems (Case A and Case B) where the rules of recursion *look* different but actually the sequence of

$[\mathbf{g}, \mathbf{h}]$ pairs generated is not altered (assuming that \mathbf{g}_0 remains the same) and hence results I and II, stated in connection with the original FTCG theorem, continue to be valid. What we want to prove next is that, for case A, these new recursive rules for generating the $[\mathbf{g}, \mathbf{h}]$ pair sequence in the context of the modified FTCG theorem are exactly the same as the recursive rules in the case of algorithm III *provided the function being minimized is strictly quadratic with a Hessian matrix that is identical to that in the FTCG theorem.* (For case B, equivalence of rules is with Algorithm II).

Let us now examine the recursive rules for generating $[\mathbf{g}_{i+1}, \mathbf{h}_{i+1}]$ from $[\mathbf{g}_i, \mathbf{h}_i]$ for algorithm III. Since $f(\mathbf{x}) = -\mathbf{d} \cdot \mathbf{x} + (1/2)\mathbf{x} \cdot \mathbf{Mx}$, $\nabla f(\mathbf{x}) = \mathbf{Mx} - \mathbf{d}$. Also since $\mathbf{g}_i = -\nabla f(\mathbf{x}_i)$ (step F)

$$\mathbf{g}_{i+1} - \mathbf{g}_i = -\mathbf{M}(\mathbf{x}_{i+1} - \mathbf{x}_i) = -\lambda_i \mathbf{Mh}_i \quad (8.11)$$

where λ_i is defined in step C as the value of λ that minimizes $f(\mathbf{x}_i + \lambda \mathbf{h}_i)$, namely $\nabla f(\mathbf{x}_i + \lambda_i \mathbf{h}_i) \cdot \mathbf{h}_i = 0$. Using the quadratic expression for f , this reduces to

$$\begin{aligned} \lambda_i &= (\mathbf{h}_i \cdot (\mathbf{d} - \mathbf{Mx}_i)) / (\mathbf{h}_i \cdot (\mathbf{Mh}_i)) \\ &= (\mathbf{h}_i \cdot \mathbf{g}_i) / (\mathbf{h}_i \cdot (\mathbf{Mh}_i)) \end{aligned} \quad (8.12)$$

using the definition of \mathbf{g}_i given above. Similarly, from step F of Algorithm III,

$$\mathbf{h}_{i+1} = \mathbf{g}_{i+1} + \gamma_i \mathbf{h}_i \quad (8.13)$$

with

$$\gamma_i = (\mathbf{g}_{i+1} \cdot \mathbf{g}_{i+1}) / (\mathbf{g}_i \cdot \mathbf{g}_i) \quad (8.14)$$

Notice that Eqs. (8.11), (8.12), (8.13) and (8.14), defining the recursion rules for generating the $[\mathbf{g}, \mathbf{h}]$ pairs, are exactly the same as those for the modified FTCG theorem (Case A) i.e. the same sequence of $[\mathbf{g}, \mathbf{h}]$ pairs will be generated in the two cases for a given \mathbf{g}_0 . Thus the results I and II from the FTCG theorem are applicable to the sequence generated from algorithm III also. In particular, if we apply the result I of the FTCG theorem to the latter sequence, it follows that \mathbf{g}_j (and thus $\nabla f(\mathbf{x}_j)$) must become the null vector for a value of j no more than n i.e. the minimum of the function f will be located in no more than n -steps. It is clear that the number of steps necessary could, in principle, be less than n if the required special choice is made for \mathbf{g}_0 . For the algorithm II the correspondence of rules of recursion will be with those for the case B of the modified theorem. Thus, here also, exact convergence to the minimum of a quadratic function is guaranteed in no more than n steps.

We have completed the demonstration that, for a quadratic function, it makes no difference as to whether one is applying the Fletcher-Reeves algorithm or the Polak-Ribiere algorithm for minimization. However, functions encountered in practice for minimization, are rarely quadratic. In these situations the only real symmetric positive definite matrix with respect to which the concept of conjugacy can be defined is the Hessian matrix at the nearby local minimum. It is clear that the application of algorithms II or III will not

create mutually conjugate directions (in the sense defined above) for line minimization nor will it be possible to locate the minimum in less than or equal to n -steps. However, since both the search algorithms guarantee a downward flow of the function, the empirical experience is that in typical applications one does get reasonably close to a local minimum after not-too-many steps. In this region the function behaves, to a very good approximation, as a quadratic function and the FTCG theorem typically ensures quick convergence to the minimum to within the preset tolerance. This is true for both algorithm II and algorithm III. However, there seems to be a preference for the Polak-Ribiere algorithm amongst practitioners. We are not sure if there is a rigorous justification for this [2].

8.3 The Geometry of the Conjugate Directions Method

We now turn our attention to the geometrical foundation of the Conjugate Directions method of minimization [3]. Let us remember the origin of the nomenclature “Conjugate Directions method”: In all the three algorithms we have seen until now, the procedure of minimization of a function of n -variables takes the form of a series of minimizations of a function of a *single* variable along directed straight lines. These series of “directed” straight lines are defined by the sequence $\mathbf{h}_0, \mathbf{h}_1, \mathbf{h}_2, \dots$ etc. The method of minimization is called a “Conjugate Directions method” if any pair of these search directions are mutually conjugate. As we have noted earlier the nomenclature of “Conjugate Directions method” is meaningful only when the function to be minimized is a quadratic function and the required positive definite matrix is the Hessian matrix of the quadratic function. However, what happens in practice is that methods (such as algorithms II and III) that guarantee the generation of conjugate directions in the context of a quadratic function are extended mechanically to more general functions and one continues to refer to the procedures as “Conjugate Directions methods”. So we confine our attention to a strictly quadratic function and explain the geometrical aspects of why convergence to the minimum in no more than n -steps is guaranteed when the directions of line minimization are taken to be mutually conjugate. This is done by mapping the original problem of minimization onto a modified problem via a coordinate transformation and showing that this equivalent problem can be solved in no more than n -steps by employing a procedure of the type encoded in algorithm I.

The most general quadratic function f has the form $f(x_1, x_2, \dots, x_n) = (1/2)(\mathbf{x} - \mathbf{x}_0) \cdot \mathbf{M}(\mathbf{x} - \mathbf{x}_0) + \theta$. Here \mathbf{x}_0 denotes the location of the minimum. Since θ is only an additive constant it does not affect the process of searching for the location of the minimum and hence will be ignored from now onwards. Let $[\lambda_i, \mathbf{u}_i]$ (with $i = 1, 2, \dots, n$) be the i -th [eigenvalue, eigenvector] pair of \mathbf{M} . We assume that the eigenvectors have been made orthonormal through standard procedures. Let $(\mathbf{x} - \mathbf{x}_0) \equiv y_1 \mathbf{u}_1 + y_2 \mathbf{u}_2 + \dots + y_n \mathbf{u}_n$. Then the

point represented by (x_1, x_2, \dots, x_n) in the original coordinate system will be represented by (y_1, y_2, \dots, y_n) in this new Cartesian coordinate system whose axes are along the eigenvectors $(\mathbf{u}_1, \mathbf{u}_2, \dots, \mathbf{u}_n)$. The functional form will change from $f(\mathbf{x})$ to $F(\mathbf{y})$ with $f(\mathbf{x}) = (1/2)(\mathbf{x} - \mathbf{x}_0) \cdot \mathbf{M} (\mathbf{x} - \mathbf{x}_0) = (1/2)[\lambda_1 y_1^2 + \lambda_2 y_2^2 + \dots + \lambda_n y_n^2] = F(\mathbf{y})$. Since all the eigenvalues of \mathbf{M} are strictly positive it is clear that the surfaces on which the value of the function are constant (from now onwards we will call them “equipotential” surfaces) will be ellipsoids in n -dimension. Finally, we can rescale the coordinate axes by the definition $z_i \equiv \lambda_i^{1/2} y_i$ for $i = 1, 2, \dots, n$. If we use this coordinate system the function now looks $G(\mathbf{z}) = (1/2)(z_1^2 + z_2^2 + \dots + z_n^2)$. The equipotential surfaces have become spherical – with the function value proportional to the square of the distance from the origin where the minimum is located. Thus we have mapped the original problem of minimizing the function f defined in the \mathbf{x} -space to the problem of minimizing the function G in the \mathbf{z} -space. Connection between the vectors \mathbf{x} , \mathbf{y} and \mathbf{z} representing the same point in the three different coordinate systems is given by

$$(\mathbf{x} - \mathbf{x}_0) = \mathbf{T}\mathbf{y} \quad (8.15)$$

where \mathbf{T} is a $n \times n$ orthogonal matrix with $T_{i,j}$ being the i -th row of the j -th eigenvector of \mathbf{M} . Also

$$\mathbf{z} = \mathbf{D}\mathbf{y} \quad (8.16)$$

where \mathbf{D} is $n \times n$ diagonal matrix with $D_{i,j} = \delta_{ij} \lambda_i^{1/2}$. Combining Eqs. (8.15) and (8.16),

$$\mathbf{z} = \mathbf{DT}^{-1}(\mathbf{x} - \mathbf{x}_0) \quad (8.17)$$

What about the mapping of directed straight lines like $\mathbf{h}_0, \mathbf{h}_1, \mathbf{h}_2, \dots$ etc? We know that points along the straight line of search from \mathbf{x}_i to \mathbf{x}_{i+1} can be written in the parametric form $\mathbf{x}_i + \lambda \mathbf{h}_i$ with λ going from zero to λ_i . Since the mapping given by equation (8.17) is linear, this search line in the x -space will be mapped onto a straight line in the z -space. If we preserve the value of λ_i in the z -space \mathbf{h}_i will be mapped onto $\mathbf{DT}^{-1} \mathbf{h}_i$. Thus if we take any two mutually conjugate search directions \mathbf{a} and \mathbf{b} in the x -space, the scalar product of their images (\mathbf{A} and \mathbf{B}) in the z -space will be

$$\begin{aligned} \mathbf{A} \cdot \mathbf{B} &= (\mathbf{DT}^{-1} \mathbf{a}) \cdot (\mathbf{DT}^{-1} \mathbf{b}) = (\mathbf{DT}^{-1} \mathbf{a})^T \mathbf{DT}^{-1} \mathbf{b} \\ &= \mathbf{a}^T \mathbf{T} \mathbf{D}^2 \mathbf{T}^{-1} \mathbf{b} \text{ (using the orthogonality property of } \mathbf{T} \text{)} \\ &= \mathbf{a}^T \mathbf{M} \mathbf{b} = 0 \text{ (since } \mathbf{a} \text{ and } \mathbf{b} \text{ are conjugate with respect to } \mathbf{M} \text{ in the } \mathbf{x} \text{-space).} \end{aligned}$$

We have thus established that search directions that are conjugate in the x -space are orthogonal in the z -space and hence the concept of conjugacy is a generalization of the more familiar concept of orthogonality.

How many steps (of the type defined in the generic algorithm I) are required to *numerically* locate the minimum of the function $G(\mathbf{z}) = (1/2)(z_1^2 + z_2^2 + \dots + z_n^2)$ – starting from a completely arbitrary initial guess? [Of course, we know *analytically* that the minimum is at $\mathbf{z} = \mathbf{0}$]. We will show next, largely

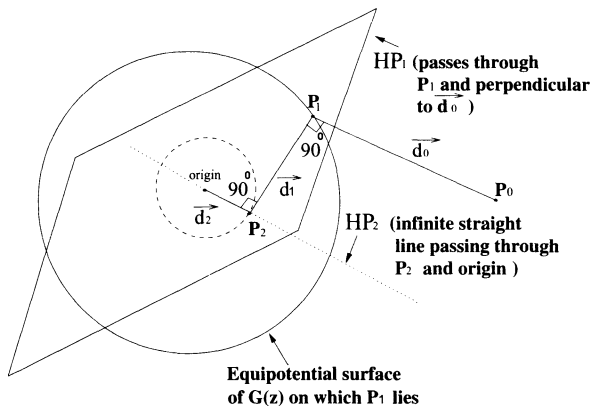


Figure 8.1: Locating the minimum of a spherically symmetric function in three dimensions.

via geometry, that this number is less than or equal to n if the directions of search are all mutually orthogonal.

Equipotential surfaces of $G(\mathbf{z})$ are hyperspheres (surfaces of dimension $(n - 1)$) with the origin $\mathbf{z} = \mathbf{0}$ at the center. So gradient of the function G is everywhere radially outwards away from the origin. Suppose we start from an arbitrary point P_0 and choose a search direction \mathbf{d}_0 along which to line minimize (see Fig.8.1 which illustrates the procedure when $n = 3$). \mathbf{d}_0 is a vector such that it is a downhill direction for $G(\mathbf{z})$. But otherwise it is completely arbitrary. Suppose P_1 is the point along \mathbf{d}_0 where the line minimization takes place. Then the gradient of $G(\mathbf{z})$ at P_1 , if it is nonzero, is in a direction perpendicular to \mathbf{d}_0 . But we already know that the gradient vector through any point passes through the origin – which is the location of the minimum of $G(\mathbf{z})$ (The line joining P_1 and P_0 is perpendicular to the line connecting P_1 to the origin). Thus it is guaranteed that a hyperplane (HP_1) that is perpendicular to \mathbf{d}_0 and passes through P_1 contains the minimum that we are searching for (Equation of HP_1 is given by $(\mathbf{z} - \mathbf{z}(P_1)) \cdot \mathbf{d}_0 = 0$). We can thus restrict our subsequent search for the minimum to this hyperplane whose dimension is one less than that of the original search space.

From P_1 we start the search in the subspace HP_1 . We have to choose a direction \mathbf{d}_1 for line minimization which guarantees (i) that we stay in the hyperplane HP_1 and (ii) that we go downhill. The first criterion is satisfied by choosing \mathbf{d}_1 to be orthogonal to \mathbf{d}_0 (remember the definition of HP_1). Other than satisfying these two criteria \mathbf{d}_1 is arbitrary. Suppose P_2 is the point where line minimization along \mathbf{d}_1 takes place. Then the gradient of the function G at P_2 is perpendicular to \mathbf{d}_1 . Again, since the gradient vector always passes through the minimum of G , a $(n - 1)$ -dimensional hyperplane passing through P_2 and perpendicular to \mathbf{d}_1 is guaranteed to contain the minimum. But we know that the minimum is also located in HP_1 . Thus the minimum is now known

to be located in the intersection of these two $(n - 1)$ -dimensional hyperplanes which are mutually orthogonal (since the two hyperplanes are perpendicular to two mutually orthogonal directions \mathbf{d}_1 and \mathbf{d}_0). And this intersection is a $(n - 2)$ -dimensional hyperplane HP_2 . The next step of search can be restricted to HP_2 . This can be implemented by taking the search direction \mathbf{d}_2 out of P_2 to be orthogonal to both \mathbf{d}_0 and \mathbf{d}_1 . Please notice that in the special case of $n = 3$ illustrated in Fig.8.1 HP_2 is just a straight line and going in the downhill direction is guaranteed to lead to the minimum.

We have thus far explicitly described the first few steps of a procedure which has the structure of the generic algorithm I with the following specificity: In step C choose the direction of line minimization to be arbitrary if it is the first step; otherwise make it orthogonal to all the previously chosen direction vectors. The logic behind making the new direction of line search to be orthogonal to all previous directions is this: At the end of every line minimization we know that the minimum must lie on a $(n - 1)$ -dimensional hyperplane perpendicular to the direction just searched and passing through the line minimum just reached. But one such new plane is generated at the end of every line minimization. How do we ensure that the next direction of search is such that we simultaneously stay on all these previously generated hyperplanes on which we know the minimum must lie? This is precisely what is accomplished by taking the new search direction to be orthogonal to all previous search directions. Since at every step we identify a new hyperplane, orthogonal to all previously discovered ones, on which the minimum must lie it is obvious that the dimension of the space in which the minimum must be located gets reduced by one in every step. Hence the search lands on the minimum after n -steps. Of course, in any of the intermediate steps, the direction vector for line minimization could accidentally be in the direction of the minimum and the total number of steps would in that case be less than n . This completes the largely geometric demonstration that the minimum of the function G can be located *numerically* in no more than n -steps.

To see what this means for the original quadratic function f consider the search trajectory of connected (and directed) straight lines generated in the process of finding the minimum of G . Generate the image of this trajectory in the \mathbf{x} -space by using equation (8.17). This image has the following properties:

- (a) It is a connected set of directed straight lines by virtue of the continuous and linear nature of the mapping between \mathbf{x} and \mathbf{z} .
- (b) The starting point and the starting direction in the x -space are arbitrary since they are so in the z -space.
- (c) It is easy to check that every directed straight segment in the x -space ends at a point where line minimization takes place for f .
- (d) By virtue of the results derived earlier, *each new search direction in the x -space will be conjugate to all previous search directions in that space with respect to \mathbf{M}* .

It should be easy to recognize that the four properties are exactly those that would characterize a “Conjugate Directions” method of minimization. Since the minimization is achieved for G in n -steps or less in the z -space same is true for f in the x -space.

The nomenclature of “Conjugate Gradient” method derives from the fact that the computation of the mutually conjugate search directions makes use of gradient information (at the points of line minimization) – as we have seen in the algorithms II and III. We have not at all discussed the issue of how line minimizations are performed in practice. A very detailed discussion on this topic can be found in [2].

Exercises Source codes for implementing the Conjugate Gradient method are available readily (for example, in [2]). We recommend that the reader puts together such a code to check the working of the method. However, a thorough understanding of the applicable line minimization algorithms should be developed before using them. The source code will require the definition of the function to be minimized and its gradient. To begin with the following two problems may be tried:

- (i) Let $f(x, y) = e^{((x-a)^2 + (y-b)^2)}$ where a and b are fixed real numbers. Write a program to find the minimum of f . Since the location of the minimum is known analytically this forms a good test problem. Warning: Apply appropriate caution to deal with the extremely rapid growth of the function away from its minimum.
- (ii) Consider a cluster of N interacting particles. The position vector of the i -th particle is denoted by \mathbf{r}_i . For the pair made up of the i -th and j -th particles the potential energy is given by the Lennard–Jones expression $w(d_{ij}) = (d_{ij}^{-12} - d_{ij}^{-6})$, where d_{ij} is the distance between the two particles. This pair potential energy is summed over all the pairs in the system to get the expression of the total potential energy. This total potential energy function has a very large number of local minima when considered as a function of the position vectors of the particles in the cluster. Write a program to locate these minima. You can vary the number of particles, dimensionality of space as well as the pair potential energy expression to generate many interesting variations.

More examples of problems such as these may be found in [4].

8.4 The Steepest Descent Method

If, in algorithm I, \mathbf{h}_k is taken to be equal to $-\nabla f(\mathbf{x}_k)$ it is called the steepest descent method since the direction in which a function decreases the fastest is that of the negative of the gradient. This conceptually simple method, devised by Cauchy, will do the job in many cases. But, due to its poor convergence

properties in many situations which are by no means uncommon, it is usually not the method of choice. The following two paragraphs elaborate on this point.

Since, near a local minimum, most sufficiently smooth functions can be approximated very well by quadratic functions we will discuss the issue of convergence only in the context of a strictly quadratic function $F_0(\mathbf{r}) = -\mathbf{d} \cdot \mathbf{r} + (1/2)\mathbf{r} \cdot \mathbf{A}\mathbf{r} + \text{a constant}$, where \mathbf{A} is symmetric and positive definite. If we now choose the location of the minimum of this function to be the origin of a new Cartesian coordinate system of which the axes are the principal axes of \mathbf{A} , the function will look like $G(\mathbf{r}') = (1/2)\mathbf{r}' \cdot \mathbf{D}\mathbf{r}' + \text{minimum value of } G \text{ (or } F_0)$, where \mathbf{D} is the diagonalized version of \mathbf{A} . Since all the eigenvalues of \mathbf{A} are positive this function will have constant values on surfaces which are generalized ellipsoids in n -dimension.

In the special case in which all the eigenvalues are identical (i.e. the constant value surfaces are spherical) the steepest descent method leads to the minimum in only one step since the negative of the gradient at any point is directed towards the location of the minimum. In all other cases the minimum is found either in one step or as the limit point of an infinite sequence of line minima generated at the end of step (D) in algorithm I (a proof of this is left to the reader as an exercise). If all the eigenvalues are distinct the one step solution is found only when the starting point lies on one of the principal axes. When some, but not all, of the eigenvalues are degenerate the dimensionality of the space of initial points which lead to the minimum in one step will be correspondingly higher but it will still be less than n . In practice the starting point in step (A) of algorithm I is chosen randomly from within a n -dimensional subdomain where the minimum is guessed to lie. Thus, except when all the eigenvalues are identical, the probability of the steepest descent method leading to the minimum in one step is zero and, quite generically, one deals with an infinite sequence of ever improving approximations to the minimum.

The trajectory of these approximations can be visualized from the following considerations: Since at the end of step D in algorithm I the derivative along the line of search is zero the gradient of the function at the endpoint must be perpendicular to the line of search. This gradient defines the next direction of search. Thus it is clear that the steepest descent method generates a sequence of connected straight lines with any two adjacent segments being mutually perpendicular. If L_1 is one such line of search that ends at the line minimum at P and L_2 is the new line of search starting from P , then P lies on a surface of constant function value to which L_1 is a tangent and L_2 is perpendicular.

What is the rate of convergence of the line minima to the function minimum? If \mathbf{x}_k and \mathbf{x}_{k+1} denote the locations of two consecutive line minima and \mathbf{x}^* is the location of the function minimum it can be shown that the ratio $[(G(\mathbf{x}_{k+1}) - G(\mathbf{x}^*))/(G(\mathbf{x}_k) - G(\mathbf{x}^*))]$ (both the numerator and the denominator are positive by definition) is bounded above by $((q-1)/(q+1))^2$ where $q = (\text{Largest eigenvalue of } \mathbf{A}) / (\text{Smallest eigenvalue of } \mathbf{A})$. When all the eigenvalues are identical this upper limit is zero as expected. It is also obvious that the convergence is very slow when the largest and the smallest eigenvalues are very

different. In such a situation a correspondingly large number of line searches are required before the degree of convergence becomes acceptable. In contrast all the other methods that we describe here converge to the minimum, for an arbitrary starting point, in no more than n steps if the function to be minimized is strictly quadratic. Some hybrid methods make use of the steepest descent technique when the minimization starts. When the minimum gets nearer some other method with a faster convergence in that region takes over.

8.5 Quasi-Newton Methods

Suppose, during the process of trying to locate the minimum of a function f , you are at a point \mathbf{x}_k close to the minimum. In this region the function is very close to being quadratic. Hence it can be Taylor-expanded around \mathbf{x}_k in the form

$$f(\mathbf{x}) = f(\mathbf{x}_k) + (\mathbf{x} - \mathbf{x}_k) \cdot \nabla f(\mathbf{x}_k) + (1/2)(\mathbf{x} - \mathbf{x}_k) \cdot \mathbf{M}(\mathbf{x} - \mathbf{x}_k) \quad (8.18)$$

where \mathbf{M} is the Hessian matrix of f (within the quadratic approximation it does not matter where it is calculated). Taking the gradient of both sides of Eq. (8.18) we get

$$\nabla f(\mathbf{x}) = \nabla f(\mathbf{x}_k) + \mathbf{M}(\mathbf{x} - \mathbf{x}_k) \quad (8.19)$$

At the point \mathbf{x}^* where the minimum is located the gradient of f is a null vector. Thus, putting $\mathbf{x} = \mathbf{x}^*$ in Eq. (8.19), this yields

$$\mathbf{x}^* = \mathbf{x}_k - \mathbf{H}\nabla f(\mathbf{x}_k) \quad (8.20)$$

where \mathbf{H} is the inverse of \mathbf{M} . Suppose the minimum finding procedure has the structure of algorithm I. Then, if in the step C we put $\mathbf{h}_k = -\mathbf{H}\nabla f(\mathbf{x}_k)$, Eq. (8.20) says that the line as well as function minimum will be found at $\lambda_k = 1$. If an arbitrary symmetric and positive definite matrix is used in place of \mathbf{H} as the premultiplier of $\nabla f(\mathbf{x}_k)$ the resulting \mathbf{h}_k will still be a downhill direction of search. But it is only when the premultiplier is \mathbf{H} (or a multiple of it) that the search will find the minimum in that step itself. This is called the Newton-Raphson method. When the function is not exactly quadratic the minimum will not be reached in one step but the convergence to it will be quadratic which means, roughly speaking, that the number significant digits upto which the answer is correct will go up by a factor of two in every iteration.

However, all this is possible only if we know the Hessian. In many cases we would like to avoid calculating the Hessian or its inverse directly (It could be because n is too large or due to some other practical difficulties of computation). In such a situation where we do not have the Hessian *before* the minimization procedure starts the following strategy suggests itself: Take \mathbf{h}_k in step C to be $-\mathbf{H}_k\nabla f(\mathbf{x}_k)$ where \mathbf{H}_k is designed to evolve with k in such a way that it always remains a symmetric positive definite matrix (so that the function at least goes downhill in every iteration) and eventually converges to \mathbf{H} . This is

exactly what is accomplished in quasi-Newton methods. The Hessian (or its inverse) matrix of n^2 second derivatives is built up step-by-step by using the gradients (each containing n first derivatives) computed at the various points visited during the monotonic approach to the minimum.

It can be seen easily that this should be possible. Consider $(n+1)$ distinct points $(\mathbf{x}_0, \mathbf{x}_1, \dots, \mathbf{x}_n)$ in the vicinity of the minimum of a strictly quadratic function with the Hessian matrix \mathbf{M} . If you take two consecutive points, \mathbf{x}_i and \mathbf{x}_{i+1} , the gradients at these two points will satisfy the condition $(\nabla f(\mathbf{x}_{i+1}) - \nabla f(\mathbf{x}_i)) = \mathbf{M}(\mathbf{x}_{i+1} - \mathbf{x}_i)$. However, unless n equals unity, one cannot get a unique solution for \mathbf{M} from this one relation since this provides only n equations whereas the Hessian has n^2 unknown real numbers in it. It is equally obvious that the Hessian *can* be determined uniquely if we combine the information available from *all* such equations that can be written by setting $i = 0, 1, \dots, (n-1)$. This completes the demonstration that the exact construction of the Hessian is possible from the knowledge of the gradient at $(n+1)$ points. When the function is not strictly quadratic the Hessian obtained will naturally be correspondingly approximate.

When $n = 1$ there are only two points in the set and the Hessian (in this case just the second derivative) can be calculated or estimated immediately from the one equation available. This is the basis of the secant method of finding the minimum for functions of one real variable. Quasi-Newton methods are generalizations of this idea to functions defined on multidimensional spaces – although actual implementation is far from straightforward. To illustrate this we now describe the oldest algorithm of this family, namely the Davidon-Fletcher-Powell (DFP) algorithm.

8.5.1 Davidon-Fletcher-Powell (DFP) algorithm

- (A) Select a point $\mathbf{x}_0 \in \mathbb{R}^n$ as the starting point of your search. If $\nabla f(\mathbf{x}_0) = \mathbf{0}$, stop; otherwise go to step (B).
- (B) Define $\mathbf{H}_0 = \mathbf{I}$ (which is the $n \times n$ identity matrix) and $\mathbf{g}_0 = \nabla f(\mathbf{x}_0)$ and set the iteration index k to 0.
- (C) Define $\mathbf{h}_k = -\mathbf{H}_k \mathbf{g}_k$.
- (D) Starting from \mathbf{x}_k move in the direction of \mathbf{h}_k and obtain the line minimum of the function i.e. minimize $f(\mathbf{x}_k + \lambda \mathbf{h}_k)$ with respect to λ in the positive λ domain. Let the minimum be at $(\mathbf{x}_k + \lambda_k \mathbf{h}_k)$.
- (E) Define $\mathbf{x}_{k+1} = \mathbf{x}_k + \lambda_k \mathbf{h}_k$.
- (F) Calculate $\nabla f(\mathbf{x}_{k+1})$.
- (G) If $\nabla f(\mathbf{x}_{k+1}) = \mathbf{0}$, stop; otherwise define

$$\mathbf{g}_{k+1} = \nabla f(\mathbf{x}_{k+1})$$

$$\delta \mathbf{g}_k = \mathbf{g}_{k+1} - \mathbf{g}_k$$

$$\delta \mathbf{x}_k = \mathbf{x}_{k+1} - \mathbf{x}_k$$

Define the vector $\mathbf{w}_k = \mathbf{H}_k \delta \mathbf{g}_k$ and set

$$\mathbf{H}_{k+1} = \mathbf{H}_k + (|\delta \mathbf{x}_k\rangle\langle\delta \mathbf{x}_k|) / (\delta \mathbf{x}_k \cdot \delta \mathbf{g}_k) - (|\mathbf{w}_k\rangle\langle\mathbf{w}_k|) / (\delta \mathbf{g}_k \cdot \mathbf{w}_k)$$

where $|\mathbf{a}\rangle\langle\mathbf{b}|$, the outer product of two vectors \mathbf{a} and \mathbf{b} , is a matrix \mathbf{Q} with $\mathbf{Q}_{ij} = a_i b_j$.

(H) Update the value of k to $k + 1$ and go to step (C).

This completes the statement of the DFP algorithm. The update formula in step (G) ensures that \mathbf{H}_k stays positive definite all through. Also when this algorithm is used to minimize a strictly quadratic function it produces exactly the same sequence of \mathbf{x} and \mathbf{h} vectors as would be produced by the Fletcher-Reeves and Polak-Ribiere algorithms (of the Conjugate Gradient variety) with the same starting point. Convergence would be exact at the end of n steps and the Hessian would also be constructed.

Because of some technical issues having to do with roundoff error etc. DFP algorithm has largely been superseded by the Broyden-Fletcher-Goldfarb-Shano (BFGS) algorithm which is different only in the update formula for \mathbf{H}_k is step (G) [2]. However, there are many other algorithms that belong to this family. We should mention here that quasi-Newton methods are also known as Variable Metric methods. The reason for this is simply that the Hessian matrix is positive definite and hence can be used to define a metric. And, of course, here this matrix varies with every iteration.

As far as comparison between Conjugate Gradient Method and Quasi-Newton methods is concerned there is really not much to choose between them. The more frequent usage of the latter may be due to historical reasons (it has been longer in existence than the CG method). Quasi-Newton methods require storage of a $n \times n$ matrix. For very large values of n this could be a problem, but with the memory available nowadays in computers being typically so large, this is not much of an issue for most problems of practical interest.

References

- [1] E. Polak, *Computational methods in Optimization: A unified approach* (Academic Press, New York, 1971).
- [2] W. H. Press, B. P. Flannery, S. A. Teukolsky and W. T. Vettering, *Numerical Recipes: The art of Scientific Computing* (Cambridge University Press, 1986).
- [3] J. R. Shewchuk, *An Introduction to the Conjugate Gradient Method* (<http://www.cs.cmu.edu/~quake-papers/painless-conjugate-gradient.pdf>)
- [4] D. Wales, *Energy Landscapes: Applications to Clusters, Biomolecules and Glasses* (Cambridge University Press, Cambridge, 2003).

Chapter 9

Optimization and Quantum Annealing

Anjan Kumar Chandra and Bikas K. Chakrabarti

9.1 Introduction

Optimization deals with problem of finding the minimum of a given cost function (the relationship between the total cost of production and the quantity of a product produced) and in the combinatorial optimisation problems the cost function depends on a large number of variables and hard problems are those for which the computational time is not bound by any polynomial in the problem size [1]. To solve hard optimization problems is a challenging task. Several techniques have been developed to get to the solution(s) of such problems. Here we will discuss about some of the problems and also the techniques that have already been implemented.

Apart from many day-to-day engineering problems, many problems in physics have turned out to be or can be transformed to optimization problems [2, 3, 4, 5]; e.g., conformations of polymers in random media, optimization of wirings on printed circuit boards, ground state of spin glasses.

An optimization problem can be described mathematically in the following way: let $\sigma = (S_1, S_2, \dots, S_N)$ be a vector with N elements which can take values from a domain $X^N : S_i \in X$. The domain X can be either discrete, for instance $X = \{0, 1\}$ or $X = \mathbb{Z}$ the set of all integers (in which case it is an integer optimization problem) or X can be continuous, for instance $X = \mathbb{R}$ the real numbers. The ultimate goal is to minimize a given cost or energy function $\mathcal{H}(S_1, S_2, \dots, S_N)$ with respect to N variables S_1, S_2, \dots, S_N subject to some constraints. The task is to find a set of values for these variables (a configuration) for which the function $\mathcal{H}(S_i)$ has the minimum value (see Fig. 9.1). In some optimization problems the set of feasible configurations from which an

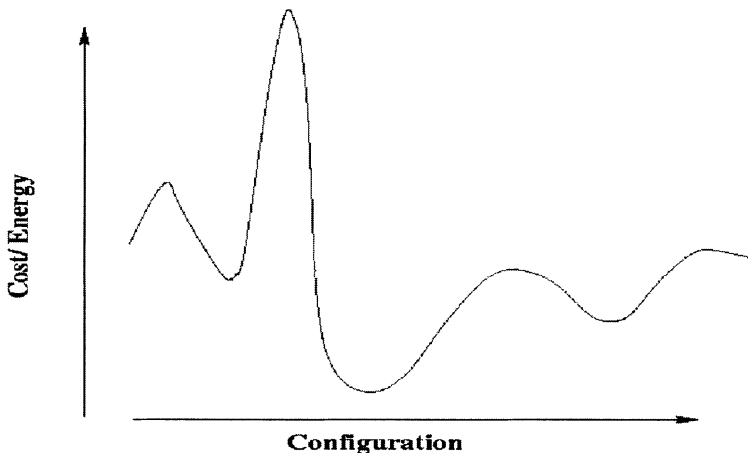


Figure 9.1: A typical cost function variation of a computationally hard problem; has a large number of local minima.

optimum is to be chosen is a finite set (for finite N) and the variables are discrete. These problems are combinatorial in nature. Certain problems can also be reduced to combinatorial problems [6].

Now we will discuss about the *time complexity* of an algorithm which describe its speed. An optimization problem is said to belong to the class P (P for polynomial), if it can be solved in polynomial time (i.e., the evaluation time varies as some polynomial in N) using polynomially bound resources (computer space, processors, etc.). The existence of such a polynomial bound on the evaluation time is interpreted as the “easiness” of the problem. Many important optimization problems seem to fall outside this class, such as the traveling salesman problem.

There is another important class of problems which can be solved in polynomial time by non-deterministic machines. This class is the non-deterministic polynomial (NP) class [7]. P is included completely in the NP class, since a deterministic Turing machine is a special case of non-deterministic Turing machine. Unlike a deterministic machine, which takes a specific step deterministically at each instant (and hence follows a single computational path), a non-deterministic machine has a host of different “allowed” steps at disposal at every instant. At each instant it explores all allowed steps and if any of them leads to the goal, the job is considered to be done. Thus it explores in parallel many paths (whose number varies roughly exponentially with time) and checks if any of them reaches the goal.

Among the NP problems, there are certain problems (known as NP -complete problems) which are such that any NP problem can be “reduced” to them using a polynomial algorithm. If one has a routine to solve an NP -complete problem of size N , then using that routine one can solve any NP

problem at the cost of an extra overhead in time that varies only polynomially with N . Problems in this class are considered to be hard, since so far a general non-deterministic machine cannot be simulated by a deterministic Turing machine (or any sequential computer with polynomially bound resources) without an exponential growth of execution time. In fact, notwithstanding some enthusiasm with quantum annealing (see later), it is widely believed (though not proved yet) that it is impossible to do so (i.e., $P \neq NP$) in principle. However, assuming this to be true, one can show that there are indeed problems in the NP class that are neither NP -complete nor P [7].

9.2 Some Combinatorial Optimization Problems

There are a large number of combinatorial optimization problems such as *Traveling salesman problem*, *Vehicle routing problem*, *Minimum spanning tree problem*, *Spin glass problem* etc. Here in this chapter we will discuss only the first and the last ones.

9.2.1 The Traveling Salesman Problem (*TSP*)

The traveling salesman problem (*TSP*) is a simple example of a combinatorial optimization problem and perhaps the most famous one. Given a set of cities and the intercity distance metric, a traveling salesman must find the shortest tour in which he visits all the cities and comes back to his starting point. It is a non-deterministic polynomial complete (NP - complete) problem.

The problem was first formulated as a mathematical problem during the 1930s in Vienna and at Harvard. Hassler Whitney at Princeton University introduced the name *traveling salesman problem*. The *TSP* has several applications such as in logistics, manufacturing microchips, genome sequencing etc. In these cases, city stands for customers, soldering points and DNA fragments and distance represents traveling times or cost, similarity measurements between DNA fragments.

In the *TSP*, the most naive algorithm for finding the optimal tour is to consider all the $(N - 1)!/2$ possible tours for N number of cities and check for the shortest of them (Fig. 9.2). Working this way, the fastest computer available today would require more time than the current age of the universe to solve a case with about 30 cities. The typical case behaviour is difficult to characterize for the *TSP* though it is believed to require exponential time to solve in the worst case. For this reason the *TSP* serves as a prototype problem for the study of the combinatorial optimization problems in general.

In the normal *TSP*, we have a N number of cities distributed in some continuum space and we determine the average optimal travel distance per city \bar{l}_E in the Euclidean metric (with $\Delta r_E = \sqrt{\Delta x^2 + \Delta y^2}$), or \bar{l}_C in the Cartesian metric (with $\Delta r_C = |\Delta x| + |\Delta y|$). Since the average distance per city (for fixed area) scales with the number of cities N as $1/\sqrt{N}$, we find that the normalized travel distance per city $\Omega_E = \bar{l}_E \sqrt{N}$ or $\Omega_C = \bar{l}_C \sqrt{N}$ become the optimised constants

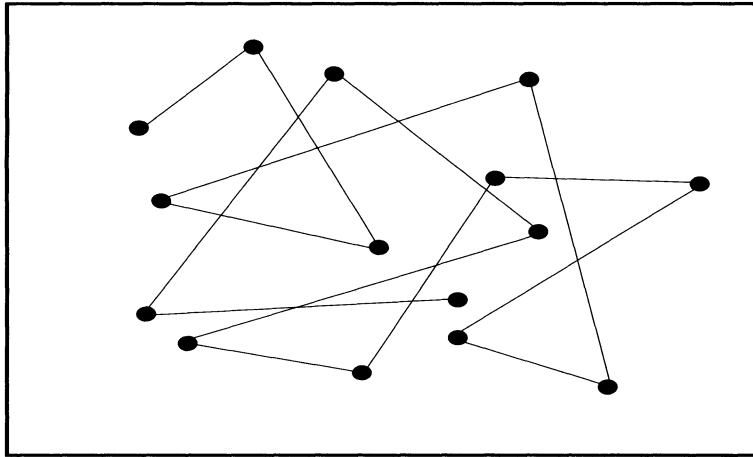


Figure 9.2: A typical move of a TSP problem on a $2d$ continuum lattice. The black dots represent cities and the lines joining them indicate the moves from one city to another.

and their values depend on the method used to optimize the travel distance.

Bounds for optimised travel distance:

Approximate analytic methods has also been employed to estimate the upper and lower bounds of Ω_E and Ω_C . The travel distance is expressed as a function of a single variable and the distance is optimized with respect to that variable [8, 9]. In one dimensional case any directed tour will solve such a problem. In two dimensions, one can reduce it (approximately) to a one dimensional problem, where the square (country) is divided into strips of width W and within each strip, the salesman visits the cities in a directed way. The total travel distance is then optimized with respect to W .

Let the strip width be W and the probability density of cities be p ($= N$ for unit area). We have a city at $(0, y_1)$ (Fig. 9.3). The probability that the next city is between distances x and $x + \Delta x$, is $pW\Delta x$. So the probability that there is no city in distance Δx is $(1 - pW\Delta x)$ and no city in such n consecutive strips of length Δx where $x = n\Delta x$, is $(1 - pW\Delta x)^n \sim e^{(-pWx)}$. The probability that there is a city between y and $y + \Delta y$, is $\Delta y/W$. Hence the probability that there is no other city within distance y is $(1 - y/W)$. The average distance between any two consecutive cities is therefore

$$\bar{l}_E = 2 \int_{x=0}^{\infty} \int_{y=0}^W \sqrt{x^2 + y^2} pW dx e^{-(pWx)} \frac{dy}{W} \left(1 - \frac{y}{W}\right) \quad (9.1)$$

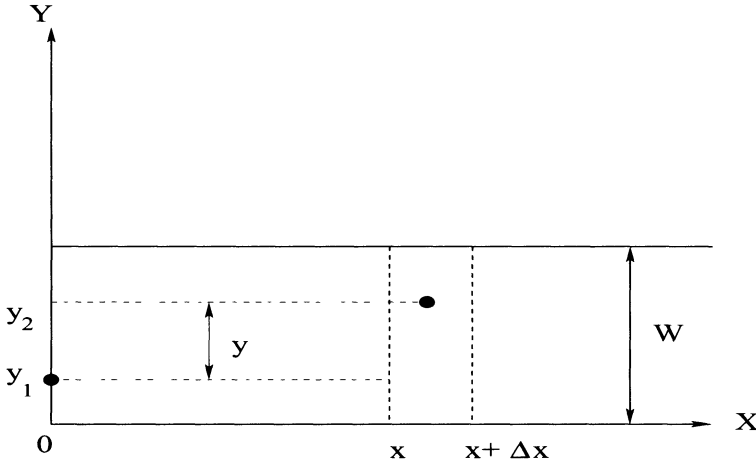


Figure 9.3: Calculating the average distance between two nearest neighbours (shown by black dots) along a strip of width W .

The factor 2 arises to take care of the fact that y can be both positive and negative. Substituting the variables by $u = pWx$ and $v = y/W$, so that

$$\bar{l}_E = 2 \int_{u=0}^{\infty} \int_{v=0}^1 \frac{1}{pW} \sqrt{u^2 + p^2 W^4 v^2} e^{-u} (1-v) du dv \quad (9.2)$$

Introducing two dimensionless quantities $\Omega_E = \sqrt{p}\bar{l}_E$ and $\tilde{W} = \sqrt{p}W$ yields

$$\Omega_E = \frac{2}{\tilde{W}} \int_{u=0}^{\infty} \int_{v=0}^1 \sqrt{u^2 + \tilde{W}^4 v^2} e^{-u} (1-v) du dv \quad (9.3)$$

Using Monte Carlo integration to evaluate the above integral, we get the minimum $\Omega_E \sim 0.92$ at normalized strip width $\tilde{W} \sim 1.73$.

In the Cartesian metric the average distance between any two consecutive cities is

$$\bar{l}_C = 2 \int_{x=0}^{\infty} \int_{y=0}^W (x+y) pW dx e^{-(pWx)} \frac{dy}{W} \left(1 - \frac{y}{W}\right) \quad (9.4)$$

Introducing $u = pWx$ and $v = y/W$ yields,

$$\bar{l}_C = 2 \int_{u=0}^{\infty} \int_{v=0}^1 \frac{1}{pW} (u + pW^2 v) e^{-u} (1-v) du dv \quad (9.5)$$

Introducing the dimensionless quantities $\Omega_C = \sqrt{p}\bar{l}_C$ and $\tilde{W} = \sqrt{p}W$ gives

$$\Omega_C = \frac{2}{\tilde{W}} \int_{u=0}^{\infty} \int_{v=0}^1 (u + \tilde{W}^2 v) e^{-u} (1-v) du dv \quad (9.6)$$

Using Monte Carlo integration to evaluate the above integral, we get the minimum $\Omega_C \sim 1.15$ at the normalized strip width $\tilde{W} \sim 1.73$.

Let us now estimate a lower bound of the minimum travel distance per city. Let the distance between any two cities be denoted by l . Then the probability that there is a city between l and $l + dl \sim (p - 1)2\pi l dl \sim 2p\pi l dl$. Now, the probability that there is no other city in the distance $l \sim (1 - \pi l^2)^{p-2} \sim e^{-(p-2)\pi l^2} \sim e^{-p\pi l^2}$. Therefore, $P(l)dl = (2p\pi l)e^{-p\pi l^2} dl$ with $\int P(l)dl = 1$. Hence the average nearest neighbour distance is

$$\bar{l}_E = \int_0^\infty l^2 e^{-p\pi l^2} dl = \frac{1}{2} \frac{1}{\sqrt{p}}$$

Therefore, a simple lower bound for $\Omega_E = 1/2$.

Assuming now random orientation of the Euclidian nearest neighbour distance l_E or Ω_E with respect to the Cartesian axes, one can easily estimate the corresponding lower bound for Ω_C as $\Omega_C = 2\Omega_E \langle |\cos \theta| \rangle = (4/\pi)\Omega_E = 2/\pi$.

TSP on a randomly diluted lattice:

The lattice version of the TSP was first studied by Chakrabarti [10 (a)]. Here the cities are represented by randomly occupied lattice sites of a two-dimensional square lattice ($L \times L$) and p is the fractional number of sites occupied. In this case, Ω_E has monotonic variation from 1 (for $p = 1$) to a constant ~ 0.79 (for $p \rightarrow 0$) and Ω_C has monotonic variation from 1 (for $p = 1$) to a constant 1.01 (for $p \rightarrow 0$) respectively [9]. The ratio Ω_C/Ω_E changes from 1 to 1.26 ($\simeq 4/\pi$) as p varies from 1 to 0. Dhar et al. [10 (b)] showed that if the average length of the shortest path per chosen site be $\Omega_C(p)$ where p is the density of chosen sites, then for a triangular lattice $\Omega_C(p)$ differs from 1 only by terms of order $(1-p)^5$. For square lattice $\Omega_C(p) = 1 +$ terms of order $(1-p)^{3/2}$. They showed that $\Omega_C(p)$ will have a monotonic variation from 1 for $p = 1$ to a constant for $p \rightarrow 0$. The constant value they found for a cartesian metric is $\sqrt{4/3}$. Ghosh et al. [10 (c)] determined the value of the constant (as $p \rightarrow 0$) for both Cartesian and Euclidean metric by applying simulated annealing technique. For the Cartesian metric they found 1.00 ± 0.05 and for Euclidean metric 0.80 ± 0.05 .

The upper and lower bounds of the normalised travel distance per city in Euclidean and Cartesian metric for both continuum and randomly diluted lattice are shown in Table 1.

Some optimisation results:

There is a large number of exact algorithms to solve this optimization problem. The most naive algorithm for finding the optimal tour is to consider all the $(N-1)!/2$ possible tours for N number of cities and check for the shortest of them. Dantzig et al. at the RAND Corporation in Santa Monica, solved an instance of 49 cities by developing the cutting plane method [11]. Karp showed in 1972 that the problem was a NP-complete one [11]. In the late 1970s and 1980, Grötschel

Table 1: Theoretical and experimental results for optimised distances in continuum and dilute lattice.

		Ω_E	Ω_C
Continuum	Theoretical ^(a)	$0.5 < \Omega_E < 0.92$	$0.64 < \Omega_C < 1.15$
	Computational ^(b)	0.7120 ± 0.0002	
Dilute Lattice	Theoretical ^(c)		$\sqrt{4/3} \sim 1.15 (p \rightarrow 0)$
	Computational ^(d)	$0.80 \pm 0.05 (p \rightarrow 0)$	$1.00 \pm 0.05 (p \rightarrow 0)$

(a) ref [8, 9], (b) [13 (c)], (c) [10 (b)] and (d) [10 (c)].

et al. exactly solved instances upto 2392 cities, using *cutting planes* and *branch-and-bound* methods [11]. Reinelt published the *TSPLIB* in 1991, a collection of benchmark instances of varying difficulty, which has been used by many research groups for comparing results. In 2005, Cook and others computed an optimal tour through a 33,810-city instance given by a microchip layout problem, currently the largest solved *TSPLIB* instance using the *Concorde TSP Solver* program which was developed in the 1990's by Applegate et al. [11]. The shortest tour length found was 66,048,945 units and the computation took almost 15.7 CPU years.

Various approximation algorithms, which quickly yield good solutions with high probability, has been formulated. Modern methods can even find solutions for millions of cities within a reasonable computational time which are just 2 – 3% away from the most optimal one. The most naive method to obtain an approximate solution of traveling salesman problem is the “greedy” heuristic algorithm [7, 12]. Suppose we have a random arrangement of N cities in a square (country) of fixed area (taken to be unity). Let us think of any tour to start-with and then make a local exchange of a pair of cities in the tour. We compute the new tour length and if it is lower than the previous one, then the greedy algorithm accepts the new tour as the starting point for further such modifications. The “Lin-Kernighan” algorithm [13 (a), 13 (b)] considers local exchange between three or more cities. For detailed discussion on local search algorithm see Sec. I.2.

Percus and Martin investigated the finite size scaling of the mean optimal tour length (Ω_E) for a Euclidean TSP [13 (c)]. They applied local-optimization heuristics such as the Lin-Kernighan [13 (b)] and chained local optimization [13 (d)]. They showed that $\Omega_E(d = 2) = (0.7120 \pm 0.0002)[1 + O(1/N)]$ and $\Omega_E(d = 3) = (0.6979 \pm 0.0002)[1 + O(1/N)]$ where d denotes the dimension of the lattice. They also showed by a mean-field approach in the limit $N \rightarrow \infty$, $\Omega_E(d) = \sqrt{d/2\pi e}(\pi d)^{1/2d}[1 + O(1/d)]$ at large d .

The essential drawback of such local search algorithms is the obvious one of getting stuck at a local minimum, where any local rearrangement in the tour does not improve the optimised tour length. The “simulated annealing method” (SA) [12, 14] is an ingenious method in achieving the global minimum of a many-body system by *slow cooling* or *annealing*. The rapid quenching of a system leads to the trapping of the system in a local minimum state. The system cannot get out of it, since the Boltzmann probability ($\sim \exp(E' - E)/kT$, for trap energy E and barrier height E') to get out of the minimum drops to zero, as the temperature becomes zero due to quenching. In the annealing, the system is slowly cooled so that as the system falls in a local trap, the finite Boltzmann probability allows the system to get out of the trap, maintaining a general flow to lower energy states as temperature decreases. Eventually the system anneals to the ground state at the lowest temperature.

In the *TSP* case, one takes the total tour length L ($= Nl$) as the energy E and one introduces a fictitious temperature T . Initially one takes T very high such that the average total tour length \bar{L} is much higher than the global minimum. The tours are then modified locally and the modified tours are accepted with probability $\sim \exp(\Delta L/kT)$ where ΔL is the change in the tour length. Here, the probability is non-vanishing even for ΔL positive as long as the temperature is non-zero. For further discussions on this method see Sec I.2.

Simulated annealing and local search algorithms optimize very effectively on small scales involving a small number of variables, but fail for larger scales that require the modification of many variables simultaneously. To deal with the large scales, “genetic algorithms” [15] use a “crossing” procedure which takes two good configurations - “parents”, from a population and finds sub-paths, either randomly or by using large parts of its parents. A population of configurations is evolved from one generation to the next using these crossings followed by a selection of the best children. However, this approach supposedly does not work well in practice since it is extremely difficult to produce two parents and cross them to make a child as good as them. This is a major drawback of the genetic algorithms and is responsible for their limited use.

Using the *Quantum annealing* (QA) method, discussed later, one can employ both thermal and quantum fluctuations to allow the downhill movement. More importantly it has the advantage of the ability to penetrate through high but narrow barriers which are hard to jump thermally. It was found that quantum annealing was more efficient than classical annealing in finding an approximately minimal tour in infinite dimension [16]. They chose a standard benchmark TSP problem, namely, the printed circuit board instance pr1002 of the TSPLIB [17]. For a detail discussion on this method and the comparative results of QA and SA see Sec I.2.

9.2.2 Spin Glass and Optimization

Spin glasses are magnetic systems with randomly competing (frustrated) interactions [18 (a),18 (b),18 (c),18 (d),18 (e)]. The spins interact ferromagnetically

or antiferromagnetically with their neighbours. The main ingredients of spin glass are: *competing nature of interactions* and *randomness*. As a consequence, there is a situation where all of the spins present in the system cannot energetically *satisfy* every interaction associated with them. This situation is called *frustration*. As a result there arise huge barriers ($O(n)$, N = system size) in the free-energy landscape of the system. In the thermodynamic limit, height of such barriers occasionally go to infinity. These barriers strongly separate different configurations of the system, so that once the system gets stuck in a deep valley in between two barriers, it practically gets trapped around that configuration for a macroscopically large time. Because of frustration, the ground state is largely degenerate. The degeneracy of the ground state of a typical spin glass model is $\exp(0.19923N)$ [19]. As discussed above, these different ground state configurations are often separated by $O(n)$ barriers, so that once the system settles down in one of them, it cannot visit the others equally often in course of time, as predicted by the Boltzmann probability factor. The system thus becomes ‘non-ergodic’ and may be described by a non-trivial order parameter distribution [18 (e)] in the thermodynamic limit (unlike the unfrustrated cooperative systems, where the distribution becomes trivially delta function-like). The spins in such a system thus get frozen in random orientations below a certain transition temperature. Although there is no long range magnetic order, i.e., the space average of spin moments vanishes, the time average of any spin is non-zero below the transition (spin-glass) temperature. The time average is treated as a measure of spin freezing or spin glass order parameter.

Several spin glass models have been studied extensively using both analytic and computer simulation techniques. The Hamiltonian for such models can be written as

$$\mathcal{H} = - \sum_{i < j} J_{ij} s_i^z s_j^z \quad (9.7)$$

where $s_i^z = \pm 1$, $i = 1, 2, \dots, N$ denote the Ising spins, interacting with random quenched interactions J_{ij} which differs in various models. Three extensively studied models are:

- (a) Sherrington-Kirkpatrick (S-K) model: J_{ij} are long-ranged and are distributed with a Gaussian probability (centered around zero), as given by

$$P(J_{ij}) = \left(\frac{N}{2\pi J^2} \right)^{\frac{1}{2}} \exp \left(\frac{-NJ_{ij}^2}{2J^2} \right) \quad (9.8)$$

- (b) Gaussian Edward-Anderson (EA) model: J_{ij} are short-ranged, but similarly distributed with Gaussian probability.
- (c) $\pm J$ Edward-Anderson (EA) model: J_{ij} 's are again short-ranged, but having a binary ($\pm J$) distribution with probability p

$$P(J_{ij}) = p\delta(J_{ij} - J) + (1-p)\delta(J_{ij} - (-J)) \quad (9.9)$$

Some optimisation results:

Finding the ground state of a spin glass is an important class of combinatorial optimization problem, which includes an NP -complete problem [20], and many other apparently different ones (such as the traveling salesman problem) can be recast in this form.

Inspite of the simplicity of the short-ranged $\pm J$ Ising spin glass, there is no accurate and reliable value for the ground state energy per spin (E_0) of the infinite system [21]. Only the upper and lower bounds have been obtained [22, 23]. Let x be the fraction of negative interactions and x_f be the fraction of frustrated squares. It has been shown that for $2d$ [22],

$$-2 + x_f \leq E_0 \leq \min \left[-2|1 - 2x|, -\frac{4}{3} \right] \quad (9.10)$$

where E_0 is the ground state energy per spin. For $3d$ the corresponding equation is,

$$-3 + \frac{3}{2}x_f \leq E_0 \leq \min \left[-3|1 - 2x|, -\frac{3}{2} \right] \quad (9.11)$$

Many different algorithms have been applied to determine spin glass ground states, like transfer matrix calculation [24 (a)], simulated annealing [12],[24 (b)], other statistical physical simulations [24 (c)], branch and cut technique [24 (d)], genetic algorithms [24 (e)],[21] and other optimization methods inspired by natural evolution [24 (f)]. The ground state energy for the $\pm J$ model as obtained from transfer matrix calculations for $x = 1/2$ is $E_0 \approx -1.4024 \pm 0.0012$ ($2d$) and $E_0 \approx -1.76 \pm 0.02$ ($3d$) where x is the fraction of negative interactions. The estimation for the Gaussian model is $E_0/\Delta J = -1.31 \pm 0.01$ ($2d$) and $E_0/\Delta J = -1.7 \pm 0.03$ ($3d$) [18 (a)], where ΔJ is the width of the distribution. Grest et al. studied the cooling rate dependence of spin glasses and showed that $E_0 \approx -1.398$ ($\pm J, 2d$), -1.791 ($\pm J, 3d$) and -1.308 (Gaussian, $2d$) [24 (b)]. The ground-state energy per spin of $\pm J$ EA model ($3d$), obtained by multicanonical simulation by Berg et al. [24 (c)] is -1.7956 ± 0.0042 . Simone et al. applied the branch and cut technique to estimate the ground state of a $2d$ spin glass with Gaussian bond distribution for system size upto 100×100 and they obtained $E_0 = -1.3177 \pm 0.0014$ [24 (d)]. Genetic algorithms were implemented to determine the ground state energies for the $\pm J$ EA model [24 (e)]. The extrapolated results for infinite size square lattice is $E_0 = -1.401 \pm 0.0015$ and for the simple cubic lattice it is $E_0 = -1.786 \pm 0.004$. Ground states of $3d$ EA $\pm J$ Ising spin glasses were calculated with a hybrid of genetic algorithm and local optimisation. The ground state energy per spin for an infinite system determined with extrapolation was $E_0 = -1.7863 \pm 0.0004$ [21]. The same method applied for $3d$ EA spin glass with exchange interactions of Gaussian distribution yields $E_0 = -1.7003 \pm 0.0008$ [21]. Stevens et al. applied mutation algorithm for determining the ground state energy for $3d$ EA $\pm J$ Ising spin glass and they obtained $E_0 = -1.75$ [24 (g)]. A new general purpose heuristic method called *extremal*

optimization was employed by Boettcher et al. to find ground state energy for the $\pm J$ Ising spin glass for 3 and 4 dimensions. They obtained $E_0 = -1.7857$ for $3d$ and $E_0 = -2.0909$ for $4d$ [24 (h)]. Quantum annealing of an EA spin glass in two dimensions (square lattice) using a transverse field for large lattice size (up to 80×80) using the path-integral Monte Carlo technique turned out to be more efficient compared to thermal annealing or classical annealing (CA) of the same system in finding the approximate ground state [24 (i), 24 (j)]. A detailed discussion on this method has been done in Sec. I.2. The residual energy $\epsilon_{res}(\tau) = \epsilon(\tau) - \epsilon_0$ is measured, where ϵ_0 is the true ground-state energy of the system (calculated by the spin-glass server using the branch-and-cut algorithms; see <http://www.informatik.uni koeln.de/lsjuenger/research/spinglass>) and $\epsilon(\tau)$ is the final energy of the system after the total annealing time τ . Classically, for a large class of frustrated disordered system it can be shown, that the residual energy decreases following some power law in the logarithm of the annealing time τ , namely, $\epsilon_{res} \sim (\ln \tau)^{-\zeta}$ with $\zeta \leq 2$ [24 (k)]. The value of exponent ζ can be much higher ($\zeta = 6$) for QA than the Huse-Fisher bound of $\zeta \leq 2$ for classical annealing [1]. For a comparative study of various methods implemented to study the $\pm J$ and Gaussian EA model, see Table 2 and 3.

The ground state energy of the infinite-range SK model was exactly solved by Parisi applying replica-symmetry-breaking (RSB) solution and found $E_0 = -0.7633$ [24 (m)] (earlier the ground state energy was determined by replica-symmetry method as $E_0 = -0.79$ [24 (l)]). The probability distribution function (PDF) of the ground state energy in the SK spin glass model is numerically determined by collecting a large statistical sample of ground states, computed using a genetic algorithm [24 (n)]. It has been shown that the PDF satisfies finite size scaling with a non-Gaussian asymptotic PDF, which can be fitted well by the Gumbel distribution for the m -th smallest element in a set of random variables, with $m \sim 6$. The Gumbel PDF for the m -th smallest element in a set of random variables has the form,

$$g_m(y) = w \exp \left[m \frac{y - u}{v} - m \exp \frac{y - u}{v} \right] \quad (9.12)$$

where u and v are rescaling parameters and w a normalisation constant. The probability distribution function of the ground state energies were also studied by Bouchaud et al. by the method of hierarchical lattices and they also obtained a Gumbel distribution for the SK model with skewness -1.139 and kurtosis 2.4 [24 (o)]. For the EA model the distribution function is Gaussian. Bottcher used the extremal optimisation method to estimate the ground state of the SK model and the value he obtained was $E_0 = -0.76324$ [24 (p)] which is very close to the exact result of Parisi. Another heuristic method called *hysteretic optimisation* method was applied by K.F. Pal [24 (q)]. It is based on the observation that magnetic samples are driven into a low-energy state when demagnetized by an oscillating magnetic field of decreasing amplitude. With this method the ground state energies can be estimated for SK spin glass systems up to 2000 spins. Recently Kim et al. [24 (r)] applied the conformational space annealing

Table 2: Optimisation results for the ground state energy per spin of the $\pm J$ and Gaussian EA model.

<i>Optimization methods employed</i>	Ground state energy/spin for models		
	$\pm J(2d)$	$\pm J(3d)$	Gaussian ($2d$)
Transfer matrix ^(a)	-1.4024 ± 0.0012	-1.76 ± 0.02	-1.31 ± 0.01
Simulated annealing ^(b)	-1.398	-1.791	-1.398
Multicanonical ^(c) simulation		-1.7956 ± 0.0042	
Branch and cut ^(d) technique			-1.3177 ± 0.0014
Genetic algorithms ^(e)	-1.401 ± 0.0015	-1.786 ± 0.004	
Hybrid of genetic ^(f) & local search		-1.7863 ± 0.0004	
Mutation algorithm ^(g)		-1.75	
Extremal optimisation ^(h)		-1.7857	

(a) [18 (a)], (b) ref [12],[24 (b)], (c) [24 (c)], (d) [24 (d)], (e) [24 (e)], (f) ref [21], (g) [24 (g)] and (h) [24 (h)]

Table 3: Optimisation results for the ground state energy per spin of the SK spin-glass model.

<i>Optimization methods</i>	Ground state energy/spin for SK spin glass
Replica symmetric method ^(a)	-0.79
Replica symmetry breaking ^(b)	-0.7633
Extremal optimisation ^(c)	-0.76324
Conformational space annealing ^(d)	-0.76321

(a) [24 (l)], (b) [24 (m)], (c) [24 (p)] and (d) [24 (r)]

to study the energy landscape of $\pm J$ SK model. They investigated the model up to system size $N = 2047$ which is till now the largest one. They found that the average ground-state energy as $\langle E_0 \rangle_N = \langle E_0 \rangle_\infty + aN^{-\omega}$ with $\omega = 0.672$ and $\langle E_0 \rangle_\infty = -0.76321$.

9.3 Details of a Few Optimization Techniques

There are some excellent deterministic algorithms for solving certain optimization problems exactly [6]. These algorithms are, however, small in number and strictly problem specific. For NP or harder problems, only approximate results can be found using these algorithms in polynomial time. Even if one can solve a NP -complete problem up to a certain approximation using some polynomial algorithm, that does not ensure that one can solve all other NP problems using the same algorithm up to the said approximation in polynomial time. Thus one has to look for some heuristic algorithms, which are based on some stochastic iterative movements. In this chapter we will discuss three such techniques namely the local search, simulated annealing and quantum annealing.

9.3.1 Local Search

In this algorithm one begins with a random configuration C_0 and makes some local changes in the configuration following some rules (stochastic or deterministic) to generate a new configuration C_1 and calculates the change in cost. If the cost is lowered then the change is accepted, otherwise the old one is retained. In the next step another such local change is attempted and thus an iterative procedure is carried on which steadily reduces the cost locally. When no further lowering is possible by any other local moves, the algorithm is stopped. In most optimization problems, there occurs many local minima in the cost configuration landscape which are far above the global minimum. Most often this algorithm leads to one of those local minima and thus we end up with a poor approximation. One can again start with some new initial configuration and get the best out of it. So an exhaustive search for the global minimum requires an exponentially large number of searches (2^N and $N!$ order of searches for an N -spin spin glass and an N -city TSP respectively).

One such heuristic method based on local search is the *Nearest-Neighbour* algorithm. In the context of TSP problem it can be explained as follows:

Choosing an arbitrary city as the starting point, the traveler moves to the nearest unvisited city. Following the above mentioned prescription, the traveler traverses all the cities and finally comes back to the starting point and hence estimates the total cost. The entire process is repeated by starting from other cities as starting points. The running time necessary for this algorithm is $O(N^2)$. For N cities randomly distributed on a plane, the average length we get from this algorithm is $1.25 \times$ *exact shortest length* [11, 25].

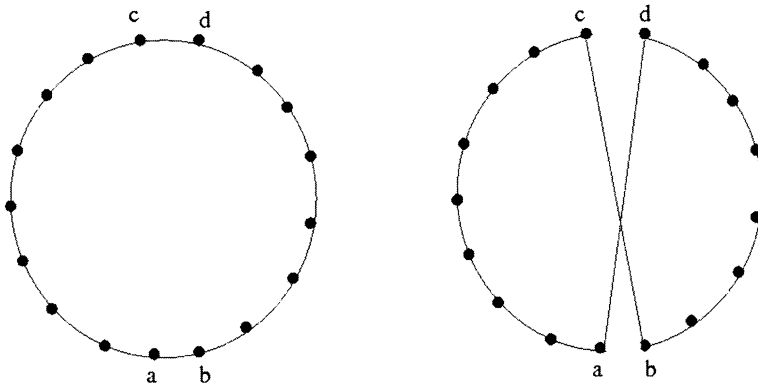


Figure 9.4: A 2-opt move

Another heuristic algorithm is the *greedy algorithm* [25]. In this algorithm, we view an instance as a complete graph with the cities as vertices and with an edge of length $l(c_i, c_j)$ between each pair $\{c_i, c_j\}$ of cities. A tour is then a Hamiltonian cycle in this graph, i.e., a connected collection of edges in which every city has degree 2. The cycle is build up as by starting with the shortest edge and repeatedly adding the shortest remaining available edge, where an edge is *available* if it is not yet in the tour and if adding it would not create a degree-3 vertex or a cycle of length less than N . The run time in this case is $O(N^2 \log N)$, which is somewhat slower than *Nearest-Neighbour* algorithm.

There is another heuristic algorithm called the *pair-exchange* heuristic [11, 25] where iteratively two edges are removed and replaced with two different edges that reconnect the fragments created due to edge removal and fetch a shorter tour. It is also called ‘2-opt’ method (Fig. 9.4) which is the general case of ‘ k -opt’ heuristic where k mutually disjoint edges are deleted and reconnected so that no isolated subtours exist. The most popular of them is the ‘3-opt’ method (Fig. 9.5) introduced by Shen Lin of Bell Labs in 1965 [11]. Instead of fixing the number k , Shen Lin and Brian Kernighan formulated a variable-opt method where they grow the set as the search process continues [13 (b)]. It was first published in 1973 and for two decades it was the most reliable one.

9.3.2 Simulated Annealing

In many optimization problems there occur many local minima in the cost-configuration landscape which are far away from the global one. Local search algorithms may lead to one of those minima and thus we end up with a wrong ground state. Starting with another new configuration may lead to another such local minima and after a large number of trials we have to sort out the best one. One way of escaping from these local minima is to introduce some noise or fluctuations in the searching process so that the searching is not uni-

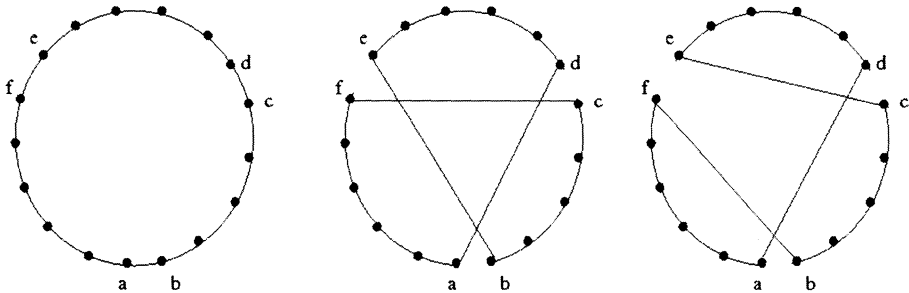


Figure 9.5: Two possible 3-opt moves.

directional (towards lower energy configuration) but also a finite probability towards higher energy states. This fluctuation may be classical or quantum.

When the fluctuation is imposed as temperature it is called *simulated annealing*. *Annealing* is a common technique used in metallurgy, where a material is heated and then cooled down slowly to increase the size of its crystals and reduce their defects. The heating helps in exploring the higher energy states (escaping from local minima) and the slow cooling gradually leads the system towards lower energy states than the previous ones. In the *simulated annealing* technique an “artificial” temperature T is introduced in the problem such that the transition probability from a configuration C_i to a configuration C_f is given by $\min\{1, \exp(-(\Delta_{if}/T))\}$, where $\Delta_{if} = E_f - E_i$, with E_k denoting the cost or energy of the configuration C_k [1]. The temperature T is reduced slowly from a high initial value following some annealing schedule. Here both ‘uphill’ as well as ‘downhill’ moves are allowed, but increasingly downhill as T approaches zero. This method was independently described by S. Kirkpatrick, C. D. Gelatt and M. P. Vecchi in 1983 [12] and by V. Cerny in 1985 [26]. The TSP was one of the first problems to which simulated annealing was applied. The general scheme is as follows:

1. Start with a solution C_i .
2. Determine a starting temperature T .
3. Choose a random neighbor C_f of C_i .
4. Set $\Delta_{if} = \text{Cost}(C_i) - \text{Cost}(C_f)$
5. If $\Delta \leq 0$, $C_i = C_f$ (downhill move)
 - else
 - Choose a random number r uniformly from $[0,1]$
 - If $r < e^{-\Delta/T}$, $C_i = C_f$ (uphill move)
6. Lower the temperature T until the state get frozen.

If the temperature is reduced logarithmically,

$$T(t) \geq N / \ln t \quad (9.13)$$

where t denotes the cooling time and N the system size, the global minimum is attained with certainty in the limit $t \rightarrow \infty$ [27]. But such a temperature schedule will take a longer time than finding by exhaustive search and is thus irrelevant in practical applications. Researchers have also used faster annealing schedules e.g., $T(t) \sim C^t$, where $C < 1$. This can be realized by performing a fixed number of trials at each temperature, after which the temperature is reduced by a typical factor of 0.98. In such *exponential cooling* scheme, the temperature will reach a value sufficiently close to zero after a polynomially bounded time and no further uphill movements are possible (freezing set in) [25].

9.3.3 Quantum Annealing

The simulated annealing technique can suffer severe set back in case of implementing it for a “non-ergodic” system. In such systems the degeneracy increases exponentially with the system size. Moreover the local minima are separated by $O(n)$ sized energy barriers, and at any finite temperature thermal fluctuations is not enough to relax the system to the global minimum by crossing those large barriers. This problem can be overridden (in many cases) by implementing quantum fluctuation and the method is called *quantum annealing*.

In quantum annealing, one adds a quantum kinetic term (say $\mathcal{H}'(t)$) with the classical one (say \mathcal{H}_0 , that has to be optimized) and reduces the quantum term from a very high initial value to zero. One can then solve the time-dependent Schrödinger equation

$$i\hbar \frac{\partial \psi}{\partial t} = [\mathcal{H}_0 + \mathcal{H}'(t)] \psi = \mathcal{H}_{tot} \psi \quad (9.14)$$

for the wave function $\psi(t)$ of the entire system $\mathcal{H}_{tot} = \mathcal{H}_0 + \mathcal{H}'(t)$. The kinetic term $\mathcal{H}'(t)$ helps the system in tunnelling through the barriers and thus come out of the local traps (Fig. 9.6). Initially the tunneling term is much higher than the classical part, so the ground state is realizable trivially. The reduction of the kinetic term is done adiabatically, it assures that the system eventually settles (at $t \rightarrow \infty, \mathcal{H}'(t) \rightarrow 0$) in one of the eigen states of \mathcal{H}_0 which is hopefully the ground state. The tunnelling term makes the apparently large barriers transparent to the system and thus the system can visit any configuration with a finite probability.

Now the crucial point in this method is the choice of $\mathcal{H}'(t)$ which can be written as $\Gamma(t)\mathcal{H}_{kin}$ where Γ is the parameter that controls the quantum fluctuations. Initially Γ is kept high so that the \mathcal{H}_{kin} term dominates. Following a certain annealing schedule this Γ term is brought to zero and as mentioned in the previous paragraph if the decrement of Γ is slow enough, the adiabatic theorem of quantum mechanics [28] assures that the system will always remain at the instantaneous ground state of the evolving Hamiltonian \mathcal{H}_{tot} . As Γ is

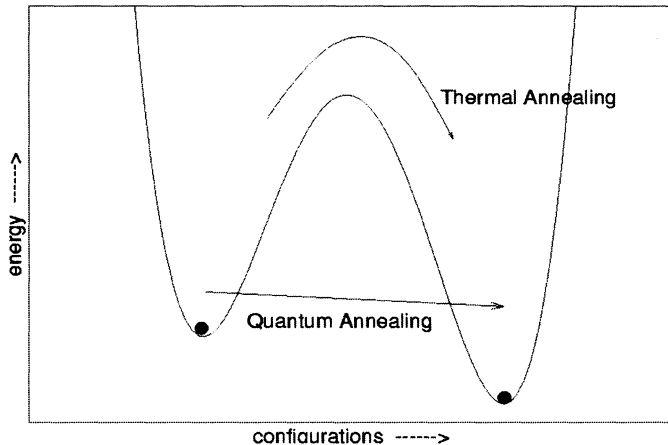


Figure 9.6: Schematic diagram of the advantage of quantum annealing over classical annealing.

finally brought to zero, \mathcal{H}_{tot} will coincide with \mathcal{H}_0 and the desired ground state is reached.

Quantum annealing can be done in several ways:

- (1) Quantum Monte Carlo annealing
- (2) Quantum annealing using real time adiabatic evolution
- (3) Annealing of a kinetically constrained system
- (4) Experimental realizations

In this chapter we will discuss only about Quantum Monte Carlo annealing.

Quantum Monte Carlo annealing:

This can be done for either finite or zero temperature. Most of the quantum Monte Carlo are done for finite temperature [29, 30], namely the path-integral Monte Carlo since it is quite simpler than zero temperature Monte Carlo methods. Again the zero temperature Monte Carlo can be done by zero temperature transfer-matrix Monte Carlo [31] and the Green's function Monte Carlo [30].

The Quantum Monte Carlo technique that has so far been used mostly is the path-integral Monte Carlo (PIMC). The basic idea of this method lies on the Suzuki-Trotter formalism [32] to map a quantum problem to a classical one. Suzuki-Trotter formalism is essentially a method to transform a d -dimensional quantum Hamiltonian into a $d + 1$ -dimensional effective classical Hamiltonian giving the same canonical partition function. As this formalism is very crucial in implementing the annealing technique, let us illustrate this mapping with an

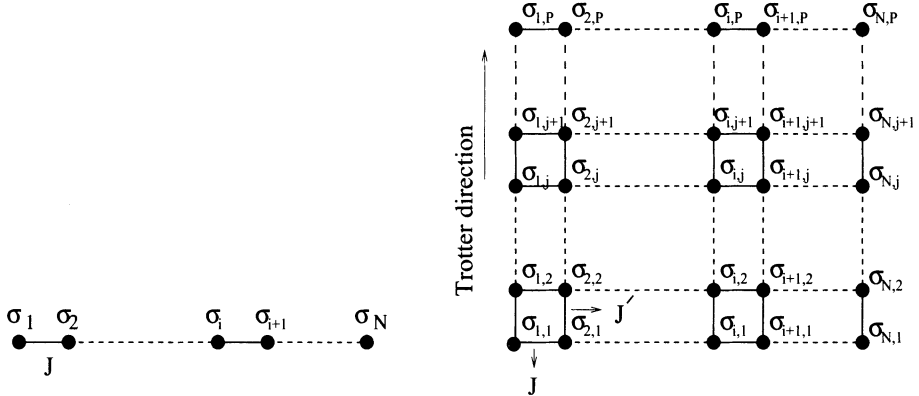


Figure 9.7: The Suzuki-Trotter mapping for a quantum one dimensional chain (shown only on the left) and an equivalent (1+1) dimensional classical system (shown only on the right). J denotes the spin-spin interaction and J' indicates the additional interaction in the Trotter direction.

example. Let us take the case of the transverse Ising system which is described by the Hamiltonian,

$$\mathcal{H}_{tot} = - \sum_{i < j}^N J_{ij} s_i^z s_j^z - \Gamma \sum_i^N s_i^x \quad (9.15)$$

By Suzuki-Trotter formalism this d -dimensional quantum model can be mapped to a $d + 1$ -dimensional classical one where the effective Hamiltonian is,

$$\mathcal{H}_{cl} = \sum_{(i,j)} \sum_{k=1}^P \left[-\frac{J_{ij}}{P} \sigma_{i,k} \sigma_{j,k} - \frac{J'}{P} \sigma_{i,k} \sigma_{i,k+1} \right],$$

where

$$J' = -(PT/2) \ln(\tanh(\Gamma/PT)). \quad (9.16)$$

Thus now corresponding to each quantum spin σ_i we have an array of P number of classical replica spins $\sigma_{i,k}$ and this new (time-like) dimension along which these classical spins are spaced is known as Trotter dimension (Fig. 9.7). Also, in addition to the previous interaction term J_{ij} , there is an additional nearest neighbour interaction J' along the Trotter direction.

Quantum annealing of a Hamiltonian \mathcal{H}_{tot} using the PIMC method consists of mapping \mathcal{H}_{tot} to its equivalent classical one and simulate it at some fixed low temperature so that thermal fluctuations are low. The quantity that is measured is the residual energy $\epsilon_{res}(\tau) = \epsilon(\tau) - \epsilon_0$, with ϵ_0 the true ground-state energy of the finite system and $\epsilon(\tau)$ the final energy of the system after reducing the transverse field strength Γ from some large initial value to zero in

a time τ . This method was first implemented by Kadowaki and Nishimori [33] in solving the TSP problem, and an extensive use of the technique was done by Santoro and Tosatti [30].

The Green's function Monte Carlo algorithm effectively simulates the real-time evolution of the wave-function during annealing which often requires *a priori* knowledge of the wave-function [30]. But as such *a priori* knowledge is not available in a number of systems (random optimization problems), the application of this algorithm seems to be very restricted.

The zero temperature transfer-matrix Monte Carlo samples the ground state of the instantaneous Hamiltonian (specified by the given value of the parameters at that instant) using a projective method, where the Hamiltonian matrix itself (a suitable linear transformation of the Hamiltonian that converts into a positive matrix, in practice) is viewed as the transfer matrix of a finite-temperature classical system of one higher dimension [1]. But the sparsity of the Hamiltonian matrix for systems with local kinetic energy terms leaves the classical system highly constrained and thus difficult to simulate for large system sizes.

Quantum annealing of the TSP:

As mentioned earlier, Quantum annealing of the TSP with a random metric (i.e., the distance d_{ij} between i th and j th cities is chosen randomly) in infinite dimension using the PIMC method was found to be more efficient than simulated annealing in finding an approximately minimal tour [16]. We will focus only on the symmetric case, where $l_{ij} = l_{ji}$. The problem can be transformed into a form where one minimizes an Ising Hamiltonian under some constraints, which we will discuss below. A tour can be represented by an $N \times N$ matrix \mathbf{T} whose elements are either 0 or 1. In case of a certain tour if the city j is visited immediately after visiting the city i , then $\mathbf{T}_{ij} = 1$ otherwise $\mathbf{T}_{ij} = 0$. Every city has to be visited once and only once in a tour. So obviously a valid tour can be represented by a matrix \mathbf{T} whose each row and each column must contain one and only one element equal to 1 and the rest are 0. For a symmetric metric, it is more convenient to work with an undirected tour matrix $\mathbf{U} = \frac{1}{2}(\mathbf{T} + \mathbf{T}^t)$, where \mathbf{T}^t , the transpose of \mathbf{T} , represents the reverse of the tour given by \mathbf{T} . Now the newly generated matrix \mathbf{U} must be a symmetric matrix having two and only two distinct entries equal to 1 in each row and column, with no two rows or two columns are identical. In terms of the \mathbf{U}_{ij} 's, the length of a tour can be represented by

$$\mathcal{H} = \frac{1}{2} \sum_{i,j=1}^N l_{ij} \mathbf{U}_{ij} \quad (9.17)$$

One can rewrite the above Hamiltonian in terms of Ising spins S_{ij} 's as

$$\mathcal{H} = \frac{1}{2} \sum_{i,j=1}^N l_{ij} \frac{(1 + S_{ij})}{2} \quad (9.18)$$

where $S_{ij} = 2U_{ij} - 1$ are the Ising spins. This Hamiltonian is similar to that of non-interacting Ising spins on an $N \times N$ lattice, with random fields l_{ij} on the lattice points $\{i, j\}$. Now to do annealing, one needs to introduce some spin-flip operations that satisfies the N^2 constraints. In the quantum case one needs to design a special transverse field (non-commuting spin-flip term) to enforce the constraints. The 2-opt move (discussed earlier) can be represented by four spin-flip operators:

$$S_{\langle k,i \rangle}^+ S_{\langle l,j \rangle}^+ S_{\langle j,i \rangle}^- S_{\langle l,k \rangle}^-$$

where the operator $S_{\langle i,j \rangle}^-$ flips down ($+1 \rightarrow -1$) the Ising spins $S_{\langle i,j \rangle}^z$ and $S_{\langle j,i \rangle}^z$ ($S_{\langle i,j \rangle}^z = (2U_{ij} - 1) = \pm 1$), when they are in the $+1$ state, and similarly for the flip-up operators $S_{\langle i,j \rangle}^+$. The quantum Hamiltonian for the TSP which implements the two-opt moves is

$$\begin{aligned} H &= H_{pot}(U) + H_{kin} \\ &= \sum_{\langle ij \rangle} l_{ij} \frac{S_{\langle ij \rangle}^z + 1}{2} \\ &\quad - \frac{1}{2} \sum_{\langle ij \rangle} \sum_{\langle i'j' \rangle} \Gamma(i, j, i', j'; t) \times [S_{\langle i',i \rangle}^+ S_{\langle j',j \rangle}^+ S_{\langle j,i \rangle}^- S_{\langle j',i' \rangle}^- + H.C.] \end{aligned}$$

where $H_{pot}(U)$ represents the classical potential energy of a given configuration (in this case, the length of a tour) and H_{kin} is a suitable kinetic energy operator providing the necessary quantum fluctuations which is eventually annealed to zero. Here the quantum coupling Γ is a real positive function and depends on both the links and and on time. The first term of the Hamiltonian represents a random external magnetic field at each site $\langle i, j \rangle$ depending on the intercity distance l_{ij} . To circumvent some difficulties, a drastic simplification is done to the kinetic term and it is replaced by a standard Ising form:

$$\tilde{H} = \sum_{\langle ij \rangle} l_{ij} \frac{S_{\langle ij \rangle}^z + 1}{2} - \Gamma(t) \sum_{\langle ij \rangle} [S_{\langle j,i \rangle}^+ + H.C.] \quad (9.19)$$

As discussed earlier, a standard benchmark TSP problem, namely, the printed circuit board instance pr1002 of the TSPLIB [17] was chosen by Martonak [16] to make a comparative study between quantum and simulated annealing. The optimal tour length $L_{opt} = 259045$ for this TSP problem is known exactly by other *ad hoc* algorithms [16]. The simulated annealing was done by a standard Metropolis Monte Carlo method with a temperature schedule starting from T_0 and decreasing linearly to zero in a Monte Carlo time τ . An optimal initial temperature was identified below which the cooling curves for various values of τ 's start to differ. This is called “*dynamical temperature*” (T_{dyn}) and it was obtained to be 100. For QA, a Path Integral Monte Carlo method was implemented for the \tilde{H} at a fixed low temperature $T = 10/3$. The quantum model is

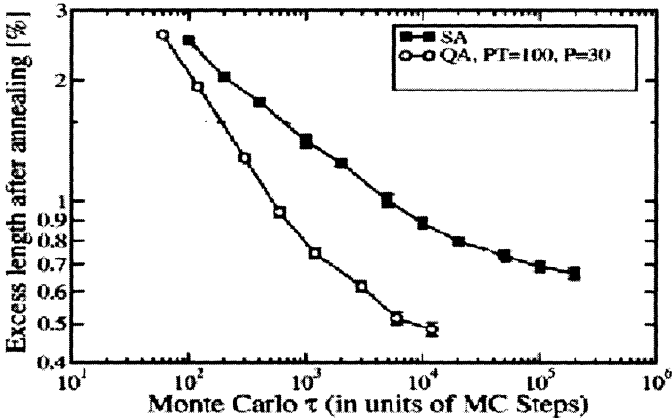


Figure 9.8: Average residual excess length found after Monte Carlo annealing for a total time τ (in MC steps), for the $N = 1002$ instance pr1002 of the TSPLIB. Quantum annealing provides residual excess lengths decaying faster than classical annealing [16].

mapped onto a classical model with an extra imaginary-time dimension, consisting of $P = 30$ ferromagnetically coupled replicas of the original spin problem at temperature PT (an obvious choice is to take $PT \sim T_{dyn}$). The transverse field Γ is annealed linearly from an initial value $\Gamma_0 = 300$ to a final value zero in a MC time τ . In both the methods, two-opt moves was used with a static neighbourhood pruning [25], which restricts the two-opt moves by allowing only a fixed number ($M = 20$) of nearest neighbours of city j to be chosen for j' . Each MC step comprises MN attempted two-opt moves (for QA, for each of the P replicas). 96 independent searches was accomplished for both the methods to average the best tour length.

Fig. 9.8 shows the results obtained for the residual error (average best-tour excess length) upon annealing for a total MC time τ , $\epsilon_{exc} = [\bar{L}_{best}(\tau) - L_{opt}] / L_{opt}$, both with SA (filled squares) and QA (open circles). The results clearly show that QA anneals more efficiently than SA.

Quantum annealing of the 2d EA spin-glass:

The quantum annealing of the 2d Edwards-Anderson (EA) model was done by Martonak et. al. [24 (i), 24 (j)] by PIMC method. The Hamiltonian of the EA model is

$$H_{EA} = - \sum_{\langle ij \rangle} J_{ij} s_i s_j \quad (9.20)$$

where $s_i = \pm 1$ are the Ising spins that occupy the sites of a d -dimensional cubic lattice, and J_{ij} are the random couplings between nearest-neighbour sites drawn from some distribution. When the couplings fluctuate randomly without a defi-

nite sign, the Hamiltonian describes a frustrated and disordered system. To find the ground state is a computationally hard problem and in three dimension it is NP complete (the ground state cannot be attained with an algorithm whose time increases as any finite power of the system size). By adding a magnetic field in the transverse direction one obtains the Ising spin glass in transverse field,

$$\mathcal{H}_{tot} = - \sum_{\langle ij \rangle} J_{ij} \sigma_i^z \sigma_j^z - \Gamma \sum_i \sigma_i^x \quad (9.21)$$

where σ_i^x, σ_i^z are Pauli matrices corresponding to site i . In order to obtain a path-integral representation of this above mentioned quantum spin-glass we apply to its canonical partition function the standard path-integral technique and map the d -dimensional quantum model onto a $d + 1$ dimensional classical model (already discussed in Sec I.1), the Hamiltonian of which can be written as,

$$\mathcal{H}_{cl} = \sum_{(i,j)}^N \sum_{k=1}^P \left[-\frac{J_{ij}}{P} \sigma_{i,k} \sigma_{j,k} - \frac{J'}{P} \sigma_{i,k} \sigma_{i,k+1} \right],$$

where

$$J' = -(PT/2) \ln(\tanh(\Gamma/PT)). \quad (9.22)$$

Martonak et al. studied the $2d$ EA model with random couplings (uniformly distributed between -2 and 2) on a 80×80 lattice with periodic boundary conditions. At the beginning of the Path Integral Quantum Annealing (PIQA), when the transverse field Γ is very large, the coupling J' between the neighbouring $2d$ layers are very weak and therefore the $(2 + 1)d$ system behaves like a collection of $2d$ systems at temperature PT . One should guarantee that $PT \geq |J|$, where $|J|$ is the average magnitude of coupling. A suitable value of the initial transverse field Γ_0 was chosen by testing several values for each P and T using a short annealing time τ . For $PT = 1$ the optimal value of Γ_0 was 3.0 and for $PT = 1.5$ and 2.0 it was 2.5.

In course of accomplishing the Metropolis algorithm, both local and global moves were allowed. A local move attempt independent spin flips at all sites in all Trotter replicas, whereas a global move means an attempt to flip simultaneously all the replicas of the same spin in all Trotter slices.

The QA procedure consisted of a linear decrease of Γ_0 to the final value $\Gamma = 10^{-8}$. Both P and T are kept constant during annealing. At each value of Γ one Monte Carlo step (MCS) (one local move followed by a global move) per spin is performed and total number of MCS performed during annealing is τ . So the total CPU time required scales with P . Finally, the Trotter slice with the minimum energy is identified and it is taken as E_{final} . The final energy was averaged over 45 realizations.

To compare it with simulated annealing (SA) or classical annealing (CA), they also started from randomly oriented spin configuration and decreased the

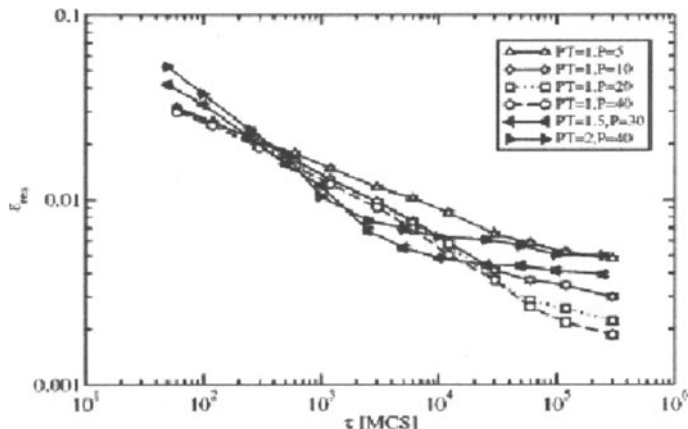


Figure 9.9: Residual energy per site obtained by PIQA for an 80×80 disordered 2d Ising model as a function of τ for different values of parameter PT and Trotter number P [24 (i)].

temperature T linearly from an initial value $T_0 = 3.0$ to zero. At each temperature they performed a MCS and continued for τ steps. The entire measurement was averaged over 45 searches.

The quantity that is measured is the dependence of residual energy $\epsilon_{res}(\tau)$ ($= \epsilon(\tau) - \epsilon_0$) on the annealing time τ . Moreover this dependence also varies inde-

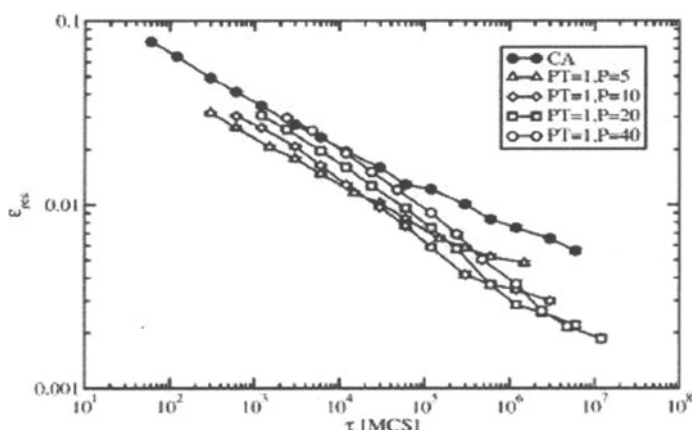


Figure 9.10: Comparison of the residual energy per site for an 80×80 disordered 2d Ising model after CA and PIQA [24 (i)].

pendently with value of PT and P . This has been shown in Fig. 9.9. Fig. 9.10 shows the comparative results for PIQA and CA. According to Huse-Fisher theoretical prediction of a logarithmic dependence of the residual energy on τ , $\epsilon_{res} \sim (\ln \tau)^{-\zeta}$ with $\zeta \leq 2$, the CPU time required to reach a given value of ϵ_{res} can be estimated. To reach the lowest value of $\epsilon_{res} = 1.857 \times 10^{-3}$ in the PIQA simulation, it took a CPU time equivalent to 1.2×10^7 MCS's whereas to reach this value by CA it will take 1.35×10^{11} MCS's. So the gain in CPU time for PIMC with respect to CA is of about four orders.

9.4 Summary

Over the past few decades a lot of effort has gone into designing algorithms to solve various optimization problems. Highly disordered and frustrated systems have very rugged cost function landscape and a challenging task is to determine the ground/optimised states for such systems. We have reviewed the results obtained for the the ground-state energy of various spin glasses employing different optimisation methods. Mapping of other hard problems like the TSP to classical spin glass models and optimization of their cost function has also been discussed. We have also discussed the limitations of the local search algorithms in optimising such problems. Techniques like the simulated annealing [12] (employing classical fluctuations) and the newly discovered quantum annealing technique [1] (employing quantum fluctuations/ tunneling) have already been implemented to study the ground state energies of such glassy systems. Quantum annealing technique has come out to be more efficient than simulated annealing technique in some cases. Experimental realizations of quantum annealing [34] has also established that this method is more effective in exploring the configuration space in the glassy phase than simulated annealing. Solving the NP hard problems in polynomial time, employing quantum annealing techniques, of course remains still an open challenge.

References

- [1] A. Das and B. K. Chakrabarti, *Rev. Mod. Phys.* **80**, 1061 (2008)
- [2] A. Hartmann and H. Rieger, *Optimization in Physics* (Wiley VCH, Darmstadt) (2002)
- [3] J. C. Angles d'Auriac, M. Preissmann and A. Seb, *J. Math. and Comp. Model.* **26** 1 (1997)
- [4] H. Rieger, in *Advances in Computer Simulation*, Lecture Notes in Physics **501** edited by J. Kertesz and I. Kondor, *Springer, Heidelberg* (1998)
- [5] M. J. Alava, P. M. Duxbury, C. Moukarzel and H. Rieger, in *Exact Combinatorial Algorithms: Ground States of Disordered Systems, Phase Transitions and Critical Phenomena* **18** edited by C. Domb and J. L. Lebowitz *Academic Press, New York* (2001)

- [6] C.H. Papadimitriou and K. Steiglitz, *Combinatorial Optimization: Algorithm and Complexity* (Dover, New York) (1998)
- [7] M. R. Garey and D. S. Johnson, *Computers and Intractability: A Guide to the Theory of NP-Completeness* (1979).
- [8] J. Beardwood, J. H. Halton and J. M. Hammersley, *Proc. Camb. Phil. Soc.*, **55**, 299, (1959); R. S. Armour and J. A. Wheeler, *Am. J. Phys.*, **51** (5), 405 (1983).
- [9] A. Chakraborti and B. K. Chakrabarti, *Indian J. Theo. Phys.*, **47** 1 (1999)
- [10] (a) B. K. Chakrabarti, *J. Phys. A: Math Gen.* **19**, 1273 (1986); (b) D. Dhar, M. Barma, B. K. Chakrabarti and A. Taraphder, *J. Phys. A: Math Gen.* **20** 5289 (1987); (c) M. Ghosh, S. S. Manna and B. K. Chakrabarti, *J. Phys. A: Math Gen.* **21** 1483 (1988)
- [11] http://en.wikipedia.org/wiki/Traveling_salesman_problem
- [12] S. Kirkpatrick, C. D. Gelatt, Jr., and M. P. Vecchi, *Science*, **220**, 671 (1983).
- [13] (a) Y. Usami and M. Kitaoka, *Int. J. of Mod. Phys. B*, **11**, 1519 (1997); (b) S. Lin and B. W. Kernighan, *Oper. Res.*, **21**, 498 (1973); (c) A. Percus and O. C. Martin, *Phys. Rev. Lett.*, **76**, 1188 (1996); D. S. Johnson, L. A. McGeoch and E. E. Rothberg, “Proceedings 7th ACM SIAM Symp. on Discrete Algorithms”, Society for Industrial and Applied Mathematics, Philadelphia York, 1996 ; (d) O. Martin, S. W. Otto and E. W. Felten, *Oper. Res. Lett.*, **11**, 219 (1992).
- [14] W. H. Press, S. A. Teukolsky, W. T. Vetterling, B. P. Flannery, *Numerical Recipes in C, Second Edition*, 444 (1992)
- [15] D. E. Goldberg, *Genetic Algorithms in Search, Optimization and Learning* (1989)
- [16] R. Martonak, G. E. Santoro, and E. Tosatti, *Phys. Rev. E*, **70** 057701 (2004)
- [17] <http://www.iwr.uni-heidelberg.de/groups/comopt/software/TSPLIB95>
- [18] (a) K. Binder and A. P. Young, *Rev. Mod. Phys.* **58** 801 (1986); (b) M. Mezard, G. Parisi and M. A. Virasoro, *Spin Glass Theory and Beyond*, World Scientific, Singapore (1987); (c) K. H. Fisher and J. A. Hertz, *Spin Glasses*, Cambridge University Press, Cambridge (1991); (d) J. A. Mydosh Spin Glasses: an Experimental Introduction Taylor and Francis, London (1993); (e) D. Chowdhury, *Spin Glass and other Frustrated Systems*, World Scientific, Singapore (1986); H. Nishimori, *Statistical Physics of Spin Glasses and Information Processing: an Introduction*, Oxford University Press, Oxford (2001)
- [19] F. Tanaka, *J. Phys. C: Solid St. Phys.* **13** L951 (1980)

- [20] F. Barahona, *J. Phys. A*, **15** 3241 (1982)
- [21] K. F. Pal, *Physica A*, **223** 283 (1996); K. F. Pal, *Physica A*, **233** 60 (1996)
- [22] S. Kirkpatrick, *Phys. Rev. B*, **16** 4630 (1977)
- [23] B. Derrida, *Phys. Rev. B*, **24** 2613 (1981)
- [24] (a) I. Morgenstern and K. Binder, *Phys. Rev. B*, **22** 288 (1980); I. Morgenstern and K. Binder, *Z. Phys. B*, **39** 227 (1980); (b) C. M. Soukoulis, K. Levin and G. S. Grest, *Phys. Rev. B*, **28** 1495 (1983); G. S. Grest, C. M. Soukoulis and K. Levin, *Phys. Rev. Lett.*, **56** 1148 (1996); (c) B. A. Berg, T. Celik and U. Hansmann, *Europhys. Lett.*, **22** 63 (1993); B. A. Berg, U. Hansmann and T. Celik, *Phys. Rev. B*, **50** 16444 (1994); (d) C. De Simone, M. Diehl, M. Junger, P. Mutzel, G. Reinelt and G. Rinaldi, *J. Stat. Phys.*, **80** 487 (1995); (e) P. Sutton, D. L. Hunter and N. Jan, *J. Physique*, **4** 1281 (1994); U. Gropengiesser, *J. Stat. Phys.*, **79** 1005 (1995); U. Gropengiesser, *Int. J. Mod. Phys. C* **6** 307 (1995); (f) D. Stauffer, *J. Stat. Phys.*, **74** 1293 (1994); E. S. Rodrigues and P. M. C. de Oliveira, *J. Stat. Phys.*, **74** 1265 (1994); D. Stauffer and P. M. C. de Oliveira, *Physica A* **215** 407 (1995); (g) M. Stevens, M. Cleary and D. Stauffer, *Physica A* **208** 1 (1994); (h) S. Boettcher and A. G. Percus, *Phys. Rev. Lett.* **86**, 5211 (2001); (i) R. Martonak, G. E. Santoro and E. Tosatti, *Phys. Rev. B* **66**, 094203 (2002); (j) G. E. Santoro, R. Martonak, E. Tosatti and R. Car, *Science* **295**, 2427 (2002); (k) D. A. Huse and D. S. Fisher, *Phys. Rev. Lett.* **57**, 2203 (1986); (l) S. Kirkpatrick and D. Sherrington, *Phys. Rev. B* **17**, 4384 (1978); (m) G. Parisi, *Phys. Rev. Lett.*, **43** 1754 (1979); **50** 1946 (1983); (n) M. Palassini, *arXiv:cond-mat/0307713v2*; (o) J.-P. Bouchaud, F. Krzakala and O. C. Martin, *Phys. Rev. B*, **68** 224404 (2003); (p) S. Boettcher, *Eur. Phys. J. B* **46**, 501 (2005); (q) K. F. Pal, *Physica A* **367**, 261 (2006); (r) S-Y. Kim, S. J. Lee and J. Lee, *Phys. Rev. B*, **76** 184412 (2007)
- [25] D. S. Johnson and L. A. McGeoch, in *Local Search in Combinatorial Optimization*, pp. 215-310, edited by E. H. L. Aarts and J. K. Lenstra *John Wiley and Sons, London* (1997)
- [26] V. Cerny, *J. Optimization Theory and Appl.* **45**, 41 (1985)
- [27] S. Geman and D. Geman, *IEEE Trans. Pattern Anal. Mach. Intell.* **6**, 721.
- [28] M. S. Sarandy, L.-A. Wu and D. A. Lidar, *Quantum Inf. Process.*, **3**, 331 (2004)
- [29] A. Das and B. K. Chakrabarti, Eds., *Quantum Annealing and Related Optimization Methods*, Lecture Notes in Physics No. 679 (*Springer-Verlag, Heidelberg*) (2005)
- [30] G. E. Santoro and E. Tosatti, *J. Phys. A* **39**, R393 (2006)

- [31] J. P. Neirotti and M. J. de Oliveira, *Phys. Rev. B* **53**, 668 (1996); M. J. de Oliveira and J. R. N. Chiappin, *Physica A* **307**, (1997); A. Das and B. K. Chakrabarti, *Phys. Rev. E* **78**, 061121 (2008)
- [32] M. Suzuki, *Prog. Theor. Phys.* **46** 1337 (1971); *Quantum Monte Carlo Methods*, Ed. M. Suzuki, *Springer-Verlag, Heidelberg* (1987)
- [33] T. Kadowaki and H. Nishimori, *Phys. Rev. E*, **58** 5355 (1998)
- [34] G. Aeppli and T. F. Rosenbaum, in *Quantum Annealing and Related Optimization Methods*, edited by A. Das and B. K. Chakrabarti, Lecture Notes in Physics No. 679 pp. 159-169 (*Springer-Verlag, Heidelberg*) (2005)

List of Authors

1. Bikas K. Chakrabarti
Theoretical Condensed Matter Physics Division and
Center for Applied Mathematics and Computational Sciences,
Saha Institute of Nuclear Physics,
1/AF, Bidhannagar, Kolkata 700 064
2. Anjan K Chandra
Theoretical Condensed Matter Physics Division and
Center for Applied Mathematics and Computational Sciences,
Saha Institute of Nuclear Physics,
1/AF, Bidhannagar, Kolkata 700 064
3. Samrath Lal Chaplot
Solid State Physics Division,
Bhabha Atomic Research Centre, Mumbai 400 085
4. Deepak Dhar
Department of Theoretical Physics,
Tata Institute of Fundamental Research,
Homi Bhabha Road, Mumbai 400 005
5. Hemant Gangwar
Center for Condensed Matter Theory, Department of Physics,
Indian Institute of Science, Bangalore 560 012
6. Sanjay Kumar
Department of Physics,
Banaras Hindu University, Varanasi 221 005
7. Prabal K Maiti
Center for Condensed Matter Theory, Department of Physics,
Indian Institute of Science, Bangalore 560 012
8. Subhankur Mitra
Solid State Physics Division,
Bhabha Atomic Research Centre, Mumbai 400 085

9. Sanjay Puri
School of Physical Sciences
Jawaharlal Nehru University, New Delhi 110 067
10. Purusattam Ray
Theoretical Physics Division,
Institute of Mathematical Sciences,
C. I. T Campus, Taramani, Chennai 600 113
11. Sitangshu Bikas Santra
Department of Physics,
Indian Institute of Technology Guwahati, Guwahati 781 039
12. Subir K. Sarkar
School of Physical Sciences,
Jawaharlal Nehru University, New Delhi 110 067

Index

- Adsorption, 63
 - polymer Chain, 63
- Alpha-quartz
 - amorphization, 218
- animals, 46–50
- Bethe lattice
 - animals on, 47
- Boron-Nitride Nanotube, 192
- Broyden-Fletcher-Goldfarb-Shano, 249
- Central limit theorem, 72
- characteristic length scale, 147
- clusters, 44–46
- coarsening, 125, 147
- Coil-Globule transition, 62
- Collapse Transition, 64
- conjugacy, 234, 236, 240, 242
- Conjugate Gradient, 231, 234, 238, 245, 249
- convexity of free energy, 15
- correlation function, 17, 25, 130, 136, 147, 148, 150, 153, 157
- Critical exponents, 25, 26, 28
- Critical phenomena, 22
- Critical slowing down, 114
- critical temperature, 42
- Davidon-Fletcher-Powell, 248
- dimensional reduction, 52
- domain growth, 125, 134–136, 147, 149, 153, 156
- duality, 41
- Dynamics of water, 189
- Equal a priori probability, 6
- Ergodicity, 6
- Error
 - Statistical, 105
 - Systematic, 106
- Error Analysis, 105
- event
 - dependent, 69
 - independent, 69
 - mutually exclusive, 69
- Exact Enumeration, 57
 - Application to polymers, 62
- expectation value, 70
- Finite Size Scaling, 106
 - first order phase transitions, 111
 - second order phase transitions, 109
- Fletcher-Reeves, 238, 240, 249
- fluctuation
 - density, 15
 - energy, 15
- Force calculation, 178
- Cell Lists, 181
- Ewald Sum, 182
- Linked List, 181
- Shifted Potential, 179
- Switching Function, 180
- Verlet List, 180
- Fortuin-Kasteleyn mapping, 115
- generalised homogeneous function, 31
- Glauber spin-flip, 131
- growth law, 135, 147, 153, 157

- heaps, 51–53
- high temperature expansion, 39
- high-temperature expansion, 41
- Homogeneity and scaling, 30
- Ising model, 37, 39–42, 44, 50, 100
 - Metropolis importance sampling, 100
- Kawasaki spin-exchange, 143
- kinetic Ising model, 127, 143, 152
- kinetics of phase transitions, 123–125, 151
- Le Chatelier’s principle, 14
- linear response theorem, 16
- local search, 257, 258, 263, 274
- low-temperature expansion, 41
- macroscopic system, 1, 4, 6
- macrostate, 4–7
- Markov chain, 72
- Markov process, 72
 - continuous time, 75
- Martin’s algorithm, 45
- MD boundary condition, 176
- MD integration schemes, 167
 - Hamilton dynamics, 172
 - Higher order integrator, 171
 - Leap-Frog Algorithm, 169
 - SHAKE Alogrithm, 175
 - Velocity-Verlet Algorithm, 170
 - Verlet Algorithm, 168
- Mean-square displacements, 204
- Metastability, 21
- Metropolis algorithm, 99
- microstate, 2–7, 9, 10
 - classical particles, 2
 - quantum particle, 3
- minimization, 231, 233, 234, 240, 241, 243–245, 247
- Model building, 163
 - force calculation, 165
- Models
 - Heisenberg, 27
 - Ising, 27
- q-state Potts, 27
- X-Y, 27
- Monte Carlo, 67, 79
- Monte Carlo Importance Sampling
 - Detailed balance, 98
 - ergodicity, 98
- Monte Carlo Sampling
 - Importance Sampling, 96
 - Simple sampling, 81
- Newton-Raphson, 247
- Optimization, 231
- percolation, 40, 42, 44, 46, 47, 84
- Percolation cluster generation, 88
 - Hoshen-Kopelman algorithm, 88
 - Leath algorithm, 89
- Percolation exponents, 88, 90, 95
- Percolation threshold, 90
- Percolation under external bias, 92
 - directed, 92
 - directed spiral, 93
 - spiral, 92
- phase ordering dynamics, 157
- phase ordering dynamics, 152, 153
- Phase transition, 17, 216
 - first order, 18
 - second order, 22
- Polak-Ribiere, 238, 240, 241, 249
- Polymers, 55, 62
- Probability, 68
 - conditional, 68
- Probability distributions, 71
 - Binomial, 71
 - Normal, 71
 - Poisson, 72
- quantum annealing, 258
- quantum annealing, 253, 263, 266, 271, 274
- Quasi-Newton, 247–249

- Random number generator, 75
 - Congruential method, 76
 - Lagged Fibonacci, 77
 - Shift register, 77
- Random number's quality test, 77
 - Correlation test, 78
 - frequency test, 78
 - parking lot test, 78
- random walk, 82
- Relaxation effects, 114
- residual energy, 268
- residual energy, 261, 274
- SAW, 56, 57
 - on Fractals, 59
- scaling relations, 31
- self-avoiding walk, 55, 83
- Series analysis, 57
- simulated annealing, 272, 274
- simulated annealing, 256, 258, 263, 265, 266, 269, 270
- Solid fullerene, 220
- spin glass, 253, 259–261, 263, 274
- statistical equilibrium, 5
- Statistical definitions
 - response functions, 13
 - thermodynamic quantities, 12
- statistical ensemble, 4
 - canonical, 4, 9
 - grand canonical, 4, 10, 11
 - microcanonical, 4, 7
- steepest descent, 246
- steepest descent, 245–247
- Structural quantities, 206
- structure factor, 147
- Structure factor
 - Dynamic, 200
 - Elastic and incoherent, 203
- structure factor, 136, 137, 148, 153, 157
- Suzuki-Trotter formalism, 267
- Swendsen-Wang algorithm, 116
- symmetry breaking, 21
- thermodynamic equilibrium, 2
- thermodynamic limit, 1, 3, 9, 16
- thermodynamic response
 - functions, 13, 15
- thermodynamic stability, 13
- Thermostat and Barostat
 - Velocity Rescaling Method, 185
 - Weak Coupling, 188
 - Weak Coupling method, 185
- traveling salesman problem, 252, 253
- universality, 25, 28
- variance, 70
- Velocity correlation function, 204
- Wolff algorithm, 118
- Zeolitic pores
 - Diffusion of hydrocarbons, 207
 - zero temperature Monte Carlo, 267